SLAC-R-825

A Precise Measurement of the Pseudoscalar Decay Constant f_{D_s} Using Charm-Tagged Events in e^+e^- Collisions at the $\Upsilon(4S)$

Jörg Stelzer

Stanford Linear Accelerator Center
Stanford University
Stanford, CA 94309

SLAC-Report-825
May 2006

Prepared for the Department of Energy
under contract number DE-AC02-76SF00515

Printed in the United States of America. Available from the National Technical Information Service, U.S. Department of Commerce, 5285 Port Royal Road, Springfield, VA 22161.

A PRECISE MEASUREMENT OF THE PSEUDOSCALAR DECAY CONSTANT f_{D_s} USING CHARM-TAGGED EVENTS IN e^+e^- COLLISIONS AT THE $\Upsilon(4S)$

A DISSERTATION
SUBMITTED TO THE DEPARTMENT OF PHYSICS
AND THE COMMITTEE ON GRADUATE STUDIES
OF STANFORD UNIVERSITY
IN PARTIAL FULFILLMENT OF THE REQUIREMENTS
FOR THE DEGREE OF
DOCTOR OF PHILOSOPHY

Jörg Stelzer
June 2006

I certify that I have read this dissertation and that, in my opinion, it is fully adequate in scope and quality as a dissertation for the degree of Doctor of Philosophy.

Rafe H. Schindler Principal Adviser

I certify that I have read this dissertation and that, in my opinion, it is fully adequate in scope and quality as a dissertation for the degree of Doctor of Philosophy.

JoAnne Hewett

I certify that I have read this dissertation and that, in my opinion, it is fully adequate in scope and quality as a dissertation for the degree of Doctor of Philosophy.

Vera Lüth

I certify that I have read this dissertation and that, in my opinion, it is fully adequate in scope and quality as a dissertation for the degree of Doctor of Philosophy.

David MacFarlane

Approved for the University Committee on Graduate Studies.

Acknowledgements

Doctoral dissertation research is meant to be an individual endeavor, an original contribution to the pool of human knowledge. High energy physics in the past twenty years however has developed into a science where results can come only from the cooperative efforts of many researchers, and where an individual, especially a graduate student must rely on the knowledge and help of many colleagues, friends, and fellow scientists.

First and foremost I thank my adviser, Rafe Schindler, who incessantly tried to pass on to me his profound knowledge in particle physics, and to make me understand the important aspects of scientific research. Especially in the last few month, when I was writing this thesis, I learned to appreciate the always open door to his office and the experience with which he guided me through this process. I'm most grateful that I have had the opportunity to work with and learn from him, and I hope that I can show in the future that his teachings have fallen on fertile soil.

I'd like to express my gratitude to Vera Lüth, JoAnne Hewett, and David MacFarlane, who readily volunteered to be part of my thesis defense committee and whose helpful comments added to the substance of this thesis. Many thanks also to Jerome Friedman for chairing this committee.

It is difficult to mention all the people who have contributed to my education, and who I am indebted to. Standing out is Peter Kim, whose profound knowledge of physics and constant support helped to overcome many hurdles, and whose kindness left a lasting impression. I also truly appreciate the many fruitful discussions I had with Steven Robertson and Bill Dunwoodie which often made me look at problems from a different perspective.

I am especially indebted to my diploma adviser Klaus Schubert and to Bill Wisniewski. They constantly supported me over the years, and I thank them for that.

Many thanks go to Steve Sekula, Paul Jackson, David Stoker, Thomas Moore, Giovanni Batagnani, Gregory Dubois-Felsman, and all members of the leptonic B&c analysis group, who contributed substantially to the success of this analysis.

I was very fortunate to be a member of the SLAC research group E, it was a wonderful experience. For that I thank Martin Perl, Su Dong, and all members of the group. In particular I thank Judy Meo and Melodi Masaniai who not only shielded me and my fellow graduates from the mundane issues of campus and SLAC bureaucracy, but also provided a wonderful atmosphere in which I could fully concentrate on my education and research.

Being far away from home wasn't always easy and I'm glad to have found good friends that I could spend time with. There are Martin Kocian, Brooks Collins, Deanna Nim, and Tom Glanzman, who I had countless dinner parties with; my friends from the early days of *BABAR*: Paul Va'vra and Gavin and Diane Nesom and their little star Katrina; my squash buddy Jochen Schwiening; and our game-night hosts Thomas and Sue Hadig. I had two great roommates, Yosem Companys and Emily Greenberg, and I was lucky to have met their wonderful families. I found good friends among my fellow graduate students: Deborah Berebichez, Hojeong Kim, Leif Wilden, Erhan Yenilmez, Anatoly Svidzinski, Alexandre Ivrii, Josh and Evonne Thompson, Mark Allen, and Kevin Yarritu. All of them I thank for their companionship during these years.

There are three people who have enriched my life at Stanford far beyond what I had imagined and whose friendship I truly cherish: Tetiana Berger-Hryn'ova, Nicolas Berger, and Erkcan Özcan. I'm thankful for the chance that let me meet and share my graduate student experience with them. If nothing else, meeting them made the years at Stanford worthwhile.

Most of all I thank my family for their everlasting, unquestioning support.

Abstract

The decay constant f_{D_s} of the pseudoscalar strange charm meson D_s^+ is an important benchmark test of the theoretical methods that quantitatively describe the non-perturbative low-energy regime of QCD, the theory of the strong interaction. A confirmation of the validity of these predictive methods, foremost lattice QCD, in the sector of heavy-light meson decay constants increases trust in the calculation of f_B, which is an important number for the measurement of the CKM matrix element V_{td} in $B^0\overline{B}^0$-mixing events.

From October 1999 through July 2004, the *BABAR* experiment, located at the PEP-II storage ring at the Stanford Linear Accelerator Center, collected 230.2 fb^{-1} of data in e^+e^- collision at $\sqrt{s} = 10.58\,\mathrm{GeV}$. In this thesis, these data are searched for $e^+e^- \to c\overline{c}$ events by identifying sets of charged and neutral pions and charged kaons, consistent with the decay of a charm meson, D^0, D^+, D_s^+, or D^{*+}. A sample of 510,000 charmed mesons with a momentum consistent with $e^+e^- \to c\overline{c}$ events is identified.

This $c\overline{c}$ event sample is searched for the decay $D_s^{*+} \to \gamma D_s^+ \to \gamma\mu^+\nu$ in the recoil of the charm meson tag, utilizing the knowledge of the tag properties to reduce background in the signal. A total 489 ± 55 decays are found to pass the selection criteria, which are chosen to maximize the significance of the signal yield. A search of the same charm-tagged event sample for the decay $D_s^{*+} \to \gamma D_s^+ \to \gamma\phi\pi^+$ resulted in the isolation of 2093 ± 99 decays, yielding in turn the ratio of the partial decay widths:

$$\frac{\Gamma(D_s^+ \to \mu^+\nu_\mu)}{\Gamma(D_s^+ \to \phi\pi^+)} = 0.143 \pm 0.018_{\mathrm{stat}} \pm 0.006_{\mathrm{sys}}\ .$$

Using the known branching fraction $\mathcal{B}(D_s^+ \to \phi\pi^+) = (4.81 \pm 0.64)\,\%$, the branching fraction $\mathcal{B}(D_s^+ \to \mu^+\nu_\mu)$, and the pseudoscalar decay constant f_{D_s} are calculated:

$$\begin{aligned}\mathcal{B}(D_s^+ \to \mu^+\nu_\mu) &= (6.65 \pm 0.81_{\mathrm{stat}} \pm 0.25_{\mathrm{sys}} \pm 0.88_{\mathrm{norm}})\,\%\,,\\ f_{D_s} &= (281 \pm 17_{\mathrm{stat}} \pm 6_{\mathrm{sys}} \pm 19_{\mathrm{norm}})\,\mathrm{MeV}\,,\end{aligned}$$

where the third error is the uncertainty in $\mathcal{B}(D_s^+ \to \phi\pi^+)$. The precision of this measurement is of the same size as the current world average. Using this measurement and the absolute measurement of f_D by the CLEO-c collaboration, a good agreement with the prediction from lattice QCD calculations is found:

$$\frac{f_{D_s}}{f_D} \Big/ \left(\frac{f_{D_s}}{f_D}\right)_{\mathrm{lattice}} = 1.01 \pm 0.11\ .$$

Yet, the uncertainties are still large and strong statements about the validity of the lattice calculation would be premature.

Preface

If you ask a person working in particle physics “What is your favourite book?” the answer will most likely not be “The ‘Review of Particle Physics’.” Yet, probably no other book has been referenced more often in publications in particle physics as exactly this one. In its current version it includes the results of 21926 measurement, reported in 6415 scientific papers, and is hence the foundation of nearly every new experiment attempted these days.

Some of these (especially the earlier) reported measurements – like the discovery of $\mathcal{P}$ and $\mathcal{CP}$ violation, the J/ψ or the τ particle, the quarks as constituents of matter, or the $W^{\pm}$ and Z^0 as the carriers of the weak and strong force – were very exciting and gave new insights into the underlying physics.

The majority of papers though might have been of less appeal to the person in a public relations office, but they are by no means of less importance. Especially in the last 15 years the emphasis of research has changed. Now it is the fine quantitative detail, precision measurements of branching ratios and assymetries, enabled by the availability of larger datasets and higher energies, that is demanded to pinpoint some of the more challenging open questions of the field.

This does not mean that the subject has turned into merely a boring taxonomic exercise. On the contrary, great theoretical issues are at stake. While the earlier Born approximation did not really test the deeper aspects of the underlying field theory, current measurements and calculations are becoming sensitive enough to do so. In this thesis, a measurement is presented that is trying to push into this realm where the theoretical models can be tested.

The thesis describes the determination of the decay rate of the D_s^+ meson, the lowest energy $c\bar{s}$ bound state, into a muon and a neutrino, $D_s^+ \to \mu^+\nu_\mu$, with very high precision. The decay constant f_{D_s} of the D_s^+ meson, which quantifies the amplitude of the wave-functions of the c and s quark at zero separation, is extracted. A precise knowledge of f_{D_s} enables theorists to validate their methods, such as lattice QCD, quark potential models, or sum rules, all of which relate basic QCD principles to obeservable quantities, and to gauge their predictions in the sector of heavy meson decay constants.

The measurement uses data produced in electron-positron collisions in the PEP-II storage ring and collected by the *BABAR* experiment. Located at the Stanford Linear Accelerator Center, it is the joint adventure of over 600 researchers from 11 countries.

In the first two chapters of this thesis an overview of the Standard Model and of the theoretical underpinnings of leptonic meson decays are presented. In chapter 3 the *BABAR* experiment is introduced, starting with the physics of CP violation in the B meson sector, before describing the accelerator, the PEP-II storage ring, and the *BABAR* detector. Chapter 4 gives an overview about the method used in the $D_s^+ \to \mu^+\nu_\mu$ analysis, which is described in detail in Chapters 5 and 6. The result and the analysis of the systematic uncertainties follow in chapter 7. In chapter 8 the thesis concludes with a discussion of the result and its implications in the field of particle physics.

Contents

List of Tables

List of Figures

Meinen Eltern

Part I

Introduction

Chapter 1

The Building of the Standard Model

In the *Standard Model of Particle Physics* 6 quarks in 3 colors (18 quarks) and 6 leptons and their antiparticles make up the fundamental fermionic constituents of matter. Leptons and quarks appear in three families, which are distinct in their masses, but nearly identical in their interactions. Three of the four forces that act between them and that we observe in nature are described in the Standard Model. The model combines the unified theory of electromagnetic and weak interactions, the GSW Model (after their inventors Glashow, Salam, and Weinberg); and the theory of the strong interaction, quantum chromodynamics or QCD.

1.1 The GSW Model of the Electroweak Interaction

The theory of the electroweak interaction is a non-Abelian gauge theory, with the gauge group $SU(2)_L \times U(1)_Y$. In it the local phase invariance of the Lagrangian is spontaneously broken such that the gauge forces acquire a finite range.

In the lightest family the matter fields are two isospin doublets ψ_L and three isospin singlets ψ_R,

Table 1.1: Charges and isospin of the fermions of the first family in the Standard Model.

Fermion field	Q	T	T_3	Y
$\begin{pmatrix}\nu_{eL}\\ e_L\end{pmatrix}$	$\begin{matrix}0\\ -1\end{matrix}$	$\frac{1}{2}$	$\pm\frac{1}{2}$	-1
e_R	-1	0	0	-2
$\begin{pmatrix}u_L\\ d_L\end{pmatrix}$	$\begin{matrix}\frac{2}{3}\\ -\frac{1}{3}\end{matrix}$	$\frac{1}{2}$	$\pm\frac{1}{2}$	$-\frac{1}{3}$
$\begin{matrix}u_R\\ d_R\end{matrix}$	$\begin{matrix}\frac{2}{3}\\ -\frac{1}{3}\end{matrix}$	$\begin{matrix}0\\ 0\end{matrix}$	$\begin{matrix}0\\ 0\end{matrix}$	$\begin{matrix}\frac{4}{3}\\ -\frac{2}{3}\end{matrix}$

$$\psi_L = \begin{pmatrix}\nu_{eL}\\ e_L\end{pmatrix} \text{ and } \begin{pmatrix}u_L\\ d_L\end{pmatrix}, \quad \text{and} \quad \psi_R = e_R,\ u_R,\ \text{and } d_R.$$

The *weak-isospin* group $SU(2)_L$ reflects the experimental fact that only left-handed fermions and right-handed anti-fermions show up in weak decay spectra. The right-handed neutrino drops out since it is neutral and assumed within the definition of the Standard Model to be massless. The left-handed doublets consist of particles of different charge (Q) within the doublet, making Q not a good quantum number in $SU(2)_L$ (Table 1.1). However, the hypercharge $Y = 2(Q - T_3)$, where T_3 is the third component of the isospin T, is a good quantum number; the corresponding operator is the generator of the $U(1)_Y$ group that commutes with $SU(2)_L$. The free (massless) fermion Lagrangian

$$\mathcal{L}_0 = \sum_i \bar{\psi}_i \imath \partial\!\!\!/ \psi_i \tag{1.1}$$

is invariant under a global $SU(2)_L \times U(1)_Y$ transformation

$$\begin{aligned} SU(2)_L: &\qquad e^{-\frac{\imath}{2} g \omega_i \tau^i} \\ U(1)_Y: &\qquad e^{-\frac{\imath}{2} g' \omega Y}, \end{aligned} \tag{1.2}$$

where the Pauli matrices τ^i are the generators for the $SU(2)_L$. The g and g' are the electroweak coupling constants, and the w's are arbitrary parameters. To achieve local gauge invariance ($w = w(x)$), the Lagrangian is replaced by its covariant form

$$\mathcal{L}_0 = \sum_i \bar{\psi}_i \imath \not{\mathcal{D}} \psi_i + \mathcal{L}_G, \tag{1.3}$$

with the covariant derivative

$$\mathcal{D}_\mu = \partial_\mu + \imath g W_{i\mu} \frac{\tau^i}{2} + \imath g' B_\mu \frac{Y}{2}. \tag{1.4}$$

This introduces the bosonic gauge fields that carry the weak and the electromagnetic force, W_i are the three gauge fields associated with $SU(2)_L$, and B is the $U(1)_Y$ gauge field. $\mathcal{L}_G$ contains the dynamics of the W_i and B.

Mass is given to the fermions and gauge bosons through the *Higgs mechanism*. Two complex scalar fields are added to the theory, which form an isospin doublet

$$\boldsymbol{\phi} = \begin{pmatrix} \phi^+ \\ \phi^0 \end{pmatrix}. \tag{1.5}$$

Their dynamics and couplings to the fermions are given by

$$\begin{aligned} \mathcal{L}_\phi = &(D_\mu \boldsymbol{\phi})^\dagger (D^\mu \boldsymbol{\phi}) - V(\boldsymbol{\phi}) \\ &- \sum_{ij} C_{ij} \left[\bar{\psi}_{iR} (\boldsymbol{\phi}^{(c)\dagger} \psi_{jL}) + (\bar{\psi}_{iL} \boldsymbol{\phi}^{(c)}) \psi_{jR} \right], \end{aligned} \tag{1.6}$$

where the potential $V(\boldsymbol{\phi}) = \mu^2 \boldsymbol{\phi}^\dagger \boldsymbol{\phi} + \lambda (\boldsymbol{\phi}^\dagger \boldsymbol{\phi})^2$ depends on two parameters μ^2 and λ, with $\mu^2 < 0$ and $\lambda > 0$. The C_{ij} are the coupling strengths of the scalar fields to the fermions. Through the mechanism of *spontaneous symmetry breaking* the kinetic term $(D_\mu \boldsymbol{\phi})^\dagger (D^\mu \boldsymbol{\phi})$ will give rise to masses for the gauge bosons, and the Yukawa coupling in $\mathcal{L}_\phi$ to masses for the fermions. That mechanism works on the premise that the scalar field $\boldsymbol{\phi}$ acquires a vacuum expectation value $\boldsymbol{v} = \langle 0 | \boldsymbol{\phi} | 0 \rangle = \binom{0}{v/\sqrt{2}}$, $v = \sqrt{-\mu^2/\lambda}$, as one of the many choices that minimize the potential $V(\boldsymbol{\phi})$. The selection of a particular ground state breaks the $SU(2)_L \times U(1)_Y$ symmetry, and only a residual symmetry $U(1)_Q$ remains. The gauge field associated with this left over symmetry is the photon $A = \sin\theta_W W_3 + \cos\theta_W B$, the massless propagator of the electromagnetic force. Here, $\theta_W = \arctan(g'/g)$ is the *weak mixing angle*. The charged and neutral propagators of the electroweak force, $W^\pm = W_1 \mp \imath W_2$ and $Z^0 = \sin\theta_W W_3 - \cos\theta_W B$, acquire masses $M_{W^\pm} = \frac{gv}{2}$ and $M_{Z^0} = \frac{gv}{2\cos\theta_W}$. Out of the four components of $\boldsymbol{\phi}$, only one survives, the neutral scalar Higgs field H.

The complete electroweak Lagrangian for one fermion family is

$$\mathcal{L}_{\mathrm{EW}} = \sum_i \bar{\psi}_i \left(\imath \not{D} - m_i - \frac{g m_i H}{2 M_W} \right) \psi_i \tag{1.7a}$$

$$- \frac{g}{\sqrt{2}} \sum_i \bar{\psi}_{iL}\, \gamma^\mu \left(T^+ W_\mu^+ + T^- W_\mu^- \right) \psi_{iL} \tag{1.7b}$$

$$- g \sin\theta_W \sum_i \bar{\psi}_i \gamma^\mu Q \psi_i\, A_\mu - \frac{g}{2\cos\theta_W} \sum_i \bar{\psi}_i \gamma^\mu (g_{iV} - g_{iA}) \psi_i\, Z_\mu \tag{1.7c}$$

$$+ \frac{g^2 v^2}{2\sin^2\theta_W} Z_\mu Z^\mu + \frac{g^2 v^2}{4} W_\mu^\dagger W^\mu + \mu^2 H^2 \quad + \quad \mathcal{L}'_{\mathrm{G}}, \tag{1.7d}$$

where $T^\pm$ are the isospin raising and lowering operators, and $g_{iV} = T_3 - 2Q\sin^2\theta_W$ and $g_{iA} = T_3$ are the vector and axial vector couplings of the fermions to the Z^0 boson. $\mathcal{L}'_{\mathrm{G}}$ contains the dynamics and the self coupling of the Higgs and of the gauge bosons. The $m_i = vC_i/2$ are the fermion masses.

It is noteworthy that the interactions of all gauge fields are determined by the electric charge $e = g\sin\theta_W$ and a single free parameter, the Weinberg angle θ_W. This shows beautifully the unification of the weak and electromagnetic interactions.

1.2 The Multigeneration Model

The incorporation of all known leptons and quarks into the theory, is more than a mere replication of the formulation for a single family. The extension to three fermion families brings out many novel features of the Standard Model, such as quark mixing, the suppression of flavor changing neutral currents, and CP violation.

Historically, the discrepancy of the coupling strengths of $\mu \to \bar{\nu}_\mu$, $d \to u$ and $s \to u$ transitions, measured in muon-decays, β-decays and the decays $\Lambda \to p e^- \bar{\nu}_e$, lead to the conclusion that the isospin partner of the u-quark is a linear combination $d' = d\cos\theta_C + s\sin\theta_C$, where θ_C is the Cabibbo angle. The Cabibbo angle measures the rotation between the *weak interaction* or *flavor eigenstates* d' and s', which participate in the electroweak interaction, and the *mass eigenstates* d and s, which govern the time evolution of the physical particle. The logical extension of this rotation to three quark families is the Cabibbo-Kobayashi-Maskawa (CKM) matrix,

$$V_{\mathrm{CKM}} = \begin{pmatrix} V_{ud} & V_{us} & V_{ub} \\ V_{cd} & V_{cs} & V_{cb} \\ V_{td} & V_{ts} & V_{tb} \end{pmatrix} \tag{1.8}$$

which is commonly given in the Wolfenstein parameterization:

$$V_{\mathrm{CKM}} = \begin{pmatrix} 1-\frac{\lambda^2}{2} & \lambda & A\lambda^3\left[\rho - \imath\eta(1-\frac{\lambda^2}{2})\right] \\ -\lambda & 1-\frac{\lambda^2}{2} & A\lambda^2(1+\imath\eta\lambda^2) \\ A\lambda^3(1-\rho-\imath\eta) & -A\lambda^2 & 1 \end{pmatrix} + \mathcal{O}(\lambda^4)\ , \tag{1.9}$$

where the elements are expanded in powers of $\lambda = |V_{us}| \approx \sin\theta_C$. A, ρ, and η are real numbers. This mixing of mass and flavor eigenstates, which in the Standard Model appears only in the quark sector, modifies the strength of the charged current in the electroweak Lagrangian (1.7b) to

$$-\frac{g}{\sqrt{2}} \sum_{q_1,q_2} \bar{\psi}_{q_1 L}\, \gamma^\mu \left(T^+ W_\mu^+ + T^- W_\mu^-\right) V_{q_1 q_2} \psi_{q_2 L} \tag{1.7b'}$$

The CKM matrix is unitary ($V_{\mathrm{CKM}}^{-1} = V_{\mathrm{CKM}}^\dagger$). It implies

$$V_{ud}V_{ub}^* + V_{cd}V_{cb}^* + V_{td}V_{tb}^* = 0\ , \tag{1.10}$$

which can be visualized by a triangle in the complex plane (Figure 1.1), called the Unitarity Triangle. Other triangles that follow from the unitarity condition have a much shorter third side compared to the other two and are not usually considered.

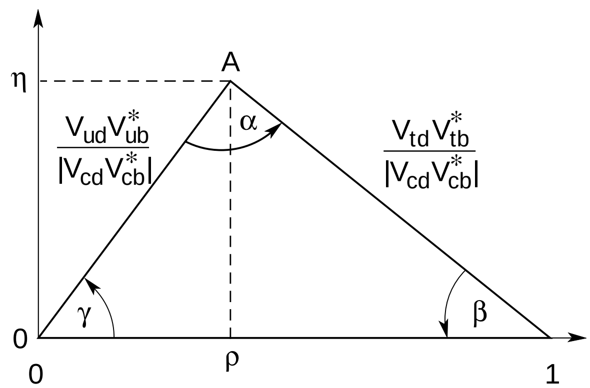

Figure 1.1: The rescaled Unitarity Triangle.

The angles of the Unitarity Triangle are given by

$$\alpha \equiv \arg\left(-\frac{V_{td}V_{tb}^*}{V_{ud}V_{ub}^*}\right),\ \beta \equiv \arg\left(-\frac{V_{cd}V_{cb}^*}{V_{td}V_{tb}^*}\right),\ \text{and } \gamma \equiv \arg\left(-\frac{V_{ud}V_{ub}^*}{V_{cd}V_{cb}^*}\right) = \pi - \alpha - \beta\ . \tag{1.11}$$

Today it is one of the primary goals of flavor physics to precisely determine the parameters of the CKM matrix, and, through independent measurements of the three angles and sides of the Unitarity Triangle, to test the unitarity hypothesis.

1.3 QCD

Quarks have an additional internal quantum number called *color*. Each quark flavor is described by a triplet in color space. QCD, the theory of the strong interaction, is a non-Abelian gauge theory, with an $SU(3)_C$ gauge group, that acts on this color space. Leptons are color singlets and are indifferent to the strong force. Nature is invariant under color transformation

$$SU(3)_C \quad : \quad e^{-\frac{i}{2}g_s\tilde{\omega}_i\lambda^i}, \tag{1.12}$$

where λ_i are the eight 3×3 Gell-Mann matrices that generate the $SU(3)_C$ color group, and g_s is the strong coupling constant. Invariance under the local gauge transformation (1.12) is guaranteed by adding another term to the covariant derivative

(1.4)

$$\mathcal{D}_\mu = \partial_\mu + \imath g W_{i\mu} \frac{\tau^i}{2} + \imath g' B_\mu \frac{Y}{2} + \imath g_s G_{i\mu} \frac{\lambda^i}{2}, \tag{1.4'}$$

Here, the $G_{i\mu}$ are the eight color gauge fields, the *gluons*, that carry the strong force. Because the color symmetry is an unbroken one, gluons are massless.

Quantum chromodynamics with its non-Abelian gauge fields has the property of being *asymptotically free*. The effective strong coupling is not a constant but a function of the energy of the involved particles; it *decreases with growing energy*. At small distances, or large energies, the effective strong coupling is small and quarks behave as free particles. In this regime, perturbative QCD is valid.

On the other hand, the strong interaction becomes *strong* at distances larger than the size of hadrons. In this energy regime, below 1 GeV, quarks and gluons are confined into color-neutral hadrons. The effective coupling becomes unity, rendering perturbative calculations, by expansion in orders of the coupling constant, useless. Instead, calculations of hadronic physics rely on phenomenology and effective field theories, which convert the unknown effects of non-perturbative QCD into parameters or functions to be determined by experiment. An example of this phenomenological approach are the meson decay constants, which will be discussed in the next chapter.

A serious candidate for calculating the low-energy properties of QCD exists, the lattice gauge theory, or LQCD, introduced in 1974 by Ken Wilson [1]. After 30 years of development it is now supported by an overwhelming agreement with experimental data to a precision of less than a few percent [2]. Yet, not all LQCD calculations have reached that level of precision. Decay constants of heavy mesons, for instance, are calculated with an error of $\approx 10\,\%$. The measurement of some of these constants would provide an important tool to verify LQCD methods in a regime where mesons masses are above 1 GeV.

Chapter 2

The Decay Constant of Pseudoscalar Mesons

2.1 Introduction

Charged mesons may decay weakly into a lepton-neutrino pair. In the case of the $\pi^{\pm}$, the lightest meson, this occurs exclusively. Figure 2.1 shows the lowest order Feynman diagram for the leptonic decay of a meson M^+ with quark content $Q\bar{q}$ into a anti-lepton l^+ and its accompanying neutrino ν_l. The quarks on the left side of the diagram

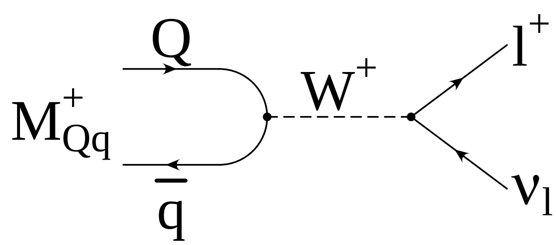

Figure 2.1: Lowest order Feynman diagram for the leptonic decay of a heavy meson in the Standart Model.

are not free, and the long-distance effects, present in the formation of the bound meson state (hadronization) cannot be evaluated directly using perturbative QCD. In general the hadronization effects in hadronic interactions are parameterized with so called

Table 2.1: Expected branching ratios for the leptonic decay modes of the heavy pseudoscalar mesons D^+, D_s^+, and B^+, expected in the Standard Model. A decay constant of 250 MeV is assumed for all three meson types.

Meson M	V_{Qq}	Lepton l	Expected branching ratio
D^+	0.224	e	1.3×10^{-8}
		μ	5.7×10^{-4}
		τ	1.5×10^{-3}
D_s^+	0.996	e	1.2×10^{-7}
		μ	5.2×10^{-3}
		τ	6.0×10^{-2}
B^+	0.004	e	1.6×10^{-11}
		μ	6.8×10^{-7}
		τ	1.5×10^{-4}

form factors, which are functions of the momentum transfer and polarization states of the hadrons involved in the interaction. For leptonic decays of pseudoscalar mesons these parameterization functions are the simplest. The initial state is unpolarized, and the s-channel momentum transfer is constant, $q^2 = m^2$. The form factor becomes a constant f_M, the *decay constant* of the meson M. The matrix element of the decay $M^+ \to l^+\nu_l$ can be written as (see Appendix A for a detailed derivation):

$$\mathcal{M} = \imath \frac{G_F}{\sqrt{2}} V_{Qq} f_M q^\mu \bar{\nu}_l \gamma_\mu (1 - \gamma_5)\, l \tag{2.1}$$

and the partial decay width as:

$$\Gamma(M^+ \to l^+\nu_l) = \frac{G_F^2}{8\pi} |V_{Qq}|^2 f_M^2 m_M m_l^2 \left(1 - \frac{m_l^2}{m_M^2}\right)^2, \tag{2.2}$$

where m_M and m_l are the meson and the lepton masses, respectively, G_F is the Fermi constant, and V_{Qq} is the CKM parameter from the annihilation of the constituent quarks. The partial width is governed by two opposing terms containing m_l^2. The first term, m_l^2, reflects helicity suppression in the weak decay of the spin-0 meson, which requires the lepton to be in its unfavored helicity state. The second term,

$(1 - m_l^2/m_M^2)^2$, is a phase space factor. As a result, the ratio of $\tau : \mu : e$ decays of the D_s^+ is $10 : 1 : 0.00002$. From (2.2) the branching ratios can be calculated using the well known heavy meson lifetimes τ_M,

$$\mathcal{B}(M^+ \to l^+\nu_l) = \tau_M \; \Gamma(M^+ \to l^+\nu_l) \; . \tag{2.3}$$

The Standard Model expectation for the branching ratios are listed in Table 2.1, assuming a decay constant for all three mesons of 250 MeV.

2.2 Theoretical Predictions for f_M

Over the years theoretical physicists have developed a large number of tools and methods to predict the observable properties of elementary particles in nature. Especially important are those tools that work in the domain of low-energy QCD. Because of the large number of calculable observables, stringent tests on the validity of these methods can be performed; the evolution of theoretical predictability of nature goes hand in hand with the advances in experimental prowess.

Some of the methods work on first principles, like the *static quark potential models*, *QCD sum rules*, or *lattice QCD*. They need only very basic input from the experiment, such as quark masses or vacuum expectation values. Other methods exploit symmetries of nature that arise under certain conditions, for instance the *heavy quark symmetry*, valid at quark masses much above Λ_{QCD}, or the *chiral symmetry*, in which the light quarks are massless. Also mentioned later is the more specific *factorization ansatz*, which explores the necessary conditions so that the rate of a hadronic decay involving a meson M can be used to deduce the decay constant f_M.

2.2.1 Static Quark Potential Models

In systems containing at least one heavy quark, such as the charm and bottom mesons, one of the earliest models created to explain the observed masses uses a non-relativistic

Schrödinger equation, with a quark potential

$$V(r) = \frac{4\alpha_s(r)}{3r} + \kappa r + \frac{8\pi\alpha_s \boldsymbol{S_Q} \cdot \boldsymbol{S_q}}{3m_q m_Q}\delta^3(\boldsymbol{r}) \ . \tag{2.4}$$

The first and third term represent the coulomb-like and hyperfine effects of single gluon exchange, respectively. The linear term is a phenomenological spin-independent confining potential. In this model, the pseudoscalar decay constant is related to the amplitude of the meson wavefunction at the origin,

$$f_M^2 = \frac{12}{M}|\psi(0)|^2 \ . \tag{2.5}$$

2.2.2 QCD Sum Rules

QCD sum rules were among the first to predict f_B and f_D [3–6]. This method was developed by Shifman, Vainshtein, and Zakharov in 1979 [7]. Sum rules are derived by representing hadrons by their constituent quark currents. The correlation function of these currents is treated in the framework of operator product expansion, where short and long-distance strong interactions are separated. While the former are calculated using perturbative QCD, the latter are parameterized in terms of universal vacuum expectation values of the quark and gluon fields. The result of the QCD calculations is then matched, via a dispersion relation, to the sum over all possible hadronic states. The set of sum rules obtained this way can be used to relate parameters of QCD such as quark masses and vacuum expectation values and observable low-energy parameters such as hadron masses and decay constants to each other. By gauging the underlying QCD parameters, experimental input from one sector, for instance the charmonium mass spectrum, can then be used to compute parameters in other sectors, such as f_{D_s}. Using the technique of QCD sum rules, a recent calculation [8] finds

$$f_{D_s} = (235 \pm 24)\,\text{MeV}, \ f_D = (205 \pm 20)\,\text{MeV}, \ \text{and} \ f_B = (203 \pm 23)\,\text{MeV} \ . \tag{2.6}$$

2.2.3 Heavy Quark Effective Theory

Heavy Quark Effective Theory (HQET) works in the limit of infinite quark mass, $m_Q \to \infty$. In this limit the heavy quark Q of a hadronic bound state, H_Q, decouples from the light quarks and gluons. In this limit Q acts as a static source of the gluon gauge field, which is independent of the mass m_Q and of the flavor of Q. In addition, the light quarks and gluons are insensitive to the spin of the heavy quark, since the chromomagnetic moment of the heavy quark, $\mu_Q = g_s/2m_Q$, vanishes in the heavy quark limit. Hence, the mass splittings of various hadrons H_Q^i, where i indicates different light quarks, are independent of m_Q and of the total spin of H_Q. This is called Heavy Quark Symmetry (HQS). It predicts that the pseudoscalar decay constants scale with the heavy quark mass as $f_M \sim m_Q^{-1/2}$.

The HQET formalism turns the qualitative predictions from HQS into quantitative statements, by systematically calculating the corrections that arise from a finite mass of the heavy quark. This is done by simultaneously expanding the QCD Lagrangian in terms of $\Lambda_{\mathrm{QCD}}/m_Q$ and $\alpha_s(m_Q) \sim 1/\ln(m_Q/\Lambda_{QCD})$.

Generally, HQET predictions of decay constants are expressed as ratios, rather than absolute values. That shows the effect of the $1/m_Q$ corrections to the infinite mass approximation, while the low-energy QCD effects cancel in the ratio. In [9] the ratio $\frac{f_B}{f_D}$ is calculated

$$\begin{aligned}\frac{f_B}{f_D} =& \sqrt{\frac{m_c}{m_b}} \left\{ \left(\frac{\alpha_s(m_c)}{\alpha_s(m_b)} \right)^{6/25} \left[1 \right.\right. \\ &\left.\left. + \frac{7}{225} \left(\pi^2 + \frac{1887}{100} \right) \frac{\alpha_s(m_c) - \alpha_s(m_b)}{\pi} + \mathcal{O}\left(\alpha_s^2\right) \right] + \mathcal{O}\left(\frac{\Lambda_{QCD}}{m_{c,b}} \right) \right\}\end{aligned} \tag{2.7}$$

However, with the value of the bare charm quark mass m_c being close to Λ_{QCD}, HQS might break and HQET might not work as well for predicting results in the charm sector.

Table 2.2: Theoretical Predictions from lattice QCD for Heavy Quark Decay Constants. The number n_f is the number of dynamical quarks included in the calculations.

Method	Year	f_B [MeV]	f_{D_s} [MeV]	f_D [MeV]
MILC [11] ($n_f = 0$)	1997	$164(^{+16}_{-14})$	$213(^{+18}_{-16})$	$194(^{+17}_{-14})$
UKQCD [12] ($n_f = 0$)	2001	195(25)	$229(^{+23}_{-12})$	$206(^{+18}_{-11})$
MILC [13] ($n_f = 2$)	2002	$190(^{+28}_{-18})$	$241(^{+29}_{-27})$	$215(^{+19}_{-17})$
MILC/HPQCD [10] ($n_f = 3$)	2005		249(16)	201(17)

2.2.4 Lattice QCD

The most popular and precise method of calculating the effects of the strong interaction at low energies is lattice QCD, where the Minkowski space-time is modeled as a 4-dimensional Euclidean lattice. Matter fields, e.g. the quarks, occupy the coordinates of the lattice, separated by the lattice spacing, a, typically $\approx \mathcal{O}(1\text{ fm})$. The gauge fields, e.g., the gluons, sit on the sites of the lattice, connecting the lattice coordinates, and exchanging four-momentum between the quarks. Observables are calculated by sampling the configuration space of possible quark-gluon arrangements and taking statistical averages. The calculations of lattice QCD can be exact only in the limit of zero lattice spacing $a \to 0$ and an infinitely large lattice volume. Working toward this limit requires immense computing resources, since the computing time grows as $T \propto L^5(1/a)^7$, where L is the lattice size. In addition the lattice simulations require a computationally expensive consideration of the dynamical quarks, or sea-quarks, u, d, and s. This is avoided in the "quenched" approximation, where the dynamical quarks are ignored. Table 2.2 summarizes recent results of lattice calculations of the charged bottom and charm meson decay constants. Reference [10] also provides a value for the ratio $f_{D_s}/f_D = 1.25 \pm 0.07$, which has a 5.4 % uncertainty. The calculation of the ratio f_{D_s}/f_D benefits from the cancellation of uncertainties from the heavy quark discretization and the bare quark masses; the ratio has a better precision than the value of f_{D_s} (6.4 %) alone. In [10] the decay constant f_D is calculated from f_{D_s} and f_{D_s}/f_D.

Problems arise when the considered quark masses are larger than one in lattice units, and the discretization errors are significant. In this case, lattice formulations of effective theories, such as HQET, can be used.

2.2.5 Factorization Ansatz

The decay constant f_{D_s} can also been determined from the hadronic decay $B^0 \to D_s^+ D^-$ [14] [15]. This method requires that in first order the low energy QCD effects present in the formation of the bound mesons states can be factorized into the $B^0 \to D^-$ transition and the D_s^+ formation,

$$\mathcal{B}(B^0 \to D_s^+ D^-)^{\frac{1}{2}} \propto F_0^{BD}(m_{D_s}^2)\, f_{D_s} \ , \tag{2.8}$$

and that the contributions of other processes, like penguin transitions, are small or precisely calculable. A value $f_{D_s} = (259 \pm 74)\,\text{MeV}$ is calculated in [14].

2.3 Experimental Status

Equation (2.2) can be used to calculate the decay constant f_M from the measured decay width $\Gamma(M^+ \to l^+\nu_l)$ and CKM parameter V_{Qq}. For the light mesons π^+ and K^+, where the leptonic branching ratios are high and the matrix elements have small errors of 0.05 % and 1 %, respectively, this has been done to great precision. The light meson decay constants have been determined as $f_{\pi^+} = (130.7 \pm 0.37)\,\text{MeV}$ and $f_{K^+} = (159.8 \pm 1.5)\,\text{MeV}$.

For the heavy mesons D^+, D_s^+, and B^+, experimental data is much more sparse. Helicity suppression makes it virtually impossible to detect the decays $M \to e\nu_e$. The much less suppressed decays $M \to \tau\nu_\tau$ are difficult to reconstruct because of at least two undetectable neutrinos in the final state. Further, the decays of D^+ and B^+ are Cabibbo suppressed.

No B^+ leptonic branching ratio has yet been measured[1]. The *BABAR* and BELLE collaborations have set upper limits on $\mathcal{B}(B^+ \to \tau^+\nu_\tau)$ which are close to the Standard Model prediction. The *BABAR* experiment also quotes an upper limit on f_B but

[1] After this thesis was written BELLE published a measurement $\mathcal{B}(B^+ \to \tau^+\nu_\tau) = 1.06 \pm 0.32_{\text{stat}} \pm 0.17_{\text{sys}}$ and $f_B = 176 \pm 25_{\text{stat}} \pm 20_{\text{sys}}$.

Table 2.3: Decay constants for heavy mesons measured by different experiments. The first and second error are statistical and systematic, respectively. For f_{D_s} the third error, if given, reflects the uncertainty in the branching ratio $\mathcal{B}(D_s^+ \to \phi\pi^+)$ which is used to determine the number of produced D_s^{*+} mesons. The values and errors of f_{D_s} are given as they were quoted in the original publication; they are not adjusted to the recent measurement of $\mathcal{B}(D_s^+ \to \phi\pi^+)$ [16]. The limit on f_B is at 90 % C.L..

Experiment	Year	f_{D_s} [MeV]	f_D [MeV]	f_B [MeV]
MARK-III [17]	1987		< 290	
WA75 [18]	1993	$232 \pm 45 \pm 20 \pm 48$		
E653 [19]	1996	$194 \pm 35 \pm 20 \pm 14$		
BES [20]	1996		$300^{+180+80}_{-150-40}$	
BES [21]	1997	$247^{+108+115}_{-69-7}$		
L3 [22]	1997	$309 \pm 58 \pm 33 \pm 38$		
CLEO [23]	1998	$280 \pm 19 \pm 28 \pm 34$		
BEATRICE [24]	2000	$323 \pm 44 \pm 12 \pm 34$		
OPAL [25]	2001	$286 \pm 44 \pm 41$		
ALEPH [26]	2002	$285 \pm 19 \pm 40$		
CLEOc [27]	2005		$222.6 \pm 16.7^{+2.8}_{-3.4}$	
BES [28]	2005		$371^{+129}_{-119} \pm 25$	
BABAR [29]	2004			< 480
PDG 2004 [30]	2004	267 ± 33		

the extraction from (2.2) includes the large uncertainty of V_{ub}. A measurement of $\mathcal{B}(B^+ \to \tau^+\nu_\tau)$ can be expected within the lifetime of the two experiments, however, it will be difficult to reach a precision on f_B of better than 10 %.

The muonic D^+ decay has been searched for in e^+e^- collisions at the $\Psi(3770)$ resonance, starting with the MARK-III Collaboration, which, in 1987, set the first upper limit for f_D of 290 MeV. Recently, the CLEO-c Collaboration published a measurement for $f_D = (223 \pm 17)$ MeV, and is expected to lower the error on f_D to 2 % in the future. The upgraded BES experiment is also expected to reach that precision, which would give a world combined error of less than 1.5 %.

The leptonic D_s^+ decays $D_s^+ \to \mu^+\nu_\mu$ and $D_s^+ \to \tau^+\nu_\tau$ have been measured by a number of experiments in a variety of environments. Their combined average is 267 MeV, with an error of 12.4 %. In order to measure a D_s^+ meson branching ratio, the produced number of D_s^+ mesons has to be known. This can be accomplished by producing $D_s^{(*)+}D_s^{(*)-}$ pairs at an energy slightly above the production threshold. The identification of one $D_s^{(*)\pm}$ determines the existence of the other. This has been done by the MARK-III and the BES experiment. All other experiments had higher center-of-mass energies and needed to measure the number of produced D_s^+ mesons through another, known, D_s^+ decay channel. The D_s^+ decay which is known most precisely is $D_s^+ \to \phi\pi^+$, with an error on the branching ratio of 14 %, determined in a single measurement by *BABAR* [16]. This uncertainty represents the largest contribution to the error on the combined f_{D_s}.

2.4 Standard Model Extensions

In extensions of the Standard Model one expects small modifications to the $D_s^+ \to \mu^+\nu_\mu$ branching ratio. In a general (supersymmetric) two-Higgs doublet model, the decay can occur via a charged Higgs particle [31].

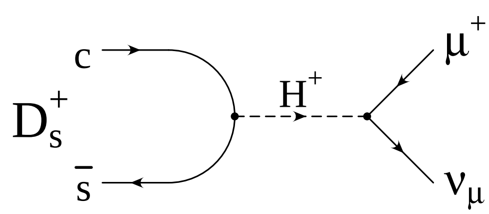

Figure 2.2: Lowest order Feynman diagram for the leptonic decay of a heavy meson in the Two-Higgs Doublet Model.

The decay through a charged Higgs boson modifies the Standard Model predictions by a factor r_H:

$$r_H = \left[1 + \frac{m_{D_s}^2}{m_{H^\pm}^2}\left(1 - \tan^2\beta\frac{m_s}{m_c}\right)\right]^2, \tag{2.9}$$

where $\tan\beta$ is the ratio of the two vacuum expectation values of the two Higgs doublets, and m_s and m_c are the bare masses of the strange and charm quark, respectively. With $m_{D_s}^2/m_{H^\pm}^2 < 0.0007$ (obtained from the lower limit $m_{H^\pm} > 78.6\,\mathrm{GeV}/c^2$ set by

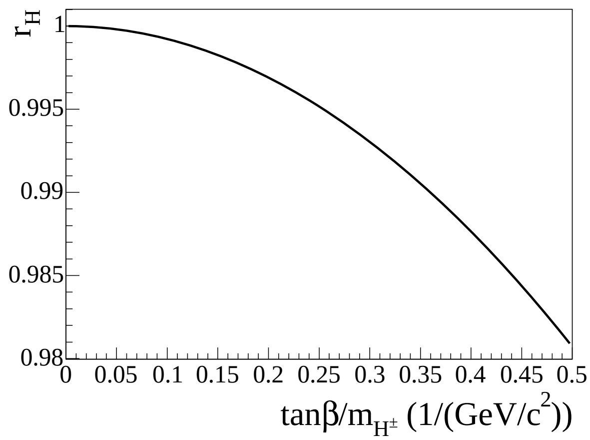

Figure 2.3: Enhancement of the Standard Model D_s^+ leptonic decay branching ratio in the Two-Higgs-Doublet-Model as a function of $\tan\beta/m_{H^\pm}$ according to (2.10). $m_s/m_c = 0.1$ is used.

the LEP experiments [32]), (2.9) can be simplified:

$$r_H \approx \left[1 - \frac{\tan^2\beta}{m_{H^\pm}^2} m_{D_s}^2 \frac{m_s}{m_c}\right]^2 . \tag{2.10}$$

r_H as function of $\tan\beta/m_{H^\pm}$ is shown in Figure 2.3.

Recently, BELLE has set an upper limit on $\tan\beta/m_{H^\pm} < 0.29\,(\mathrm{GeV}/c^2)^{-1}$ [33], using their measured upper limit on $\mathcal{B}(B^+ \to \tau^+\nu_\mu)$. Figure 2.3 shows that with this limit on $\tan\beta/m_{H^\pm}$ the charge Higgs contribution to $\mathcal{B}(D_s^+ \to \mu^+\nu_\mu)$ is less than 1 %.

2.5 The Decay Constant and the Unitarity Triangle

As mentioned earlier in chapter 1.2, the determination of the angles and sides of the Unitarity Triangle in Figure 1.1 is one of the primary tasks of flavor physics. Various groups have taken up the task to compile all available measurements and fit for the parameters ρ and η. The result of the "CKMfitter" group [34] are shown in Figure 2.4. Currently all measurements are consistent with each other, confirming the unitarity assumption. A more rigid statement could be made if the length of the upper right

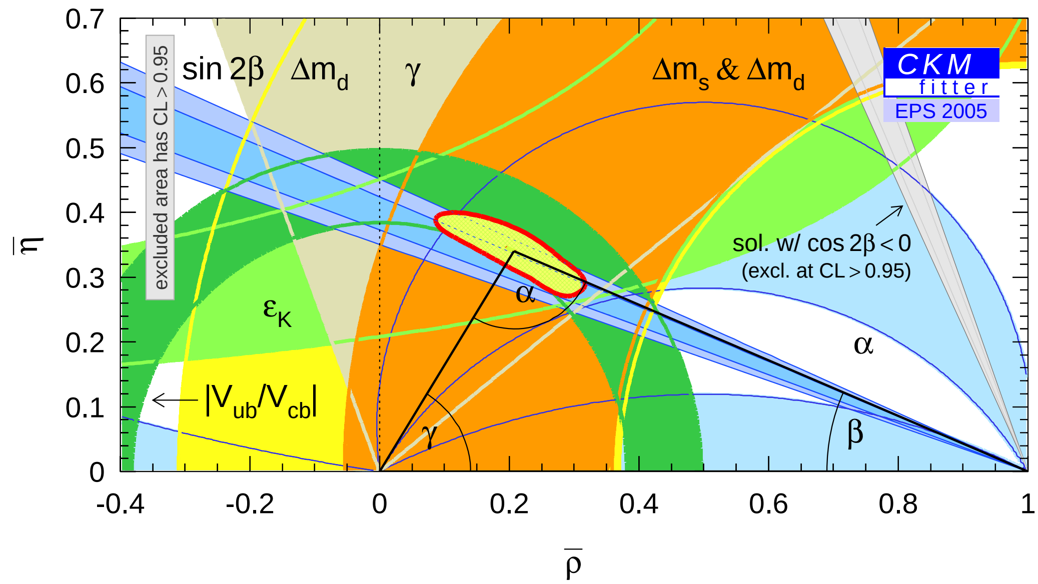

Figure 2.4: The global CKM fit in the $\bar{\rho}$–$\bar{\eta}$ plane. The constraints on V_{td}, determined from the measurements of Δm_d and of $\Delta m_d/\Delta m_s$ are indicated by the orange and by the yellow band, respectively.

side of the triangle in Figure 2.4 would have a smaller uncertainty. That length is given by $|(V_{td}V_{tb})/(V_{cd}V_{cb})|$, with V_{td} having a considerably larger error than the other three CKM matrix elements. The value of V_{td} is directly determined from the mass difference Δm_d of the heavy and the light neutral B_d meson.

The mass difference is the cause of neutral B meson oscillations. In the oscillation Feynman diagram, which is depicted in Figure 3.1 on page 27, the $\Delta B = 2$ flavor change happens through intermediate top-quarks that couple to the quarks of the B^0 with V_{tb} and V_{td}. The relation between Δm_d and V_{td} is given by

$$\Delta m_d = \frac{G_F^2}{6\pi^2}\eta_B m_B \hat{B}_B f_B^2 m_W^2 S\left(\frac{m_t^2}{m_W^2}\right)|V_{tb}V_{td}^*|^2 , \tag{2.11}$$

where $\hat{B}_B = 1.4 \pm 0.1$ [35] is the so-called bag parameter, calculated in lattice QCD, and $\eta_B = 0.55$ comes from short distance QCD corrections in next-to-leading order.

$S(x)$ is the result of the calculation of the box diagram,

$$S(x) = x\left(\frac{1}{4} + \frac{9}{4}\frac{1}{1-x} - \frac{3}{2}\frac{1}{(1-x)^2}\right) - \frac{3}{2}\left(\frac{x}{1-x}\right)^3 \ln x \ . \tag{2.12}$$

With $\Delta m_d = (0.509 \pm 0.004)\ \mathrm{ps}^{-1}$ [36] being measured to a precision of 1.4 %, the uncertainty in V_{td} is almost entirely due to that of $f_B\sqrt{\hat{B}_B} = 210 \pm 24$ [37].

With the ratio $\xi \equiv f_B\sqrt{\hat{B}_B}/f_{B_s}\sqrt{\hat{B}_{B_s}}$, the ratio of Δm_d to Δm_s, the mass difference between the heavy and the light B_s meson, can be written as

$$\frac{\Delta m_d}{\Delta m_s} = \xi^2 \left|\frac{V_{td}}{V_{ts}}\right|^2 \ . \tag{2.13}$$

In the calculation of ξ most sources of uncertainty vanish, (although some larger uncertainties remain,) and unquenched lattice QCD computes $\xi = 1.21 \pm 0.06$ [38]. With the current world average, $\Delta m_s > 16.6\ \mathrm{ps}^{-1}$ at 95 % C.L. [36], a upper limit can be placed on the value of V_{td}, which is tighter than that from Δm_d alone[2].

It has been said before, that an $\mathcal{O}(5\,\%)$ measurement of f_B is not feasible with the current or near future experiments. It is up to theory to determine a precise value for f_B. It is therefore critical to provide results from high precision measurements, which can be used by theoreticians to test and gauge their calculation tools. Such an important measurement is that of the decay constant f_{D_s}.

[2] After this thesis was written CDF published a measurement $\Delta m_s = (17.33^{+0.42}_{-0.21\,\mathrm{stat}} \pm 0.07_{\mathrm{sys}})\ \mathrm{ps}^{-1}$ and $|V_{td}/V_{ts}| = 0.208^{+0.008}_{-0.007\,\mathrm{stat+sys}}$.

Part II

The Experiment

Chapter 3

The *BABAR* Experiment

3.1 The Physics Case For *BABAR*

The group of Lorentz transformations includes not only the proper continuous transformations, but also the discrete parity transformation $\mathcal{P}$ (the negation of space coordinates), charge conjugation $\mathcal{C}$ (the interchange of particle and antiparticle), and time reversal $\mathcal{T}$. One of the most beautiful properties of quantum field theories, which was first formulated by E. Noether for continuous transformations, is that, whenever a physical system is invariant (symmetric) under such a transformation it leads to a conserved quantity. Nature seems to take advantage of the simple mathematical representation of symmetry laws. It is only logical, and from an aesthetic viewpoint desirable, that the discrete transformations $\mathcal{P}$, $\mathcal{C}$, and $\mathcal{T}$ also preserve the laws of physics, and perhaps even lead to the conservation of associated quantities, if they can be found.

However, $\mathcal{P}$ is not a symmetry of Nature. By 1956 empirical evidence had mounted (the so called θ-τ puzzle) that parity is violated in weak decays. In a Nobel Prize winning work T.D.Lee and C.N.Yang proposed a number of experiments on β-decays, and hyperon and meson decays, that would provide the necessary proof for or against parity conservation in weak interactions. Carried out by C.S.Wu and colleagues in late 1956, it was found in the study of decays ${}^{60}_{27}\mathrm{Co} \rightarrow {}^{60}_{28}\mathrm{Ni} + \mathrm{e}^- + \bar{\nu}_\mathrm{e}$ that parity is indeed maximally violated in the weak interaction.

At the same time (in fact even before the experimental results of Wu's group were published) it was realized by Landau, that the symmetry could be recovered, if $\mathcal{P}$ was combined with $\mathcal{C}$, the symmetry of charge-conjugation. This satisfactory, but short lived picture was shattered, when in 1964 in another Nobel Prize winning work *CP* violation in neutral $K^0/\bar{K}^0$ meson system was discovered. It was found that the *CP*-odd long lived component of the neutral kaon system, $(|K^0\rangle - |\bar{K}^0\rangle)$, could decay into two pions, which are a *CP*-even state.

Since then no new *CP*-violating phenomena had been observed although the CKM mechanism offers a theoretical framework for *CP* violation outside the K system, in particular in the bottom sector. But, is this is the only mechanism for *CP* violation to appear? Does it occur only in charged currents, as the SM predicts? Could *"New Physics"*, induced by loop effects of virtual new particles, appear in *CP* asymmetries? The study of B meson decays could help to answer these questions.

In addition, the *BABAR* physics program comprises an extensive effort in the area of charm and τ decays.

3.1.1 *CP* Violation in the *B* Meson System

In the study of *CP* violation in the B meson system the oscillation of neutral B mesons is of particular interest. Neutral B mesons are described by two sets of two eigenstates:

- *Flavor eigenstates*, $|B^0\rangle$ and $|\overline{B}^0\rangle$, with well defined quark content, which are relevant in production and decay processes of the neutral B.

- *Mass eigenstates*, $|B_L\rangle$ and $|B_H\rangle$, with well defined mass and lifetime, which describe the time development of the system.

The mass eigenstates can be written as linear combinations of the flavor eigenstates

$$a|B^0\rangle + b|\overline{B}^0\rangle, \tag{3.1}$$

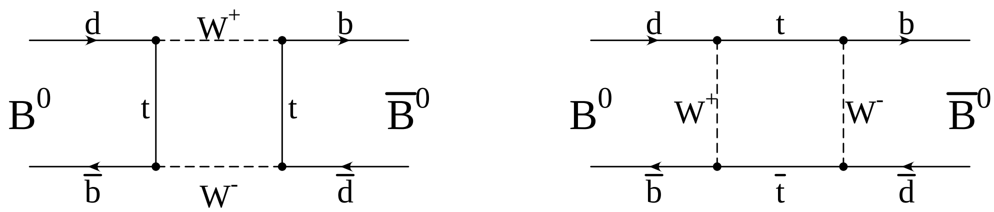

Figure 3.1: Feynman Diagram describing the oscillation of the B^0–$\overline{B}^0$ meson system.

and evolve according to the Schrödinger equation

$$\imath \frac{d}{dt}\begin{pmatrix} a \\ b \end{pmatrix} = \boldsymbol{H}\begin{pmatrix} a \\ b \end{pmatrix} \equiv \left(\boldsymbol{M} - \frac{\imath}{2}\boldsymbol{\Gamma}\right)\begin{pmatrix} a \\ b \end{pmatrix}, \tag{3.2}$$

where $\boldsymbol{M}$ and $\boldsymbol{\Gamma}$ are hermitian 2×2 matrices. *CPT* invariance requires the diagonal elements H_{11} and H_{22} to be identical. The off-diagonal elements describe the mixing probability of the flavor eigenstates, $|B^0\rangle \leftrightarrow |\overline{B}^0\rangle$. The mixing occurs through the weak interaction according to the box diagrams in Figure 3.1. The mass eigenstates

$$|B_L\rangle = p|B^0\rangle + q|\overline{B}^0\rangle \quad \text{and} \tag{3.3}$$

$$|B_H\rangle = p|B^0\rangle - q|\overline{B}^0\rangle \tag{3.4}$$

are found by solving (3.2), giving the ratio:

$$\frac{q}{p} = -\left(\frac{M_{12}^* - \frac{\imath}{2}\Gamma_{12}^*}{M_{12} - \frac{\imath}{2}\Gamma_{12}}\right)^{\frac{1}{2}} = -\frac{2(M_{12}^* - \frac{\imath}{2}\Gamma_{12}^*)}{\Delta m_B - \frac{\imath}{2}\Delta\Gamma_B}, \tag{3.5}$$

where $\Delta m_B \equiv m_H - m_L$ and $\Delta\Gamma_B \equiv \Gamma_H - \Gamma_L$ are the difference in the mass and in the decay width, respectively, of the heavy and the light mass eigenstates.

Independent of the description in the Standard Model, *CP* violation in the B meson system can be established by the *BABAR* experiment in three different ways:

- ***CP* violation in decay or "*direct CP violation*":** The amplitude A_f of a decay $B \to f$ and that of its *CP* conjugate $\overline{B} \to \bar{f}$, $\bar{A}_{\bar{f}}$, have different magnitude, $|\bar{A}_{\bar{f}}/A_f| \neq 1$. The interference of two or more processes with different weak and strong phases, contributing to that decay, is necessary for this type of *CP* violation to occur. The contributing processes also have to be similar in the magnitude of their decay amplitude. Any *CP* asymmetries in charge B decays,

$$a_f = \frac{\Gamma(B^+ \to f) - \Gamma(B^- \to \bar{f})}{\Gamma(B^+ \to f) + \Gamma(B^- \to \bar{f})}, \tag{3.6}$$

are from *CP violation in decay*. For this type of *CP* violation it is difficult to relate the measured asymmetry a_f to the underlying Standard Model parameters. It requires knowledge of the strong phase shift between the amplitudes, the calculation of which introduces larger hadronic uncertainties. The asymmetry in terms of the amplitudes is given by:

$$a_f = \frac{1 - |\bar{A}/A|^2}{1 + |\bar{A}/A|^2} \ . \tag{3.7}$$

Although the asymmetries can be large, the effect is rare, since it is suppressed by small decay rates.

- ***CP* violation in mixing or "*indirect CP violation*":** The mass eigenstates $p|B^0\rangle \pm q|\overline{B}^0\rangle$ are different from the *CP* eigenstates $\left(|B^0\rangle \pm e^{\imath\alpha}|\overline{B}^0\rangle\right)$ or, equivalently, $|p/q| \neq 1$. At *BABAR*, this effect could be observed through asymmetries in the semileptonic decays of neutral B mesons, which do not exhibit direct *CP* violation ($A_{B^0 \to l^+\nu X} = A_{\overline{B}^0 \to l^- \bar{\nu} X}$). The asymmetry is given by

$$a_{\mathrm{sl}} = \frac{\Gamma\left(\overline{B}^0(t) \to l^+\nu X\right) - \Gamma\left(B^0(t) \to l^-\bar{\nu} X\right)}{\Gamma\left(\overline{B}^0(t) \to l^+\nu X\right) + \Gamma\left(B^0(t) \to l^-\bar{\nu} X\right)}, \tag{3.8}$$

where $B^0(t)$ and $\overline{B}^0(t)$ denote the timely evolution of an initially pure B^0 and an initially pure $\overline{B}^0$ state.

The neutral B meson decay width difference $\Delta\Gamma_B$ arises from decay channels common to B^0 and $\overline{B}^0$, whose branching ratios are assumed to be small. With a measured Δm_B approximately of the same size as Γ_B, it is a safe assumption that $\Delta\Gamma_B \ll \Delta m_B$ and $q/p = -|M_{12}|/M_{12}$. Therefore the asymmetry

$$a_{\rm sl} = \frac{1 - |q/p|^4}{1 + |q/p|^4} \tag{3.9}$$

is expected to be small, $\mathcal{O}(10^{-2})$.

- ***CP* violation in interfering decays with and without mixing:** This manifestation of *CP* violation occurs in the decays of neutral B mesons into *CP* eigenstates, f_{CP}. A neutral B^0, for instance, can decay either directly into f_{CP} or evolve in time into a $\overline{B}^0$ and then decay into f_{CP}. Both processes interfere. It is hence possible to observe a time-dependent asymmetry

$$a_{f_{CP}} = \frac{\Gamma\left(B^0(t) \to f_{CP}\right) - \Gamma\left(\overline{B}^0(t) \to f_{CP}\right)}{\Gamma\left(B^0(t) \to f_{CP}\right) + \Gamma\left(\overline{B}^0(t) \to f_{CP}\right)} \ . \tag{3.10}$$

With the introduction of $\lambda_{f_{CP}} = \frac{q}{p}\frac{\bar{A}_{f_{CP}}}{A_{f_{CP}}}$, which is independent of phase conventions, (3.10) can be written as

$$a_{f_{CP}} = \frac{(1 - |\lambda_{f_{CP}}|^2)\cos(\Delta m_B t) - 2\Im(\lambda_{f_{CP}})\sin(\Delta m_B t)}{1 + |\lambda_{f_{CP}}|^2} \ . \tag{3.11}$$

For modes with no direct *CP* violation, again using the assumption $|q/p| = 1$, this simplifies to

$$a_{f_{CP}} = -\Im(\lambda_{f_{CP}})\sin(\Delta m_B t) \ . \tag{3.12}$$

In cases where the decay is dominated by a single decay amplitude, a clean relationship between the measured asymmetry and the underlying Standard Model description of *CP* violation can be obtained.

The observability of this type of *CP* violation also requires that the lifetime of the neutral B meson is at least comparable to the oscillation frequency, $\Delta m_B/\Gamma_B \gtrapprox 1$. A ratio $\Delta m_B/\Gamma_B = 0.774 \pm 0.009$ [30] has been measured.

An example for the third type of CP violation is the decay $B^0 \rightarrow J/\psi\, K_S^0$. For this,

$$\lambda_{J/\psi\, K_S^0} = -\left(\frac{V_{tb}^* V_{td}}{V_{tb} V_{td}^*}\right)\left(\frac{V_{cs}^* V_{cb}}{V_{cs} V_{cb}^*}\right)\left(\frac{V_{cd}^* V_{cs}}{V_{cd} V_{cs}^*}\right), \tag{3.13}$$

where the first term is from the $B^0\overline{B}^0$ mixing, the second from the ratio $\frac{\bar{A}_f}{A_f}$ and the third from the $K^0\overline{K}^0$ mixing. Hence,

$$\Im\left(\lambda_{J/\psi\, K_S^0}\right) = \sin 2\beta\ , \tag{3.14}$$

and, with (3.12), the angle 2β can be directly measured through a time-dependent comparison of the decay widths of $B^0(t) \rightarrow J/\psi\, K_S^0$ and $\overline{B}^0(t) \rightarrow J/\psi\, K_S^0$.

3.1.2 Time-Dependent Analysis of Neutral *B* Decays

At the $\Upsilon(4S)$ resonance at 10.58 GeV neutral and charged B-meson pairs are produced. The B mesons in a $B^0\overline{B}^0$ pair are produced in a coherent state; at any time one meson is always a B^0 and one a $\overline{B}^0$. Neutral B mesons can decay into final states that uniquely identify the meson, either as B^0 or as $\overline{B}^0$. The reconstruction of such a decay at a certain time t_0, called "tagging", precisely determines the identity of the other B meson at t_0. The time evolution and decay of that B can now be studied.

The size of the oscillation wavelength, $c/\Delta m_B$, of the CP asymmetry in (3.12) is $\approx$ 600 μm. With the B mesons being produced almost at rest, this translates into $\approx$ 40 μm in the rest frame of the $\Upsilon(4S)$, a distance that is too small to be resolved with the available technology of vertex detectors. If, however, the rest frame of the $\Upsilon(4S)$ is boosted, the oscillation wavelength in the observer's frame grows. At $\beta\gamma = 0.56$, for instance, $c/\Delta m_B$ becomes $\approx$ 290 μm, well within the resolution of the silicon strip detectors of today.

This spurred the idea of building asymmetric energy storage rings, which became the PEP-II. At the interaction point the *BABAR* detector was constructed, optimized for the boosted $\Upsilon(4S)$ frame.

3.2 PEP-II

The Positron Electron Project in its second version, PEP-II, is an asymmetric energy electron-positron collider, operating at the $\Upsilon(4S)$ resonance at 10.58 GeV. It consists of two 2.2 km long rings, one storing electrons at 9 GeV, the other positrons at 3.1 GeV. This asymmetry in the beam energies results in a boost of the $\Upsilon(4S)$ in the laboratory frame of $\beta\gamma = 0.56$. PEP-II has reached a luminosity of 1.04×10^{34} cm^{-2}s^{-1} in the fall of 2005; other parameters are listed in tab. 3.1.

Electrons and positrons are injected into the two rings from the 3 km long SLAC linac. At the beginning of the linac a thermionic electron gun provides a high intensity unpolarized electron beam of about 10 MeV. Electrons are emitted from an electrically heated tungsten filament, grouped into bunches, and, in a first accelerator section, brought up to an energy of 1.19 GeV. To reduce the lateral spread, the beam is transferred into the north damping ring, in which the electron bunches are transversly damped through synchrotron radiation and longitudinal acceleration. The beam is then re-injected into the main accelerator, where the electrons are accelerated to their final energy of 9.0 GeV. Positrons are created by using half of the produced electrons and colliding them with a cooled tungsten target, located two third down the linac. The positrons in the resulting electron-positron pairs are collimated and sent back to the beginning of the accelerator structure. After bried storage in the south damping ring to reduce their emittance they are re-injected into the main accelerator, where they are brought to their final energy of 3.1 GeV. Both beams are then injected into the two PEP-II storage ring, electrons clockwise and positrons counterclockwise, when viewed from above.

The demand for a high luminosity of 3.0×10^{33} cm^{-2}s^{-1}, which is necessary to achieve the *BABAR* physics goals, sets new challenges for the design of the PEP-II storage rings. The luminosity at the interaction point (IP) is given by

$$\mathcal{L} = \frac{N_+ N_- f_C}{A}, \tag{3.15}$$

where $N_{+/-}$ are the number of particles in the positron and electron bunches, f_C is

Table 3.1: Design PEP-II parameters and status in May 2005.

Parameter	Design	May 2005
Beam Parameters		
Beam energy (e^+/e^-) (GeV)	3.1/9.0	3.1/9.0
Beam current (e^+/e^-) (A)	2.14/1.48	2.45/1.55
Circumference (m)	2199.318	2199.318
Emittance ϵ_x (e^+/e^-) (nm rad)	96/48	30/50
Emittance ϵ_y (e^+/e^-) (nm rad)	3.86/1.93	1.25/2.10
Number of bunches	1658	1588
Bunch length (mm)	10	11
Particles per bunch ($\times 10^{10}$)	5.9/4.1	7.1/4.5
Interaction Region Parameters		
β^*_x (e^+/e^-) (cm)	37/75	50/28
β^*_y (e^+/e^-) (mm)	15/30	11/11
σ^*_x (e^+/e^-) (μm)	190/190	170/170
σ^*_y (e^+/e^-) (μm)	7.6/7.6	7.3/7.3
Crossing angle	0	0
Luminosity ($\times 10^{33}$ cm^{-2}s^{-1})	3.00	9.21

the collision frequency and A is the overlapping area of the beams. For two head-on colliding beams with a Gaussian particle distribution in the horizontal (x) and vertical (y) direction, that area is given by

$$A = 2\pi\sqrt{(\sigma^{*2}_{x,+} + \sigma^{*2}_{x,-})(\sigma^{*2}_{y,+} + \sigma^{*2}_{y,-})}, \tag{3.16}$$

where $\sigma^*_{x/y,\pm}$ are the beam sizes in x and y for the positron and electron beam at the IP. The limitations induced by beam-beam interaction effects are discussed best if the luminosity is written as a function of the beam-beam tune shift ξ, which is the perturbation of the transverse phase of one beam due to the influence of the other beam. It is, for instance for the positron beam and the y coordinate, defined as:

$$\xi_{y,+} = \frac{r_e}{2\pi}\frac{N_-\beta^*_{y,+}}{\gamma_+\sigma^*_{y,-}(\sigma^*_{x,-} + \sigma^*_{y,-})} \ . \tag{3.17}$$

Here, $r_e = 2.82 \times 10^{-15}$ m is the classical electron radius, γ_+ is the positron beam energy in units of the positron mass, and $\beta^*_{y,+}$ is the positron beam β-function at the IP in vertical direction. At the time PEP-II was designed no asymmetric energy colliders existed and the consequences of beam-beam dynamics for intense beams were not completely understood. A careful approach was to choose the beam parameters such that the dynamics closely resembles that of a symmetric-energy, single-ring collider. This is the so-called *transparency symmetry* condition, which inter alia includes the pairwise equality of the tune shifts, $\xi_{x/y,+} = \xi_{x/y,-}$, and of the beam sizes at the IP, $\sigma^*_{x/y,+} = \sigma^*_{x/y,-}$. For PEP-II all four beam parameters were designed to be equal, $\xi_{x/y,\pm} = 0.03$. With the transparency symmetry condition the luminosity can be written as

$$\begin{aligned} \mathcal{L} &= \frac{1}{2er_em_e}\left(\frac{EI}{\beta_y}\right)_{+/-}\xi_y\left(1+\frac{\sigma^*_y}{\sigma^*_x}\right) \\ &= 2.17 \times 10^{34}\,\mathrm{cm}^{-2}\mathrm{s}^{-1}\left(\frac{E\,[\mathrm{GeV}]\,I\,[A]}{\beta_y[\,\mathrm{cm}]}\right)_{+/-}\xi_y\left(1+\frac{\sigma^*_y}{\sigma^*_x}\right) \end{aligned} \tag{3.18}$$

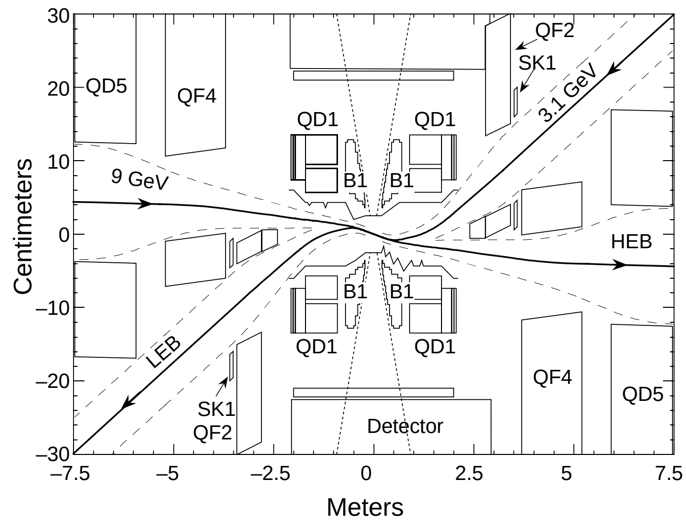

Figure 3.2: The PEP-II interaction region.

The beam-beam tune shift ξ_y is not really a free parameter, but depends intrinsically on the nature of the beam-beam interaction. It has been observed at previous e^+e^- colliders [39] that at low currents the luminosity grows according to $\mathcal{L} \propto N_+N_-$, indicating the independence of the beam size from the current and $\xi \propto I$. At high currents the luminosity relates linearly to the beam current, $\mathcal{L} \propto N_\pm$. The area of the beam also grows with the beam current, $A \propto I$, leaving ξ constant. At previous colliders this plateau was found between $\xi = 0.03$ and $\xi = 0.05$; for PEP-II the plateau lies between 0.045 and 0.065. This limit on the tune-shift and the saturation of the beam at high currents prevents an arbitrary increase in luminosity through an increase in the stored current.

Beam-beam interactions also lead to an increased population of non-Gaussian tails in the beam density distribution. This is particularly true for the y direction, due to the absence of bending magnets in the vertical plane. These tails are a limiting factor in the beam lifetime.

The asymmetry and desired high luminosity of the PEP-II machine have also resulted in a extraordinary design for the interaction region (Figure 3.2). Instead of colliding the two beams at an angle, the magnet system bends the beams into a head-on collision path and separates their paths afterward. This challenging design

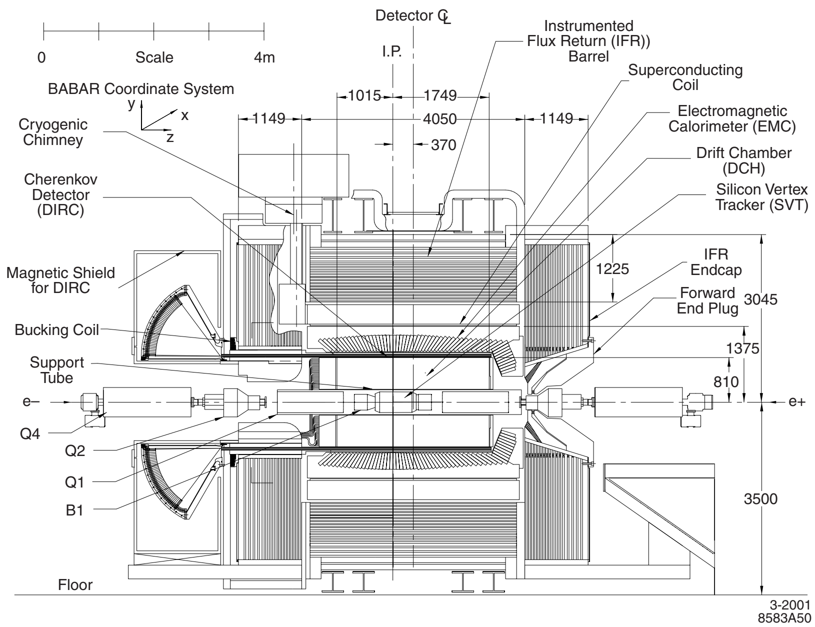

Figure 3.3: Longitudinal view through the *BABAR* detector. All dimensions are in mm.

allows greater scalability of the beam currents while keeping the beam backgrounds manageable. The magnets used in the interaction region are permanent magnets made of a rare-earth-cobalt alloy, Sm_2Co_{17}, which has a high magnetic field, $B = 1.05\,\mathrm{T}$. The quality of the magnets depends critically on their exact magnetization, their fabrication involved thousands of precisely machined and magnetized blocks of the alloy.

The choice of the PEP-II beam energies is a compromise that balances two arguments. While the simulations of beam-beam interactions argue for equal damping times in the two rings, which is more easily accomplished with a reduced energy asymmetry, the magnetic separation of the beams at the interaction region becomes easier when the energy asymmetry increases.

3.3 The Apparatus

The primary goal of the *BABAR* experiment, the time-dependent measurement of *CP* asymmetry in the $B^0\overline{B}^0$ meson system is reflected in the design of the detector. The necessity for a boosted center-of-mass frame requires the detector geometry to be asymmetric, such that in the direction of the boost, the angular coverage with active detector components, needs to be much higher than in the opposite direction. That design scheme has been followed by all the major subsystems.

In order to introduce some of the terminology and to aid in the understanding of the detector geometry the definition of the *BABAR* coordinate system will be given here. The z-axis of the systems is given by the center axis the cylindrical drift chamber. The y-axis is pointing up, and, to complete the right-handed coordinate system, the horizontal x-axis points away from the center of the ring. The direction of the positive z-axis is also referred to as the forward direction. It coincides with the direction of the electron beam, and hence with the direction of the event boost. Due to the layout of the interaction region, there is a $1°$ angle between the beam direction and the z-axis; beam axis and z-axis are distinct.

The *BABAR* detector, though optimized for analyzing the neutral B meson system, is a multipurpose detector, allowing for a wide variety of analyzes. As such it follows the classic design of an inner and outer tracker, a Cherenkov device, an electromagnetic calorimeter, a superconducting coil producing the magnetic field, and a muon system that also acts as a carrier of the external magnetic flux. As a whole the detector has been optimized to satisfy the following performance requirements:

- Good vertex resolution with special attention to the z component for a good separation of the two B meson vertices.

- Maximum geometric acceptance in the center-of-mass system to reconstruct all the spherically distributed products of the decay of the B mesons.

- Good discrimination of e, μ, π, K, and p to distinguish the different decay channels of the $B^{\pm}$ and B^0 meson.

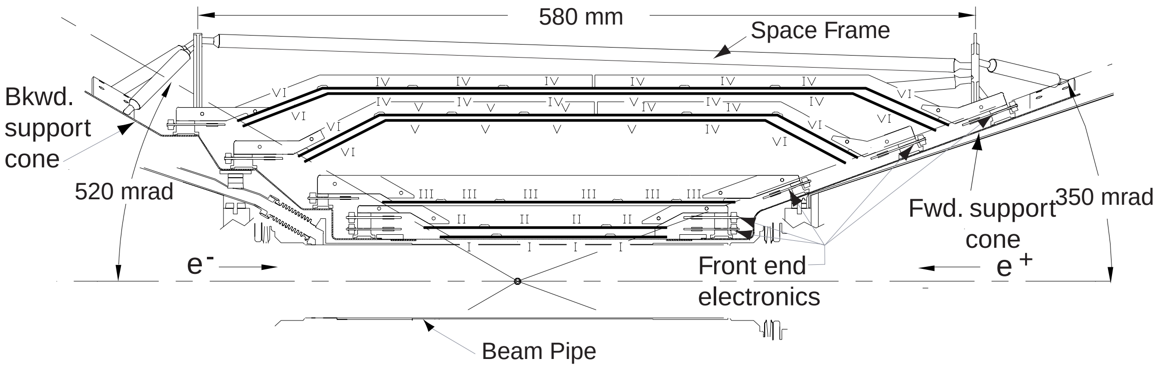

Figure 3.4: The SVT. The roman numerals show the position and indicate the size of the silicon wafers within the layers.

- Tracking and clustering over a wide transverse momentum $60\,\mathrm{MeV/c} < p_t < 4\,\mathrm{GeV/c}$ and energy range $20\,\mathrm{MeV} < E_{em} < 9\,\mathrm{GeV}$

In the following the detector subsystems are described. They are presented in the order they would appear to a particle starting at the interaction point (IP) traveling outward. Special attention is paid to the particular role each subsystem plays in achieving the performance requirements listed above. In addition, the trigger and data acquisition systems are described.

3.3.1 The Silicon Vertex Tracker

The main task of the Silicon Vertex Tracker (SVT) is the reconstruction of the primary decay vertices of the B mesons. To achieve the desired accuracy in the decay time difference of the two B mesons, a single vertex resolution of 80 μm is required. The SVT further provides track information for particles of less than $100\,\mathrm{MeV}/c$ transverse momentum, which, due to their bending in the magnetic field, do not reach the main tracking system. The device consists of five cylindrical layers of double sided silicon strip sensors. The three inner layers consist of 6 modules, layers 4 and 5 of 16 and 18 respectively. Each module consists of between 4 and 8 individual silicon crystals, or wafers, which exist in 6 different sizes. The wafers are 300 μm thick and have readout strips on both sides. Between the two sides the readout strips have a relative stereo angle of 90°, allowing for a reconstruction of both coordinates of the track passing each layer. The SVT consists of about 150,000 readout channels. The innermost layer is located at 3 cm distance from the interaction point, the outermost layer at 15 cm. The angular coverage ranges from $\theta = 17.2\,^\circ$ to $\theta = 150\,^\circ$, limited by the geometry of the beam guiding magnets near the interaction region. The three inner layers of the SVT are designed to precisely measure the impact parameter of the tracks. They reach a single hit resolution of 10–15 μm, depending on the incident angle of the track. The limiting factor on the hit resolution is the uncertainty in the track direction introduced by multiple scattering in the silicon. The two outer layers main purpose is to track particles with low transverse momentum and to link the inner SVT hits to the track information provided by the drift chamber. The single hit resolution of 30–40 μm is sufficient in these modules.

3.3.2 The Drift Chamber

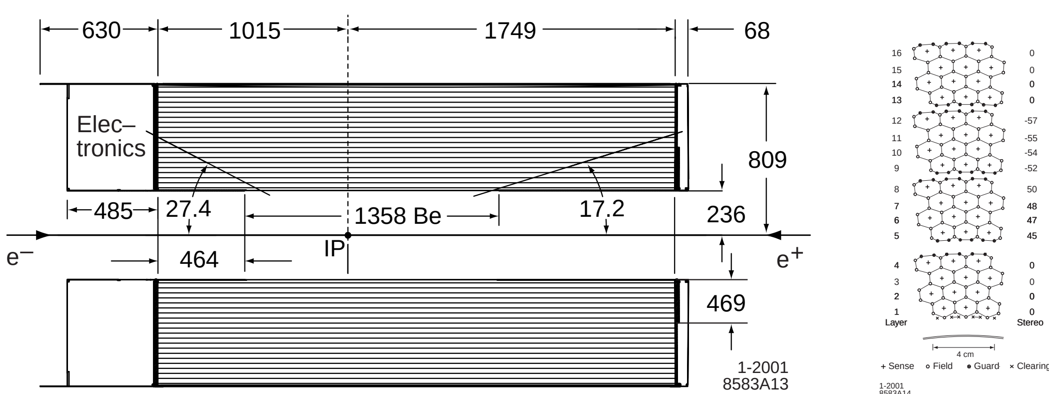

Figure 3.5: The Drift Chamber. The units are millimeter, IP indicates the interaction point.

The Drift Chamber (DCH) is the main component for reconstructing charged particles with transverse momenta above 100 MeV/c. The reconstructed tracks provide the momentum of the particles and the specific energy loss, along their trajectory, through ionization, dE/dx. Because the ionization loss depends on the momentum p and the mass m of the particle $dE/dx(p/m)$, it is used for identifying the particle type, in particular at low momentum and in regions where no other means of identification are available. The DCH endplates are made of aluminum. The inner cylinder is made of beryllium and the outer of carbon-fiber, minimizing the Coulomb scattering probability of the tracks. The inner radius of the DCH is 24 cm, the outer radius is 81 cm.

The volume of the DCH is segmented into 7104 hexagonal drift cells of a length of 2.80 m. The edges of each drift cell are defined by low mass gold-plated aluminum field wires. In the center of each cell a gold-plated tungsten-rhenium sense wire is located. The sense wires are kept at about 1960V. Together with the grounded field wires they create the electric field. The DCH is filled with a low Z helium-isobutane gas-mixture (80 %:20 %) at 4 mbar above atmospheric pressure. Charged particles that traverse the drift chamber ionize the gas molecules. The ionization electrons are accelerated toward the sense wire, producing secondary ionization. From the drift time and the electric field the distance at which a particle passes the sense wire is estimated. The correspondence between drift time and distance is determined empirically using $e^+e^- \to e^+e^-$ and $e^+e^- \to \mu^+\mu^-$ events.

In the radial direction the drift cells are organized in 40 layers, with groups of 4 layers making up a super layer. The super layers are aligned either parallel to the z-axis (*axial layer* A), or at a small angle (*stereo layer* U, V), necessary to provide track information in the z coordinate. The arrangement of axial and stereo layers is $A\ UVA\ UVA\ UVA$. The stereo angles range from 45 mrad in the inner super layer to 75 mrad in the outer super layer.

The DCH covers a polar angle $17^\circ < \theta < 150^\circ$. The position resolution achieved varies between 100 μm and 200 μm, depending on the drift distance. The energy loss resolution is 7.5 %.

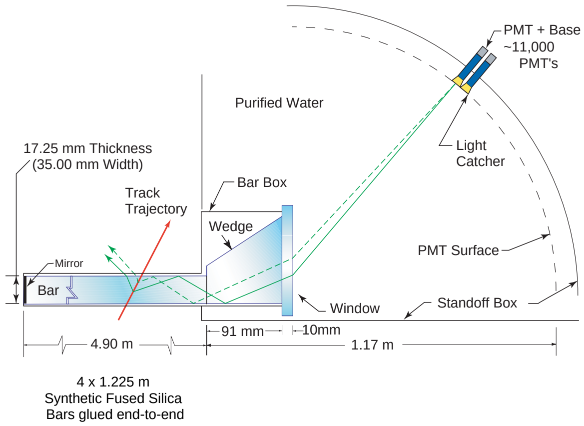

Figure 3.6: The DIRC principle.

3.3.3 The Cherenkov Device

The Detector of Internally Reflected Cherenkov (DIRC) light is the main device for particle identification (PID) at the *BABAR* detector. It provides excellent separation of charged pions and kaons up to $4.2\,\mathrm{GeV}/c$.

Charged particles passing through matter emit Cherenkov radiation if their speed, βc, exceeds the speed of light in the material, c/n, n being the refractive index of the material. Cherenkov detectors work either as threshold detectors, which only detect the onset of Cherenkov radiation light at $\beta = 1/n$, or more sophisticated as ring imaging Cherenkov (RICH) detectors, which measure β.

The DIRC belongs to this second class of Cherenkov devices. As such it is designed to measure the angle at which the Cherenkov photons are emitted with respect to the flight direction of the emitting charged particle. The fundamental relation between the Cherenkov angle θ_C, the half angle of the Cherenkov cone, the velocity of the charged particle, and the index of refraction of the traversed material is

$$\cos(\theta_C) = \frac{1}{n\beta} \tag{3.19}$$

Photon detectors determine the position and arrival time of the incident photons. In order to measure θ_C, the photons must be projected, “imaged”, onto a detector, such that the photon angle can be determined. In a novel design the DIRC separates

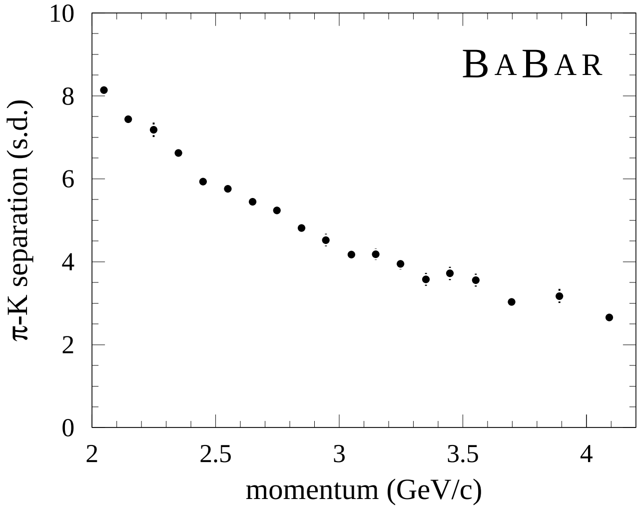

Figure 3.7: The DIRC performance.

the two stages of the production of Cherenkov light and the projection of the light cone, by taking the image of the Cherenkov cone outside the detector and the path of the particle. In its unique approach it uses fused silica bars ($\langle n \rangle = 1.474$ averaged over the wavelengths of the photons produced) as the radiator for the Cherenkov light as well as the transmitter that takes the Cherenkov cone image out of the central detector through internal reflection. The DIRC consists of 144 fused silica bars ($1.7 \times 3.5 \times 490$ cm), located outside the DCH. They cover an azimuthal angle of about 93% and range from $\theta = 25.5\,°$ to $\theta = 141.4\,°$. At the backward end of the detector the bars meet the so called standoff box, a semi-globe with a radius of 120 cm equipped with 10,752 photomultipliers. It is filled with purified water to better match the refractive index of the silica, such that the projected Cherenkov ring pattern has a smaller diameter than in an air-filled standoff box. The DIRC reaches a resolution on θ_C of 2.5 mrad. The π/K separation power, defined as the difference of the mean Cherenkov angles for pions and kaons at a given momentum, divided by the resolution, is about $8\,\sigma$ at 2 GeV/c, declining to about $2.5\,\sigma$ at 4.1 GeV/c (Figure 3.7).

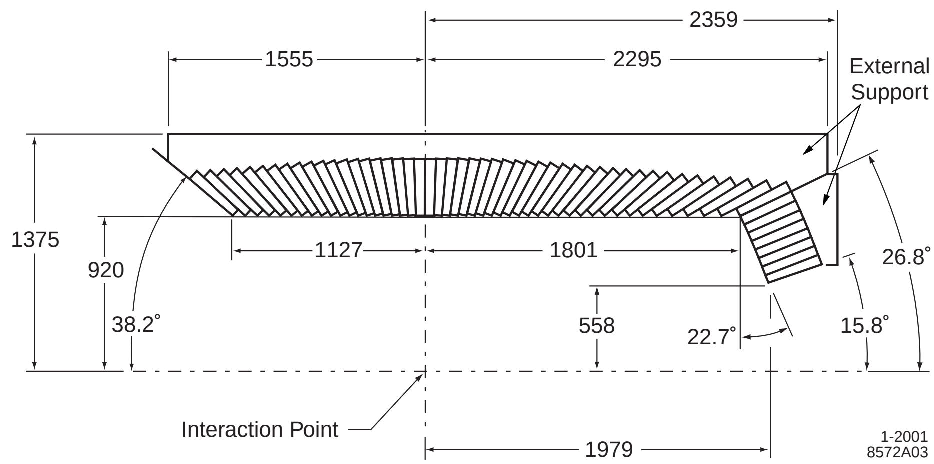

Figure 3.8: Schematic view of the EMC.

3.3.4 The Electromagnetic Calorimeter

The Electromagnetic Calorimeter (EMC) has three major tasks. The first is the reconstruction and energy measurement of photons. The dominant source of photons are π^0 mesons, which decay to a photon pair. The second task of the EMC is the precise measurement of the invariant mass of these photon pairs, so that π^0 mesons can be identified and their momentum be measured. Third, by measuring the energy of charged particles that is deposited in the EMC, and comparing it to their momentum, the EMC helps in identifying electrons and positrons. These, unlike charged particles of any other type, deposit almost their entire energy in the calorimeter.

During the passage through matter, most of the energy loss of high energy electrons and positrons occurs as bremsstrahlung, while high energy photons lose their energy predominantly through production of e^+e^- pairs. Through repetition of these two processes a cascade of pair-produced electrons and positrons, and bremsstrahlung photons of ever lower energies develops, an *electromagnetic shower*. The energy of the particles in the cascade eventually falls below the critical energy, E_c (for most materials $E_c = 10..50\,\mathrm{MeV}$), at which point it is dissipated through ionization and excitation of the traversed matter. The parameter which governs the energy loss is the material dependent radiation length X_0, which is the mean distance over which a high-energy electron loses all but $1/e$ of its energy. Other particles do not form electromagnetic showers in the EMC, but dissipate energy only through minimum ionization or a hadronic shower.

Scintillators are materials which release at least a fraction of the dissipated energy as photons in the optical spectrum. The amount of produced light is directly proportional to the dissipated energy of the incident particle. Often scintillators are doped with atoms of a different material, that shift the scintillation light to a wavelength, more convenient for the light detection.

The *BABAR* EMC consists of 6580 cesium-iodide crystals doped with thallium. The length of the crystals in units of X_0 varies between 16.0 and 17.5. The angular coverage of the EMC ranges from $\theta = 15.8\,^\circ$ to $\theta = 141.8\,^\circ$. An energy resolution of

$$\frac{\sigma_E}{E} = \frac{2.32 \pm 0.30\,\%}{\sqrt[4]{E(\mathrm{GeV})}} \oplus (1.85 \pm 0.12)\,\% \tag{3.20}$$

and an angular resolution of

$$\sigma_{\theta,\phi} = \frac{(3.87 \pm 0.07)\ \mathrm{mrad}}{\sqrt[2]{E(\mathrm{GeV})}} + (0.00 \pm 0.04)\ \mathrm{mrad} \tag{3.21}$$

are achieved.

The electron identification efficiency for electrons used in the $D_s^+ \to \mu^+\nu_\mu$ analysis is above 90 %, with less than 0.2 % misidentification probability for charged pions.

3.3.5 The Superconducting Coil

Located outside the EMC is a superconducting coil, providing a 1.5 T solenoidal magnetic field. The coil operates at a current of 4596 A, storing an energy of 27 MJ.

3.3.6 The Instrumented Flux Return

The flux of the magnetic field that bends charged particle tracks in the DCH has to follow a closed loop, preferably guided by a ferromagnetic material. The Instrumented Flux Return (IFR), the outermost system of the *BABAR* detector, consists of a large number of steel plates that provide that guidance. The IFR is also used to identify

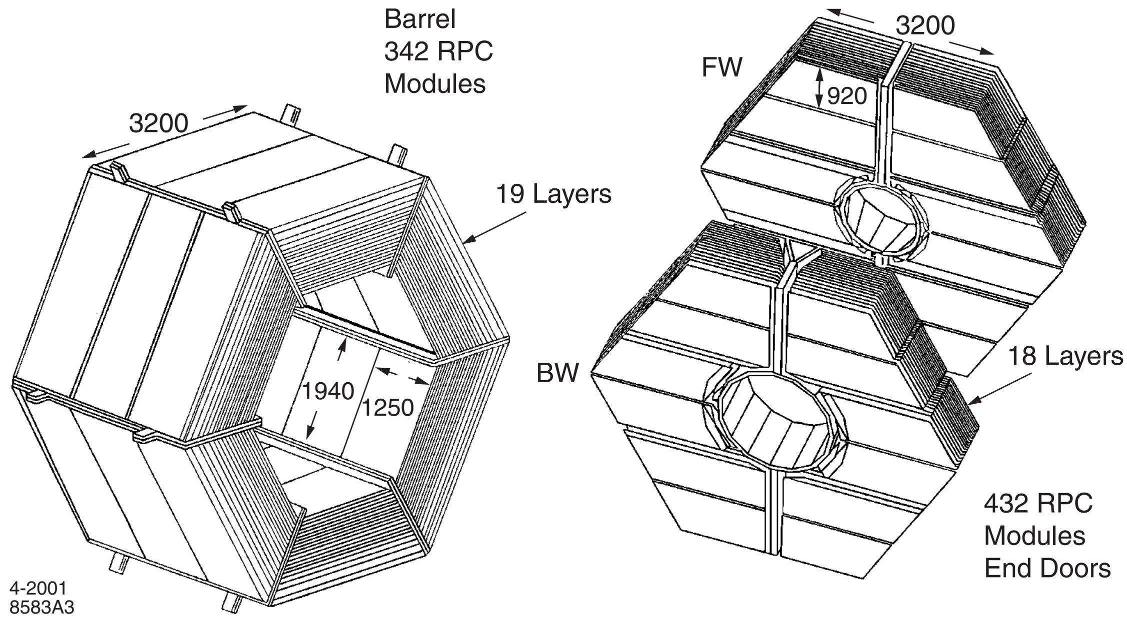

Figure 3.9: Schematic view of the IFR.

muons and detect neutral hadrons, primarily K_L. Hadrons are very likely to interact in the steel plates of the IFR leaving a detectable hadronic shower. Muons, immune to the strong interaction, pass through the IFR losing energy primarily through ionization and thus leaving only a single track.

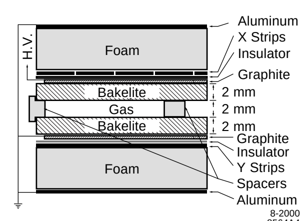

Figure 3.10: Cut view of a RPC.

To detect these traces of charged particles or hadronic showers, the gaps between the steel plates are filled with Resistive Plate Chambers (RPCs) that detect the passing of a charged particle. The RPCs are made of two 2 mm thick bakelite (phenolic polymer) sheets, which have a high resistivity of 10^{11}–$10^{12}\,\Omega\,\mathrm{cm}$. The sheets are separated by a 2 mm gap, filled with a gas mixture that consists of 56.7 % argon, 38.8 % 1,1,1,2-tetrafluoroethane (‘Freon 134a’), and 4.5 % isobutane. The exterior surfaces of the bakelite are coated with graphite, and a voltage of 8 kV is applied between the two graphite layers. A charged particle traversing the chamber ionizes

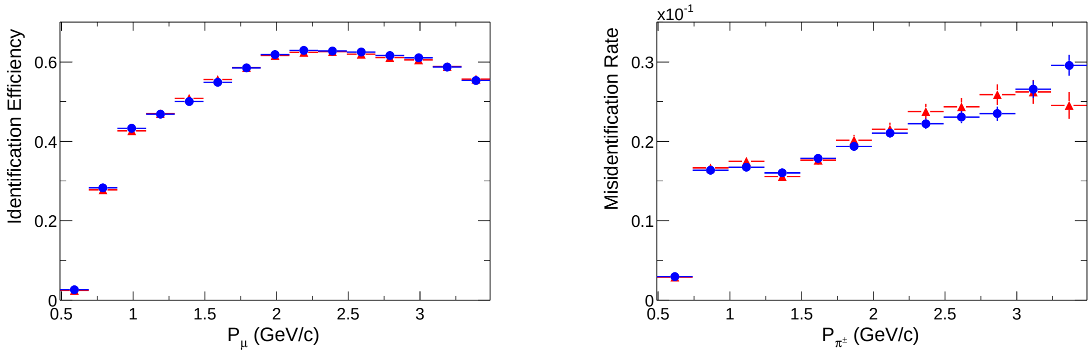

Figure 3.11: Performance of the muon identification system. Shown is the muon efficiency (left) and the misidentification probability of pions as muons (right) as a function of the muon momentum, in simulation (red triangles) and in data (blue bullets).

the gas and a discharge occurs across the gap. Due of the high resistivity of the bakelite the locally drained charge can not be replenished quickly and the current stops. Insulated aluminum strips on both sides of the graphite detect the image charge of the discharge. The strips are oriented with a relative angle of 90°, providing position information of the track in both coordinates of the RPC plane.

A high purity muon sample is of great importance for the $D_s^+ \to \mu^+\nu_\mu$ analysis. Figure 3.11 shows the quality of the muon identification. For the muons used in this analysis the efficiency is between 60 % and 80 %, with a misidentifiation rate of pions as muons below 3 %. A contributing factor to the performance is the IFR track finding algorithm using a Kalman filter, which is described in detail in Appendix B.

The performance of the RPCs has declined dramatically since the start of *BABAR* in 1999, leading to the eventual replacement with limited streamer tubes in the barrel portion of the IFR. The reasons for the RPC efficiency loss are not entirely clear, RPCs which have been replaced in the forward endcap in 2002, show an excellent performance.

3.3.7 The Trigger System

At the most basic level, the *BABAR* Trigger system decides, which events observed by the *BABAR* detector are to be recorded. Trusted with that important task, its performance affects the quality of every single analysis done on *BABAR* data.

At the design luminosity of 3×10^{33} cm^{-2}s^{-1} or 3 Hz/nb, interesting physics events, such as $e^+e^- \to b\overline{b}$, $e^+e^- \to q\overline{q}$ ($q = u$, d, s,and c), or $e^+e^- \to \tau^+\tau^-$, occur at a total rate of about 15 Hz, (Table 3.3). Beam background events contribute at the much higher rate of 20 KHz and need to be rejected. In addition, a sizable event rate comes from $e^+e^- \to e^+e^-$ (Bhabha) events (120 Hz in the detector acceptance) and $e^+e^- \to \mu^+\mu^-$ events (3 Hz). A modest percentage of these must be retained for calibration purposes. The trigger system is designed to maintain a very high efficiency for interesting physics events, while keeping the total rate of events to be recorded and processed below 200 Hz. The precise requirements on the trigger efficiency for various physics data samples are listed in Table 3.2.

Physics Sample	ϵ [%]
$\Upsilon(4S) \to B\overline{B}$	99 $\pm$ 0.5
$e^+e^- \to c\overline{c}$	95 $\pm$ 2.0
$e^+e^- \to \tau^+\tau^-$	95 $\pm$ 2.0
Two photon events	90 $\pm$ 5.0
Continuum $q\overline{q}$	95 $\pm$ 2.0

Table 3.2: Trigger efficiency requirements for the main *BABAR* physics data samples.

In addition to the high efficiency and selectiveness for physics events several other design criteria had to be met. The trigger efficiency needs to be measurable with high accuracy to allow a precise measurement of various branching ratios. The trigger system also needs to be stable in the presence of large and varying beam backgrounds, and, in light of the anticipated increase of the PEP-II luminosity, flexible.

The trigger consists of two stages, a hardware *Level 1 Trigger*, reducing the event rate to about 3 kHz, and a software *Level 3 Trigger*, reducing the event rate to 200 Hz, at which they are written to storage.

The Level 1 Trigger

Figure 3.12 illustrates the role of the Level 1 Trigger in the *BABAR* data readout chain. The raw, digitized data from the detectors subsystems' front end electronics (FEE) are continuously stored in the circular time buffers of the FEE of each detector

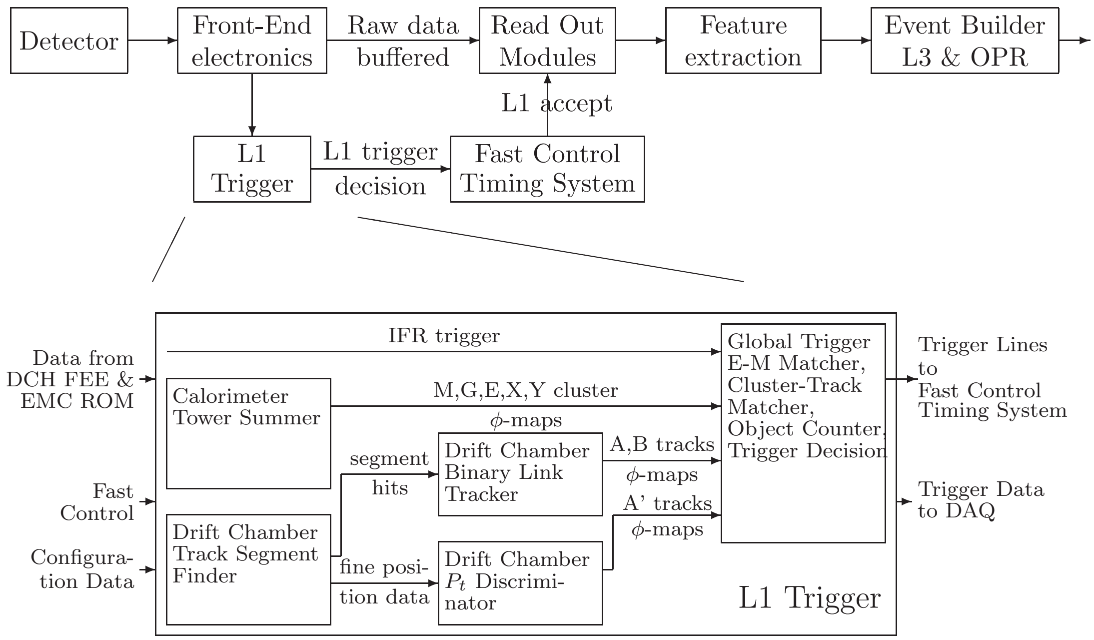

Figure 3.12: Data readout chain of the *BABAR* detector, driven by the Level 1 Trigger.

subsystem, synchronized with the beam-beam interactions, waiting to be read out. Prior to the buffer read-out Drift Chamber, Calorimeter and IFR FEE send data to the Level 1 Trigger hardware, which decides whether an event is interesting enough to be considered further. A positive trigger decision, together with timing information from the EMC, or if not available from the DCH, is passed on to the Fast Control Timing System (FCTS). The FCTS sends a *L1-Accept* signal to the read-out-modules, which initiates the sequence

- Readout of the circular front-end buffers into an event queue, to guaranty a smooth data transfer off the detector.
- Collection of the data in the Read Out Modules.
- Feature extraction, the software aided removal of unnecessary information, like low energy calorimeter noise, etc., and calibration of the data.
- Event building and distribution to the Level 3 Trigger farm, thereby the Level

1 Trigger decisions are added to the event.

- Level 3 Trigger logging decision and event storage.

The Level 1 Trigger decision is based on information (*trigger primitives*) from the DCH and the EMC, which is reconstructed in dedicated subsystem trigger hardware and assembled in the global trigger (GLT).

The Drift Chamber Trigger (DCT) consists of three components, the Track Segment Finder (TSF), the Binary Link Tracker (BLT), and the p_t Discriminator (PTD). At a rate of 3.72 MHz (every 64 beam crossings) each of the 7104 cells in the DCH sends a signal to the DCT, if it has received a hit. The DCT logically arranges the DCH cells in 1776 segments. A segment is an X-shaped group of eight cells that spans a superlayer. The TSF uses a lookup table to find the signature of a straight track passing through the segment. The identified segments are then mapped onto the DCH geometry in terms of 320 supercells, 10 superlayers, each divided into 32 sectors in ϕ. With that map the BLT forms short (long) tracks, moving radially outward from the IP to superlayer 6(10). In addition the PDT checks the same track segments for tracks with a high-transverse momentum ($p_t > 0.6$ GeV/c), starting from superlayer 7 and 10 and moving radially inward toward the IP. Finally the DCT passes three types of trigger primitives to the GLT: 16=bit ϕ-maps of short, long, and high-p_t tracks.

In order to quickly provide trigger information the EMC has been divided into 280 towers, seven-fold along θ and forty-fold along ϕ. Dedicated hardware on the EMC front-end electronics sums the energy of all crystals within a tower and with an energy above a threshold of 20 MeV. The 280 tower energies are the input for the EMC Trigger (EMT). For the various particle types and event topologies, the EMT defines clusters primitives with several energy cuts, and for different regions of the calorimeter. Some clusters span the entire θ range of the EMC, and with energy thresholds of 120, 160, and 500 MeV, they trigger on minimum ionizing particles, low energy photons, and high energy photons, respectively. Another cluster primitive uses only the last two towers in the backward barrel and is sensitive to one prong Bhabha and $\gamma\gamma$ events. A fifth type of cluster that uses only the endcap towers is used only in connection with other clusters and tracks, primarily to veto background.

The EMT passes five 20-bit ϕ-maps to the GLT.

The IFR trigger, which detects mainly $\mu^+\mu^-$ and cosmic ray events, is not used in the trigger decision, but stored with the event for diagnostic purposes.

On the Global Trigger board the cluster and track objects are combined to get additional information about the event topology. The GLT attempts to match the angular location of DCT and EMT primitives. Based on the result of the matching the GLT can issue up to 24 different types of trigger, called *trigger lines*. Those are passed to the Fast Control and Timing System (FCTS), which can optionally mask or prescale them. If a valid trigger remains after this step, a *L1 Accept* is issued, and the readout chain triggered.

After data are read from the buffers of the FEE, and collected and sparsified by the Read Out Modules (VersaModular Eurocard (VME) crates), they are routed to a designated farm processor via the VME backplane. That processor, called the Event Builder, assembles the event from the various independent sub-detectors. The Event Builder then directs the event to one of the 32 processors of the Level 3 Trigger farm.

The definition of the GLT triggers is configurable (the definitions can be loaded into a field programmable gate array (FPGA) at the beginning of data taking), satisfying the criteria of a highly flexible trigger system. Two of the most basic *trigger lines*, based on either DCT or EMT information alone, one requiring just two long DCT tracks, the other just two l60 MeV EMT clusters. This orthogonality of trigger criteria ensures the measurability of the trigger performance.

The Level 3 Trigger

Of the 2 KHz rate of events, put out by the Level 1 Trigger, 95% are still beam-induced background. The Level 3 Trigger, with access to the entire event data and the Level 1 Trigger primitives, comprises detailed event reconstruction and classification algorithms, allowing for a sound background rejection, while maintaining a high efficiency on physics events.

The majority of Level 1 background triggers comes from lost beam particles interacting with the beampipe end flanges at $z = \pm 20$ cm or the synchrotron mask at $z = -50$ cm. Hence, it is necessary to have a adequate z resolution for the origin of the reconstructed tracks.

The Level 3 tracking algorithm uses Level 1 track segments from the TSF as seeds for the pattern recognition and timing information from the DCH wires for the individual drift times. The algorithm consists of three stages, track pattern finding, event t_0 finding, and track fitting. The output is a fitted helix-approximations of the particle tracks. From the five helix parameters and the magnetic field the track three momentum is determined.

The Level 3 clustering algorithm uses sparsified information from the EMC, gained by applying an energy threshold of 20 MeV and a time window of 1.3 μs on the signal of each crystal. With only a few dozen crystals remaining, neighboring relations are established. Clusters of neighboring crystals are kept if their total energy exceeds 100 MeV. For those a cluster central position and average time is calculated.

Events are stored for later analysis if they at fullfill a two-DCH-track or a two-EMC-cluster criteria. In addition, the Level 3 Trigger matches the tracks to cluster locations, information which is used to identify electrons and to lower the Bhabha event rate.

The combined efficiency of the Level 1 and Level 3 Triggers is better than 99.9 % for generic $B\overline{B}$ events, clearly exceeding the design requirements. About 97 % of $q\overline{q}$ and 92 % of $\tau^+\tau^-$ events are also retained. Additionally, samples of (radiative) Bhabha, $\mu^+\mu^-$, and random trigger events for the purpose of calibration, background diagnostics, and the offline measurement of the luminosity, are accepted.

3.4 Detector Datasets, Monte Carlo Simulated Data, and Event Reconstruction

Since its start in October 1999 *BABAR* has recorded more than 320 fb^{-1} of e^+e^- data at a center of mass energy of 10.58 GeV, the peak of the $\Upsilon(4S)$ resonance, and about 25 fb^{-1} at 10.54 GeV, 3.3 standard deviations below the resonance $\Upsilon(4S)$. These two modes of data taking are called *on-peak* and *off-peak* running. In e^+e^- collisions at $\sqrt{s} = m_{\Upsilon(4S)}$, all types of quark-antiquark pairs, with exception of the top-quark,

Table 3.3: Production cross-sections at $\sqrt{s} = 10.58\,\mathrm{GeV}$. The e^+e^- cross-section is the effective cross-section, expected within the experimental acceptance.

$e^+e^- \rightarrow$	Cross-section [nb]
$b\bar{b}$	1.05
$c\bar{c}$	1.30
$s\bar{s}$	0.35
$u\bar{u}$	1.39
$d\bar{d}$	0.35
$\tau^+\tau^-$	0.94
$\mu^+\mu^-$	1.16
e^+e^-	≈ 40

are produced. Lepton-antilepton pairs of all three flavors are also produced, the production cross-sections are listed in Table 3.3.

Due to periods between data taking, allocated for repair and upgrade of the detector and the accelerator, the dataset has been split into parts, within each of which the detector and running conditions largely unchanged. Those parts of the dataset have been dubbed *Run 1* through *Run 5*; their sizes are listed in Table 3.4. For this analysis on-peak and off-peak data from *Run 1* through *Run 4* are used, a total of 230 fb^{-1}. This data contains about 300 million produced $c\bar{c}$ pairs.

The extraction of the branching ratio of the decay $D_s^+ \rightarrow \mu^+\nu_\mu$ requires detailed studies of the production and the decay of the signal and various background processes in e^+e^- data, using Monte Carlo simulated events. The simulation of *BABAR* physics involves two steps, *event generation* and *detector simulation*. The event generation is handled by the software packages Jetset [40] and EvtGen [41]. Jetset simulates the fragmentation and hadronization process of quark pairs using the Lund string model. It so, for instance, predicts the production rate and the momentum spectrum of D_s^{*+} mesons in $e^+e^- \rightarrow c\bar{c}$ events. EvtGen is an event generator that implements many detailed models that describe the physics of B- and D-meson decays. EvtGen also has an interface to Jetset, so it can simulate the decay of D mesons produced in the fragmentation of $c\bar{c}$ quark pairs.

The path of simulated long-lived particles through the detector in the presence of

Table 3.4: Partitioning of the *BABAR* dataset into run periods of stable detector conditions.

Label	Period	Luminosity [fb^{-1}]	
		On Peak	Off Peak
Run 1	Oct 22nd, 1999 – Oct 28th, 2000	19.29	2.33
Run 2	Feb 10th, 2001 – Jun 30th, 2002	59.40	6.83
Run 3	Dec 8th, 2002 – Jun 27th, 2003	30.63	2.39
Run 4	Sep 17th, 2003 – Jul 31st, 2004	99.41	9.93
Run 5	Jul 31st, 2004 – still in progress	70.97	4.00

the magnetic field, their interaction with the detector material, the development of hadronic or electromagnetic showers, and the response signal of the active detector components is simulated by GEANT4 [42]. To introduce the beam background – particles produced in interactions of the beam or of synchrotron radiation with the beam pipe – into simulated data, the detector response to simulated particles is mixed with the signal response of the real detector taken without any trigger conditions.

The output of the simulation is such, that the *BABAR* event reconstruction software can analyze simulated data identically to real detector data. In simulated data it is further possible to relate reconstructed event primitives, such as charged-particle tracks or calorimeter showers, to the true particles produced by the event generators of EVTGEN. This technique, called *truth-matching*, is enormously useful in the study of simulated events, since it reveals the true identity of reconstructed particles and decays.

Part III

Analysis

Chapter 4

Analysis Overview

The goal of this analysis is the measurement of the branching ratio of the decay $D_s^+ \to \mu^+\nu_\mu$. A variety of alternative methods are conceivable:

1. *BABAR* data contain a considerable number of D_s^+ and D_s^{*+} mesons that are produced in decays of B mesons. These are mainly decays $B^0 \to D^{(*)-}D_s^{(*)+}$ with a total branching fraction of about 4 %, and decays $B^+ \to \bar{D}^{(*(*))0}D_s^{(*)+}$ with about 9 %. The data contain about 2.7×10^7 such decays, and with an expected branching ratio $\mathcal{B}(D_s^+ \to \mu^+\nu_\mu) = 5\times10^{-3}$ and with $\mathcal{B}(D_s^{*+} \to \gamma D_s^+) = 94.2 \pm 2.5\,\%$ [30], about 130,000 B decays with a subsequent $D_s^+ \to \mu^+\nu_\mu$ decay are expected be present in the *BABAR* data. In events in which the opposite B meson and the accompanying $D^{(*(*))0}$ or $D^{(*)-}$ meson are fully reconstructed, the invariant mass of the B–D system should then equal the D_s^+ meson mass, and a monoenergetic single muon would indicate the $D_s^+ \to \mu^+\nu_\mu$ decay. Using this technique, *BABAR* has published a result for the branching ratio $\mathcal{B}(D_s^+ \to \phi\pi^+) = (4.81 \pm 0.52 \pm 0.38)\,\%$ [16]. Given the ten times lower branching ratio and the only slightly larger reconstruction efficiency of $D_s^+ \to \mu^+\nu_\mu$ compared to $D_s^+ \to \phi\pi^+$, the statistical error on a measurement of $\mathcal{B}(D_s^+ \to \mu^+\nu_\mu)$ using this technique would be about 30 %.

2. A large fraction (60 %) of D_s^+ mesons in the *BABAR* data originate from the decay $D_s^{*+} \to \gamma D_s^+$, with the D_s^{*+} meson produced in the fragmentation of $c\bar{c}$

quark pairs. Reconstructing the decay $D_s^+ \to \mu^+\nu_\mu$ from a muon and the missing four-momentum leads to a very broad D_s^+ mass peak, due to the errors in the measured missing energy and momentum. These errors largely cancel in the calculation of the mass difference of the reconstructed D_s^{*+} and D_s^+ candidates, improving the resolution of the signal peak. Therefore, the decay $D_s^+ \to \mu^+\nu_\mu$ can be reconstructed in the decay chain $D_s^{*+} \to \gamma D_s^+ \to \gamma\mu^+\nu$, with a minimum momentum requirement on the D_s^{*+} meson to ensure the D_s^{*+} mesons are produced solely in $c\overline{c}$-fragmentation. The reference decay $D_s^{*+} \to \gamma D_s^+ \to \gamma\phi\pi^+$ is also reconstructed, and the partial decay width ratio $\Gamma(D_s^+ \to \mu^+\nu_\mu)/\Gamma(D_s^+ \to \phi\pi^+)$ is measured. Using the known branching ratio $\mathcal{B}(D_s^+ \to \phi\pi^+)$, the branching ratio of the signal $\mathcal{B}(D_s^+ \to \mu^+\nu_\mu)$ is determined. This method was followed by the CLEO collaboration [23]. One of the weaknesses of the early *BABAR* detector was its poor muon detection efficiency and large hadron misidentification rate. In a previous analysis, it was shown that the high pion misidentification rate leads to a large background from light-quark $q\overline{q}$ fragmentation events, which could not easily be modeled and subtracted.

3. Analogous to method 2, the signal decay $D_s^+ \to \mu^+\nu_\mu$ is again reconstructed in the decay chain $D_s^{*+} \to \gamma D_s^+ \to \gamma\mu^+\nu$, and the reference decay $D_s^{*+} \to \gamma D_s^+ \to \gamma\phi\pi^+$ is used to measure the branching ratio $\mathcal{B}(D_s^+ \to \mu^+\nu_\mu)$. The large background from light quark $q\overline{q}$ pairs is suppressed by restricting the search for the signal to events containing an explicitly reconstructed decay of a charm meson, D^0, D^+, D_s^+, and D^{*+}, the *tag*. The correlation of the charm content of the tag and the signal can be used to suppress random background events even further.

This analysis follows the course of method 3. The general method is discussed in more detail in the next section. The backgrounds in this analysis are presented in the section after. Two further sections describe the special particle identification efficiency correction method that is applied in this analysis, and the Monte Carlo simulated event samples.

4.1 The Method of Analysis

The decay $D_s^+ \to \mu^+\nu_\mu$ has a neutrino in the final state, which is not detectable in the detector and can only be inferred from the energy and momentum that is missing in the event after all other long lived particles present in the event have been reconstructed. Often a number of particles are not measured by the detector, either because of reconstruction inefficiencies or because of the limited angular detector acceptance. Other particles may not have their true flavor correctly identified, so that their energy is wrongly predicted from the momentum measurement. All this leads to a large uncertainty in the energy and momentum that may be assigned to the neutrino, and mainfests itself in a the poor mass resolution of the D_s^+ meson that is reconstructed using the neutrino four-momentum.

About 60 % of D_s^+ mesons in the *BABAR* data originate from the decay $D_s^{*+} \to \gamma D_s^+$ with the D_s^{*+} meson produced in events $e^+e^- \to c\bar{c}$. Because the errors in the measured missing energy and momentum largely cancel in the calculation of the mass difference of the reconstructed D_s^{*+} and D_s^+ candidates, the resolution of the mass difference is much better than that of the D_s^+ mass. Therefore, this analysis is performed using the decay chain $D_s^{*+} \to \gamma D_s^+ \to \gamma\mu^+\nu$, which improves the signal to background ratio.

The analysis is further restricted to events in which the D_s^{*+} meson is produced solely in $c\bar{c}$-fragmentation. These events are identified using a charm tagging technique.

The following approach is taken to reduce the non-charm $q\bar{q}$ events. Events are initially selected where a charm meson (the *tag*) is fully reconstructed or *tagged* in one of many decay modes. An important property that is common to all tagging decay modes is that the charm quantum number of the tag can be inferred from unambiguously the charge of the tag or its decay products. Excluding a small amount of doubly Cabibbo-suppressed decays of the D^0, where kaon charge predicts the wrong tag charm number, that tag correctly predicts the charge of the muon in the $D_s^+ \to \mu^+\nu_\mu$ signal decay. The precise makeup of this tag sample, e.g. the charm decay modes used for reconstructing D meson candidates, is given in the next chapter.

The presence of a charm meson tag largely eliminates lighter $q\bar{q}$ events (where $q = u$, d, or s), but does not exclude charm production from B meson decays. Requiring the tagged charm meson to have high enough momentum, with the momentum threshold chosen near the kinematic limit for charm from B decays – such as $B \to Dl\nu$ – reduces the contribution from B meson decays in a model independent fashion. The upper momentum limit for a D meson from a two-body B decay is given by

$$p_{\mathrm{tag}} = \frac{M_B^2 - M_{\mathrm{tag}}^2}{2M_B} \ , \tag{4.1}$$

which leads to the momentum limit in the center of mass system

$$p_{\mathrm{tag}}^{*\,\mathrm{max\,from\,B}} = \begin{cases} 2.503\,\mathrm{GeV/c} & \text{if the tag is a } D^0, \\ 2.502\,\mathrm{GeV/c} & \text{if the tag is a } D^{\pm}, \\ 2.468\,\mathrm{GeV/c} & \text{if the tag is a } D_s^{\pm}, \\ 2.416\,\mathrm{GeV/c} & \text{if the tag is a } D^{*\pm} \ . \end{cases} \tag{4.2}$$

In this analysis a lower momentum cutoff of $2.35\,\mathrm{GeV}/c$ is chosen for all but the $D^{*\pm}$ tag mode, for which a minimum momentum of $2.30\,\mathrm{GeV}/c$ is required. This allows a very small number of D mesons from B decays to enter the tag sample.

Particle candidates which make up the charm tag will subsequently be referred to as the “tag side” of the event, while all remaining tracks and neutral clusters belong to what will be designated the “recoil side”.

The balance of this analysis outline is focused on the recoil side where the photon from the D_s^{*+} cascade and the muon candidate from the D_s^+ decay itself are searched for. As already stated, the charm of the tag side uniquely determines the charge of the recoil-side muon. By requiring signal muon candidates to have this charge, the number of background events in which hadrons are wrongly identified as muons is reduced by 50 %. Detailed knowledge of the kinematics and the particle content of the tag side also allows for an improvement in the missing energy and momentum resolution in the event. The signal for the decay chain $D_s^{*+} \to \gamma D_s^+ \to \gamma\mu^+\nu$ manifests itself in the classic mass difference (ΔM) between the reconstructed D_s^{*+} and D_s^+, formally,

$$\Delta M = M(\gamma\mu^+\nu_\mu) - M(\mu^+\nu_\mu) \; . \tag{4.3}$$

The signature is an excess of events in the vicinity of $144\,\mathrm{MeV}/c^2$. The expected shape of the signal peak is derived from detailed simulation of the decay $D_s^{*+} \to \gamma D_s^+ \to \gamma\mu^+\nu$ in the *BABAR* detector. Requirements on the kinematic properties of the muon, neutrino, and the D_s^{*+} of reconstructed signal candidates are made. The precise requirements are selected to optimize the significance of the resulting branching ratio measurement, where the significance is the measured branching ratio divided by its statistical uncertainty. The signal detection efficiency is derived from the *BABAR* Monte Carlo simulation of the decay $D_s^{*+} \to \gamma D_s^+ \to \gamma\mu^+\nu$ in $c\bar{c}$ events.

Backgrounds other than from correctly tagged $c\bar{c}$ events are estimated from the tag mass sidebands in data. Correctly tagged $c\bar{c}$ events with a semileptonic charm or a leptonic tau decay with a final state muon are estimated by replacing the muon identity requirement with that of an electron and correcting for the difference in muon and electron detection efficiency. Other backgrounds are estimated from *BABAR* Monte Carlo simulation. Section 4.2 details the estimation of the background processes for this analysis.

The measurement of the branching ratio of the signal ultimately requires a determination of the number of produced D_s^{*+} mesons in the parent population. For this analysis the parent population are the charm tagged events, and the number of D_s^{*+} mesons therein is determined by simultaneously reconstructing another D_s^{*+} decay chain, $D_s^{*+} \to \gamma D_s^+ \to \gamma\phi\pi^+$, in this set of charm tagged events. The branching fraction of $D_s^+ \to \phi\pi^+$, that is necessary to extract the branching ratio of $D_s^+ \to \mu^+\nu_\mu$, was independently measured by the *BABAR* collaboration to be $(4.81 \pm 0.52 \pm 0.38)\,\%$ [16]. The $13\,\%$ error of this measurement will be part of the error of $\mathcal{B}(D_s^+ \to \mu^+\nu_\mu)$, but will be quoted separately.

Relating the $D_s^+ \to \mu^+\nu_\mu$ and $D_s^+ \to \phi\pi^+$ decays to each other also has the advantage of minimizing the uncertainties arising from the tag reconstruction, since the tagging efficiencies largely cancel in the ratio of the two D_s^+ decays.

4.2 Background Estimation

Background events from different sources will pass all signal selection criteria. There are five different sources of background to this analysis, and different strategies are followed to estimate them. The background categories are described in detail in the following, and are summarized in Table 4.1.

I. **Fake Charm Tag.** On the tag side of the event a random combination of tracks and clusters can pass all criteria for a charm tag, including having a mass within two standard deviations of the nominal value.

   All background events $e^+e^- \to q\bar{q}$ $(q = u, d, s)$ and $e^+e^- \to \tau\tau$ are necessarily fake tags. In events $e^+e^- \to c\bar{c}$ the tag can also be in correctly reconstructed. Also most $b\bar{b}$ background events fall into this background category, since real charm mesons coming from a B decay are otherwise excluded kinematically by the aforementioned momentum cut, and hence all signatures of a charm meson must be erroneous, passing the momentum cut only because of the random combinations of tracks.

   These events can produce a non-negligible background on the signal side, moderated largely by the choice of tag purity and tagging efficiency that is desired. This background circumvents the hadron misidentification suppression obtained by knowledge of the correct or expected muon charge.

   The most suitable method to measure the size and shape of this background is a sideband subtraction using the charm-tag mass distribution. The validity of this subtraction method will be demonstrated first using simulated events, before being applied to data.

II. **Correct Charm Tag.** Events in this background category have a correctly reconstructed charm tag, and as a result of the requirement of a minimum tag momentum of 2.35 GeV/c, must have been produced in $c\bar{c}$ fragmentation. On the recoil side, there are several distinct and enumerable backgrounds to $D_s^+ \to \mu^+\nu_\mu$ through the D_s^{*+} cascade.

Table 4.1: Overview of the five different background categories, listing their sources and the anticipated treatment. The name of the background category, in *italic* will be used throughout this thesis.

	Bkgd category	Event types	Treatment
I	*Fake Tag*	events with a randomly generated charm signature – all light $q\overline{q}$, $b\overline{b}$, $\tau\tau$ events, some $c\overline{c}$ events contribute	Sideband in charm tag mass distribution used to determine shape and size
II	*Real Tag*	$c\overline{c}$ events	
II(a)i	*Leptonic* μ	$D^+_{d/s} \to \mu^+\nu_\mu$	Shape and relative size are estimated from Monte Carlo simulation.
II(a)ii	*Leptonic* τ	$D^+_{d/s} \to \tau^+\nu_\tau$, and $\tau^+ \to \mu^+\nu_\mu\bar{\nu}_\tau$	Lepton universality. Up to a phase space correction, $\tau \to e\nu_e\nu_\tau$ and $\tau \to \mu\nu_\mu\nu_\tau$ have the same branching ratio. Electron substituted, efficiency corrected, signal selection on data determines background shape and size.
IIb	*Semileptonic*	$D_q \to X\mu\nu_\mu$	Lepton universality. $D_q \to Xe\nu_e$ has the same branching ratio as $D_q \to X\mu\nu_\mu$. Electron substituted, efficiency corrected, signal selection on data determines background shape and size.
IIc	*Combinatoric*	Random combinations on signal side	Shape and relative size are estimated from Monte Carlo simulation.

a) **Feed down From True Leptonic Decays in the Recoil.** There are two major contributors to this category.

   i. First, there is $c\bar{c} \to D^+_{d/s} \to \mu^+\bar{\nu}_\mu$ where the $D^+_{d/s}$ is a direct fragmentation product rather than the $D^{*+}_{d/s}$ cascade but is combined with a random photon. While this process contributes to the final ΔM distribution, it is a non-peaking background. For this case, the shape and relative size of these backgrounds will be determined from Monte Carlo simulation, while the overall scale is left as a free parameter in the final fit.

   ii. Second are the D^{*+}_s cascades, where the final leptonic decay goes through a τ: $c\bar{c} \to D^{*+}_s \to \gamma D^+_s \to \tau^+\nu_\tau$, where $\tau^+ \to \mu^+\nu_\mu\bar{\nu}_\tau$. These decays are not strongly helicity-suppressed, making them more prevalent, and because only neutrinos are missing, they peak in the final ΔM distribution. Additionally, the leptonic mode $c\bar{c} \to D^+_s \to \tau^+\nu_\tau$, with $\tau^+ \to \mu^+\nu_\mu\bar{\nu}_\tau$, where the D^+_s combines with a random photon, are also addressed within this background category. The leptonic τ branching ratios are equal $\mathcal{B}(\tau^+ \to \mu^+\nu_\mu) = \mathcal{B}(\tau^+ \to e^+\nu_e)$, hence backgrounds in this category are automatically removed by the same method applied for category IIb.

b) **Feed down From Semileptonic Decays in the Recoil.** This category includes all events $D_q \to X\mu\nu_\mu$, where X can be one of $K^\pm$, $\pi^\pm$, K^0, π^0, ϕ, ω, etc. Lepton universality implies that the branching ratios $D_q \to X\mu\nu_\mu$ and $D_q \to Xe\nu_e$ must be approximately equal. By repeating the analysis, substituting an identified electron for the muon and correcting for their relative identification efficiencies, the precise size and shape of this background can be extracted from the data. This technique does not subtract the signal $D^+_s \to \mu^+\nu_\mu$, since the pure electronic decays, $D^+_s \to e^+\nu_e$, are strongly helicity suppressed.

c) **Combinatorics in the Recoil.** A sizable portion of the background is expected to be from events with a correctly reconstructed tag, but a misidentified pion, kaon, or proton on the signal side. Usually these misidentified particles randomly combined fake a signal that is expected to have no peaking component. The decay $D_s^{*+} \to \gamma D_s^+ \to \tau^+\nu_\tau$ (branching ratio 6 %) with $\tau^+ \to \pi^+(\pi^0)\nu_\tau$ and the π^+ wrongly identified as muon is also listed in this category, despite its signal like appearance. Due to the lack of a control sample that could be used to simulate these decays, the shape of this background is estimated from Monte Carlo simulated events.

Ideally all background contributions should be estimated from real data to minimize the dependence on the Monte Carlo simulation and the associated assumptions about the underlying physics and the behaviour of the detector. This has been largely accomplished in this analysis and only the *Leptonic* μ (II(a)i) and the *Combinatoric* (IIc) backgrounds are estimated from Monte Carlo simulation. The data derived elimination of $D_s^+ \to \tau^+\nu_\tau$ decays by subtraction of the electron-substituted sample is important, because it makes this analysis a pure measurement of $D_s^+ \to \mu^+\nu_\mu$.

4.3 Particle Identification Correction

The agreement of Monte Carlo simulated data and real data taken with the *BABAR* detector is good, but not perfect. The simulation of the detector response to particles interacting with the detector is only an estimate. Some reasons for the shortcomings in simulating the detector response are

- the slowly changing performance of various detector components due to aging and repair,
- the incomplete detector model used by the simulation software, which does not include all the fine structure and material that is built into the detector, and
- the limitations in the understanding of particle interactions with the detector material, for instance the shape of electromagnetic or hadronic showers.

Table 4.2: Partitioning of the *BABAR* dataset into periods of constant particle selector performance. In numbers in parantheses are the runs, that mark the beginning and ending of the period.

Table	Period
`run1-1900V`	Oct 22nd, 1999 (9932) – Jul 11th, 2000 (14471)
`run1-1960V`	Jul 11th, 2000 (14472) – Oct 28th, 2000 (17106)
`run2-2001`	Feb 10th, 2001 (18149) – Dec 23rd, 2001 (25007)
`run2-2002`	Jan 12th, 2002 (25281) – Jun 30th, 2002 (29435)
`run3`	Dec 8th, 2002 (32955) – Jun 27th, 2003 (39320)
`run4`	Sep 17th, 2003 (40228) – Jul 31st, 2004 (50635)

This limited predictability of the detector response also includes the indentification efficiency and misidentification rate for $\mu^{\pm}$, $e^{\pm}$, $\pi^{\pm}$, $K^{\pm}$, and protons. However, it is crucial to the success of this analysis that the $\mu^{\pm}$, $e^{\pm}$, $K^{\pm}$, and $\pi^{\pm}$ detection efficiencies are known at a level that their uncertainties are not the dominating source of the systematic error on the results. To have the PID efficiencies in Monte Carlo simulated data resemble those in real data as closely as possible, data derived efficiencies are applied to simulated events.

In this analysis the method of *PID weighting* is used. Real data control samples, in which the true nature of a particle is known with very high probability, are used to measure the efficiencies of the particle identification tools, the *PID selectors*. The efficiencies of the PID selectors are also measured on control samples derived from Monte Carlo simulated events. The definition of these *PID control samples* is given in Section 4.3.1. This section also describes how the PID selector efficiencies are measured. The measured efficiencies are stored in *PID efficiency tables*, separate for Monte Carlo simulation and for real data. The PID efficiency tables are organized by particle type, charge, and selection criteria. They are split into ranges in time over which the PID performance was stable (Table 4.2).

Simulated particle efficiencies are corrected to match real data using *MC-to-data PID weights*, which are the ratios of real data to Monte Carlo simulated efficiencies, found in the corresponding data and Monte Carlo PID efficiency tables. Additionally, *electron-to-muon PID weights* are calculated for simulated events and data. These weights are the ratios of muon to electron efficiencies, found in the PID efficiency tables corresponding to the muon and electron PID selectors that are used in this analysis. The weights are used to correct for the different PID selector efficiencies in the reconstruction of decays, such as $D_s^{*+} \to \gamma D_s^+ \to X\mu^+\nu_e$ and $D_s^{*+} \to \gamma D_s^+ \to Xe^+\nu_e$, which are, up to phase space differences of $3\,\%$, identical in size and shape due to lepton universality.

In this analysis only the tracks on the signal side from the $D_s^+ \to \mu^+\nu_\mu$ and $D_s^+ \to \phi\pi^+$ decays are considered for PID efficiency correction. Tracks that make up the charm tag and other tracks in the events are not adjusted in Monte Carlo events. That will not influence the result of this analysis, since the tagging efficiency cancels in the $D_s^+ \to \mu^+\nu_\mu$ to $D_s^+ \to \phi\pi^+$ ratio.

4.3.1 Definition of the PID Control Samples

The PID control samples are defined as follows.

Muon Control Sample

The muon control sample consists of events $e^+e^- \to \mu^+\mu^-\gamma$ extracted from the *BABAR* dataset applying the following criteria.

- The event must contain exactly two oppositely-charged tracks, both with a transverse momentum of at least $100\,\mathrm{MeV}/c$, a minimum of 12 DCH hits, and an polar angle restricted to $0.41 < \theta < 2.54$ rad. The point of closest approach of the track to the IP has to be within 1.5 cm in the xy-plane and within 10 cm along the z-axis of the IP.

- The event must contain at least one photon candidate. Photon candidates are neutral EMC clusters with an energy of at least $30\,\mathrm{MeV}$ and a maximum lateral moment of the energy distribution in the EMC, LAT < 0.8.

The muon mass is assigned to each of the two tracks. For each photon candidate γ in the event the invariant mass of the two-track-and-photon system ($M(\mu\mu\gamma)$) is calculated. The photon candidate γ with $M(\mu\mu\gamma)$ closest to the event mass ($\sqrt{s} = M(e^+e^-)$) is considered the signal photon (γ_1), and $|\sqrt{s} - M(\mu\mu\gamma_1)| < 0.5\,\mathrm{GeV}/c^2$ is required. No other photon candidate with an energy of more than 50 MeV is allowed in the event. The distance of the signal photon γ_1 to the nearest track has to be more than 30 cm.

A kinematic fit is applied to the two-track-and-photon system. In the fit the tracks are constrained to have a common vertex within the beam spot, the invariant mass $M(\mu\mu\gamma_1)$ is constrained to $\sqrt{s}$, and the momentum $p(\mu\mu\gamma_1)$ is constrained to the total beam momentum. The χ^2 probability of the fit is required to be above > 0.01, and the energy of the fitted photon must be larger than 1.5 GeV.

Muon candidates are selected if the opposing track satisfies the loose muon criteria, which is based on the traversed interaction length, and the agreement of the measured track with the minimum ionizing particle hypothesis.

Electron Control Sample

The electron control sample consists of events $e^+e^- \to e^+e^-\gamma$. Two control samples are defined. The first is based on the following criteria:

- The event must contain exactly two oppositely-charged tracks, one track with a momentum between 4.0 and $6.0\,\mathrm{GeV}/c$, the other with less then $3.5\,\mathrm{GeV}/c$ in the laboratory frame.
- A neutral calorimeter cluster of at least 0.5 GeV must be present and more than 0.2 rad removed from where the low momentum track enters the EMC.
- The energy-deposit of the high momentum particle in the EMC must be at least half its momentum.
- The sum of the two track momenta and the energy of all neutral clusters must be above 11.0 GeV.

The low momentum track is taken as the electron candidate.

The second control sample is selected by the following requirements:

- The event must contain exactly two oppositely-charged tracks, the highest track momentum must be below 4.7 GeV/c.
- A neutral calorimeter cluster with $0.0001 < M_{\mathrm{LAT}} < 0.8$ (5.1) of at least 0.1 GeV must be present.

Tracks are accepted as electron candidates if the second track has $E_{\mathrm{EMC}}/p > 0.85$. This sample is used for electrons between 3.5 and 4.7 GeV.

Charged Pion Control Sample

The charged pion control sample consists of $\tau^+\tau^-$ events with a 3–1 topology. A τ^+ lepton decays with a probability of 99.9 % into a final state that contains either one or three charged particles, a τ-neutrino, and perhaps a number of other neutral particles. The decays into three charged particles are dominated by the decay $\tau^+ \to \pi^+\pi^+\pi^-\bar{\nu}_\tau$. Identifying events $e^+e^- \to \tau^+\tau^-$ with one $\tau^\pm$ decaying into a one-charged-particle final state and the other $\tau^\mp$ decaying into a three-charged-particle final state results in a very clean sample of charged pions covering a wide momentum spectrum. About 25 % of all decays of $e^+e^- \to \tau^+\tau^-$ events are of this type. An event is selected as a τ–3–1 event if it has

- a thrust $T > 0.925$, and
- exactly 4 tracks, satisfying a tight track criterion, with zero total charge, and a 3–1 topology.

The tight track criterion requires that the transverse momentum is at least 100 MeV/c, and that the track has at least 20 DCH hits. The distance between the tracks point of closest approach to the IP and the IP itself must be less than 1 cm in the xy-plane, and less than 3 cm along z. The tracks are required have a CM momentum $p^* < 4.5$ GeV/c. The decision about the event's 3–1 topology is based on the dot products of the CM momentum vectors of the 4 tracks with each other. A track is considered a 1-prong candidate if the dot products with the three other tracks are all negative. An event is considered to have a 3–1 topology if it has exactly one 1-prong candidate. After the single track has been identified, the 3-prong invariant mass is required to be $0.7 < m_{3p} < 1.6\,\text{GeV}/c^2$, and the invariant masses of all two-track combinations must be larger than $0.15\,\text{GeV}/c^2$.

All tracks on the three-prong side are selected as pion candidates.

Charged Kaon Control Sample

The charged kaon control sample is derived from kaons in the decay $D^{*+} \to \pi^+ D^0 \to K^-\pi^+$. The D^0 candidates are reconstructed from pairs of oppositely-charged tracks. One track is assigned the kaon mass, the other the pion mass. The invariant mass of the $K^\pm$–$\pi^\mp$ pair must be between 1.4 and $2.32\,\text{GeV}/c^2$. A mass-vertex-constrained χ^2-fit is applied to the $K^\pm$–$\pi^\mp$ pair. A charged pion of less than $0.5\,\text{GeV}/c$ is added to the fitted D^0 meson candidate to from D^{*+} meson candidates. Requirements are made on

- the mass of the D^{*+} candidate, $1.99 < M(D^0\pi^+) < 2.03\,\text{GeV}/c^2$,
- the D^*–D^0 mass difference, $0.14375 < \Delta M_{D^{*+}-D^0} < 0.14715\,\text{GeV}/c^2$,
- the kaon helicity angle in the D^{*+} frame, $\cos\theta_{\text{hel}}(D^{*+}, K^-) < -0.9$,
- the angle between the kaon and the pion laboratory frame $\alpha(K^+, \pi^+) < 0.4$, and
- the angle between the D^0 and the soft pion in the laboratory frame $\alpha(D^0, \pi_s) < 2.0$.

The track with assumed kaon mass is selected as charged kaon candidate.

4.3.2 PID Efficiencies and PID Tables

The efficiencies of the PID selectors, which is the percentage of particles of a certain type ($\mu^\pm$, $e^\pm$, $\pi^\pm$, $K^\pm$, or proton) that satisfy the PID selector requirements, vary with particle momentum and detector region. The functional dependence $\epsilon^{y|x}(p, \theta, \phi)$ of the selection efficiencies of the certain particle type, x, and a particular PID selector, y, is not given in a close analytical expression, but in form of a three-dimensional lookup-table, $b \rightarrow \epsilon_b^{y|x}$, or *PID-Table*.

The bins b are defined by their boundaries $(p_b^{\min}, p_b^{\max}, \theta_b^{\min}, \theta_b^{\max}, \phi_b^{\min}, \phi_b^{\max})$. They are disjunct and cover the entire phase space, such that the association $B(p, \theta, \phi) = b$ is always existent and unique; exactly one bin b satisfies $p_b^{\min} < p < p_b^{\max}$, $\theta_b^{\min} < \theta < \theta_b^{\max}$, and $\phi_b^{\min} < \phi < \phi_b^{\max}$ for any given $(p,\ \theta,\ \phi)$.

The efficiency $\epsilon_b^{y|x}$ for each bin b for a given particle type, x, and a particular selector, y, is given by

$$\epsilon_b^{y|x} = \frac{N_b^{\mathrm{pass}\, y|x}}{N_b^x}\,, \tag{4.4}$$

where N_b^x is the number of particles of type x that fall into the bin b, $(B(p, \theta, \phi) = b)$, and $N_b^{\mathrm{pass}\, y|x}$ is the number among them that fullfill the criteria of the PID selector y.

The muon, electron, and charged pion control samples are very clean, the numbers N_b^x and $N_b^{\mathrm{pass}\, y|x}$, $(x = \mu^\pm, e^\pm$, and $\pi^\pm)$, are determined by simply counting. The numbers for $x = K^\pm$ are determined in a χ^2 fit of the $\Delta M_{D^{*+}-D^0}$ peak from the charged-kaon control sample $D^{*+} \rightarrow \pi^+ D^0 \rightarrow K^- \pi^+$.

The PID-tables do not only define, for instance, the muon efficiency of a particular muon selector, $(x = \mu^\pm,\ y = \mu - \text{selector})$, but also the misidentification rate of, for instance, charged pions as muons, $(x = \pi^\pm,\ y = \mu - \text{selector})$.

4.4 Tracking Efficiency Correction

The track reconstruction efficiency in Monte Carlo simulation agrees well with data, and only a small MC-to-data correction needs to be applied to simulated events. The correction is applied on a track by track basis, following the same procedure as the PID efficiency MC-to-data correction. The tracking efficiency as a function of momentum, polar angle, and azimuthal angle is determined in simulated events and in data. The track reconstruction efficiencies in Monte Carlo and in data, are stored in tracking efficiency lookup-tables. The data to Monte Carlo efficiency ratio, which gives the *MC-to-data track weights*, is also stored in momentum and angle dependent lookup-tables. The control sample that is used to determine the tracking efficiencies are $e^+e^- \to \tau^+\tau^-$ events with a 3–1 decay topology. These are the same events as those used for the charged pion control sample, but with a selection that places requirements on only two out of the three tracks on the 3-prong side. That way, the reconstruction and selection efficiency of tracks can be studied on the third track.

The control sample is selected from events with between 3 and 5 charged tracks, which must come within 1 mm in xy and 3 cm in z of the IP. The most isolated track must be a well-identified electron or muon. The decay of the other τ is partially reconstructed from two charged pions, The two pions must either form a ρ^0 meson candidate, identifying the decay $\tau^+ \to \rho^0\pi^+$, or they must be both of opposite lepton-charge identifying the decay $\tau^+ \to \pi^+\pi^+\pi^-$. The third charged pion to be present in the decay represents the candidate for the tracking efficiency studies. Because of the three neutrinos in the event, the momentum and direction of the third pion have to be estimated from kinematic constraints of the whole event.

4.5 Monte Carlo Samples

In this analysis the following Monte Carlo simulated event samples, summarized in Table 4.3, are used:

- A sample of signal decays produced in charm fragmentation, $e^+e^- \to c\bar{c} \to D_s^{*+} \to \gamma D_s^+ \to \gamma\mu^+\nu$, is used to study the signal distribution of various selection variables, and to optimize the signal selection cuts. This sample is also used to measure the signal detection efficiency. The charm quark in the recoil of the signal fragments *generically*, according to the JETSET fragmentation model. This sample is referred to as the *signal Monte Carlo sample*.

- A sample of $D_s^+ \to \phi\pi^+$ decays produced in charm fragmentation, $e^+e^- \to c\bar{c} \to D_s^{*+} \to \gamma D_s^+ \to \gamma\phi\pi^+$, is used to study the distribution of various variables for the $D_s^{*+} \to \gamma D_s^+ \to \gamma\phi\pi^+$ selection. This sample is also used to measure the $D_s^{*+} \to \gamma D_s^+ \to \gamma\phi\pi^+$ detection efficiency. The charm quark in the recoil of the

$D_s^+ \to \phi\pi^+$ fragments generically. This sample is referred to as the $\phi\pi^+$*-signal Monte Carlo sample.*

- The major sources of backgrounds for this analysis are investigated using generic decay samples. Generic samples are samples of simulated decays in which the decay mode composition is chosen such that it agrees with nature as far as our knowledge reaches. This is achieve through applying a mixure of fragmentation and hadronization models and specific measured decay rates. The fragmentation process in events $e^+e^- \to c\overline{c}$ and $e^+e^- \to q\overline{q}$, ($q = u,\ d,\ s$), is modeled by the JETSET program, the subsequent decay of the produced hadrons is done according various decay models within EVTGEN. Production and decay of $B^0\overline{B}^0$ and B^+B^- meson pairs produced in the decay of the $\Upsilon(4S)$ resonance are simulated by EVTGEN. Since only a fraction of the B decays are known, JETSET fills in to simulate the remaining percentage of B decays according to a generic hadron decay model. The simulation of the decay of τ-pairs is performed by KK2F [43] and TAUOLA [44], within EVTGEN. KK2F models the τ-pair production in e^+e^- events, while TAUOLA is responsible for the decays of the τ-meson.

The Monte Carlo samples, their size and luminosity equivalent are listed in Table 4.3.

Table 4.3: Signal and generic Monte Carlo samples, their size and equivalent luminosity. The luminosity equivalent for the generic Monte Carlo sample is calculated using the production cross-sections from Table 3.3, the signal luminosity equivalent is calculated based on the the current PDG values $\mathcal{B}(D_s^+ \to \mu^+\nu_\mu) = 5.0 \times 10^{-3}$ and $\mathcal{B}(D_s^{*+} \to \gamma D_s^+ = 0.95)$, the $e^+e^- \to c\bar{c}$ production cross-section, and a D_s^{*+} production rate in c-quark fragmentation of 9 %, estimated from generic $c\bar{c}$ Monte Carlo simulation.

Monte Carlo Sample	# Events	Lumi [fb^{-1}]
$D_s^{*+} \to \gamma D_s^+ \to \gamma\mu^+\nu$	1,284,786	2188.0
$D_s^{*+} \to \gamma D_s^+ \to \gamma\phi\pi^+$	2,192,000	790.2
$e^+e^- \to c\bar{c}$	415,371,501	319.5
$e^+e^- \to q\bar{q}$, $q = u, d, s$ (uds-sample)	673,385,000	320.7
$e^+e^- \to B\overline{B}$	530,812,000	1011.1
$e^+e^- \to B^+B^-$	564,916,000	1076.0
$e^+e^- \to \tau\tau$	345,706,000	367.8

Chapter 5

The Charm Tag

In this chapter the formation of a large sample of charm mesons, D^0, D^+, D_s^+, and D^{*+}, reconstructed in a hadronic decay mode, is discussed. The identified charm mesons are subsequently used to identify or *tag* events $e^+e^- \to c\bar{c}$. This chapter starts by briefly describing a preliminary event selection, applied to suppress QED background. The reconstruction of the charm meson candidates in their more dominant hadronic decay modes is then detailed. In each event, only one charm meson candidate is kept and called the *tag*. The description of the tag selection concludes this chapter.

5.1 Preliminary Selection

A large number of events in the *BABAR* dataset are Bhabha, di-muon, and di-tau events, $e^+e^- \to l^+l^-$ ($l = e$, μ, and τ, respectively). These QED background events have a small number of final state particles which are largely produced back-to-back. To reduce this background component early on, the following requirements are made prior to any other:

- The normalized second Fox-Wolfram moment, R_2 [45], in the CM frame (a measure for the collinearity, or back-to-backness of the particle tracks) is calculated and required $R_2 < 0.95$.

- A minimum of three tracks originating near the IP is required. The distance between the point of closest approach to the IP of each track and the IP must be less than 1.5 cm in the xy-plance, and less than 10 cm along the z-direction.

5.2 The Definition of the Tag Sample

Charm mesons D^0, D^+, D_s^+, and D^{*+} mesons are fully reconstructed in several hadronic decay modes. These decay modes make up the *charm meson tag sample*. Common to all modes of the tag sample is that they allow an unambiguous determination of the charm quantum number of the tag. Unless D^0–$\overline{D}^0$ mixing occured prior to the decay, or the decay proceeded through a doubly Cabibbo suppressed amplitude, correctly reconstructed tag candidates predict the charge of the $D_s^{*\pm}$ on the signal side, since the tag and the signal are the charm particles that formed in the fragmentation of $c\overline{c}$ quark pairs. The decay modes that make up the tag sample, together with their charm content, are listed in Table 5.1.

5.3 Reconstruction of Tag Candidates

The tag candidates are reconstructed in their weak decay from different daughter particles; charged and neutral pions and kaons, ϕ and ρ^+ mesons. These particles are selected by making the following requirements.

Good Charged Tracks The lifetime of the weakly decaying pseudoscalar charm mesons is between 100 and 300 μm/c, that of the vector meson D^{*+}, which decays strongly and electromagnetically, is even shorter. Charged particle tracks from decays of these mesons originate near the IP. A requirement is made that tracks at their point of closest approach to the IP must lie within 1.5 cm in the xy-plane and within 10 cm in the z direction of the IP. An exception is made for charged pions from the decay of K_S^0 mesons, which have a larger lifetime of 2.68 cm/c.

Table 5.1: The tag sample composition. Listed are the charm quantum number, the branching fraction (PDG 2004 [30]), and the minimum required momentum in the CM frame ($p^{*\,\mathrm{min\,reco}}_{\mathrm{tag}}$) for each tag mode.

Index	Decay Mode	Charm	Branching Fraction [%]	$p^{*\,\mathrm{min\,reco}}_{\mathrm{tag}}$ [GeV/c]
1	$D^0 \rightarrow K^-\pi^+$	+1	3.80 $\pm$ 0.09	2.35
2	$D^0 \rightarrow K^-\pi^+\pi^0$	+1	13.0 $\pm$ 0.8	2.35
3	$D^0 \rightarrow K^-\pi^+\pi^+\pi^-$	+1	7.46 $\pm$ 0.31	2.35
4	$D^+ \rightarrow K^-\pi^+\pi^+$	+1	9.2 $\pm$ 0.6	2.35
5	$D^+ \rightarrow K^-\pi^+\pi^+\pi^0$	+1	6.5 $\pm$ 1.1	2.35
6	$D^+ \rightarrow K^0_S\pi^+$	+1	1.41 $\pm$ 0.09	2.35
7	$D^+ \rightarrow K^0_S\pi^+\pi^0$	+1	4.4 $\pm$ 1.5	2.35
8	$D^+ \rightarrow K^0_S\pi^+\pi^+\pi^-$	+1	3.6 $\pm$ 0.5	2.35
9	$D^+ \rightarrow K^+K^-\pi^+$	+1	0.89 $\pm$ 0.08	2.35
10	$D^+ \rightarrow K^0_S K^+$	+1	3.0 $\pm$ 0.3	2.35
11	$D^+_s \rightarrow \phi\rho^+$	+1	6.7 $\pm$ 2.3	2.35
12	$D^+_s \rightarrow K^0_S K^+$	+1	1.8 $\pm$ 0.6	2.35
13	$D^{*+} \rightarrow D^0\pi^+$	+1	67.7 $\pm$ 0.5	2.3
13a	$D^0 \rightarrow K^0_S\pi^+\pi^-$		2.98 $\pm$ 0.18	0.0
13b	$D^0 \rightarrow K^0_S\pi^+\pi^-\pi^0$		5.5 $\pm$ 0.7	0.0
13c	$D^0 \rightarrow K^0_S K^+K^-$		0.52 $\pm$ 0.05	0.0
13d	$D^0 \rightarrow K^0_S\pi^0$		1.15 $\pm$ 0.11	0.0

Photons A photon candidate is an EMC cluster – a collection of crystals with a minimum deposited energy of 10 MeV – or part of an EMC cluster that is consistent with a single particle shower. The total energy must be higher than 30 MeV and the lateral moment, M_{LAT}, of the candidates energy distribution must be less than 0.8. The lateral moment is defined as

$$M_{\mathrm{LAT}} = \frac{\sum_{i=2}^{n} E_i\, r_i^2}{\sum_{i=2}^{n} E_i\, r_i^2 + 25\,\mathrm{cm}^2 (E_0 + E_1)}\,, \tag{5.1}$$

where E_i is the energy of the i-th crystal belonging to the photon candidate and r_i is its distance from the shower center, measured in cm. The crystal indices are ordered with descending energy. No charged track must be associated with the photon candidate. The momentum direction of the candidate photon is taken as the vector pointing from the IP to the shower center.

Charged Pions Good charged tracks with transverse momenta of 100 MeV/c and at least 12 DCH hits are considered as charged pion candidates. Based on dE/dx information from the SVT and the DCH, and on the Cherenkov angle and the number of Cherenkov photons from the DIRC, likelihoods for a particle being a charged pion, a charged kaon, and a proton are calculated, L_π, L_K, and L_p, respectively. For charged pions $L_K/(L_K + L_\pi) < 0.98$ and $L_p/(L_p + L_\pi) < 0.98$ is required.

Soft Charged Pions from $D^{*+} \to D^0\pi^+$ Good charged tracks with CM momenta of less than 450 MeV/c are considered as charged pion candidates for the D^{*+} decay in the tag mode $D^{*+} \to D^0\, \pi^+$.

Charged Kaons Good charged tracks are also candidates for charged kaons. With the calculated $\pi^\pm$, $K^\pm$, and $p^\pm$ likelihoods, charged kaon candidates are further required to have $L_K/(L_K + L_\pi) > 0.2$ or $L_p/(L_p + L_\pi) > 0.2$.

Primary Event Vertex The primary event vertex (PEV) is a more accurate estimate of the e^+e^- collision point than the nominal center of the interacion region, the interaction point (IP), which is only determined by the layout of the interaction region. The PEV is determined by a χ^2-fit of good charged tracks to a common vertex point. If the fit probability is less than 1 %, the track with the highest χ^2 contribution is removed and the fit repeated. The fitted vertex is the PEV.

Neutral Pions Neutral pions are reconstructed from two photon candidates that are assumed to originate at the PEV. The invariant mass of the photon pair has to be between 124 and 145 MeV/c^2, and the total momentum in the laboratory frame must be above 200 MeV/c. The four-momentum is then recomputed using a constrained fit, fixing the invariant mass $M(\gamma\gamma)$ to the nominal π^0 mass.

Neutral Kaons Candidates for K_S^0 meson are constructed from two oppositely charged tracks to which the pion mass is assigned. After a loose requirement of $0.3 < M(\pi^+\pi^-) < 0.7\,\mathrm{MeV}/c^2$ on the invariant mass, the K_S^0 candidate is refined through a vertex constrained fit. A fit probability $P_{\mathrm{fit}} > 0.002$ is required, and the distance of the vertex from the events primary vertex must larger than 2 mm in the $r - \phi$ plane. The recomputed mass must be within 9.5 MeV/c^2 of the nominal K^0 mass of 497.6 MeV/c^2 [30].

ϕ Mesons Candidates for ϕ mesons are constructed from two charged kaon candidates in the $\phi \to K^+K^-$ decay mode. The invariant mass of the kaon pair is required to be within 40 MeV/c^2 of the nominal ϕ mass of 1019.5 MeV/c^2 [30]. A vertex constrained fit is then applied to the kaon pair, the fit quality must be above 0.0005. The refitted mass must be within 18 MeV/c^2 of the nominal ϕ mass.

ρ^+ Mesons Candidate ρ^+ mesons reconstructed in their dominant decay mode $\rho^+ \to \pi^+\pi^0$. The charged and neutral pion candidates must fulfill the charged and neutral pion criteria, respectively. The invariant mass of the pion pair is required to be within 320 MeV/c^2 of the nominal ρ^+ mass of 768 MeV/c^2. A constrained fit is then applied to the pion pair, with the events primary vertex as the assumed ρ^+ decay vertex. The fit quality is ensured with a requirement on the fit probability, $P_{\text{fit}} > 0.001$. The refitted mass must then be within $160\,\text{MeV}/c^2$ of the nominal ρ^+ mass.

All available candidates of tag decay products are combined to form the tag candidates. The four-momenta of tag candidates of the tag modes 1–12 (Table 5.1), are calculated in a constrained χ^2-fit, with all daughter particles constrained to a common vertex. The probability of the fit is required to be greater than 0.001.

A vertex-constrained fit is also applied to the D^0 candidates for the modes 13a–13d, with an additional mass constraint. No restrictions on the fit probability are applied. The fitted D^0 candidates are combined with soft charged pion to form D^{*+} candidates. The mass difference between the D^{*+} and the D^0 candidates must be between 120 and 170 MeV, where the nominal mass difference is 145 MeV [30]. A vertex constrained fit is performed on the $\pi^+ D^0$ combination, and a fit probability $P_{\text{fit}} > 0.0001$ is required.

As indicated in Table 5.1, tag candidates must have a minimum momentum of $2.35\,\text{GeV}/c$ in the CM frame. An exception is the D^{*+} tag candidates of tag mode 13 whose CM momentum must be above $2.30\,\text{GeV}/c$. The mass distribution for each tag mode is shown in Figure 5.1, Figure 5.3, and Figure 5.5 for generic Monte Carlo simulated events and in Figure 5.2, Figure 5.4, and Figure 5.6 for data events. A Gaussian distribution on top of a linear function is fitted to each tag mass distribution. This determines the mean, $M_{\text{tag}}^{\text{MC/Data}}$, and the width, $\sigma_{\text{tag}}^{\text{MC/Data}}$, of the tag mass peak, as well as the sizes of the signal tag yield above the background. The estimated mean and width for each tag mode are listed for simulated events in Table 5.2 and for data in Table 5.3. In addition the tables contain the *purity* of each mode, which is obtained from the fit. The purity is defined as

$$P_{2\sigma} = \frac{s_{2\sigma}}{s_{2\sigma} + b_{2\sigma}}, \tag{5.2}$$

where $s_{2\sigma}$ and $b_{2\sigma}$ are the fitted signal and background yields within $2\,\sigma_{\text{tag}}^{\text{MC/Data}}$ of the

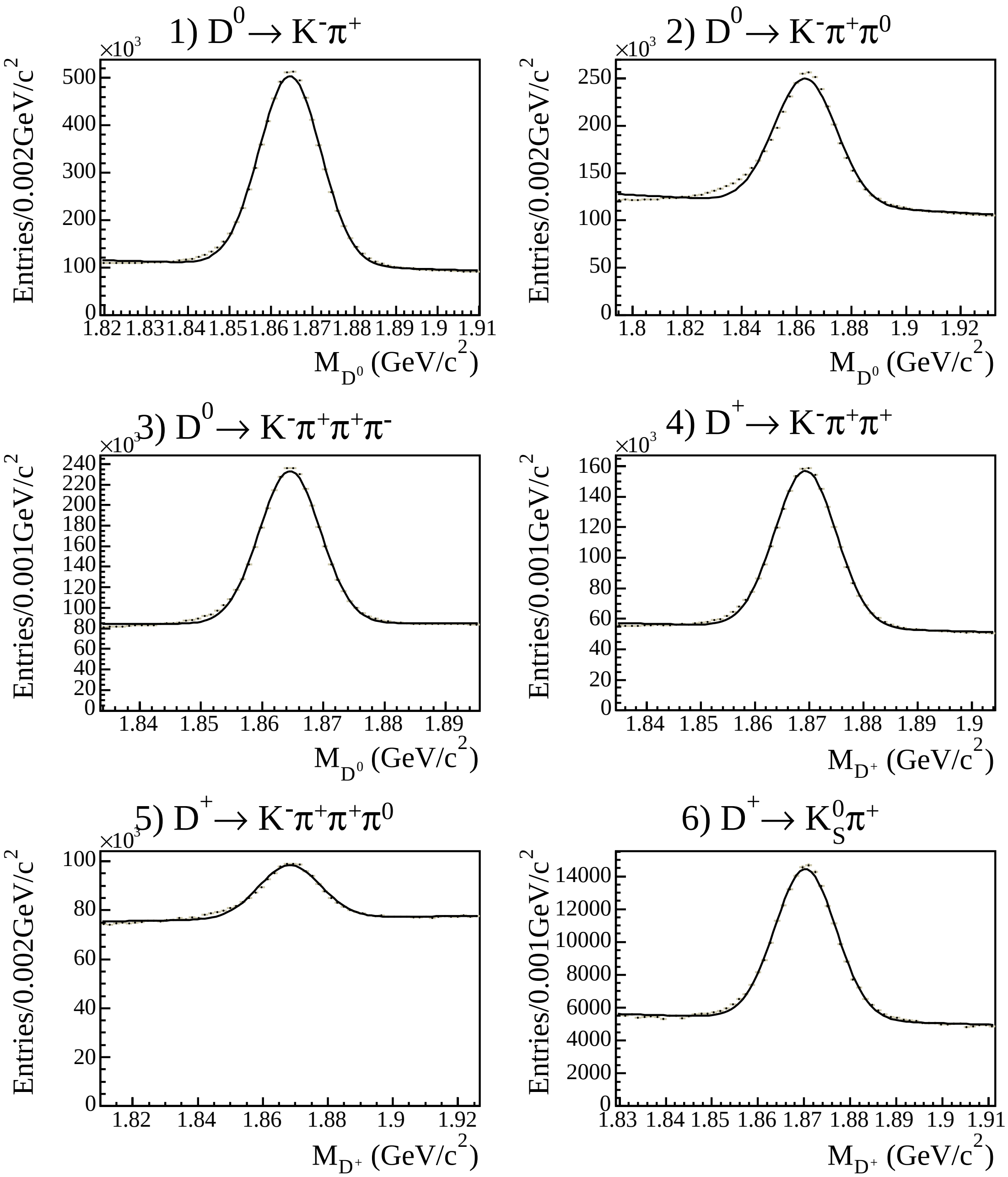

Figure 5.1: Distribution of the tag meson mass for the tag modes 1–6 in generic Monte Carlo events (combined $c\bar{c}$, $b\bar{b}$, uds, $\tau\tau$). Fitted is a Gaussian distribution on top of a linear background. The fitted values for $M_{\text{tag}}^{\text{MC}}$ and $\sigma_{\text{tag}}^{\text{MC}}$ are used to define the tag signal and sideband regions for Monte Carlo samples.

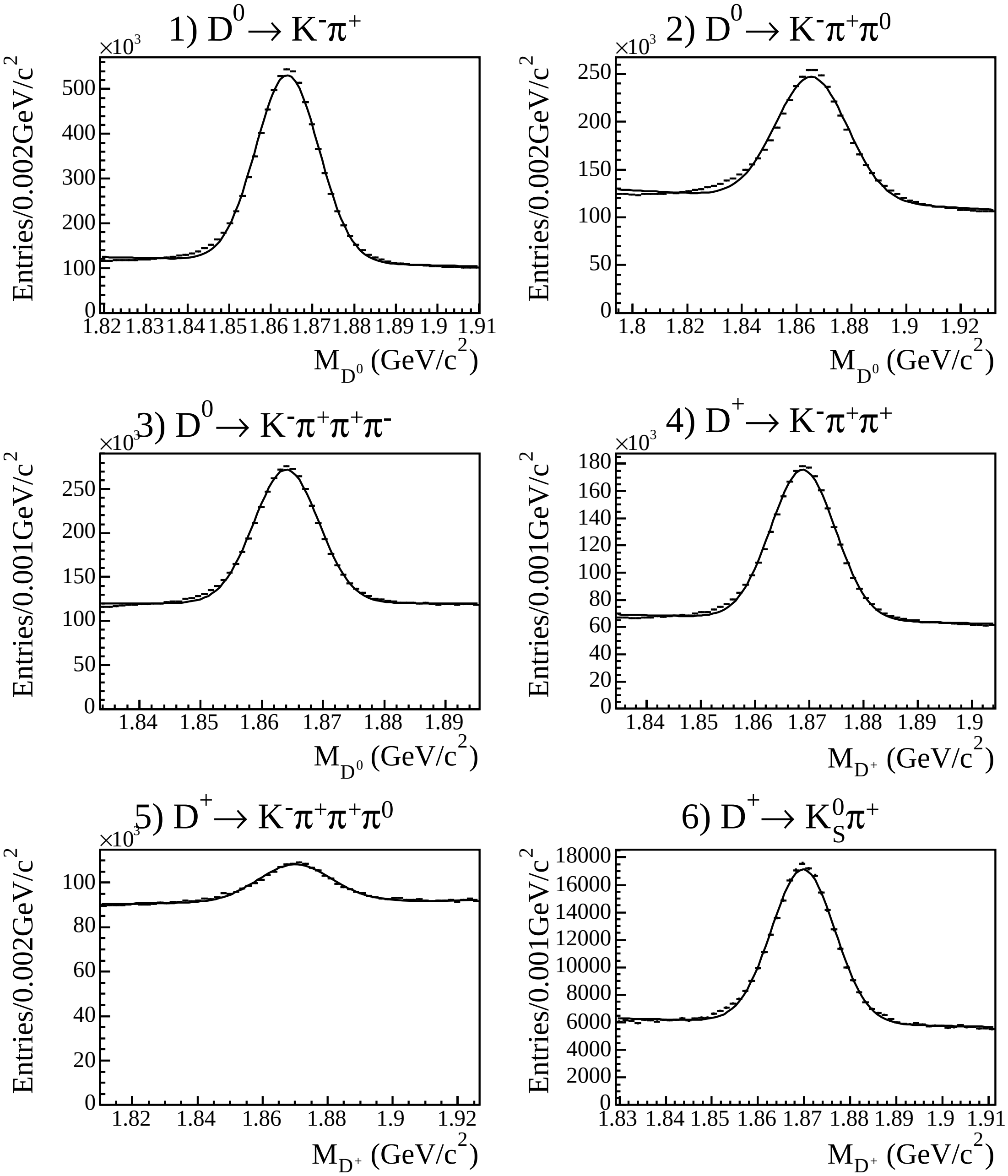

Figure 5.2: Distribution of the tag meson mass for the tag modes 1–6 in data events. Fitted is a Gaussian distribution on top of a linear background. The fitted values for $M_{\rm tag}^{\rm Data}$ and $\sigma_{\rm tag}^{\rm Data}$ are used to define the tag signal and sideband regions for data.

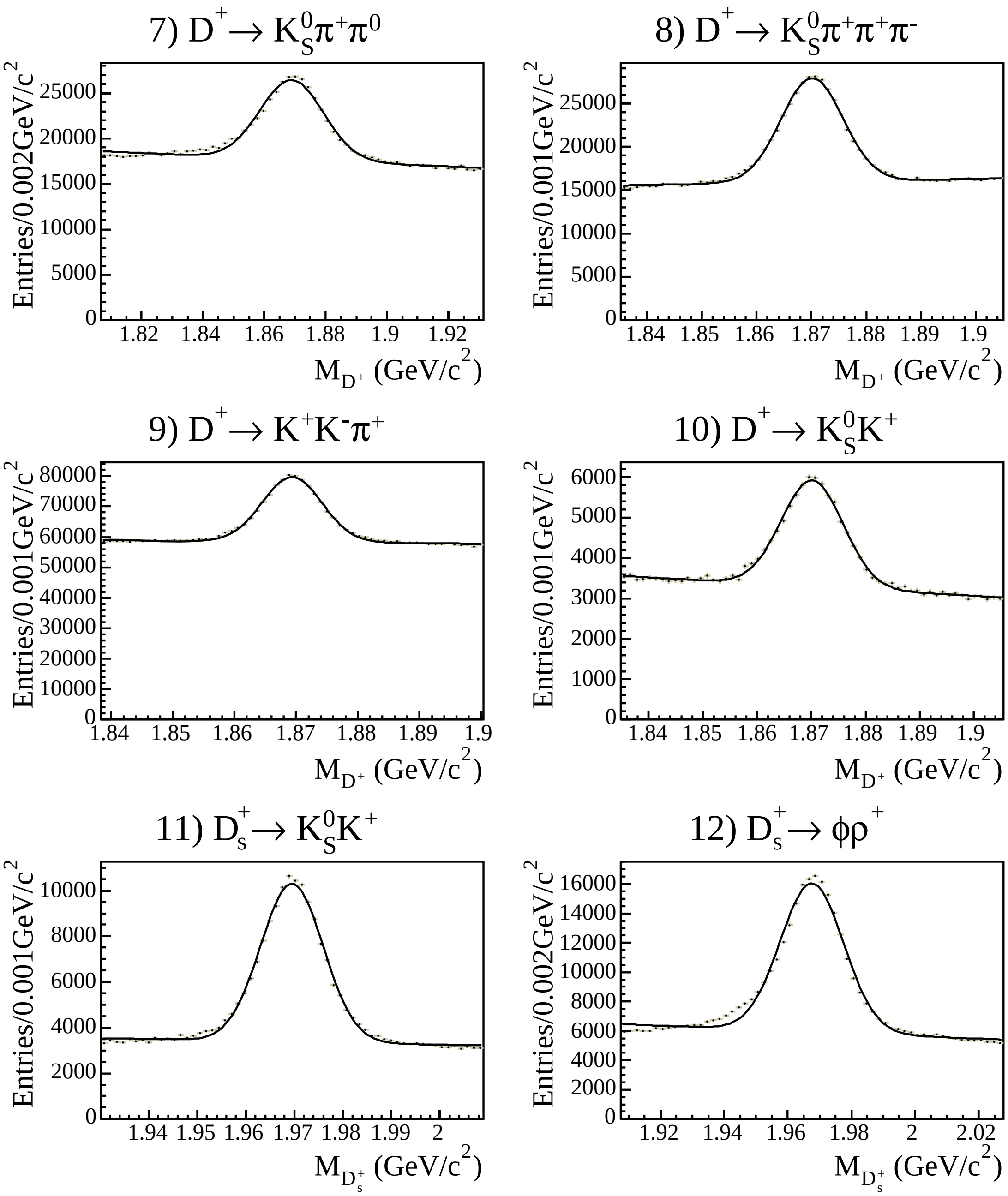

Figure 5.3: Distribution of the tag meson mass for the tag modes 7–12 in generic Monte Carlo events (combined $c\bar{c}$, $b\bar{b}$, uds, $\tau\tau$). Fitted is a Gaussian distribution on top of a linear background. The fitted values for $M_{\text{tag}}^{\text{MC}}$ and $\sigma_{\text{tag}}^{\text{MC}}$ are used to define the tag signal and sideband regions for Monte Carlo samples.

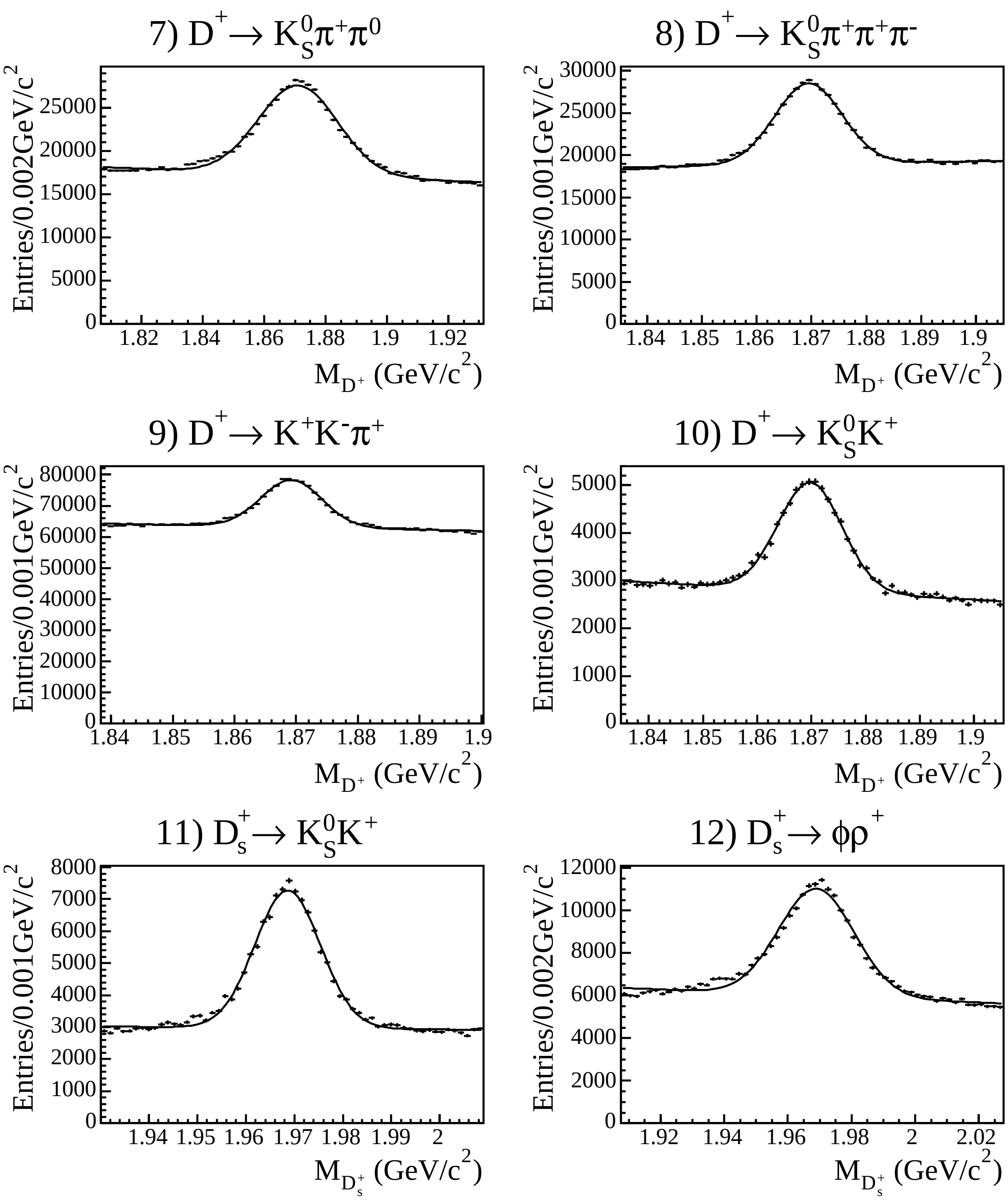

Figure 5.4: Distribution of the tag meson mass for the tag modes 7–12 in data events. Fitted is a Gaussian distribution on top of a linear background. The fitted values for $M_{\rm tag}^{\rm Data}$ and $\sigma_{\rm tag}^{\rm Data}$ are used to define the tag signal and sideband regions for data.

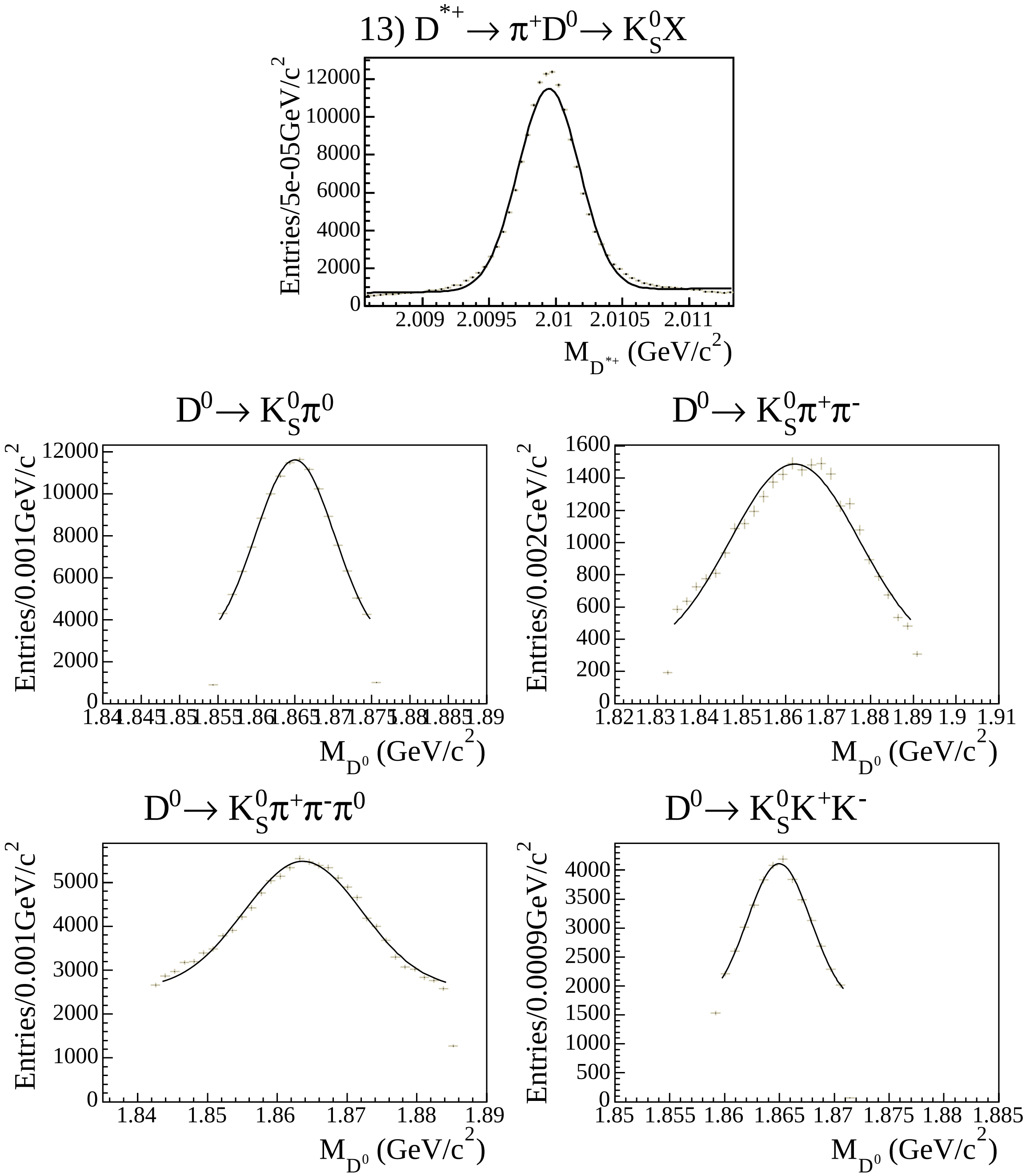

Figure 5.5: Distribution of the tag meson mass for the tag mode 13 ($D^{*+} \to \pi^+ D^0$) and of the D^0 mass in the four submodes 13a–13d, in generic Monte Carlo events (combined $c\bar{c}$, $b\bar{b}$, uds, $\tau\tau$). For the D^{*+} tag mode a Gaussian distribution on top of a linear background is fitted. The fitted values for $M_{\text{tag}}^{\text{MC}}$ and $\sigma_{\text{tag}}^{\text{MC}}$ are used to define the tag signal and sideband regions for Monte Carlo samples. The submodes are fitted with a simple Gaussian distribution.

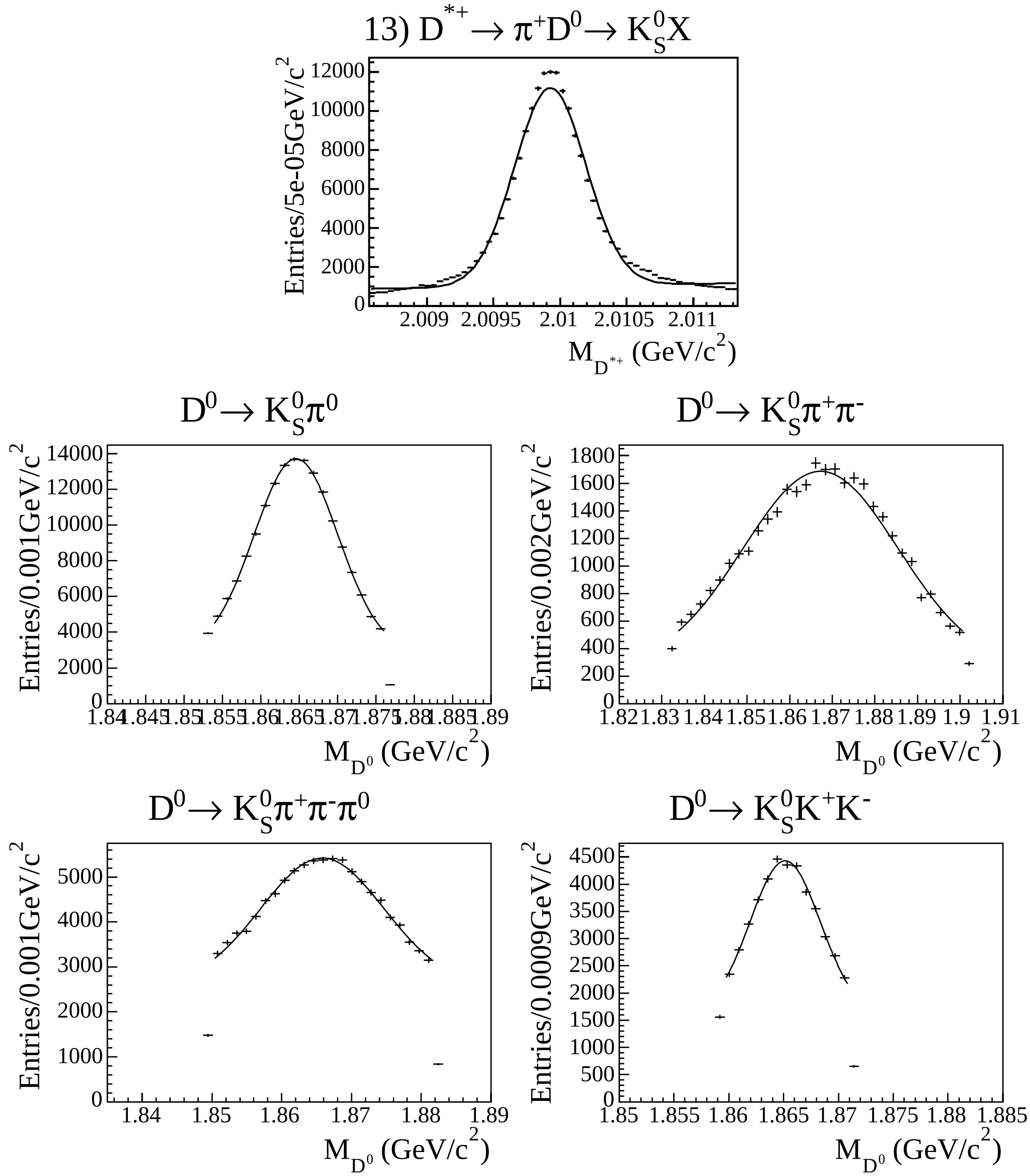

Figure 5.6: Distribution of the tag meson mass for the tag mode 13 ($D^{*+} \to \pi^+ D^0$) and of the D^0 mass in the four submodes 13a–13d, in data events. For the D^{*+} tag mode a Gaussian distribution on top of a linear background is fitted. The fitted values for $M_{\text{tag}}^{\text{Data}}$ and $\sigma_{\text{tag}}^{\text{Data}}$ are used to define the tag signal and sideband regions for data. The submodes are fitted with a simple Gaussian distribution.

mean $M_{\mathrm{tag}}^{\mathrm{MC/Data}}$.

A comparison between simulated and data events shows that the difference in the mean between simulation and data, $M_{\mathrm{tag}}^{\mathrm{MC}} - M_{\mathrm{tag}}^{\mathrm{Data}}$, ranges from -2 MeV to 1 MeV. Tag modes that contain a π^0 or a ρ^+ have a lower mean in Monte Carlo simulation. The width of the tag mass peak tends to be smaller in simulation, prominently again in modes with a π^0 or a ρ^+ (Figure 5.7).

For each tag mode a signal and two sideband regions in the tag mass distribution are defined. While the signal region contains a large number of tag candidates that are correctly reconstructed charm mesons, the sideband should contain almost none. The purpose of the tag candidates in the sidebands is to simulate those tag candidates in the signal region that are not charm mesons. These fake tag candidates in the signal region can than be removed through a *sideband subtraction*.

The signal region is defined $\pm 2\,\sigma_{\mathrm{tag}}^{\mathrm{MC/Data}}$ around the fitted mean mass, $M_{\mathrm{tag}}^{\mathrm{MC/Data}}$. The sideband regions extend from 3 to $6\,\sigma_{\mathrm{tag}}^{\mathrm{MC/Data}}$ on either side of $M_{\mathrm{tag}}^{\mathrm{MC/Data}}$. The width of the sidebands is chosen 50 % larger than the signal region in order to lower the statistical uncertainty arising from the sideband subtraction. The definitions of the tag signal and sideband regions for simulated and data events are listed in Tables 5.4 and 5.5, respectively.

The total number of tag candidates in data disagrees with the Monte Carlo prediction (Figure 5.8 through Figure 5.10). The reasons are:

- The branching fractions of the charm decay used in some tag modes, have an error of up to 30 %. This would explain the discrepancy in the D_s^+ meson tag modes.

- The track multiplicity in simulated events might be different from data, due to imperfections in the quark fragmentation model, or to the mixing of the beam background into the simulated events. This would justify the higher random combinatoric backgrounds in the modes $D^0 \to K^-\pi^+\pi^+\pi^-$, $D^+ \to K^-\pi^+\pi^+\pi^0$, or $D^+ \to K_S^0\pi^+\pi^+\pi^-$, all of which have four or more particles in the final state.

- The PID efficiency correction is not applied to the tag side of the event.

Table 5.2: Tag mass mean and width, and purity for each tagging modes in Monte Carlo.

Mode	$M_{\rm tag}^{\rm MC}$ [GeV/c^2]	$\sigma_{\rm tag}^{\rm MC}$ [MeV/c^2]	$P_{2\sigma}$ [%]
$D^0 \to K^-\pi^+$	1.865	7.34	69.3
$D^0 \to K^-\pi^+\pi^0$	1.863	11.18	40.7
$D^0 \to K^-\pi^+\pi^+\pi^-$	1.865	5.00	50.9
$D^+ \to K^-\pi^+\pi^+$	1.869	5.65	52.8
$D^+ \to K^-\pi^+\pi^+\pi^0$	1.868	9.40	14.7
$D^+ \to K_S^0\pi^+$	1.870	6.63	50.8
$D^+ \to K_S^0\pi^+\pi^0$	1.869	10.06	23.1
$D^+ \to K_S^0\pi^+\pi^+\pi^-$	1.870	5.63	30.6
$D^+ \to K^+K^-\pi^+$	1.869	4.84	17.7
$D^+ \to K_S^0 K^+$	1.870	5.69	32.4
$D_s^+ \to K_S^0 K^+$	1.970	6.36	54.1
$D_s^+ \to \phi\rho^+$	1.968	9.69	49.7
$D^{*+} \to \pi^+ D^0 \to K_S^0 X$	2.010	0.22	87.5

Table 5.3: Tag mass mean and width, and purity for each tagging modes in data.

Mode	$M_{\rm tag}^{\rm Data}$ [GeV/c^2]	$\sigma_{\rm tag}^{\rm Data}$ [MeV/c^2]	$P_{2\sigma}$ [%]
$D^0 \to K^-\pi^+$	1.864	7.50	68.1
$D^0 \to K^-\pi^+\pi^0$	1.866	12.75	39.6
$D^0 \to K^-\pi^+\pi^+\pi^-$	1.864	5.24	42.8
$D^+ \to K^-\pi^+\pi^+$	1.869	5.90	49.5
$D^+ \to K^-\pi^+\pi^+\pi^0$	1.870	11.02	10.0
$D^+ \to K_S^0\pi^+$	1.870	6.83	52.5
$D^+ \to K_S^0\pi^+\pi^0$	1.871	12.60	26.4
$D^+ \to K_S^0\pi^+\pi^+\pi^-$	1.869	6.07	22.9
$D^+ \to K^+K^-\pi^+$	1.869	4.97	12.4
$D^+ \to K_S^0 K^+$	1.870	5.89	33.0
$D_s^+ \to K_S^0 K^+$	1.969	6.62	45.3
$D_s^+ \to \phi\rho^+$	1.969	11.45	32.7
$D^{*+} \to \pi^+ D^0 \to K_S^0 X$	2.010	0.26	83.2

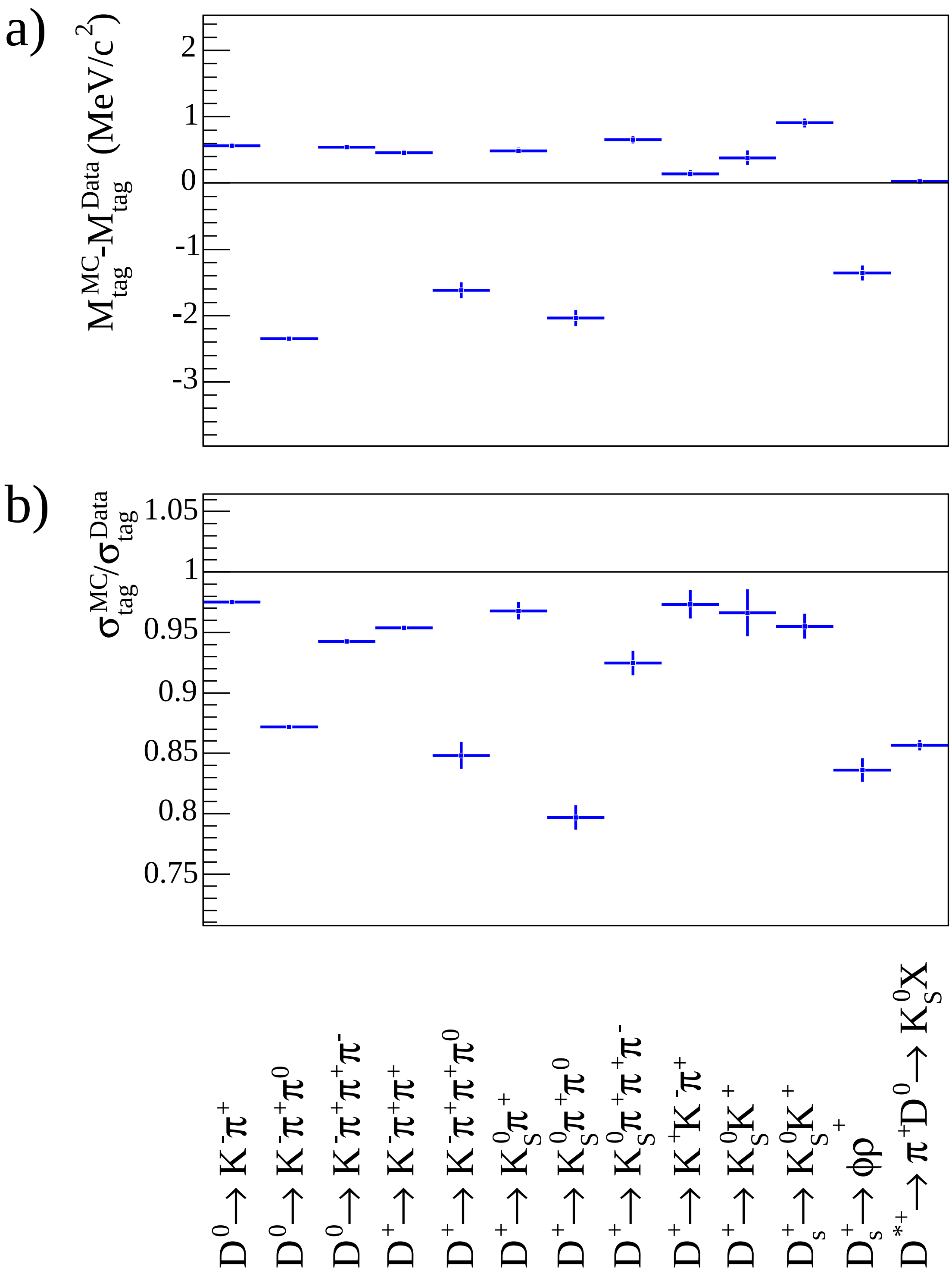

Figure 5.7: Differences in a) the tag mass mean and b) the tag mass width between simulated events and data.

Table 5.4: Definition of tag signal and sideband regions for each tag mode in simulated events.

Mode	Peak Region [MeV]	Sideband Region [MeV] Left	Right
$D^0 \to K^-\pi^+$	1.850 – 1.879	1.820 – 1.843	1.887 – 1.909
$D^0 \to K^-\pi^+\pi^0$	1.841 – 1.886	1.796 – 1.830	1.897 – 1.930
$D^0 \to K^-\pi^+\pi^+\pi^-$	1.855 – 1.875	1.835 – 1.850	1.880 – 1.895
$D^+ \to K^-\pi^+\pi^+$	1.858 – 1.881	1.835 – 1.852	1.886 – 1.903
$D^+ \to K^-\pi^+\pi^+\pi^0$	1.850 – 1.887	1.812 – 1.840	1.897 – 1.925
$D^+ \to K_S^0\pi^+$	1.857 – 1.884	1.831 – 1.850	1.890 – 1.910
$D^+ \to K_S^0\pi^+\pi^0$	1.849 – 1.889	1.809 – 1.839	1.899 – 1.929
$D^+ \to K_S^0\pi^+\pi^+\pi^-$	1.859 – 1.881	1.836 – 1.853	1.887 – 1.904
$D^+ \to K^+K^-\pi^+$	1.860 – 1.879	1.840 – 1.855	1.884 – 1.898
$D^+ \to K_S^0K^+$	1.859 – 1.882	1.836 – 1.853	1.887 – 1.904
$D_s^+ \to K_S^0K^+$	1.957 – 1.982	1.931 – 1.950	1.989 – 2.008
$D_s^+ \to \phi\rho^+$	1.948 – 1.987	1.909 – 1.939	1.997 – 2.026
$D^{*+} \to \pi^+D^0 \to K_S^0X$	2.0095 – 2.0104	2.0086 – 2.0093	2.0106 – 2.0113

Table 5.5: Definition of tag signal and sideband regions for each tag mode in data.

Mode	Peak Region [MeV]	Sideband Region [MeV] Left	Right
$D^0 \to K^-\pi^+$	1.849 – 1.879	1.819 – 1.842	1.887 – 1.909
$D^0 \to K^-\pi^+\pi^0$	1.840 – 1.891	1.789 – 1.827	1.904 – 1.942
$D^0 \to K^-\pi^+\pi^+\pi^-$	1.854 – 1.875	1.833 – 1.848	1.880 – 1.895
$D^+ \to K^-\pi^+\pi^+$	1.857 – 1.881	1.834 – 1.851	1.887 – 1.904
$D^+ \to K^-\pi^+\pi^+\pi^0$	1.848 – 1.892	1.804 – 1.837	1.903 – 1.936
$D^+ \to K_S^0\pi^+$	1.856 – 1.883	1.829 – 1.849	1.890 – 1.911
$D^+ \to K_S^0\pi^+\pi^0$	1.846 – 1.896	1.795 – 1.833	1.909 – 1.947
$D^+ \to K_S^0\pi^+\pi^+\pi^-$	1.857 – 1.882	1.833 – 1.851	1.888 – 1.906
$D^+ \to K^+K^-\pi^+$	1.859 – 1.879	1.839 – 1.854	1.884 – 1.899
$D^+ \to K_S^0K^+$	1.858 – 1.882	1.834 – 1.852	1.887 – 1.905
$D_s^+ \to K_S^0K^+$	1.955 – 1.982	1.929 – 1.949	1.989 – 2.008
$D_s^+ \to \phi\rho^+$	1.946 – 1.992	1.900 – 1.935	2.003 – 2.038
$D^{*+} \to \pi^+D^0 \to K_S^0X$	2.0094 – 2.0105	2.0084 – 2.0092	2.0107 – 2.0115

However, the mismatch between the simulated tag yields and the tag yields found in data is of no concern in this analysis. Since only the ratio of the decay rates of $D_s^+ \to \mu^+\nu_\mu$ to $D_s^+ \to \phi\pi^+$ in tagged events is measured, the tagging efficiency itself can remain unknown.

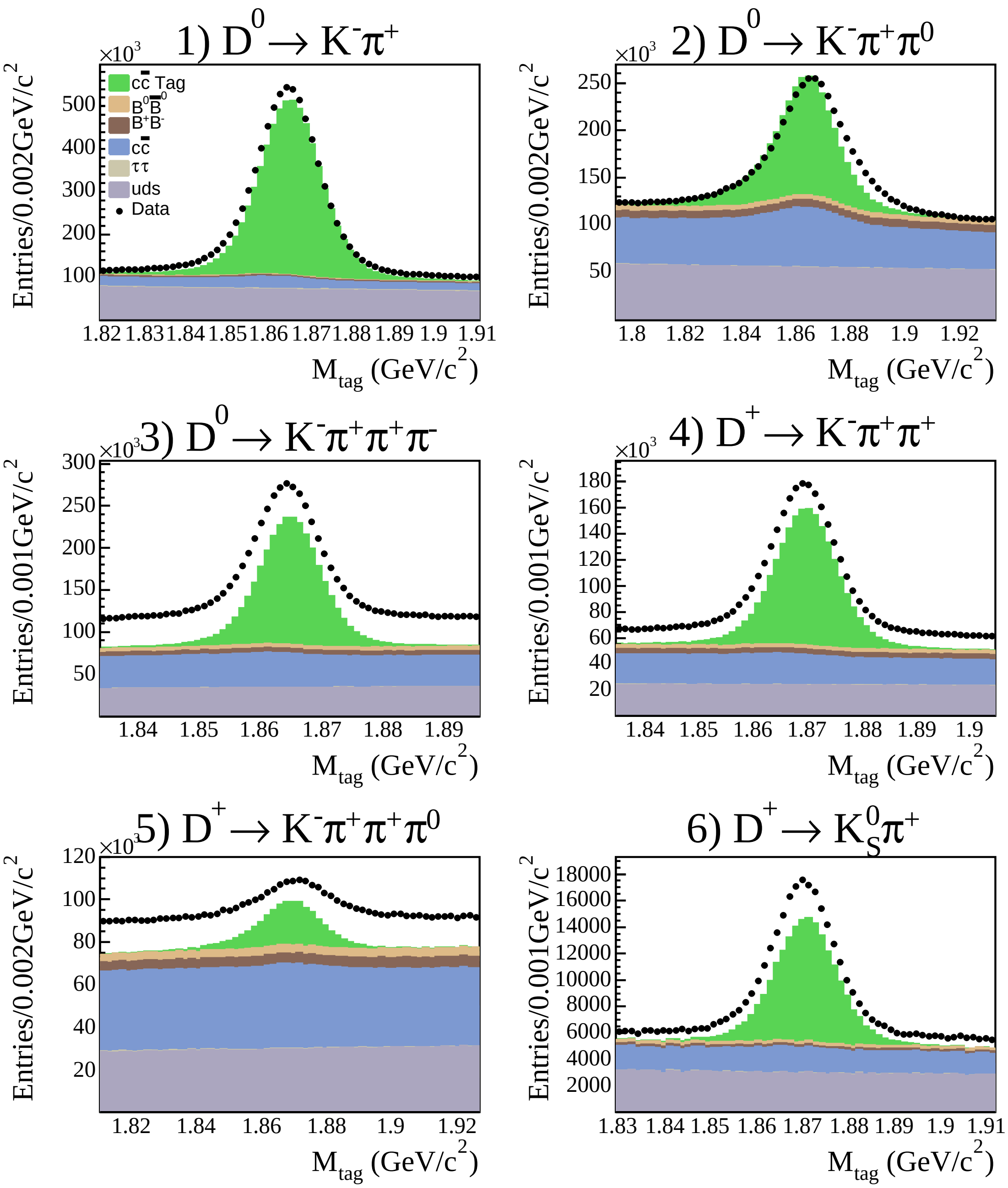

Figure 5.8: Tag mass distribution in generic Monte Carlo simulated events (histograms) and in data (black markers) for tag modes 1–6. The simulation is normalized to the data luminosity.

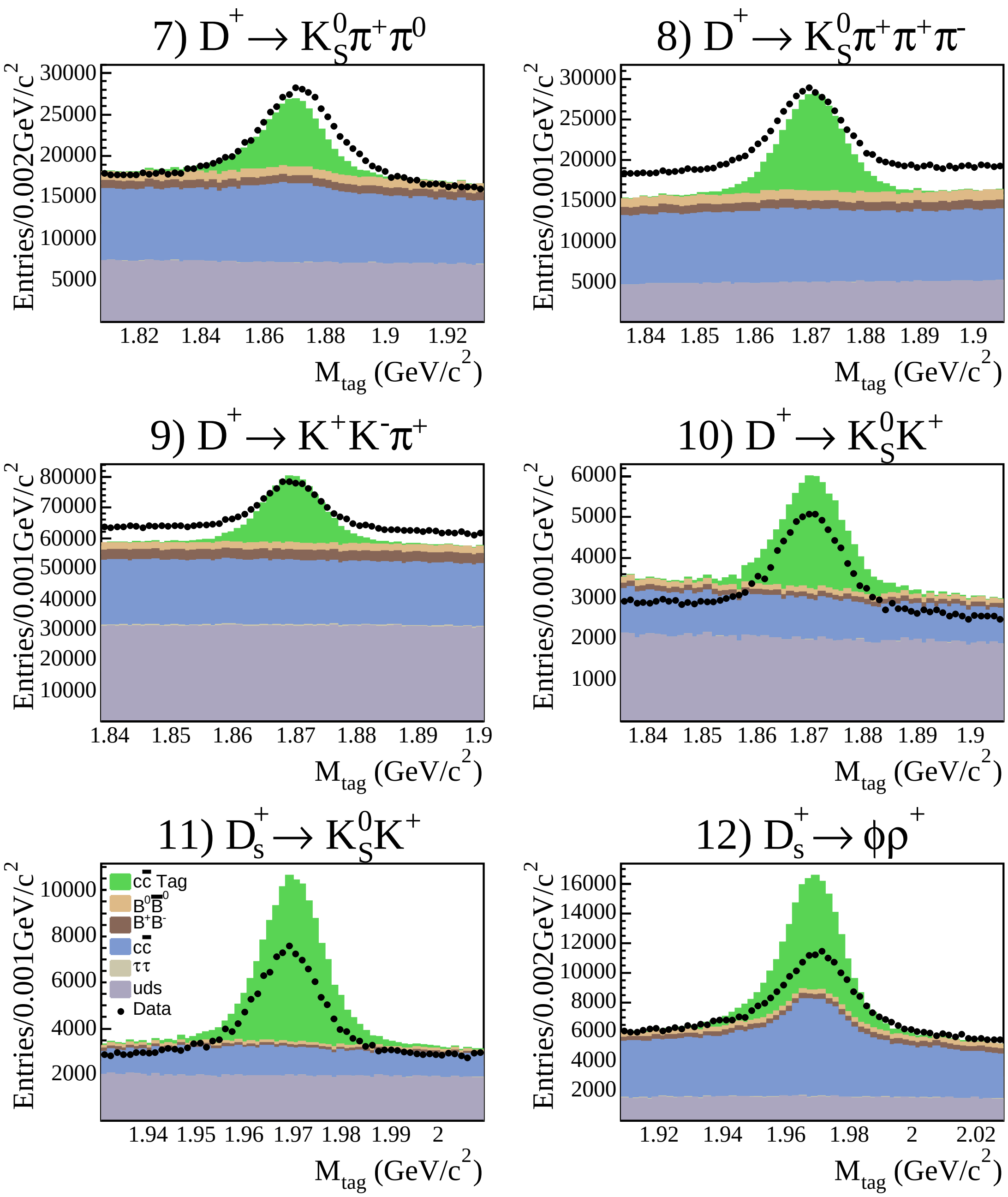

Figure 5.9: Comparison of the tag mass distribution in simulated events and data for tag modes 7–12. The simulation is normalized to the data luminosity.

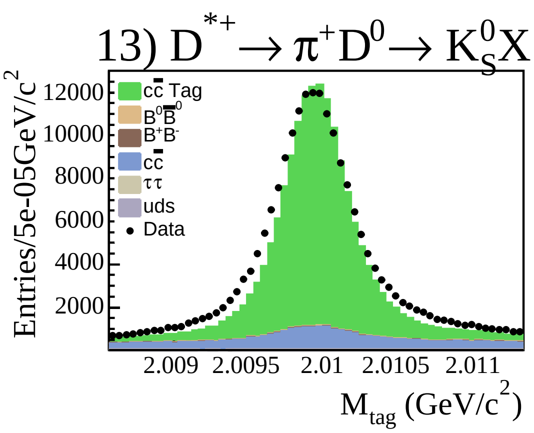

Figure 5.10: Comparison of the tag mass distribution in simulated events and data for tag mode 13. The simulation is normalized to the data luminosity.

5.4 The Tag Selection

Figure 5.11 shows the *tag multiplicity* distribution, which is the number of tag candidates in the signal or the sideband region in an event. While most events with at least one tag candidate have a tag multiplicity of one, a fraction of events (18 %) has a tag multiplicity of two or higher. This analysis follows the strategy that in any event only a single tag candidate is designated as tag, while all others tag candidates are discarded.

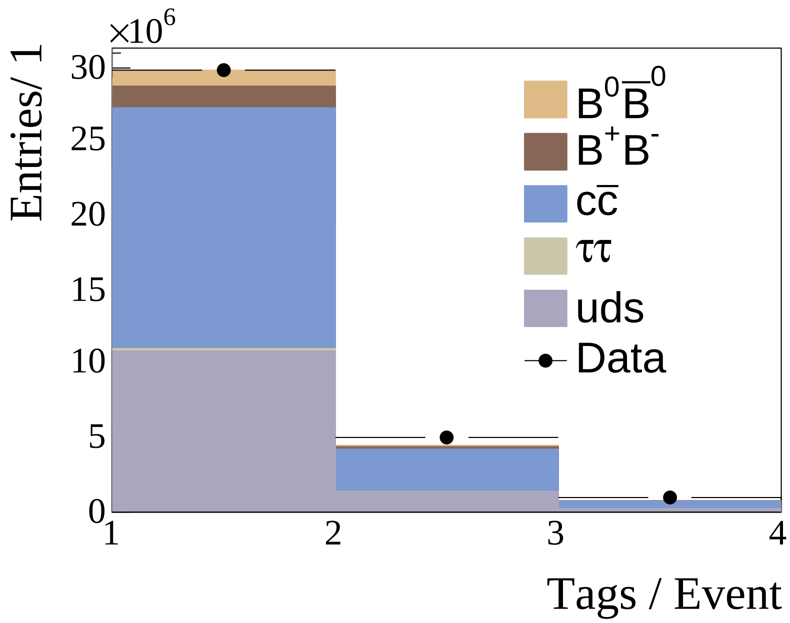

Figure 5.11: Tag multiplicity in events with at least one tag candidate. The Monte Carlo distribution is scaled in size to agree with the data in the first bin.

To determine that single tag, the tag modes are ordered according to their purity, as it is measured in data, listed in Table 5.3. Only tag candidates that are in the signal or the sideband regions are considered. The designated tag is selected by choosing the tag candidate of the purest mode among the available candidates. If multiple candidates of the same mode qualify as the tag, the one with the highest vertexing probability among them is taken. For the selection it is not relevant if the tag is in the signal or the sideband regions. Figures 5.12 through 5.13 show the tag mass distribution after the selection of the best tag candidate. This singled out tag candidate is referred to simply as the *tag* in the subsequent analysis.

The tag yields in the signal and the sideband regions in generic Monte Carlo simulation, and in data are compared in Table 5.6. The simulation, scaled to the data luminosity, predicts 520,000 tags in the signal region after the sidebands are subtracted, while in data 510,000 tags are obtained.

Table 5.6: Tag yield for MC and data in peak (P) and sideband (S) region. the sideband yields are scaled by $\frac{2}{3}$, to accomodate the 50 % larger size of the sidebands.

Mode	Monte Carlo			Data		
	P	S	$P-S$	P	S	$P-S$
$D^0 \to K^-\pi^+$	149810	41037	108772	163962	50586	113376
$D^0 \to K^-\pi^+\pi^0$	249965	136310	113656	250631	132888	117743
$D^0 \to K^-\pi^+\pi^+\pi^-$	213990	95525	118465	230878	115975	114903
$D^+ \to K^-\pi^+\pi^+$	157940	66134	91806	161599	70627	90972
$D^+ \to K^-\pi^+\pi^+\pi^0$	96665	79309	17356	104935	91275	13660
$D^+ \to K^0_S\pi^+$	15138	6486	8653	16957	6905	10052
$D^+ \to K^0_S\pi^+\pi^0$	32425	24205	8220	36649	24883	11766
$D^+ \to K^0_S\pi^+\pi^+\pi^-$	32147	21012	11135	29609	21390	8219
$D^+ \to K^+K^-\pi^+$	69462	55724	13738	60308	51321	8987
$D^+ \to K^0_S K^+$	6412	4238	2174	4851	3129	1722
$D_s^+ \to K^0_S K^+$	10323	4651	5673	6259	3029	3230
$D_s^+ \to \phi\rho^+$	11391	5052	6339	8274	5175	3099
$D^{*+} \to \pi^+ D^0 \to K^0_S X$	13080	1500	11580	13225	1855	11370
Total:	1058748	541182	517566	1088137	579040	509097

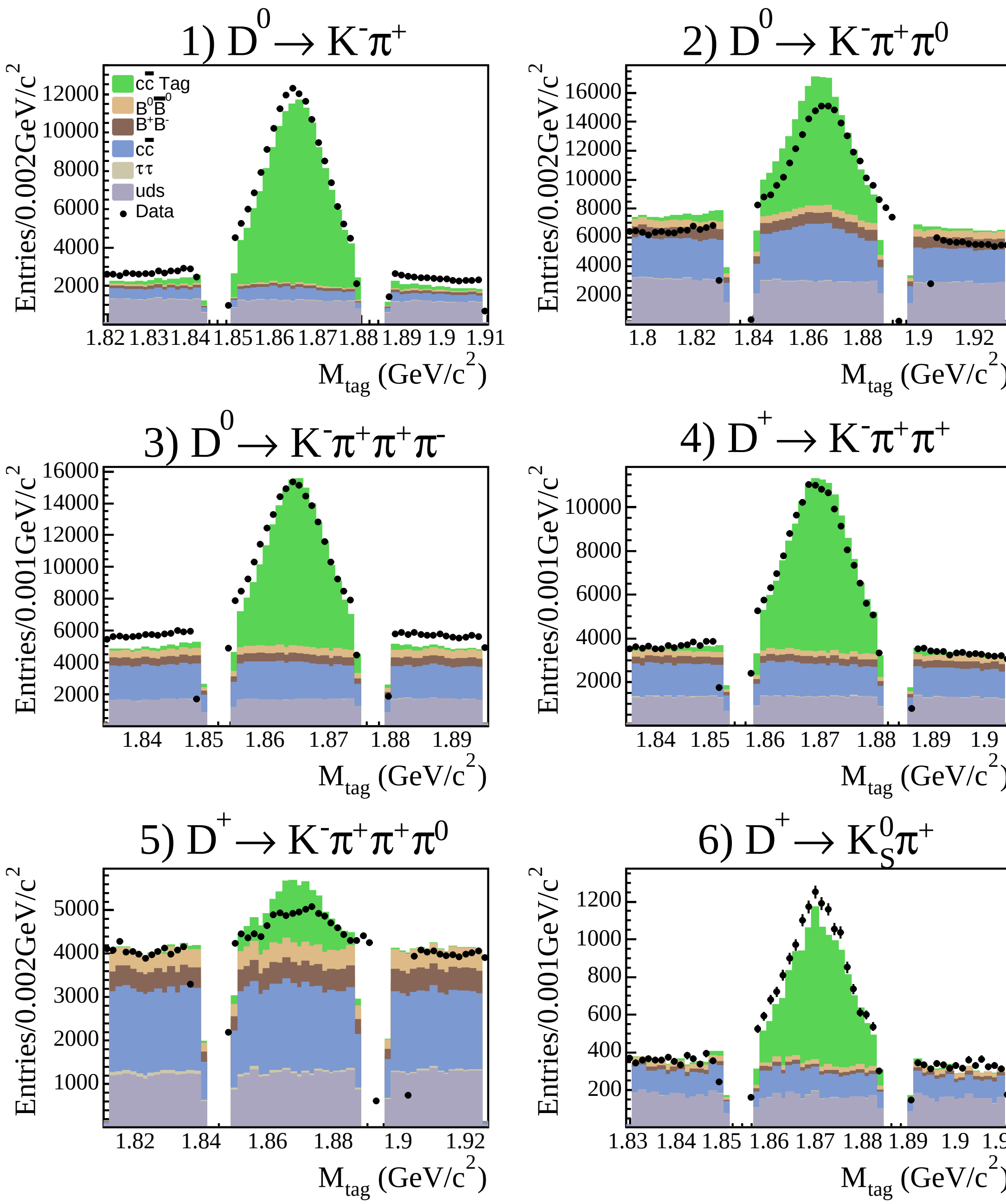

Figure 5.12: Comparison of the tag mass distribution in simulated events and data for tag modes 1–6. The simulation is normalized to the data luminosity.

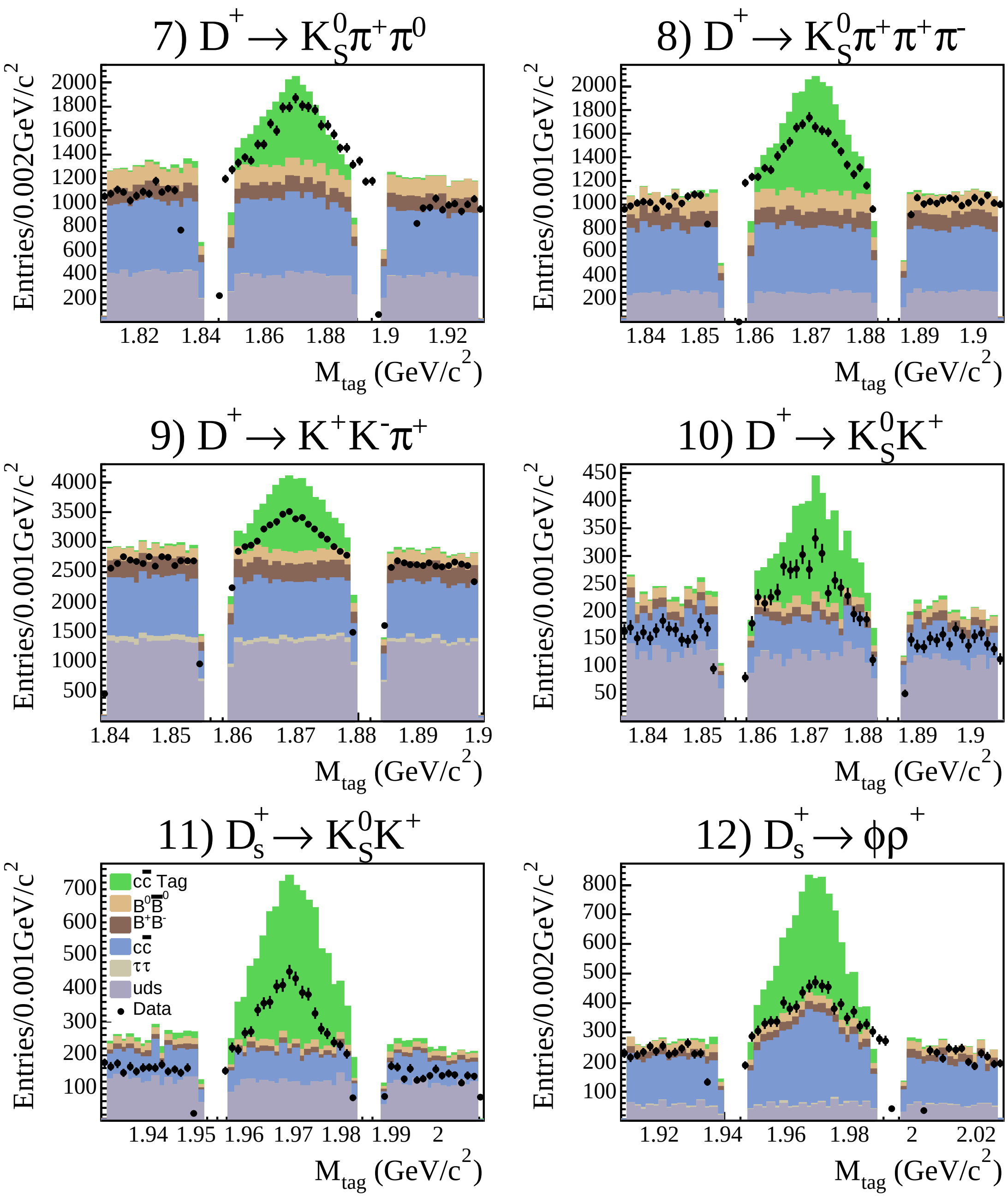

Figure 5.13: Comparison of the tag mass distribution in simulated events and data for tag modes 7–12. The simulation is normalized to the data luminosity.

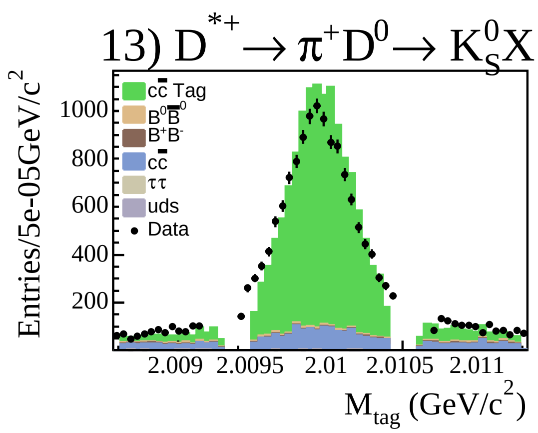

Figure 5.14: Comparison of the tag mass distribution in simulated events and data for tag mode 13. The simulation is normalized to the data luminosity.

Chapter 6

Signal Analysis

In this chapter the reconstruction of the decay chain $D_s^{*+} \to \gamma D_s^+ \to \gamma\mu^+\nu$ in the recoil of a charm tag is described. First, the reconstruction of the signal decay is described, with particular attention to the reconstruction of the neutrino. Next, production and decay properties of the signal decay are investigated, to find these that can be used to set the signal events apart from the background. The optimal choice of selection variables is tehn evaluated by optimizing the statistical significance of the final result. With the set of selection cuts so defined, the signal reconstruction efficiency and the shape of the signal ΔM distribution are determined. Finally, an extensive discussion of the contributing backgrounds in this analysis, and of how they are estimated, is presented. In this analysis two different control samples are employed, whose description follows next. The decay $D^{*0} \to \gamma D^0 \to \gamma K^-\pi^+$ is used to validate the simulated signal efficiency, while the decay $D^{*+} \to \pi^+ D^0 \to \pi^+ K^- l^+ \nu_l$ checks the PID efficiency correction method, applied to estimate the semileptonic and the leptonic τ background. At the end of the chapter the analysis of the decay $D_s^{*+} \to \gamma D_s^+ \to \gamma\phi\pi^+$, which is used to measure the number of D_s^{*+} mesons in the tag sample, is discussed.

6.1 Signal Reconstruction

The decay $D_s^{*+} \to \gamma D_s^+ \to \gamma \mu^+ \nu$ is reconstructed in the recoil of the tag. Only tracks and clusters that are not part of the tag decay are considered muons and photon candidates. The charge of the muon candidate has to be of opposite sign than the tag charm quantum number.

Muon candidates Candidate muons have to originate near the IP. The distance between the IP and the point of closest approach of the candidate track to the IP has to be less than 1.5 cm in the xy-plane and less than 10 cm along the z-direction. The momentum in the CM frame must be above 1.2 GeV/c. The muon candidate has to satisfy a neural net based muon PID selector. The neural net classifies particles based on the following input:

- The energy deposited in the EMC,
- the number of IFR hit layers,
- the measured number of traversed interaction lengths in the IFR, λ_{meas},
- $\Delta\lambda$, the difference between the number of traversed interaction lengths expected for a minimum ionizing particle of momentum p and λ_{meas},
- the χ^2/d.o.f. of a third order polynomial fit to the IFR position measurements in the different RPC layers,
- the χ^2/d.o.f. of the IFR position measurements with respect to the track extrapolation,
- the continuity of the track,
- the average multiplicity of hit signal readout strips per IFR layer and the standard deviation.

Photon candidates Candidate photons must fullfil the requirements detailed in Section 5.3. The minimum energy of the photon candidate in the CM frame is 115 MeV.

Neutrino The neutrino four-momentum is calculated from the measured missing four-momentum in the event. The missing momentum is a good estimate for the neutrino momentum for three reasons.

- The tag is fully reconstructed in a hadronic decay mode. This eliminates the important source of high energy neutrinos from semileptonic charm decays. Except for the decay of charged kaons or pions, which happens rarely inside the detector, no other neutrinos should be present in the event.
- The fragmentation of $c\bar{c}$ pairs at the $\Upsilon(4S)$ energy produces mostly two jets of particles, which are back to back. With the tag direction pointing into the angular acceptance of the detector, the majority of all particles produced in the fragmentation process also point into the detectro acceptance.
- Long lived neutral kaons, K_L^0, are not easily identified with the *BABAR* detector. Since the EMC represents only 0.8 hadronic interaction length, only 50 % of K_L^0 decay in the EMC with a typical energy deposit of 30 %. However, since the tag carries already more than 60 % of the available energy on the tag side, the contribution of the K_L^0 to the missing momentum is limited.

To further improve the resolution on the mass difference, ΔM, of the D_s^{*+} and the D_s^+ meson, a special neutrino fitting procedure, described in the next section, is employed.

6.2 Neutrino Reconstruction

The total four-momentum in the laboratory frame, $\breve{p}_{\mathrm{tot}}$, is calculated by adding the four-momenta of all good charged tracks, $\breve{p}_{\mathrm{trk}}$, and all photon candidates, $\breve{p}_{\mathrm{phot}}$, in the event, that are not part of the tag, to the tag four-momentum:

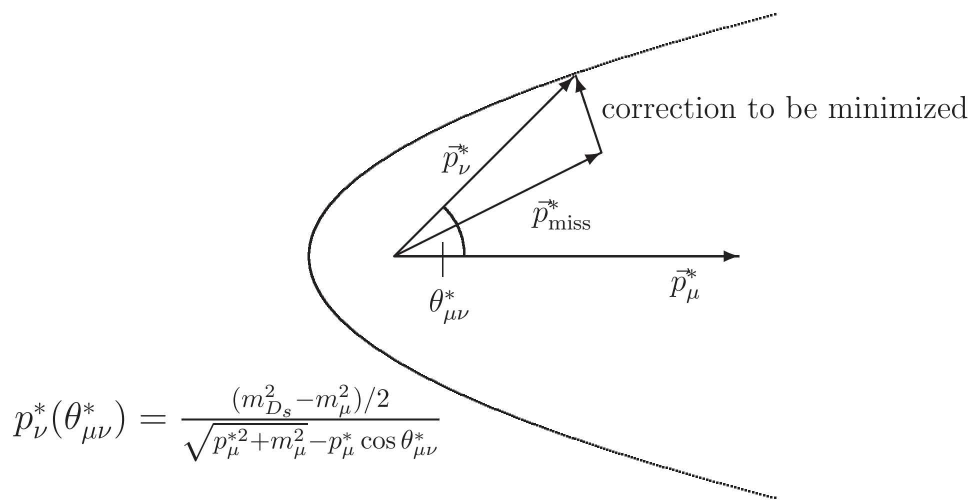

Figure 6.1: Neutrino reconstruction. The drawing plane is defined by the muon and missing momentum vectors. The parabola is given by (6.3).

$$\breve{p}_{\text{tot}} = \sum_{\text{trk},\neg\text{tag}} \breve{p}_{\text{trk}} + \sum_{\text{phot},\neg\text{tag}} \breve{p}_{\text{phot}} + \breve{p}_{\text{tag}} \tag{6.1}$$

The track and photon requirements are detailed in Section 5.3. The missing four-momentum in the laboratory frame, $\breve{p}_{\text{miss}}$, is calculated by subtracting $\breve{p}_{\text{tot}}$ from the four-momentum of the $\Upsilon(4S)$. The missing four-momentum is boosted into the CM frame to obtain

$$\breve{p}^*_{\text{miss}} \equiv (E^*_{\text{miss}}, \vec{p}^*_{\text{miss}}) \tag{6.2}$$

The neutrino momentum resolution can be improved if the invariant mass of the muon-neutrino pair is constrained to the nominal D_s^+ mass. Compared to the missing momentum, the muon momentum is measured very precisly. Therefore only the missing momentum will be adjusted to satisfy the D_s^+ mass constraint. For the two body decay $D_s^+ \to \mu^+\nu_\mu$, given the muon CM momentum, p^*_μ, the neutrino CM momentum, p^*_ν, can be written as a function of the muon–neutrino opening angle $\theta^*_{\mu\nu}$ in the CM frame:

$$p^*_\nu(\theta^*_{\mu\nu}|p^*_\mu, m_\mu, m_{D_s}) = \frac{m^2_{D_s} - m^2_\mu}{2\left(\sqrt{p^{*2}_\mu + m^2_\mu} - p^*_\mu \cos\theta^*_{\mu\nu}\right)}\,. \tag{6.3}$$

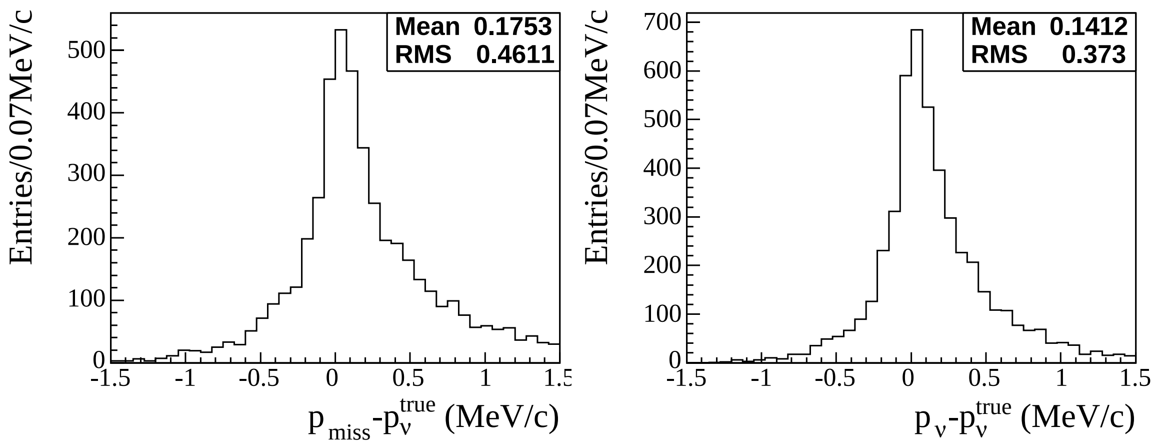

Figure 6.2: Neutrino momentum resolution improvement. Shown is the difference between a) the missing momentum and b) corrected neutrino momentum and the neutrino momentum in simulated signal decays. The muon momentum is larger than 1.2 GeV/c. A correctly reconstructed tag with a momentum above 2.35 GeV/c is required in the event.

This equation describes a three-dimensional parabola around the muon momentum vector. The higher the muon momentum, the narrower the parabola. The muon and the missing momentum vectors span a plane that disects this parabola, as depicted in Figure 6.1. The momentum vector of the neutrino, $\vec{p}^*_\nu$, from the $D_s^+ \to \mu^+\nu_\mu$ decay can lie anywhere on the parabola, but most likely near the missing momentum vector. Therefore, the neutrino momentum vector that is used in the further analysis is chosen such that the difference to the missing momentum vector, $|\vec{p}^*_{\text{miss}} - \vec{p}^*_\nu|$ is minimized. The improvement in the neutrino momentum is shown in Figure 6.2. The neutrino CM four-momentum is given by

$$\breve{p}^*_\nu = (|\vec{p}^*_\nu|, \vec{p}^*_\nu) \ . \tag{6.4}$$

This method of finding the optimal neutrino momentum, does not have a quality criteria in terms of a fit probability. However the difference of the missing and the neutrino momentum, p_{corr}, is a good indicator for signal event. It is defined as

$$p_{\text{corr}} = |\vec{p}^*_{\text{miss}}| - |\vec{p}^*_\nu|. \tag{6.5}$$

Compared to background events, signal decays typically require only a small correction to the missing momentum, and p_{corr} is centered at 0, (Figure 6.7).

All muon candidates are combined pairwise with the neutrino four-momentum and D_s^+ candidates are formed. All D_s^+ candidates, which after the neutrino fitting procedure have the nominal D_s^+ mass, are combined pairwise with the photon candidates to form D_s^{*+} candidates. The mass difference $\Delta M = M(D_s^{*+}) - M(D_s^+)$ is calculated. The signature of the signal is a narrow peak in the ΔM distribution at 145 MeV.

6.3 Signal Selection

This analysis is a "cut-and-count" analysis. To select the signal and suppress the background, a number of variables are chosen for which requirements, or "cuts", are applied. After the selection the signal yield is fitted for, providing the "count" of signal events.

The variables that are described in the following sections are based on properties of the reconstructed muon, neutrino, photon, D_s^+, and D_s^{*+} candidates. They are chosen due of their potential to separate signal from background.

The cut values (with the exception of the photon energy) are chosen such that the signal selection and background rejection would result in the highest possible statistical significance of the signal yield in data. The significance is defined as the ratio of the signal yield s to its statistical uncertainty, $s/\sqrt{s+b}$, where b is size of the background under the signal. Both numbers are simulated estimates, scaled to the data luminosity according to Table 4.3. The optimization procedure is described in a later section. However, to convey their benefits, the optimized cut values are already shown in the following discussion of the selection variables.

Photon center of mass energy Requiring a minimum photon energy aids in reducing the background from random combinations with photons other than the signal photon. Even in signal events random photons result in a significant background. The photon energy is required to be above 115 MeV, the reason for this value will be given in the cut optimization section. The optimum (with respect to the statistical significance of the signal yield) photon energy cut would be at 145 MeV. However, the low photon energy cut directly influences the ΔM distribution at the lower edge. A shift in the photon energy cut from 115 MeV to 150 MeV would move the low end shoulder of the photon background from 80 MeV to 130 MeV, near the location of the signal peak. This would lead to a larger uncertainty in the fitted signal yield. The cut is set at:

$$E^*_\gamma > 115\,\mathrm{MeV} \tag{6.6a}$$

The distribution of the energy of single photons in simulated events and in data is shown in Figure 6.3.

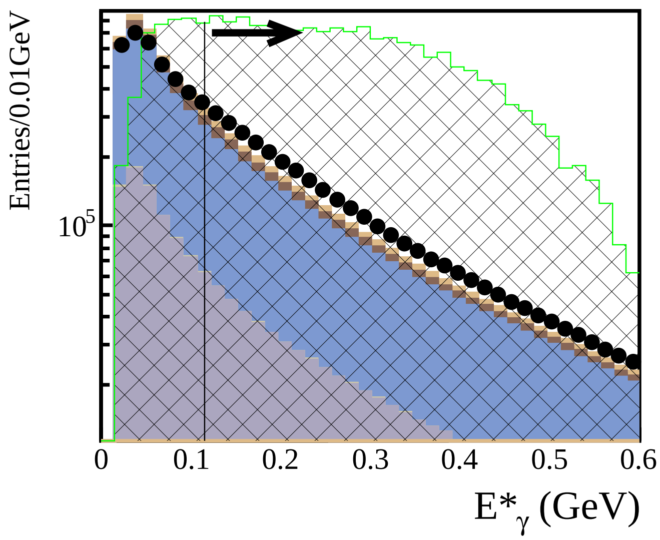

Figure 6.3: Single photon energy in the CM. The data are represented by black markers, the various generic Monte Carlo samples are the color coded solid histograms. The Monte Carlo is scaled to the data luminosity with an additional factor (0.984) for the difference in tag yield between MC and data. The signal Monte Carlo (green hashed) is arbitrarily scaled for better visibility. The tag is required to be in the tag signal region.

Tag Signal Charge Correlation The modes in the tag sample are chosen such that the charge of the signal $D_s^{*\pm}$ can be predicted. Combinatoric background from fake hadrons in uds, $b\bar{b}$, and $c\bar{c}$ events shows a much weaker charge correlation, the desired factor of two in the rejection of these backgrounds can be obtained. Semileptonic charm decays on the signal side will not be affected by this requirement. With Q^c_{tag} and Q^c_{signal} being the charge of the charm quark on the tag and the signal side, one can define the charge product QP and require:

$$QP = \frac{3}{2}Q^c_{\mathrm{tag}} * \frac{3}{2}Q^c_{\mathrm{signal}} = -1 \ . \tag{6.6b}$$

The distribution of QP in simulated events and in data are shown in Figure 6.4.

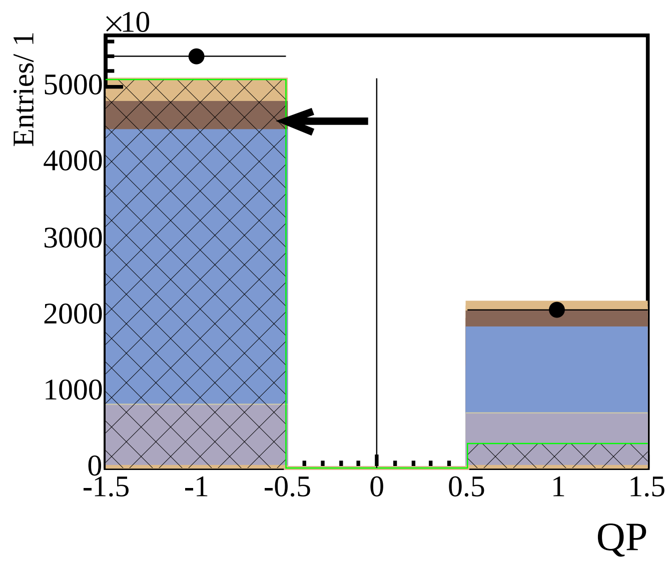

Figure 6.4: Product of tag and signal charm quantum number. The data are represented by black markers, the various generic Monte Carlo samples are the color coded solid histograms. The Monte Carlo is scaled to the data luminosity with an additional factor (0.984) for the difference in tag yield between MC and data. The signal Monte Carlo (green hashed) is arbitrarily scaled for better visibility. The tag is required to be in the tag signal region.

Angle Between the Muon in the D_s^+ Frame and the D_s^+ in the D_s^{*+} Frame Unlike the signal D_s^+, a large number of random D_s^+ combinations have the muon candidate aligned with the D_s^+ flight direction. The angle α_{μ,D_s} is defined as the angle between the muon direction in the D_s^+ frame and the D_s^+ flight direction in the CM frame, and the selection requires

$$\cos \sphericalangle(\mu, D_s^+) < 0.90 \ . \tag{6.6c}$$

The distribution of $\cos \sphericalangle(\mu, D_s^+)$ is shown in Figure 6.5.

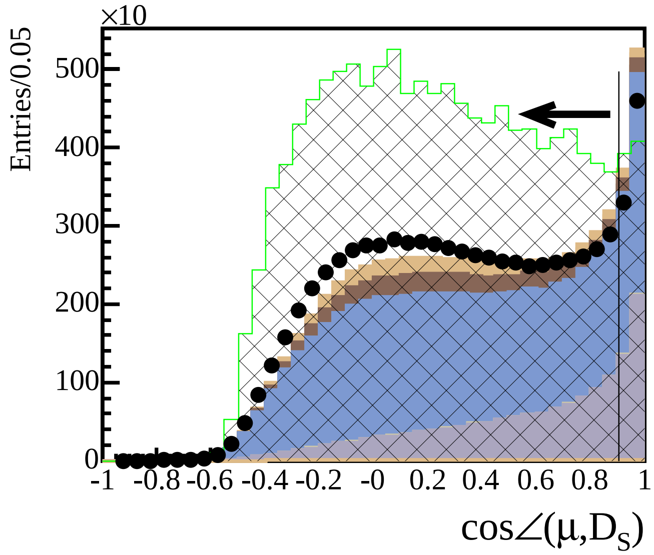

Figure 6.5: The cosine of the angle between the muon in the D_s^+ frame and the D_s^+ in the CM frame. The data are represented by black markers, the various generic Monte Carlo samples are the color coded solid histograms. The Monte Carlo is scaled to the data luminosity with an additional factor (0.984) for the difference in tag yield between MC and data. The signal Monte Carlo (green hashed) is arbitrarily scaled for better visibility. The tag is required to be in the tag signal region.

Missing CM Energy Due to the existence of a neutrino in the signal decay, the missing energy, $E^*_{\rm miss}$, equation (6.2) in Section 6.2, is higher in signal events than in background events. It is required

$$E^*_{\rm miss} > 0.38\,\text{GeV} \;. \tag{6.6d}$$

The missing energy distribution in simulated events and in data are shown in Figure 6.6.

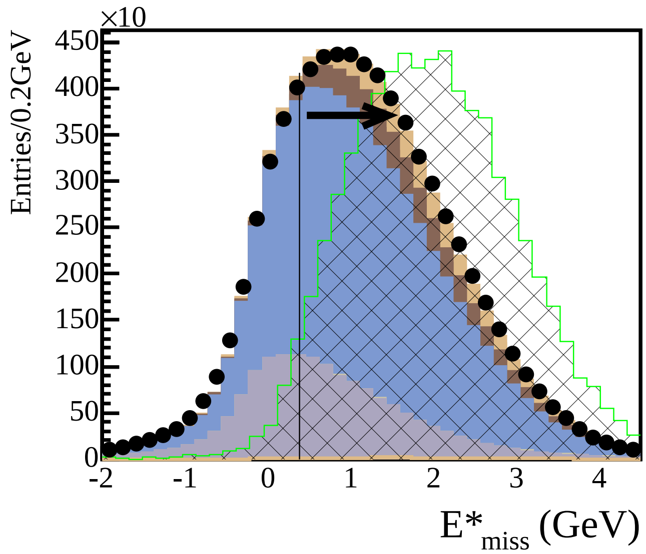

Figure 6.6: Distribution of the missing energy in the CM frame. The data are represented by black markers, the various generic Monte Carlo samples are the color coded solid histograms. The Monte Carlo is scaled to the data luminosity with an additional factor (0.984) for the difference in tag yield between MC and data. The signal Monte Carlo (green hashed) is arbitrarily scaled for better visibility. The tag is required to be in the tag signal region.

Neutrino correction The difference between the missing momentum and the corrected neutrino momentum, p_{corr} (6.5), is a good indicator of the validity of the $D_s^+ \to \mu^+\nu_\mu$ hypothesis. The distribution of p_{corr} is shown in Figure 6.7. While signal events peak at 0, background events are centered at a much lower value. The selection requires:

$$p_{\mathrm{corr}} = |\vec{p}^{\,*}_{\mathrm{miss}}| - |\vec{p}^{\,*}_{\nu}| > -0.06\,\mathrm{GeV/c} \tag{6.6e}$$

The distribution of p_{corr} in simulated events and in data are shown in Figure 6.7.

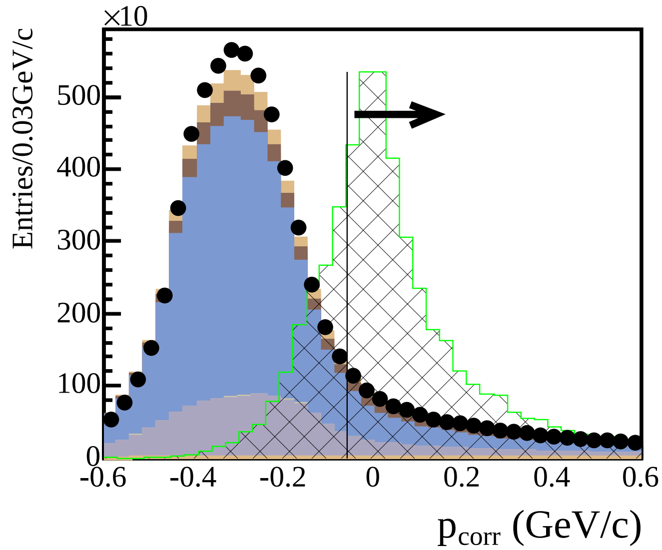

Figure 6.7: Distribution of the variable p_{corr}. The data are represented by black markers, the various generic Monte Carlo samples are the color coded solid histograms. The Monte Carlo is scaled to the data luminosity with an additional factor (0.984) for the difference in tag yield between MC and data. The signal Monte Carlo (green hashed) is arbitrarily scaled for better visibility. The tag is required to be in the tag signal region.

Neutrino CM polar angle Requiring a minimum polar angle for the neutrino direction in the CM frame, θ^*_ν, rejects events where the missing momentum is due to lost particles along the beam pipe. Simulation indicates that a similar restriction for the backward direction is not necessary. The neutrino polar angle in the CM frame is shown in Figure 6.8. The selection requires

$$\theta^*_\nu > 0.67\,\mathrm{rad} \tag{6.6f}$$

The distribution of neutrino polar angle in simulated events and in data are shown in Figure 6.8.

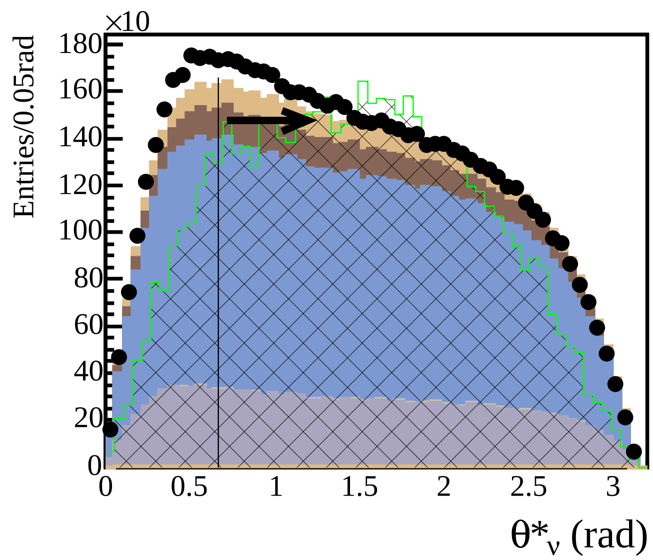

Figure 6.8: Distribution of the neutrino polar angle in the CM frame. The data is represented by black markers, the various generic Monte Carlo samples are the color coded solid histograms. The Monte Carlo is scaled to the data luminosity with an additional factor (0.984) for the difference in tag yield between MC and data. The signal Monte Carlo (green hashed) is arbitrarily scaled for better visibility. The tag is required to be in the tag signal region.

D_s^{*+} center of mass momentum Signal events exhibit a higher D_s^* momentum than the majority of background events, presumably because of the leading particle effect in the fragmentation. The two charm quarks in the fragmentation of $c\bar{c}$ carry most of the energy from the initial two-body decay at 10.58 GeV. The selection requires:

$$p^*_{D_s^{*+}} > 3.55\,\mathrm{GeV/c} \tag{6.6g}$$

The distribution of the CM momentum of the D_s^{*+} candidates is shown in Figure 6.9.

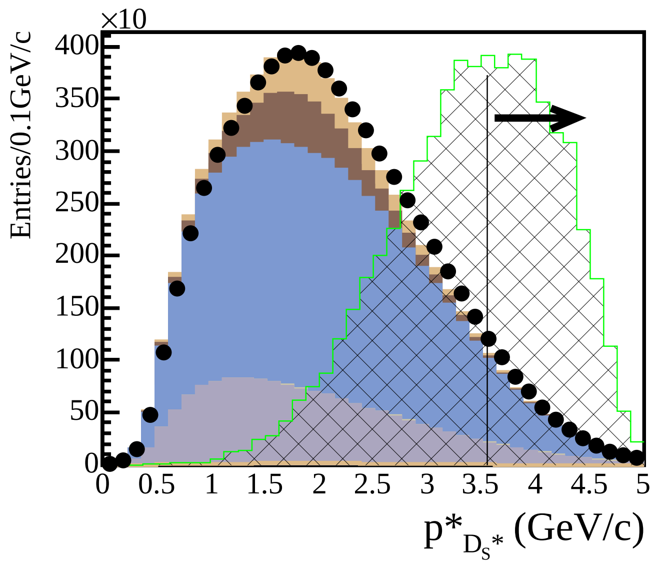

Figure 6.9: Distribution of the reconstructed CM momentum of the D_s^{*+} meson candidate. The data are represented by black markers, the various generic Monte Carlo samples are the color coded solid histograms. The Monte Carlo is scaled to the data luminosity with an additional factor (0.984) for the difference in tag yield between MC and data. The signal Monte Carlo (green hashed) is arbitrarily scaled for better visibility. The tag is required to be in the tag signal region.

Rejection of $e^\pm$ from $\gamma \to e^+e^-$ This requirement is not intended to improve the signal selection. Rather it is chosen in foresight of the subtraction of the semileptonic and leptonic τ backgrounds (background categories IIb and II(a)ii), for which the electron-substituted event reconstruction and selection will be used. The major difference between electrons and muons is their mass and hence QED behavior. While the lighter electrons can be produced in the photon conversion process, $\gamma \to e^+e^-$, muons can not.

The electron-positron pair in this process has a zero opening angle at the photon decay vertex. The decay itself requires the presence of an electromagnetic field to conserve energy and momentum, hence the conversion process happens in the detector material, for instance the beam pipe. An electron candidate is considered the daughter of a converted photon, and thus rejected, if it satisfies any of the following two criteria:

- The difference between the electron polar angle of the polar angle of any other charged track that does not belong to the tag, $|\theta_e - \theta_{\mathrm{trk}}|$, is less than 20 mrad.
- For each charged-track – electron pair, with the charged track not being part of the tag, two circles are found, that are the projections of the electron and the charged-track trajectory onto the xy-plane. The distance of the two circle-centers, $\vec{r}_{\mathrm{trk}}$ and $\vec{r}_e$, must not lie within 2 mm of the sum of the two radii:

$$||\vec{r}_{\mathrm{trk}} - \vec{r}_e| - |\vec{r}_{\mathrm{trk}}| - |\vec{r}_e|| > 2 \text{ mm} \quad \text{for all charged tracks not part of the tag .}$$

Muons are affected by the photon-conversion veto in the same way non-photon-conversion electrons are. Since the electron substituded background event sample is designed to closely resemble the muon backgrounds from semileptonic D and from τ decays, this photon conversion veto is applied also to the muon candidates.

6.4 Cut Optimization

The measurement of any particular physical quantity, e.g. a branching ratio, is always accompanied by a statistical uncertainty, which is due to the finite size of dataset that the result is drawn from. The central value of the measured quantity divided by the statistical uncertainty is the statistical *significance* of the measurement. Ideally the experimenter seeks to maximize the significance of the signal in an unbiased fashion by adjusting the cuts using simulation in advance of examining the data. For this purpose the significance as a function of the cut values on the previously described variables is studied and a set of optimal cuts is obtained. The statistical significance of a signal S above a background B is given by

$$\frac{N_S}{\sigma_{S+B}} = \frac{N_S}{\sqrt{\sigma_S^2 + \sigma_B^2}} \, , \tag{6.7}$$

where N_S is the simulated estimation of the number of signal events in the data, σ_S and σ_B are the statistical uncertainties of the signal and the background, respectively. The statistical uncertainty on the signal is $\sigma_S = \sqrt{N_S}$.

In the calculation of the background uncertainty, σ_B, the contributions from the tag sideband and the electron-substituted selection sample have to be included. The four statistically independent samples, μ-tag-signal, μ-tag-sideband, e-tag-signal, and e-tag-sideband, will be added, with the respective scaling factors $(+1, -\frac{2}{3}, -1, +\frac{2}{3})$. The factor $\frac{2}{3}$ for the samples μ-tag-sideband and e-tag-sideband is due to the 50 % larger tag sideband compared to the tag signal region. The background statistical uncertainty is:

$$\begin{aligned} \sigma_B^2 &= \sigma_{\mathrm{tag\,signal}}^2 + \sigma_{\mathrm{tag\,sbnd}}^2 \\ &= N_{\mathrm{bkgd},\,\mu}^{\mathrm{tag\,signal}} + N_{\mathrm{bkgd},\,e}^{\mathrm{tag\,signal}} + N_{\mathrm{signal},\,\mu}^{\mathrm{tag\,signal\,(fake)}} \\ &\quad + \frac{4}{9}\left(N_{\mathrm{bkgd},\,\mu}^{\mathrm{tag\,sbnd}} + N_{\mathrm{bkgd},\,e}^{\mathrm{tag\,sbnd}} + N_{\mathrm{signal},\,\mu}^{\mathrm{tag\,sbnd}}\right) \, . \end{aligned} \tag{6.8}$$

Here, N_*^* is the Monte-Carlo-predicted, luminosity-scaled, number of events that

Table 6.1: Selection requirements obtained from the cut optimization. These values are applied in the signal selection; in the remainder of this thesis only rounded values are quoted.

Variable	Cut Value
$\cos \sphericalangle(\mu, D_s^+)$	< 0.9036
E^*_{miss}	$> 0.3847\,\text{GeV}$
p_{corr}	$>$ -0.0574 GeV/c
θ^*_ν	$> 0.668\,\text{rad}$
$p^*_{D_s^{*+}}$	$> 3.5514\,\text{GeV}/c$

satisfy certain selection criteria. The superscripts indicate whether the tag is in the tag signal or the tag sideband region. The subscripts describe, which type of Monte Carlo data is used (generic background or signal Monte Carlo), and whether the reconstructed lepton candidate is required to be a muon or an electron. For $N^{\text{tag signal (fake)}}_{\text{signal},\,\mu}$ only fake tags are considered, since events with a true tag and a signal decay are not background.

With (6.8) and $\sigma_S = \sqrt{N_S}$, the significance (6.7) is maximized. The cuts on the following variables are varied in a five-dimensional, simultaneous fit [46]. The angle $\sphericalangle(\mu, D_s^+)$, the missing energy, E^*_{miss}, the neutrino momentum correction, p_{corr}, the neutrino polar angle in the CM frame, θ^*_ν, and the D_s^{*+} candidate CM momentum, $p^*_{D_s^{*+}}$. Table 6.1 lists the cut values that maximize the significance of the selection. The significance as a function of the cut value is shown in Figure 6.10 for each of the five selection variables, as well as for the photon energy. Figure 6.11 shows the distributions for each variable, after cuts on all other variables have been applied.

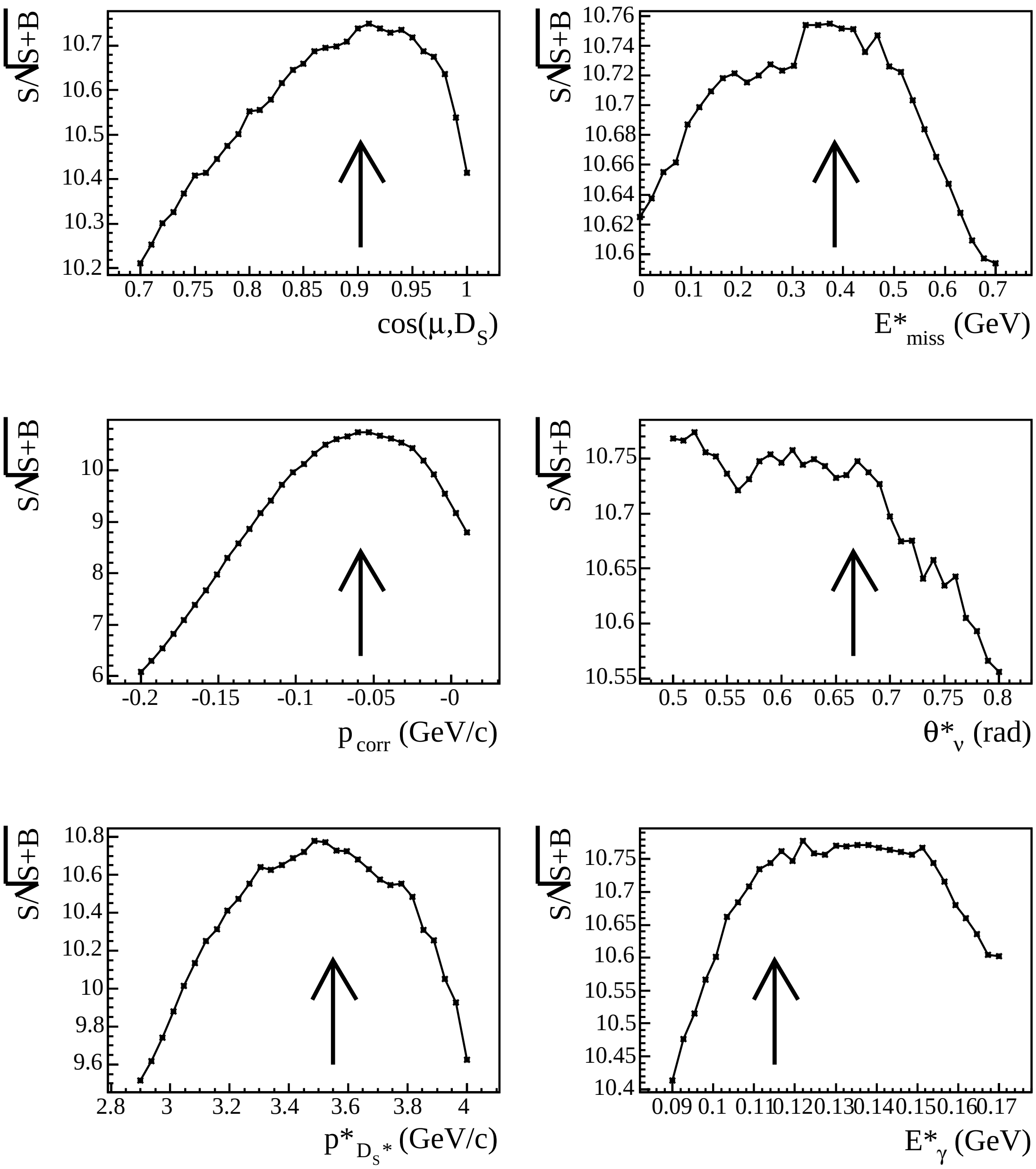

Figure 6.10: The significance as a function of the cut value for each of the quantities. With the exception of the photon energy, the arrows indicate the position of the cut found to be the optimum one by the optimization procedure. The cut on the photon energy has been picked such that it is already close to the plateau. Setting the cut around 150 MeV would distort the background distribution, making it difficult to separate signal and background cleanly.

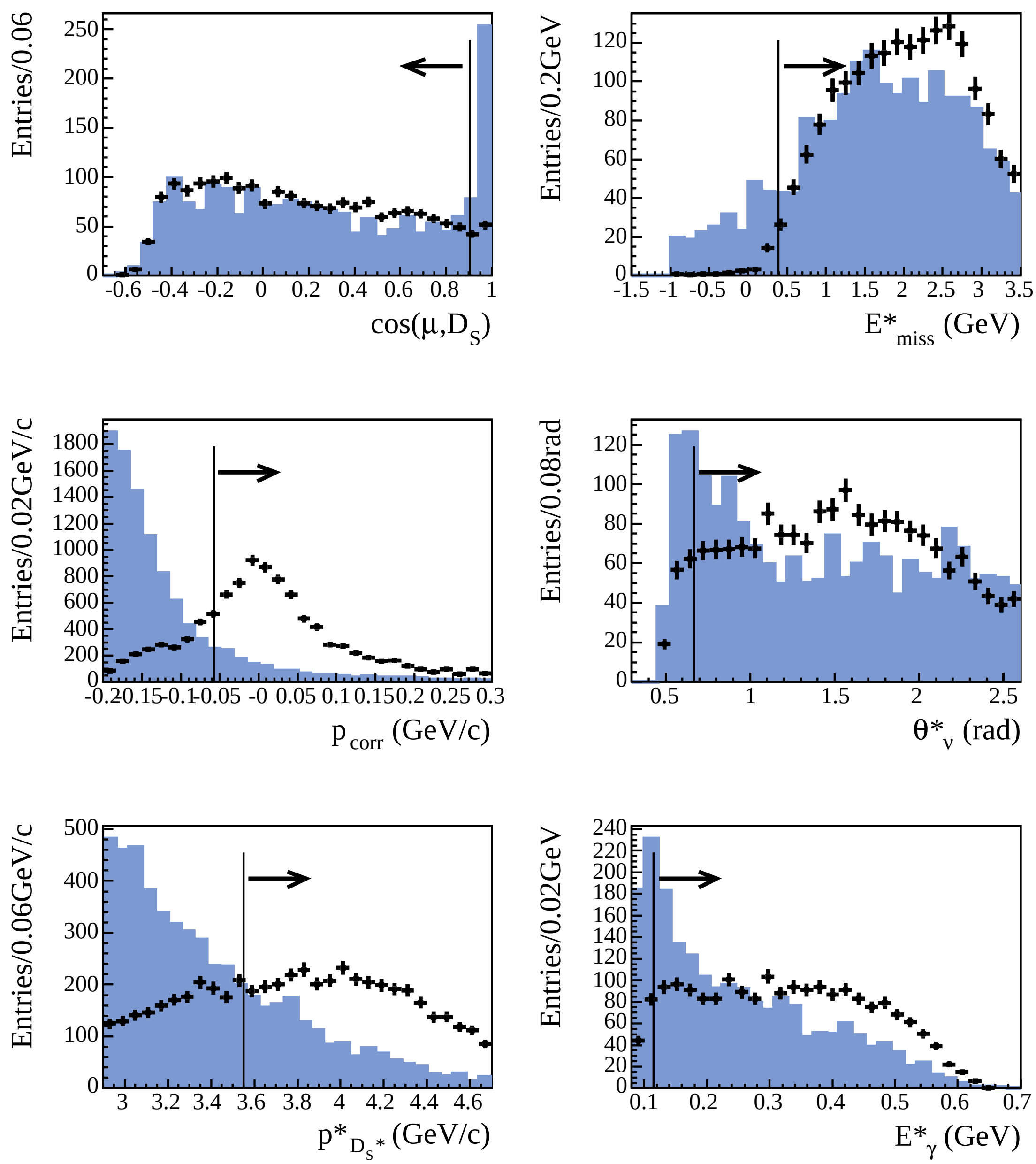

Figure 6.11: Simulated distributions of the selection variable after the all other cuts are been applied. The simulated signal is represented by black symbols. The blue solid histogram are the generic Monte Carlo samples, combined according to (6.8).

Table 6.2: Event-based signal selection efficiency determined for simulated signal events. The last column gives the estimated number of events in the data. A real tag is required in the event.

Selection Cut	Selection Efficiency		
	By Cut	Cumulative	
	[%]	[%]	[Events]
Tag	-	100.00 ± 0.00	4783
$\mu(1.2\,\mathrm{GeV/c}) + \gamma(30\,\mathrm{MeV})$	41.19	41.19 ± 0.23	1970
$E_\gamma > 115\,\mathrm{MeV}$	95.69	39.41 ± 0.23	1885
$QP = -1$	99.81	39.34 ± 0.23	1882
$\cos\sphericalangle(\mu, D_s^+) < 0.90$	94.48	37.17 ± 0.23	1778
$E^*_{\mathrm{miss}} > 0.38\,\mathrm{GeV}$	97.48	36.23 ± 0.23	1733
$p_{\mathrm{corr}} > -0.06\,\mathrm{GeV/c}$	72.61	26.31 ± 0.21	1258
$\theta^*_\nu > 0.7\,\mathrm{rad}$	82.36	21.67 ± 0.19	1037
$p^*_{D_s^{*+}} > 3.55\,\mathrm{GeV/c}$	53.70	11.64 ± 0.15	557
No e from $\gamma \to ee$	99.54	11.58 ± 0.15	554
True Signal	70.23	8.13 ± 0.13	389

6.5 Determination of the Signal Efficiency

The signal selection efficiency is determined using the signal Monte Carlo event sample; simulated events $e^+e^- \to c\bar{c} \to D_s^{*+} \to \gamma D_s^+ \to \gamma\mu^+\nu$, where the recoiling charm fragments generically. The size of the signal Monte Carlo sample represents about 9.5 times the data luminosity (Table 4.3). The efficiency is studied in events, for which the tag is correctly reconstructed, as confirmed by its truth-match.

To correct for the different muon selection efficiencies in simulated events and in data, each event is weighted by the candidate muon *MC-to-data PID weight*, which is described in Section 4.3. In addition, each event is weighted by the candidate muon *MC-to-data track weight*, to correct for the different track reconstruction efficiencies in simulated events and in data, (Section 4.4). The selection efficiency in correctly tagged events, $\epsilon_{\mu\nu}$, is

$$\epsilon_{\mu\nu} = (8.13 \pm 0.13)\,\% \ . \tag{6.9}$$

Table 6.3: Event reduction in the selection process in generic Monte Carlo and in data. The number of events in the generic background Monte Carlo is scaled to match the data luminosity. A tag in the tag signal region is required.

Selection cut	$c\bar{c}$ [Events]	uds [Events]	$b\bar{b}$ [Events]	$\tau\tau$ [Events]	Data [Events]
Tag	686394	204990	129555	4776	1088137
$\mu(1.2\,\mathrm{GeV/c}) + \gamma(30\,\mathrm{MeV})$	616251	187178	118910	3952	1029421
$E_\gamma > 115\,\mathrm{MeV}$	593553	179951	114029	2406	989439
$QP = -1$	456583	96233	76916	1947	722808
$\cos \sphericalangle(\mu, D_s^+) < 0.90$	418060	72159	73122	1778	658103
$E^*_{\mathrm{miss}} > 0.38\,\mathrm{GeV}$	355761	47779	68857	1728	546631
$p_{\mathrm{corr}} > -0.06\,\mathrm{GeV/c}$	39906	12765	26510	398	92593
$\theta^*_\nu > 0.7\,\mathrm{rad}$	26363	7938	21128	353	63099
$p^*_{D_s^{*+}} > 3.55\,\mathrm{GeV/c}$	3004	779	231	184	5756
No e from $\gamma \to ee$	2964	750	231	183	5704

The marginal efficiencies as the selection progresses are listed in Table 6.2, together with the number of events, expected in the dataset. In Table 6.3, the reductions of background events in the different generic Monte Carlo samples, with each cut, are listed. The table also contains the effect of the selection cuts on data.

For simulated candidate decays that satisfy all selection criteria the $\Delta M = M(D_s^{*+}) - M(D_s^+)$ is shown in Figure 6.12.

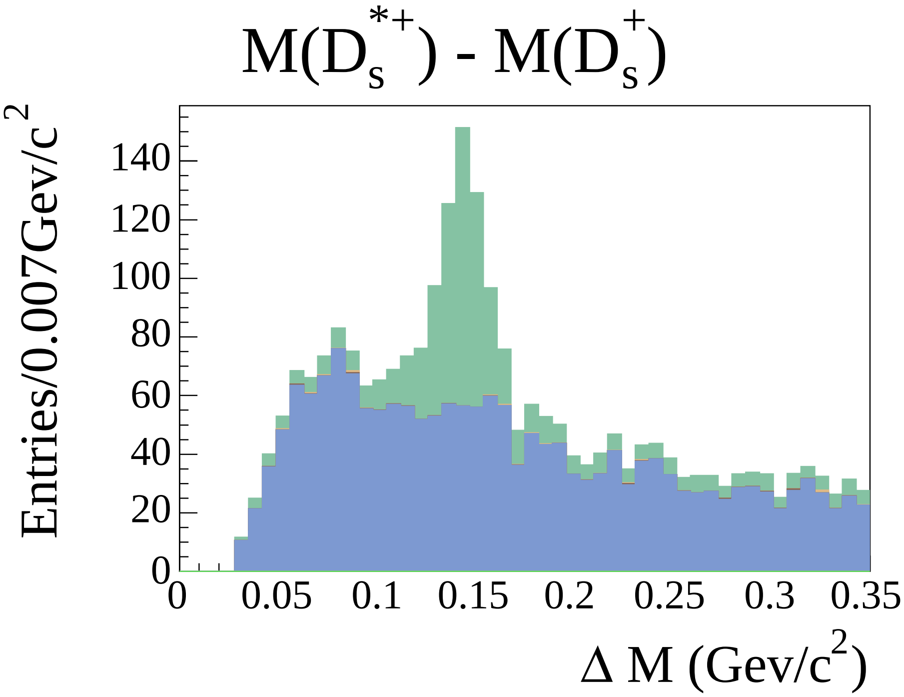

Figure 6.12: ΔM distributions of candidates satisfying the signal selection requirements in simulated events. The existence of a real tag in the event is required. Shown is signal Monte Carlo (green) on top of generic $c\bar{c}$ (blue) Monte Carlo. A few events that feed down from $B^0\overline{B}^0$ and B^+B^- generic Monte Carlo (light and dark brown) can be seen.

6.6 Shape of the Signal ΔM Distribution

The yield of signal events in data is extracted from a χ^2 fit to the $\Delta M = M(\mu\nu\gamma) - M(\mu\nu)$ distribution. The fitted signal shape is determined from thruth-matched signal decays in the signal Monte Carlo sample. The events must have a correctly reconstructed tag and the signal candidate must pass the signal selection cuts.

Three different distribution were considered to model the signal shape, a Gaussian, a Crystal Ball function, and a double Gaussian distribution. The double Gaussian, ((6.10), distribution is found to describe the simulated signal best (Figure 6.13).

$$\mathcal{PDF}_{\mu\nu\,\mathrm{signal}}(x|\mu_1,\sigma_1,\Delta_\mu,\sigma_2,f) = \frac{f}{\sqrt{2\pi\sigma_1^2}}\; e^{-\frac{(x-\mu_1)^2}{2\sigma_1^2}} + \frac{1-f}{\sqrt{2\pi\sigma_2^2}}\; e^{-\frac{(x-(\Delta_\mu+\mu_1))^2}{2\sigma_2^2}} \tag{6.10}$$

The parameters determined in the fit are

$$\begin{gathered} \mu_1 = 143.2\,\mathrm{MeV/c^2}\,,\ \sigma_1 = 8.7\,\mathrm{MeV/c^2}\,,\ \Delta_\mu = -2.1\,\mathrm{MeV/c^2}\,, \\ \sigma_2 = 23.4\,\mathrm{MeV/c^2}\,,\ f = 0.611\ . \end{gathered} \tag{6.11}$$

Simulated signal events that pass the signal selection and have a truth-matched tag in the signal recoil, always have the muon candidate matched to the true signal muon. However, in about 60 % the photon candidate is found not be the true signal photon. The ΔM distribution of this random photon background, (top plot in Figure 6.14), is described by the function $\mathcal{PDF}_{\mathrm{photon}}$ (6.12), which is a function that is often used to parameterize $M(D^*) - M(D)$ backgrounds.

$$\mathcal{PDF}_{\mathrm{photon}}(x|\Delta M_0,a,b,c) = \left(1 - e^{-\frac{x-\Delta M_0}{c}}\right)\left(\frac{x}{\Delta M_0}\right)^a + b\frac{x-\Delta M_0}{\Delta M_0} \tag{6.12}$$

The parameters of $\mathcal{PDF}_{\mathrm{photon}}$, determined in a χ^2-fit, are

$$\Delta M_0 = 24.9\,\mathrm{MeV/c^2}\,,\ a = -0.520\,,\ b = 0.003\,,\ c = 0.053\ . \tag{6.13}$$

The combined signal and photon background is shown in the bottom plot of Figure 6.14.

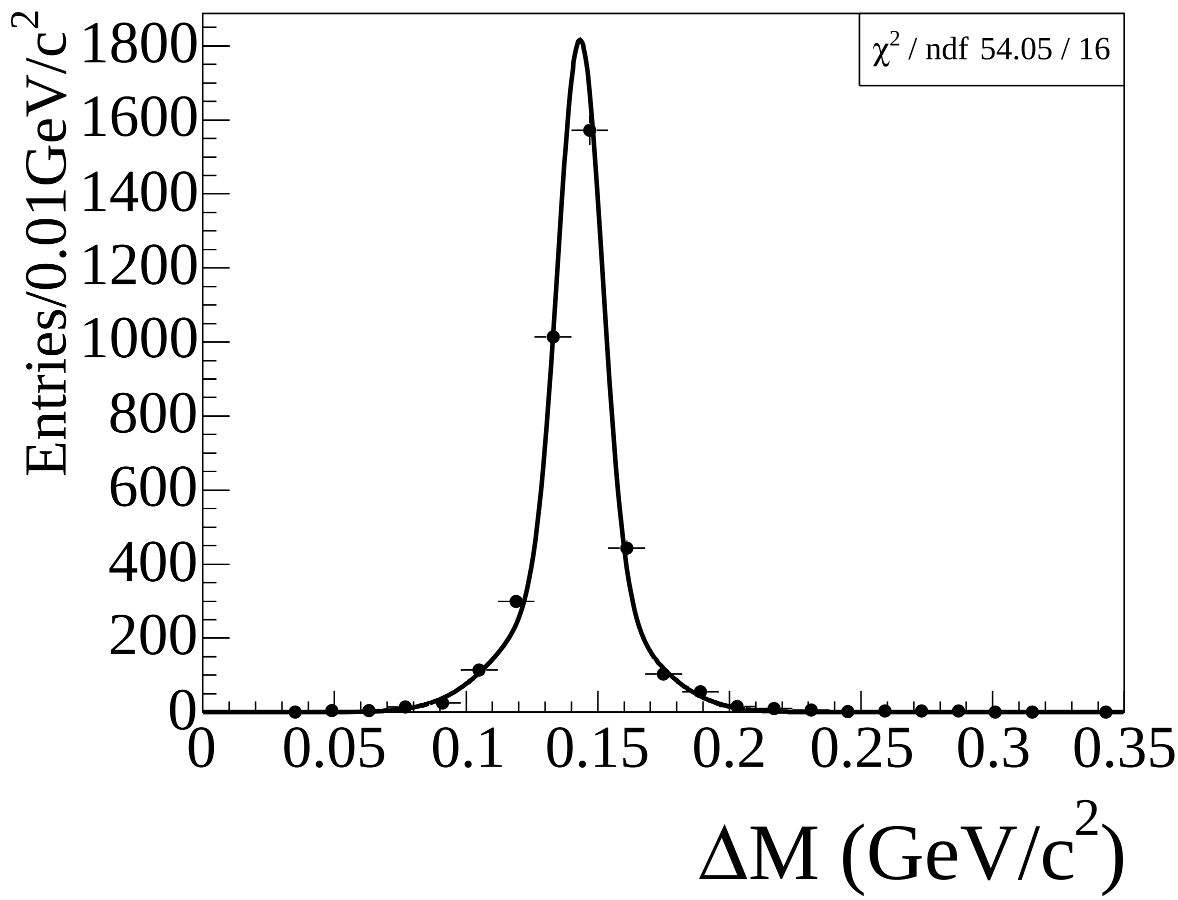

Figure 6.13: The signal ΔM distribution in simulated signal events in the recoil of a real tag. A double Gaussian distribution, $\mathcal{PDF}_{\mu\nu\,\mathrm{signal}}$, is fitted.

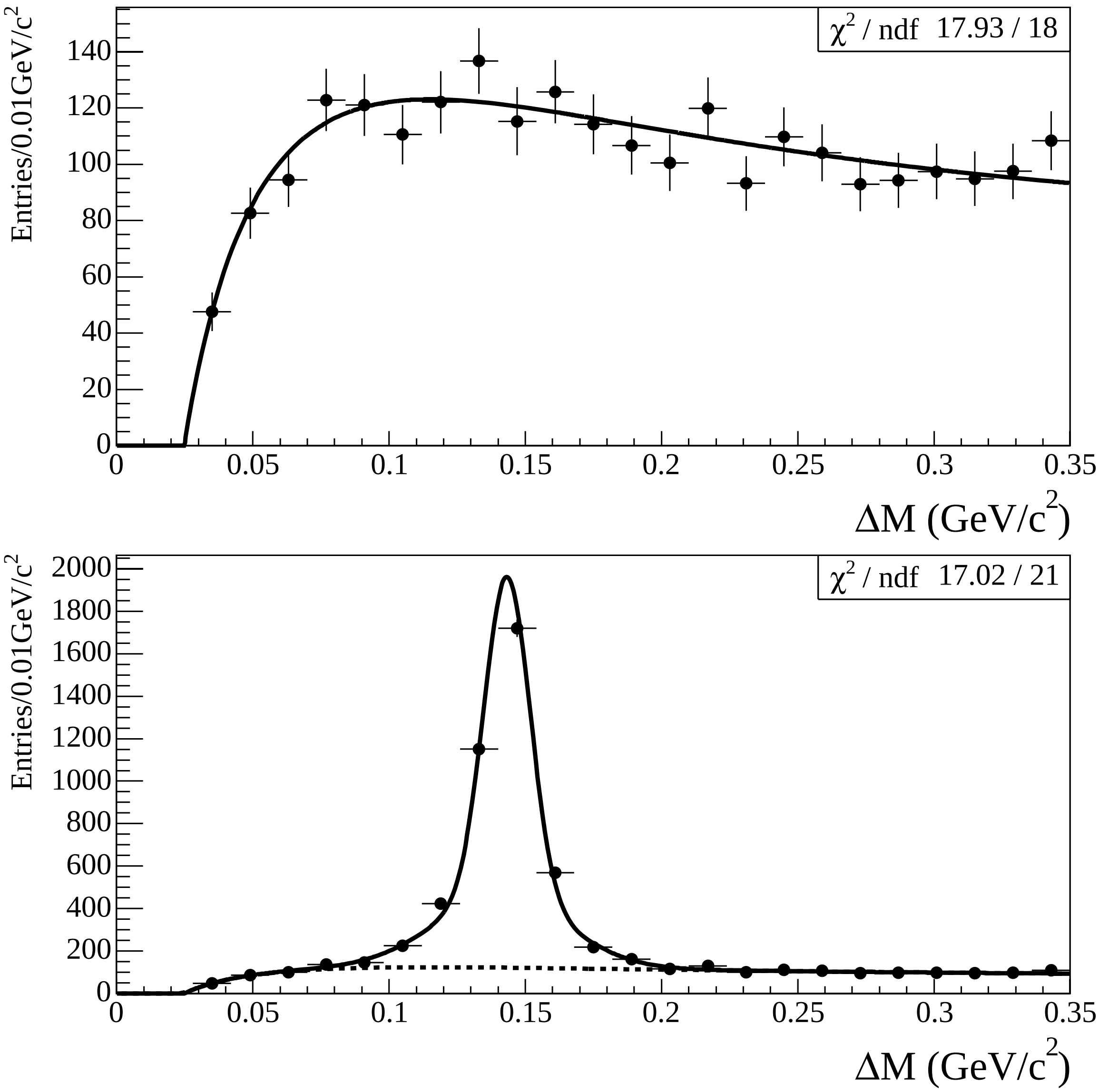

Figure 6.14: The ΔM distribution of the random photon background in simulated signal events (top plot). An empiric background function, $\mathcal{PDF}_{\text{photon}}$, is fitted. The bottom plot combines the signal and the random photon background from simulated signal events.

6.7 Background Estimation

With the identification of a charm particle in the event, the tag, a significant part of the background rejection is already accomplished. This section explains the details of how the remaining backgrounds are treated in the analysis. The background classification was already introduced in Section 4.2, in this section each background category is described in detail. Table 6.4 gives a summary of the signal candidates expected, from simulation, to remain in the different background categories, after the signal selection cuts have been applied. Figure 6.15 shows the ΔM distribution for these background categories.

Table 6.4: Signal candidates in generic Monte Carlo samples, that pass the selection criteria, listed by background category. Only candidates are counted with $\Delta M < 0.35\,\mathrm{GeV}/c^2$; the tag is required to lie in the tag signal region. The yield is scaled to the luminosity. Thus, the numbers reflect the background to be expected in data, before the tag sidebands are subtracted. Categories II(a)i through IIc sum up to 58.2 %

Background Category		# cands	%
I	Fake charm tag	1602	41.8
II	Correct charm tag	2234	58.2
$\sum$		3835	100.0
II(a)i	Leptonic μ	782	20.4
II(a)ii	Leptonic τ	244	6.4
IIb	Semileptonic	763	19.9
IIc	Combinatoric	444	11.6

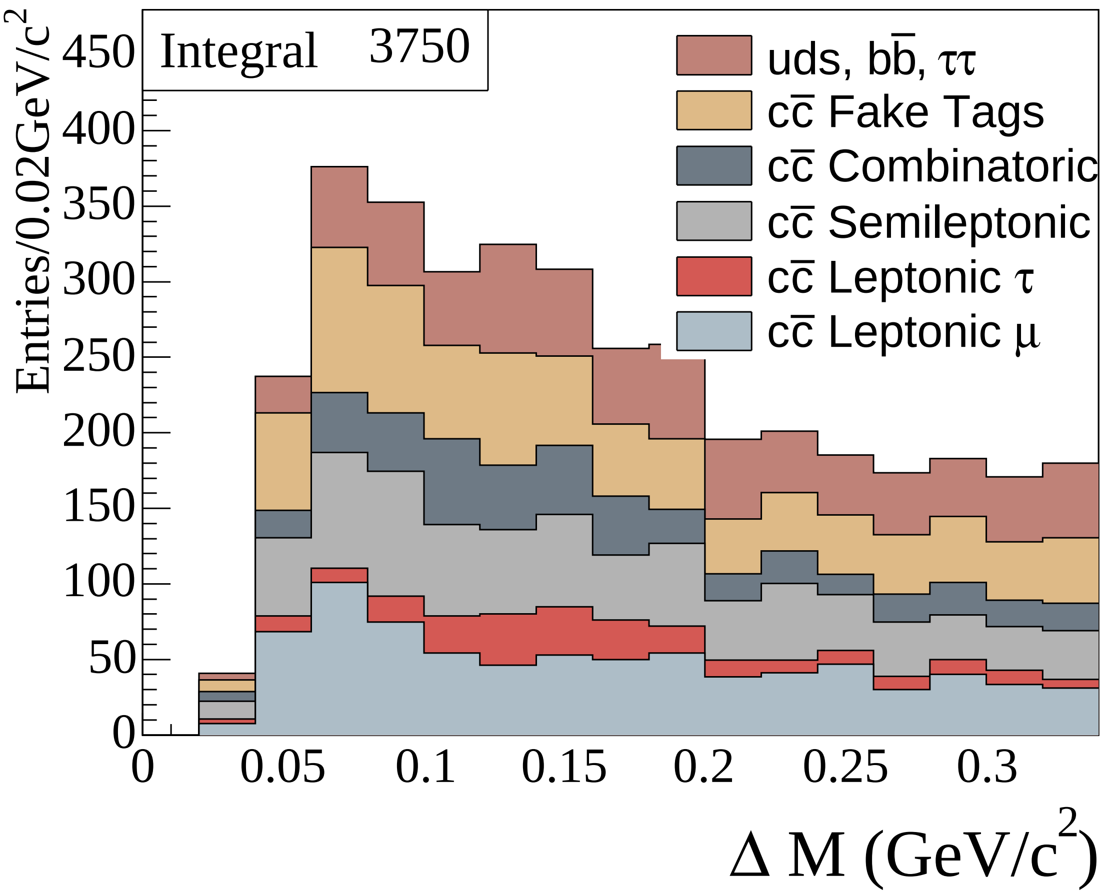

Figure 6.15: Combined ΔM distribution for the different background categories, scaled to data luminosity. The tag is required to lie in the tag signal region. From the top to the bottom the backgrounds are: • uds, $B^0\overline{B}^0$, B^+B^-, and $\tau^+\tau^-$ events (Cat. I), • $c\bar{c}$ events with a fake tag (Cat. I), • correctly tagged events with combinatoric signal background (Cat. IIc), • correctly tagged events with $D \to X\mu^+\nu_\mu$ signal background (Cat. IIb), • correctly tagged events with $\tau^+ \to \mu^+\nu_\mu\bar{\nu}_\tau$ signal background (Cat. II(a)ii), and • correctly tagged events with $D^*_{(s)} \to D^+_{(s)} \to \mu^+\nu_\mu$ signal background (Cat. II(a)i).

6.7.1 Category I: Fake Charm Tag

Events $e^+e^- \to q\overline{q}$, $q = u$, d, s, and $e^+e^- \to \tau^+\tau^-$ cannot contain a charm meson and therefore belong to this background category. Signal candidates from $B^0\overline{B}^0$ and B^+B^- events are also considered part of this category, although about 20 % of the charm tags reconstructed in $B\overline{B}$ decays in these events are correctly reconstructed tags. Fake tag candidates can also be produced in $c\overline{c}$ events. Figure 6.16 shows the ΔM distributions of signal candidates in tagged events, which are of this background type. The tag sidebands are used to evaluate the shape and the size of this background.

The validity of this method is demonstrated using generic Monte Carlo events. Table 6.5 gives the account of the number of tags in the tag signal and sideband regions before any signal selection cuts were applied. The signal selection is assumed to be independent of the tag mass, therefore the tag signal to sideband ratio should not change with the application of the selection requirements.

Table 6.5: Tag yield peak to sideband ratio in Monte Carlo.

MC Sample	Peak [Events]	Sideband [Events]	Peak/Sideband Ratio
uds	204990	205245	0.999 ± 0.004
$\tau\tau$	4775	4863	0.982 ± 0.028
$b\overline{b}$	129555	108808	1.191 ± 0.006
$c\overline{c}$ (fake tag)	253635	242668	1.045 ± 0.004

For uds and $\tau^+\tau^-$ events the tag signal-to-sideband ratio is consistent with 1. For generic $B^0\overline{B}^0$ and B^+B^- decays the tag signal region yields 20 % more tags than the sidebands. This is due to the tag momentum requirement, which does not entirely eliminate real D-mesons. However, the $B\overline{B}$ background is small ($\mathrm{I_{BB}}$ in Figure 6.16). After the tag sidebands and the electron-substituted signal candidates are subtracted, about 3 $B\overline{B}$ events are expected under the ΔM signal peak. They will be part of the background fit.

For generic $c\overline{c}$ Monte Carlo the number of fake tags in the tag signal region is determined by counting only tags that are not truth matched. For some tag modes

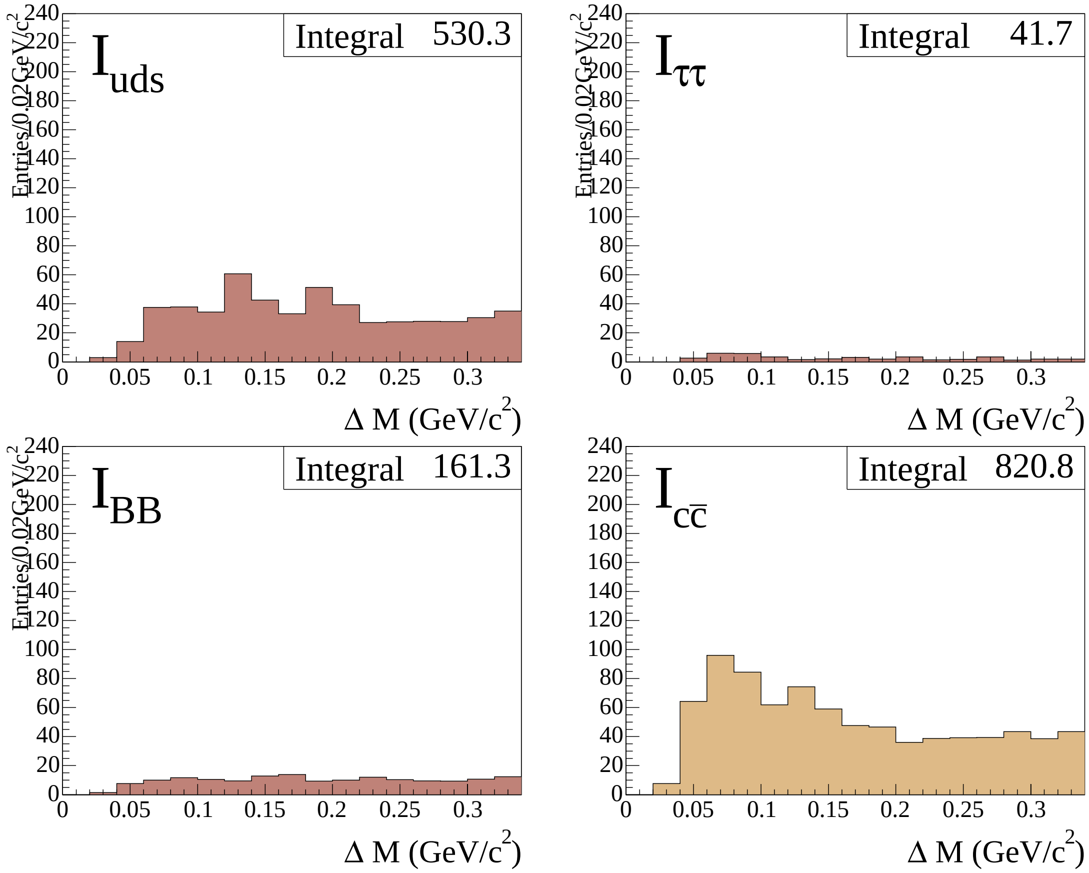

Figure 6.16: ΔM distribution of signal candidates in simulated uds, $B\bar{B}$, $\tau^+\tau^-$, and fake-tag $c\bar{c}$ events, scaled to the data luminosity. The tag lies in the tag signal region.

the truth matching algorithm does not work all the time. The mode $D^{*+} \to D^0\pi^+$ (Figure 5.10) is an example, where the association between true and reconstructed particle, in this case the slow pion, is not always made. For some modes another decay exists that has the same set of final particles. For instance the decay $D^0 \to K^-\pi^+\pi^0$ (Figure 5.8) can proceed through a K^* resonance. The final state of the decay $D_s^+ \to \phi\rho^+$ can also be reached in a non-resonant $D_s^+ \to \phi\pi^+\pi^0$ decay (Figure 5.9). In both cases the truth matching algorithm is inefficient in recognizing these tag candidates as real tags. This inefficiency leads to an ostensive 4 % higher fake tag yield in the tag signal than in the tag sideband region. Since this excess is caused by a not truth-matched real tags, the discrepancy has however no ramifications for the final result. This study conclusively shows that the tag sidebands can be used to estimate the background from fake tag events.

The remaining backgrounds are from events that do have a real tag reconstructed, and which are therefore not removed by the tag sideband subtraction. Those are discussed in the following.

6.7.2 Categories II(a)ii and IIb: Leptonic τ and Semileptonic Charm Decays

Witin the Standard Model *lepton universality* is well established. The electroweak coupling strength of a lepton to the $W^\pm$ (1.7b) and to the Z^0 (1.7c) is the same for all three families. Lepton universality has been confirmed to a high degree of precision, for instance by measurements of leptonic τ decays [47]. Differences in decay rates are due only to the different masses of the electron, the muon, and the τ-meson, which influences the decay rate:

- *Helicity suppression:* In the purely leptonic decay of pseudoscalar mesons (Section 2.1), the leptons are produced in an unfavoured helicity state. The probability of a spin flip goes like m^2 which enhances the rates of decays to the heavier leptons (μ and τ-lepton) over that to an electron.

Table 6.6: Differences in the muonic and electronic decay rates.

Leptonic Decay		e/μ Ratio	Cause
$D_s^+ \to \mu^+\nu_\mu$	$D_s^+ \to e^+\nu_e$	2.3×10^{-5}	helicity suppression
$D^0 \to K^-\mu^+\nu_\mu$	$D^0 \to K^- e\nu_e$	1.03	phase space
$\tau^+ \to \mu^+\nu_\mu\bar{\nu}_\tau$	$\tau^+ \to e\nu_e\bar{\nu}_\tau$	1.028	phase space

- *Phase space:* In decays where the phase space available for the produced lepton is close to the lepton mass, the decay rate is suppressed compared to the same decay but with a lighter final-state lepton.

It is fortunate that the decay $D_s^+ \to e\nu_e$ is heavily suppressed, compared to the signal decay $D_s^+ \to \mu^+\nu_\mu$, while semileptonic charm and $\tau^+ \to l^+\nu_l\bar{\nu}_\tau$ decays appear at a nearly equal rate in the muon and the electron channel, Table 6.6.

For this reason, lepton universality is used in this analysis to determine the size and shape of background from events in which charm mesons or baryons, (X_c), decay semileptonically, $X_c \to X\mu\nu_\mu$, or letonically, $X_c \to \tau\nu_\tau \to \mu\bar{\nu}_\mu\nu_\tau$. This is accomplished by repeating the event reconstruction and signal selection, with an electron requirement replacing the muon requirement, while retaining the requirement of a tag, lying in the tag signal region. The reconstruction of the signal proceeds as in the case of the muon, as described in Section 6.1. The only change is the replacement of the muon mass m_μ in (6.3) with the electron mass, for the neutrino-momentum fitting procedure. The signal-selection criteria, introduced in Section 6.3, are applied. Table 6.7 gives a summary of the *electron-signal* candidates remaining after the signal selection is applied. Since the electron signal is intended to describe the background in events with a real tag, the tag sidebands are subtracted. The resulting *sideband-subtracted electron-signal* event sample is then used to describe and subtract the backgrounds of category II(a)ii and IIb. In addition there is a small combinatoric background of approximately 10 events, after the tag sideband subtraction. Those events are randomly distributed between $\Delta M = 50$ and $350\,\mathrm{MeV}$. The combinatoric background fit accounts for that source.

Table 6.7: Electron-signal candidates in generic Monte Carlo samples, that pass the selection criteria, listed by background category. Only candidates are counted with $\Delta M < 0.35\,\mathrm{GeV}/c^2$; the tag is required to lie in the tag signal region. The yield is scaled to the luminosity. Thus, the numbers reflect the background to be expected in data, before the tag sidebands are subtracted. Categories II(a)i through IIc sum up to 57.2 %

Background Category		# cands	%
I	Fake charm tag	477	42.8
II	Correct charm tag	639	57.2
$\sum$		1116	100.0
II(a)i	Leptonic μ	0	0.0
II(a)ii	Leptonic τ	153	13.8
IIb	Semileptonic	465	41.6
IIc	Combinatoric	20	1.8

The detailed requirements on the electron candidate are as follows: The candidate has to originate near the IP; the distance between the IP and the point of closest approach of the candidate track to the IP has to be less than 1.5 cm in the xy-plane and less than 10 cm along the z-direction. The electron candidate has to satisfy a likelihood based electron PID-selector. The PID-selector decision is based on:

- the energy deposited in the EMC, in units of the track momemtum, E_{dep}/p,
- the lateral moment of the electromagnetic shower in the EMC, M_{LAT} (5.1),
- the azimuthal angular difference between the point where the track enters the EMC and the reconstructed shower center,
- the Cherenkov angle θ_C, measured by the DIRC, and
- the specific energy loss, dE/dx, in the DCH.

Two additional requirements are applied, $0.5 < E_{\mathrm{dep}}/p < 1.5$, and $N_{\mathrm{cry}} > 4$, where N_{cry} is the number of EMC crystals that are part of the EMC shower cluster. Using these electron candidates, the signal selection is performed.

The differences between electrons and muons comes from their different detection efficiencies, and the greater susceptibility of electrons to radiative QED processes. Crucial to the success of this background estimation method are two requirements:

- The muon and electron detection efficiencies in the data must be precisely known, and corrected for. Technically, this is achieved by using the electron-to-muon PID weights (Section 4.3), which are calculated from control samples derived from data.

- Before the application of the 1.2 GeV/c CM momentum requirement, the energy loss of electrons through Bremsstrahlung $e \rightarrow \gamma e$ must be recovered to obtain a good agreement between the electron and muon momentum distributions. This is achieved by adding the energy of identified bremsstrahlung photons to the energy of the electron candidate.

The validity of both methods is tested using the generic $c\bar{c}$ Monte Carlo event sample, with a true identified semileptonic charm decay in the recoil of a tag. The validity of both methods is again verified in data, using the control sample $D^{*0} \rightarrow \gamma D^0 \rightarrow \gamma K^- l^+ \nu$.

Electron-to-Muon Efficiency Correction Study

The muon and electron efficiencies have been measured in simulated events and in data using dedicated control samples. The electron-to-muon PID efficiency weights are calculated as the efficiency ratio, (Section 4.3).

Simulated generic $c\bar{c}$ events are used to study the electron-to-muon detection efficiency correction. Only events in which a muon or an electron candidate with a CM momentum above 1.2 GeV/c is reconstructed are considered. By matching the lepton candidate to its true identity, its origin in a semileptonic charm decay is verified. A real tag is required in the event.

The electron-to-muon PID weight (Section 4.3) is applied to the electron candidates. The momentum spectrum before and after the PID correction is shown in Figure 6.17.

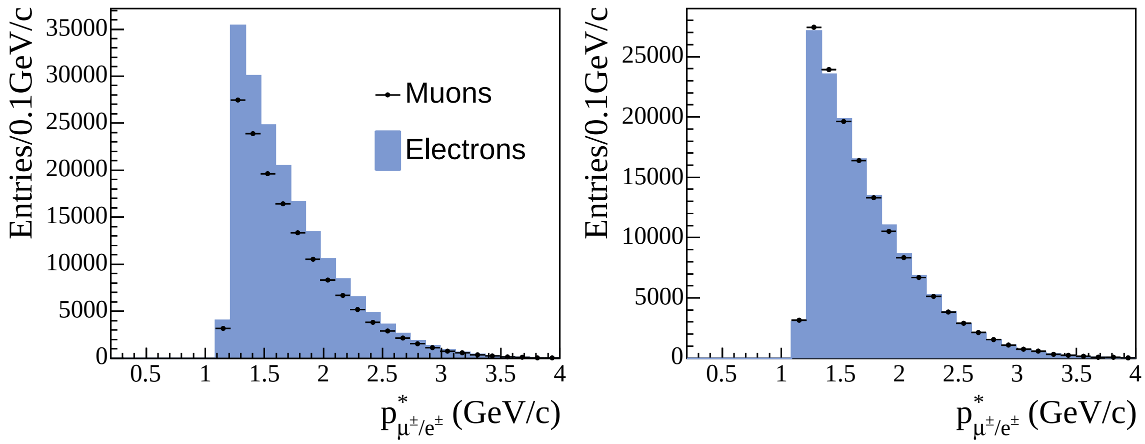

Figure 6.17: Comparison of the muon and electron momentum spectra in semileptonic charm decays, without and with PID efficiency correction. The detection efficiency for electrons at *BABAR* is higher than for muons (left plot). After the application of the electron-to-muon PID weight, the momentum spectra agree well. The bremsstrahlung recovery for electrons has been applied in both plots.

Bremsstrahlung Loss Recovery for Electrons

Unlike muons, electrons and positrons radiate a non-negligible fraction of their energy through the process $e^{\pm} \to e^{\pm}\gamma$, (right plot in Figure 6.18). To conserve energy and momentum this process requires an external electromagnetic field, provided either by the nucleii of the traversed matter or by the magnetic bending field. In the first case the process is called bremsstrahlung, in the second synchrotron radiation. Electrons of 1 GeV in the *BABAR* magnetic field of 1.5 T lose about 5 MeV energy due to synchrotron radiation, while traversing the DCH; this energy loss scales with E^2/GeV^2.

Dominant is the energy loss through bremsstrahlung, which happens in the material of the SVT and in the beam pipe, and hence before the electron momentum is measured by the DCH. Therefore, prior to applying the minimum CM momentum requirement on the electron candidates in the electron-signal selection, the bremsstrahlung energy loss must be recovered.

Electrons emit bremsstrahlung photons at a small angle along their direction of flight, (left plot in Figure 6.18). Identifying those photons and adding their energy

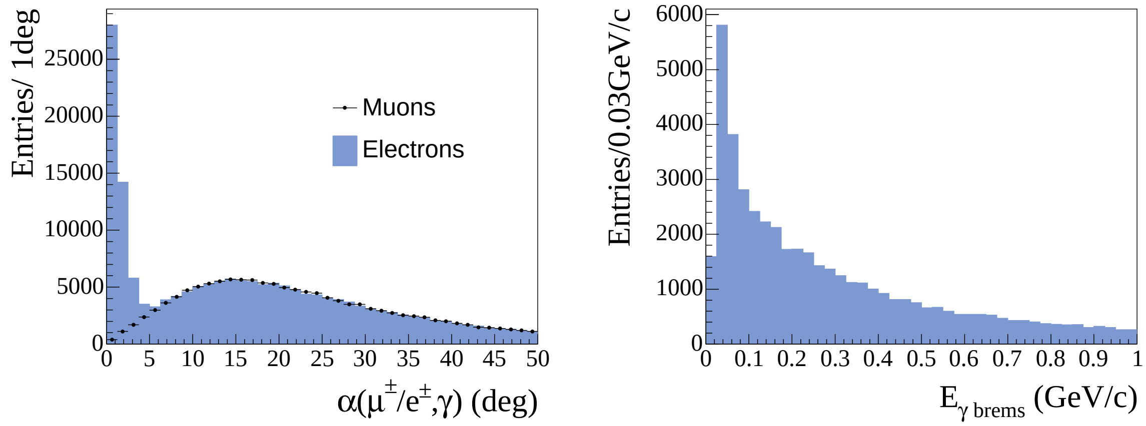

Figure 6.18: Properties of bremsstrahlung photons. On the left the angle α between muons/electrons and nearest photon is shown. The muon sample is scaled to match in size the electron sample (above 5 °). The bremsstrahlung photons at low α are evident. On the right the energy distribution for real bremsstrahlung photons (identified by truth-matching) is drawn.

to that of the electron candidate regains most of the lost energy.

For each electron candidate we define a window in the polar and azimuthal angle, θ and ϕ, around the electron flight direction (θ_e, ϕ_e) at the IP. All photon candidates, as defined in Section 5.3, falling within this window are considered bremsstrahlung photons; their four momentum is added to that of the electron. The window is defined by

$$\Delta\theta = \theta_\gamma - \theta_{e^\pm} \in [-30, 40] \text{ mrad} \tag{6.14}$$

$$\Delta\phi_{e^\pm} = \phi_\gamma - \phi_{e^\pm} \in \begin{cases} [-50, X] \text{ mrad for electrons,} \\ [X, 50] \text{ mrad for positrons,} \end{cases}, \tag{6.15}$$

where $X = \phi_{\text{intersect}} - \phi_{e^\pm}$ is the azimuthal angular difference between the $e^\pm$-track intersection with the EMC and its direction at the IP. Figure 6.19 shows the $\Delta\theta$ and $\Delta\phi_{e^\pm}$ distribution for real bremsstrahlung photons.

The effect of the recovery of the bremsstrahlung losses is shown in Figure 6.20. It demonstrates convincingly that with the application of both, the electron-to-muon

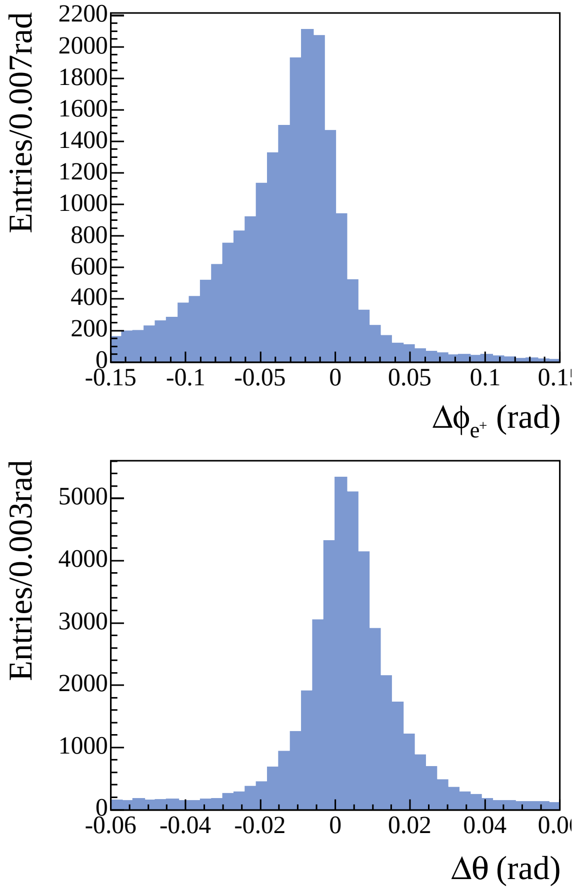

Figure 6.19: Angular difference between the direction of real bremsstrahlung photons and the parent electron direction at the IP.

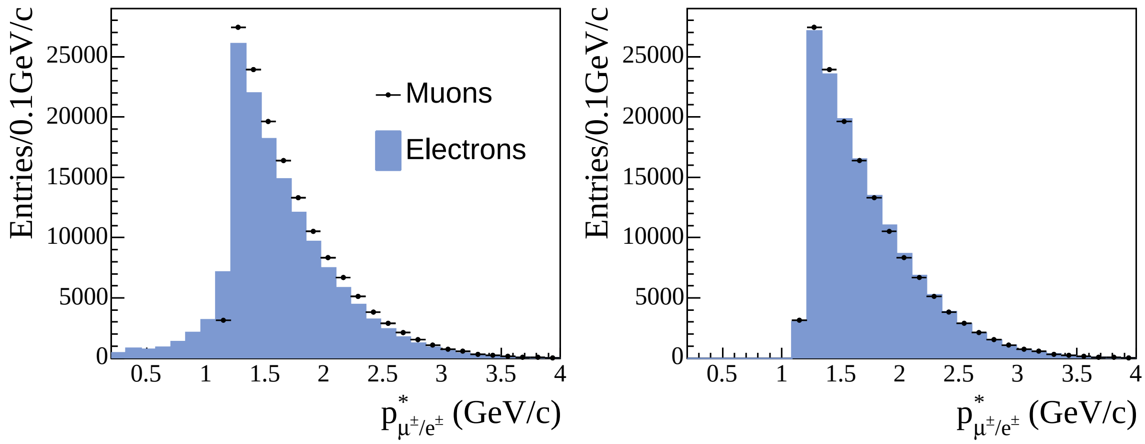

Figure 6.20: Comparison of the muon and electron momentum spectra in semileptonic charm decays, without (left) and with (right) the recovery of bremsstrahlung energy losses. After the bremsstrahlung loss recovery, the momentum spectra agree well. The PID efficiency correction for electrons has been applied in both plots. (On the left, below 1.2 GeV/c, the distribution consists only of electron candidates that have a momentum higher than 1.2 GeV/c after applying the bremsstrahlung recovery procedure. Other electron candidates are not stored in the reduced dataset that is used for the analysis.)

PID efficiency correction and the bremsstrahlung energy loss recovery, the differences between electrons and muons can be corrected for, and the tag-sideband-subtracted events that pass the electron-signal selection can be used to properly describe the signal backgrounds of the Categories II(a)ii and IIb.

6.7.3 Category II(a)i: Leptonic Charm Decays into a Muon

The remaining two background categories – real tag events with the signal side being either a charm state decaying leptonically, $X_c^+ \to \mu^+\nu_\mu$ (Category II(a)i), or a random photon–charged-hadron pair faking a signal (Category IIc). Since no suitable event samples, that could be used to estimate these two backgrounds, were identified in data, both backgrounds need to be evaluated from Monte Carlo simulated generic $c\bar{c}$ events. The background Category IIc is described in the next section.

The background Category II(a)i, purely leptonic decays of charm mesons or baryons into a muon-neutrino pair, consists of about 95 % of events with the decays $D^{*+}_{(s)} \to \pi^0 D^+_{(s)} \to \mu\nu_\mu$ or $D^+_{(s)} \to \mu\nu_\mu$ in the recoil of a real tag. The remaining events contain decays of the higher-excitation charm meson states, $D_1(2420)^0$ and $D^*_2(2460)^0$. The ΔM distribution of these background events exhibits two distinct components. The first component is from decays $D^{*+}_{(s)} \to \pi^0 D^+_{(s)} \to \pi^0\mu^+\nu_\mu$, where the reconstructed signal photon comes from the slow π^0 of the $D^{*+}_{(s)}$ decay. That component is limited to ΔM values between 40 and 100 MeV, (top plot in Figure 6.21). In addition to simulated generic $c\bar{c}$ events, two dedicated Monte Carlo samples are used to study this component. One sample contains events $e^+e^- \to c\bar{c} \to D^{*+}_s \to \pi^0 D^+_s \to \pi^0\mu^+\nu_\mu$ and represents about 7.0 times the dataset. The other contains events $e^+e^- \to c\bar{c} \to D^{*+} \to \pi^0 D^+ \to \mu^+\nu_\mu$ and is 4.3 times larger than the dataset. In both samples the other charm quark fragments and decays generically. This component is best described by a double-Gaussian, (6.16), which satisfactorily accomodates the lower and upper edge of the distribution.

$$\mathcal{PDF}_{\gamma\,\mathrm{from}\,\pi^0}(\Delta M|\mu_1,\sigma_1,\Delta_\mu,\sigma_2,f) = \frac{f}{\sqrt{2\pi}\sigma_1}e^{-\frac{1}{2}\frac{(\Delta M-\mu_1)^2}{2\sigma_1^2}} + \frac{1-f}{\sqrt{2\pi}\sigma_2}e^{-\frac{1}{2}\frac{(\Delta M-(\Delta_\mu+\mu_1))^2}{2\sigma_2^2}} \tag{6.16}$$

The parameters of $\mathcal{PDF}_{\gamma\,\mathrm{from}\,\pi^0}$, determined by the fit, are

$$\mu_1 = 74.9\,\mathrm{MeV/c^2}\,,\ \sigma_1 = 13.2\,\mathrm{MeV/c^2}\,,\ \Delta_\mu = -20.9\,\mathrm{MeV/c^2}\,,\ \text{and}\ \sigma_2 = 6.1\,\mathrm{MeV/c^2}\ . \tag{6.17}$$

If the photon is selected from any other source, the distribution of ΔM does not exhibit any striking feature, (bottom plot in Figure 6.21). The function $\mathcal{PDF}_{\mathrm{random}\,\gamma}$ (6.18), the same function that is used for the random photon background in simulated signal events (6.12), is used to describe this background.

$$\mathcal{PDF}_{\mathrm{random}\,\gamma}(\Delta M|\Delta M_0,a,b,c) = \left(1-e^{-\frac{\Delta M-\Delta M_0}{c}}\right)\left(\frac{\Delta M}{\Delta M_0}\right)^a + b\frac{\Delta M-\Delta M_0}{\Delta M_0} \tag{6.18}$$

The parameters of $\mathcal{PDF}_{\mathrm{random}\,\gamma}$, determined by the fit, are

$$\Delta M_0 = 24.2\,\mathrm{MeV/c^2}\,,\ a = -0.724\,,\ b = -0.002\,,\ \text{and}\ c = 1.426\ .$$

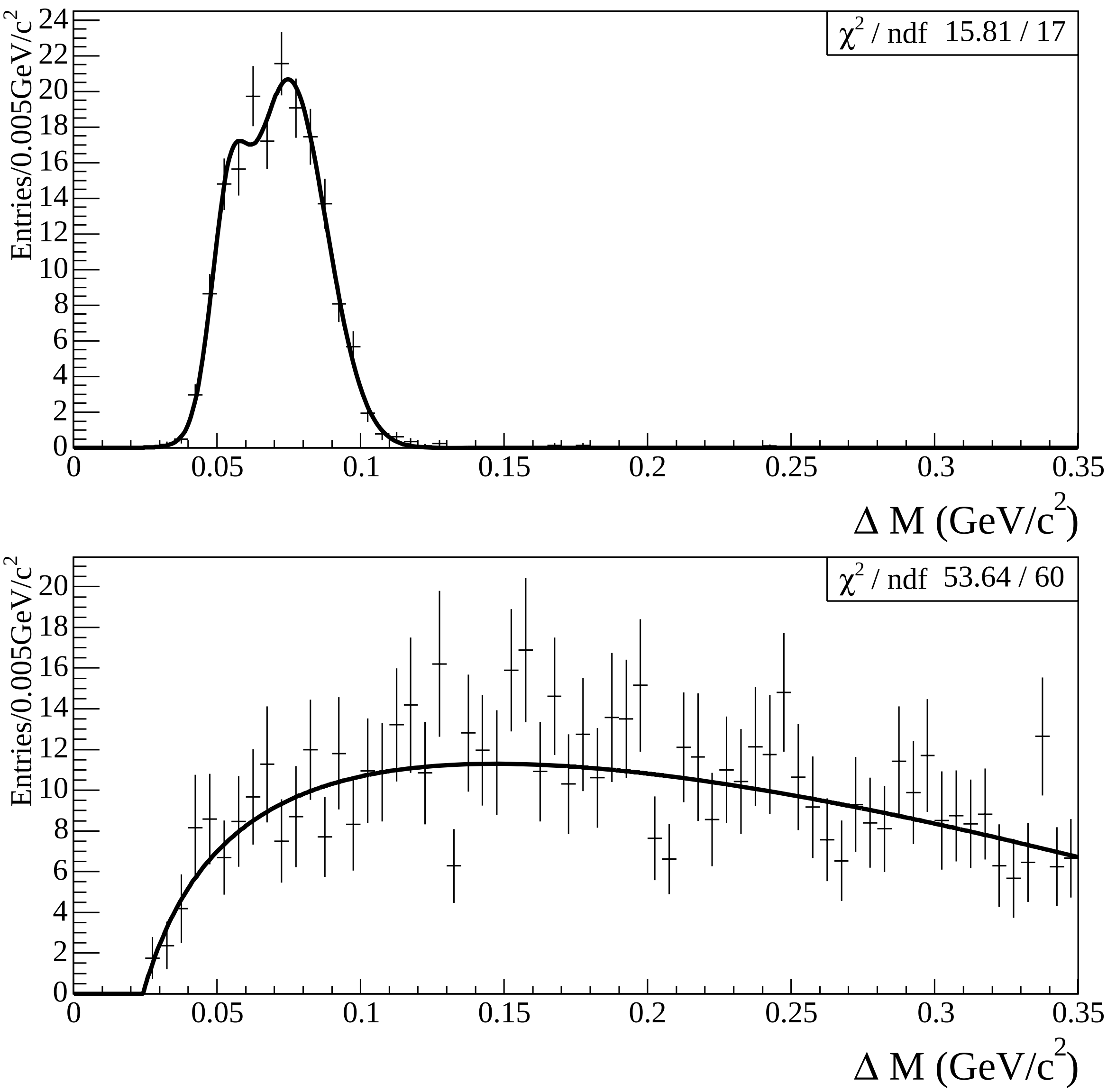

Figure 6.21: Distribution of ΔM of the two components of background Category II(a)i. The top plot shows candidates in which the selected signal photon is a daughter of the π^0 from the $D^{*+}_{(s)} \to \pi^0 D^+_{(s)}$ decay; it is derived from two dedicated Monte Carlo samples: $c\bar{c} \to D^{*+}_{(s)} \to \pi^0 D^+_{(s)} \to \mu^+\nu_\mu$. The bottom plot shows the remaining background, where a reconstructed $D^+_{(s)} \to \mu^+\nu_\mu$ decay is paired with a random photon, (excluding those in the upper plot). It is derived from the generic $c\bar{c}$ Monte Carlo sample.

6.7.4 Category IIc: Combinatoric Background

This background category includes all events which contain a real tag, and where the signal muon candidate is a misidentified charged pion, charged kaon, or proton. It also includes events where muons from in-flight decays of charged kaons and pions, $\pi^+/K^+ \to \mu^+\nu_\mu$, fake a signal. In studies of generic $c\bar{c}$ Monte Carlo events about 12 % of background signal candidates with $\Delta M < 350\,\mathrm{MeV}/c^2$ are found to belong to this category.

The ΔM distribution of signal candidates consists of two components. The first component are decays $D_s^{*+} \to \gamma D_s^+ \to \tau^+\nu_\tau$, with a subsequent τ-decay, $\tau^+ \to \bar{\nu}_\tau\pi^+(\pi^0)$, in which the π^+ is misidentified as muon. These events have been studied using a small Monte Carlo sample of $c\bar{c}$ events in which one charm quark fragments into a D_s^{*+} meson, which decays like $D_s^{*+} \to \gamma D_s^+ \to \tau^+\nu_\tau$, and the τ decays generically. The other charm quark fragments generically. This Monte Carlo sample represents only 25 % of the dataset, the limited sample size is countered by dropping the muon identification requirement. The events passing the selection are weighted by the rate at which pions are misidentified as muons, (Section 4.3.2). The ΔM distribution of this background is described by a Gaussian, (6.19), shown in the top plot of Figure 6.22.

$$\mathcal{PDF}_{\mathrm{fake}\,\pi\,\mathrm{from}\,\tau}(\Delta M|\mu,\sigma) = \frac{1}{\sqrt{2\pi}\sigma}e^{\frac{(\mu-\Delta M)^2}{2\sigma^2}} \tag{6.19}$$

The paramaters of $\mathcal{PDF}_{\mathrm{fake}\,\pi\,\mathrm{from}\,\tau}$, determined by a χ^2-fit, are

$$\mu = 133.3\,\mathrm{MeV/c^2} \;\text{ and }\; \sigma = 6.5\,\mathrm{MeV/c^2}\;. \tag{6.20}$$

The other event candidates that contribute to this background exhibit no peaking feature in the distribution of ΔM and are described by (6.21), shown in the bottom plot of Figure 6.22. These events are studied using the generic $c\bar{c}$ Monte Carlo simulated event sample. This background parameterization is already used to describe the random photon backgrounds in simulated signal events (6.12) and in purely muonic

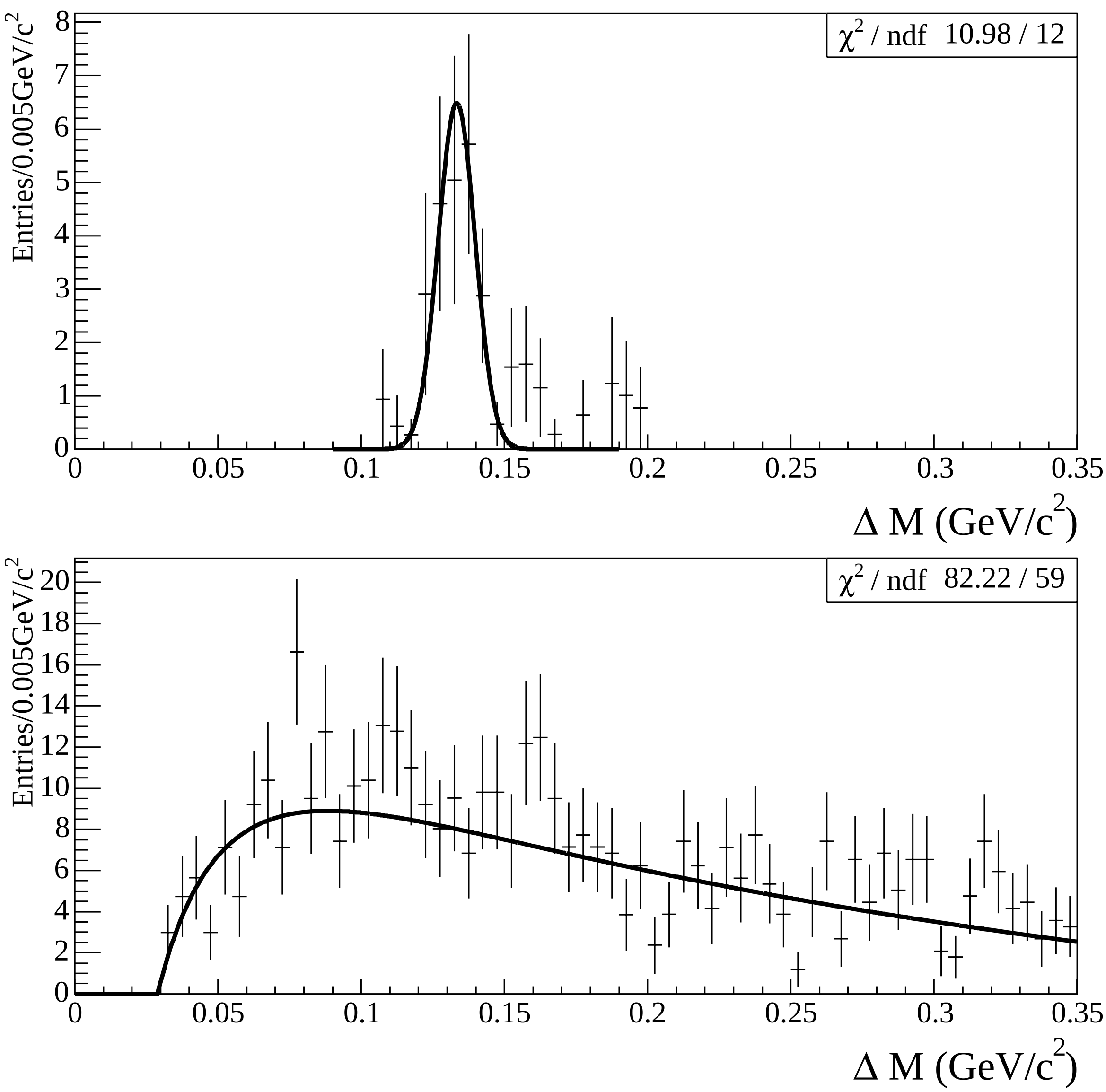

Figure 6.22: Distribution of ΔM of the two components of background Category IIc. The top plot shows candidates from the decays $D_s^{*+} \to \gamma D_s^+ \to \tau^+\nu_\tau$, with a subsequent τ-decay $\tau^+ \to \bar{\nu}_\tau\pi^+(\pi^0)$, in which the π^+ is misidentified as muon. It is determined in simulated $c\bar{c}$ events in which this mode recoils against a charm tag. The muon requirement is not applied, the events are weighted by the measured rate with which pions are misidentified as muons. The bottom plot contains the remaining background, correctly tagged events in which the signal muon is a misidentified $\pi^\pm$ or $K^\pm$. The events are selected in the generic $c\bar{c}$ Monte Carlo sample.

charm decays (6.18).

$$\mathcal{PDF}_{\mathrm{fake}\,\pi/\mathrm{K/p}}(\Delta M|\Delta M_0,a,b,c) = \left\{\left(1-e^{-\frac{\Delta M-\Delta M_0}{c}}\right)\left(\frac{\Delta M}{\Delta M_0}\right)^a + b\frac{\Delta M-\Delta M_0}{\Delta M_0}\right\} \tag{6.21}$$

The parameters of $\mathcal{PDF}_{\mathrm{fake}\,\pi/\mathrm{K/p}}$, determined by the fit, are

$$\Delta M_0 = 28.9\,\mathrm{MeV/c^2}\,,\ a=-0.642\,,\ b=-0.010\,,\text{ and } c=0.046\ . \tag{6.22}$$

6.7.5 Combined Background PDF

After the tag sideband and the electron-signal candidates are subtracted, different backgrounds remain. In the previous two sections the ΔM parameterizations of these different background contribution were introduced. Twice the same background parameterization was used to describe a random background, (6.18) and (6.21). The same function also describes the ΔM distribution of the random photon background in signal Monte Carlo events, given by (6.12). It is appropriate to combine all three backgrounds described by this same function into one, and describe their distribution by $\mathcal{PDF}_{\mathrm{comb}}$ (6.23).

$$\mathcal{PDF}_{\mathrm{comb}}(\Delta M|\Delta M_0,a,b,c) = \left(1-e^{-\frac{\Delta M-\Delta M_0}{c}}\right)\left(\frac{\Delta M}{\Delta M_0}\right)^a + b\frac{\Delta M-\Delta M_0}{\Delta M_0} \tag{6.23}$$

The parameters of $\mathcal{PDF}_{\mathrm{comb}}$, determined by a χ^2 fit (top plot of Figure 6.23), are

$$\Delta M_0 = 26.2\,\mathrm{MeV}/c^2\ \ a=-0.417\ \ b=-0.008\ \ c=0.047\ . \tag{6.24}$$

The entire background in Categories II(a)i and IIc, (bottom plot of Figure 6.23), is described by

$$\mathcal{PDF}_{\mathrm{total\ Bkgd}} = f_1\mathcal{PDF}_{\gamma\,\mathrm{from}\,\pi^0} + f_2\mathcal{PDF}_{\mathrm{fake}\,\pi\,\mathrm{from}\,\tau} + f_3\mathcal{PDF}_{\mathrm{comb}}\,, \tag{6.25}$$

where $\mathcal{PDF}_{\gamma\,\mathrm{from}\,\pi^0}$ and $\mathcal{PDF}_{\mathrm{fake}\,\pi\,\mathrm{from}\,\tau}$ are given in (6.16) and (6.19), respectively.

The parameters f_1, f_2 and f_3 are determined from the size of the three contributions, as shown in Figure 6.21 (top), Figure 6.22 (top), and Figure 6.23 (bottom). They are:

$$f_1 = 0.837\,,\ f_2 = 0.105\,,\ \text{and}\ f_3 = 59.6\ . \tag{6.26}$$

The f_i do not add up to one, since the function $\mathcal{PDF}_{\text{comb}}$ is not normalized, $\int_0^{0.35} \mathcal{PDF}_{\text{comb}}(\Delta M)\, d\Delta M \neq 1$.

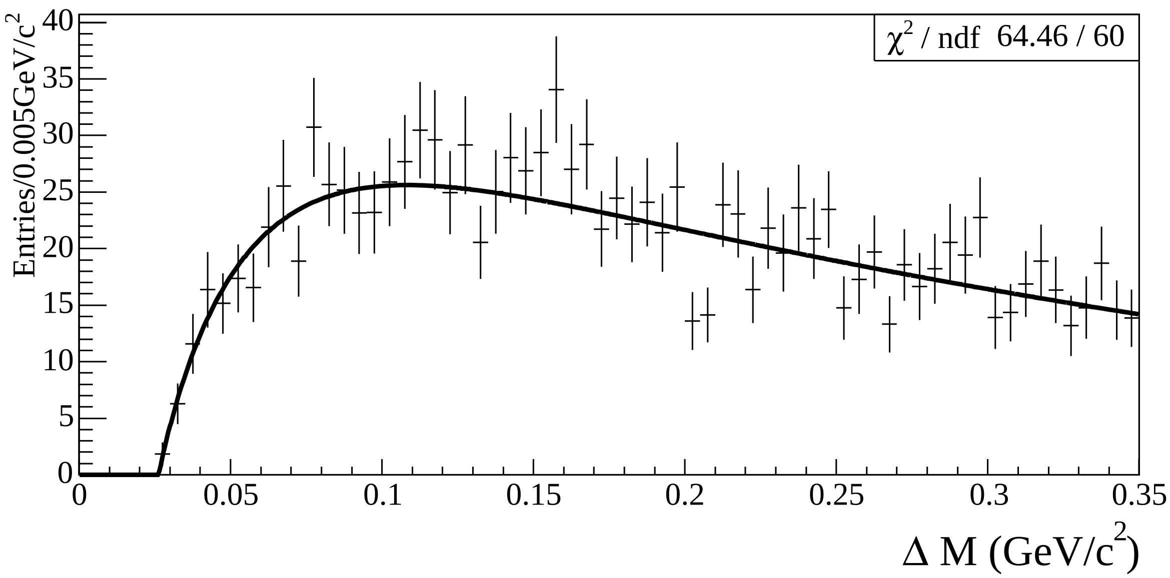

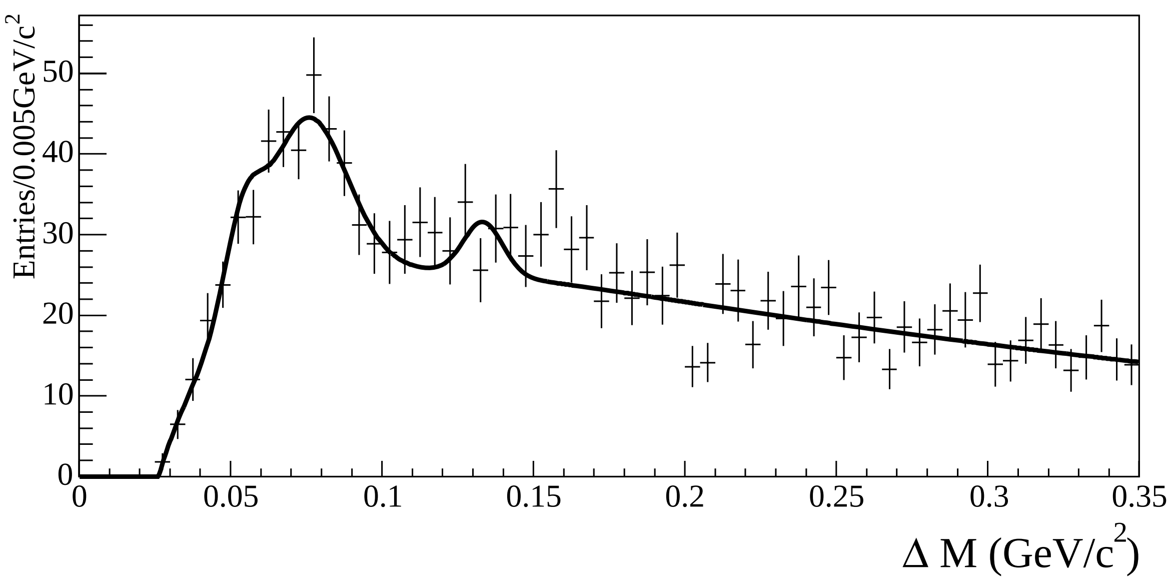

Figure 6.23: ΔM background distribution. The top plot shows the combination of all backgrounds that are described by the same function, as it is shown in Figure 6.14 (top), Figure 6.21 (bottom), and Figure 6.22 (bottom). The χ^2-fit of $\mathcal{PDF}_{\text{comb}}$ is applied. The bottom plot shows the combination of all backgrounds of Category II(a)i and Category IIc.

6.8 Monte Carlo – Data Comparison

One cannot expect the Monte Carlo and data tagging efficiency to agree very well for several reasons. As stated earlier, no PID correction on the particles that make up the tag has been applied. Inclusive charm production and decay is not completely understood and hence not accurately modeled in our Monte Carlo events. However, for this analysis the tagging efficiency does not need to be known very precisely; by taking the ratio of tagged $c\bar{c} \to D_s^{*+} \to \gamma D_s^+ \to \gamma\mu\nu$ to tagged $c\bar{c} \to D_s^{*+} \to \gamma D_s^+ \to \gamma\phi\pi$ event yields, the tagging efficiency cancels in first order.

It is however of importance to understand the manner with which the simulation of the signal impacts the analysis. For this reason the data control sample $D^{*0} \to \gamma D^0 \to \gamma K^- \pi^+$ is selected and studied. A second control sample is used to validate the electron-to-muon detection efficiency correction in data. This control sample consists of identified data events $D^{*+} \to \pi^+ D^0 \to \pi^+ K^- l^+ \nu_l$, where the symbol l stands for electrons and muons. Both control samples are selected in the recoil of a real tag, which implies the application of the tag-sideband subtraction.

6.8.1 Control Sample $D^{*0} \to \gamma D^0 \to \gamma K^- \pi^+$

Decays of the type $D^{*0} \to \gamma D^0 \to \gamma K^- \pi^+$ are used to study how well the variables that are used in the signal selection are modeled in the simulation, exploiting the kinematic similarity of the decays $D^0 \to K^- \pi^+$ and $D_s^+ \to \mu^+ \nu_\mu$. In this study the reconstruction of the neutrino momentum from the missing momentum is of particular interest. Since the reconstruction of the missing momentum involves the entire event, the study tests the simulation of the charm fragmentation process on the tagging and the signal side, as well as testing the simulation of the particle reconstruction efficiency and the detector acceptance. Since the decay widths of the D^0 and the D_s^+ are small compared to the detector resolution, the conclusions of the Monte Carlo – data comparisons of the control sample are valid for the signal decay $D_s^+ \to \mu^+ \nu_\mu$. The study would also reveal any large differences between the signal ΔM distribution in simulated events and in data.

In the sample of charm tagged events the decay chain $D^{*0} \to \gamma D^0 \to \gamma K^- \pi^+$ in

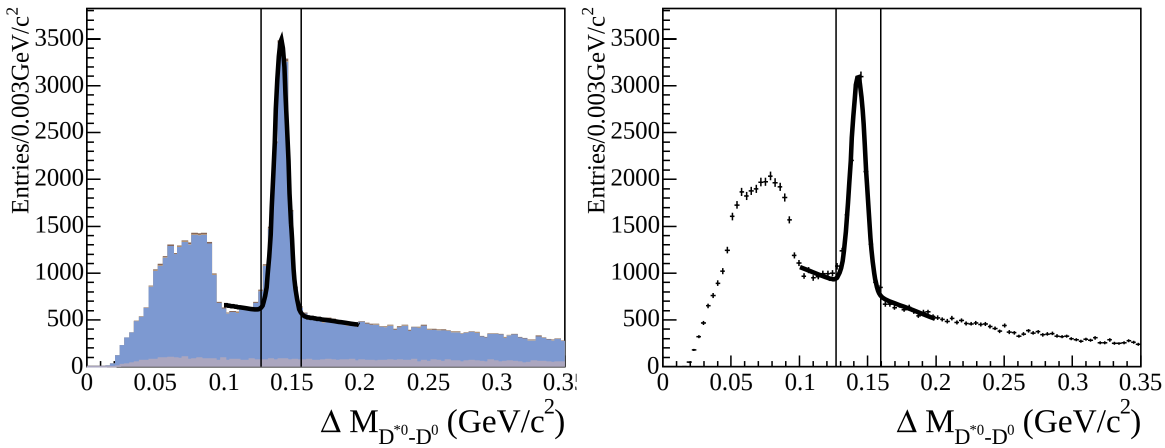

Figure 6.24: Selection of $D^{*0} \to \gamma D^0 \to \gamma K^-\pi^+$ in generic $c\bar{c}$ Monte Carlo events (left) and in data (right). Candidates within 3σ of the peak are selected for the control sample. Sidebands are defined between $4\,\sigma$ and $7\,\sigma$ on both sides of the peak.

the recoil of a tag is reconstructed. For the decay $D^0 \to K^-\pi^+$, the almost identical selection criteria as for the selection of the tag mode $D^0 \to K^-\pi^+$ (Section 5.3) are used. The exception is the requirement on the D^0 momentum, which is replaced by a requirement of a minimum kaon momentum of $1.2\,\mathrm{GeV}/c$ in the CM frame. This cut resembles the signal selection more closely, where a requirement on the muon momentum, ($p^*_\mu > 1.2\,\mathrm{GeV}/c$), but none on the D_s^+-momentum, is made.

In events with a reconstructed decay $D^0 \to K^-\pi^+$, that D^0 is not considered a tag candidate, but a candidate for the control sample; at least one other tag candidate must be present in the event. That depletes the tag samples of the tag mode $D^0 \to K^-\pi^+$, however, because of the independence of the tag from its recoil, this is a second order effect.

Candidate D^0 with a mass within 3 standard deviations of the esimated mean for the D^0 mass in reconstructed $D^0 \to K^-\pi^+$ decays are selected, (Table 5.3). The selection of photon candidates is described in Section 5.3. Photon candidates with a CM energy of more than $100\,\mathrm{MeV}$ are added to the D^0 candidates to form D^{*0} candidates. No mass constraint fit is applied on the D^0. Figure 6.24 shows the D^{*0}–D^0 mass difference, $\Delta M_{D^{*0}-D^0}$. The estimators for mean and width of the $\Delta M_{D^{*0}-D^0}$ signal peak, determined by a χ^2 fit of a Gaussian distribution, are listed in Table 6.8.

Table 6.8: Estimated yield, mean, and width of the D^{*0}–D^0 mass difference in decays $D^{*0} \to \gamma D^0 \to \gamma K^- \pi^+$, determined in generic Monte Carlo events and in data.

	Monte Carlo Events	Data
N	10224 ± 113	8916 ± 144
Mean μ	$(142.3 \pm 0.1)\,\mathrm{MeV}/c^2$	$(143.1 \pm 0.1)\,\mathrm{MeV}/c^2$
Standard Deviations σ	$(4.9 \pm 0.1)\,\mathrm{MeV}/c^2$	$(5.5 \pm 0.1)\,\mathrm{MeV}/c^2$

A requirement $|\Delta M_{D^{*0}-D^0} - \mu| < 3\,\sigma$ is made. This defines the events that comprise the control sample. Additionally, $\Delta M_{D^{*0}-D^0}$ sidebands are defined between 4 and 7 σ on either side of μ. These sidebands are used to describe the events that are background to the control sample.

The nominal muon mass is then assigned to the charged kaon candidate, while the charged pion is removed from the event. With the kaon assigned the muon identity and mass, the signal reconstruction is performed.

Figure 6.25 shows the distributions of the variables which are used in the signal selection, E^*_γ, $\cos(\mu, D_s^+)$, E^*_{miss}, p_{corr}, θ^*_ν, and $p^*_{D_s^*}$, as they are found in the control sample in generic Monte Carlo and in data. The $\Delta M_{D^{*0}-D^0}$ sidebands are subtracted in these distributions to remove events that are background to the control sample. These distributions are used later to estimate the systematic uncertainty in the signal selection efficiency.

The signal selection requirements are applied to the control sample events, reconstructed as a $D_s^+ \to \mu^+ \nu_\mu$ signal candidate. The signal ΔM distributions in simulation and data are compared at each selection step. No subtraction of $\Delta M_{D^{*0}-D^0}$-sideband sample is applied, since the ΔM and $M_{D^{*0}-D^0}$ are highly correlated, and the ΔM distribution of $M_{D^{*0}-D^0}$-sideband sample does not describe the ΔM distribution of the control sample background at all. The following $\mathcal{PDF}_{\mathrm{CS}\,1}$ is fitted to the ΔM

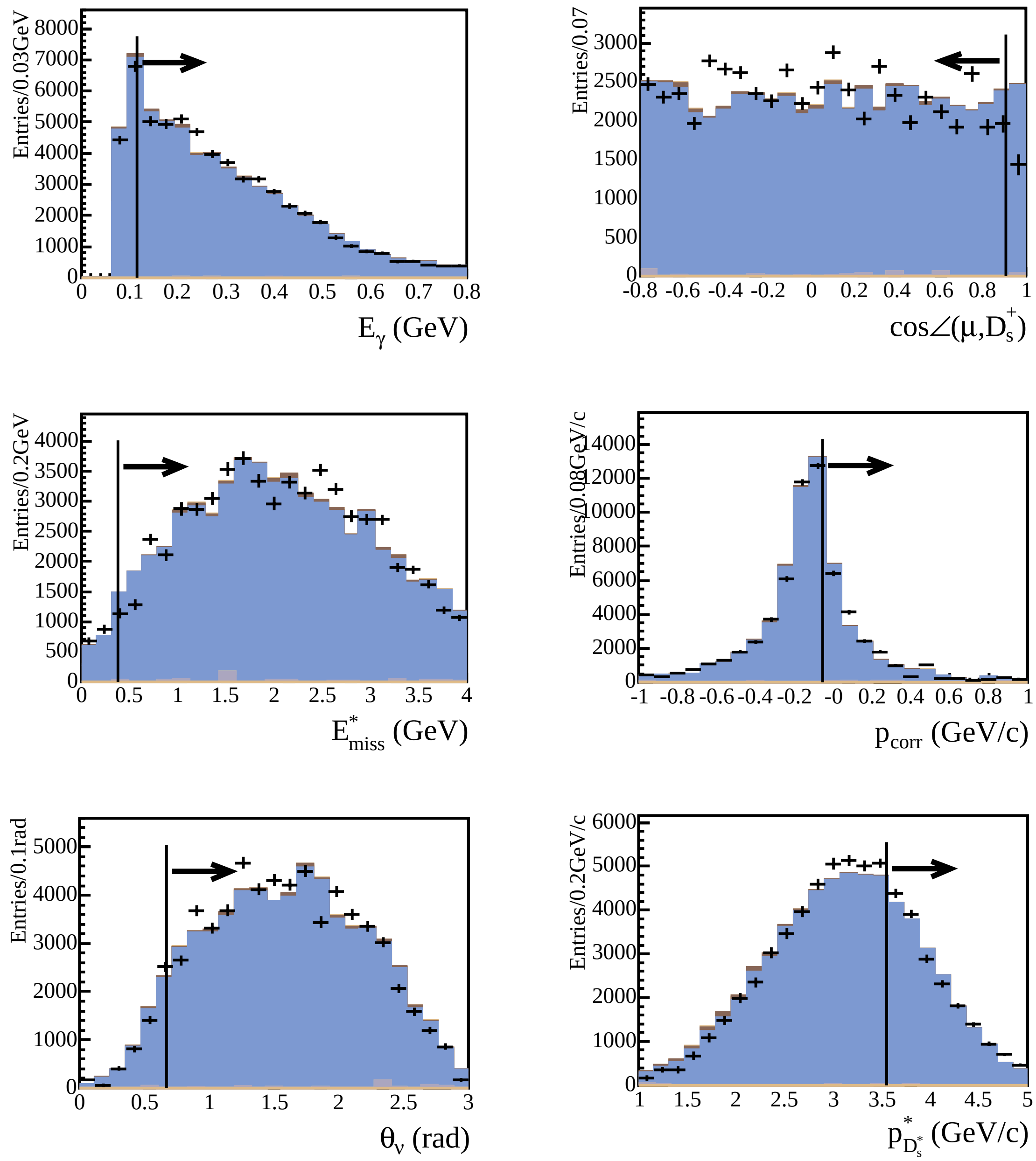

Figure 6.25: Distribution of the signal selection variables in the control sample $D^{*0} \rightarrow \gamma D^0 \rightarrow \gamma K^- \pi^+$. The solid histograms are generic Monte Carlo events, scaled to the data luminosity. The black markers are data, scaled to match the simulated events in area. The events in the $\Delta M_{D^{*0}-D^0}$ sidebands are subtracted.

distribution:

$$\mathcal{PDF}_{\mathrm{CS}\,1}(\Delta M|\mu,\sigma,\Delta M_0,a,b,c,f_{\mathrm{bkgd}}) = \\ \frac{1-f_{\mathrm{bkgd}}}{\sqrt{2\pi}\sigma}e^{-\frac{(\Delta M-\Delta M_0)^2}{\sigma^2}} + f_{\mathrm{bkgd}}\left(\left(1-e^{-\frac{x-\Delta M_0}{c}}\right)\left(\frac{x}{\Delta M_0}\right)^a + b\frac{x-\Delta M_0}{\Delta M_0}\right) \quad (6.27)$$

Table 6.9 and Table 6.10 show the development of the χ^2 fitted estimators for the mean and the width in Monte Carlo and data, as the selection progresses. Data shows a consistently higher mean (about 1.0 %) and width (about 2.5 %) than simulation.

These values do not change as the selection progresses, until the last selection requirement is applied. With the application of the last requirement, $p^*_{D_s^{*+}} > 3.55\,\mathrm{GeV}/c$, the mean is lowered by $2\,\mathrm{MeV}/c^2$ in both, simulated events and data. The width decreases by $2\,\mathrm{MeV}/c^2$ in simulated events and by $1\,\mathrm{MeV}/c^2$ in data. The discrepancy in width between Monte Carlo and data is 8 %. This artificial mismatch has its origin in the control sample selection requirements. Since events in the control sample are required to have a $\Delta M_{D^{*0}-D^0}$ consistent with a $D^{*0} \to \gamma D^0$ decay, the reconstructed ΔM distribution is artificially enhanced in the region around $145\,\mathrm{MeV}/c^2$. With the very selective requirement $p^*_{D_s^{*+}} > 3.55\,\mathrm{GeV}/c$, that background enhancement becomes even more pronounced. With the control sample background levels in Monte Carlo and in data being very different, the width of the ΔM peak is very different, the higher background level in data causing the wider ΔM distribution. The top plot of Figure 6.26 shows the fit to the ΔM distributions in Monte Carlo and in data, after all selection criteria but the last are applied. The bottom plot shows the fit on ΔM after all selection criteria are applied. With the control sample selection process being the origin of the sudden change in the mean and width of the ΔM peak, that effect is considered an artifact of the control sample selection. The estimated mean and width of the ΔM peak before the application of the cut $p^*_{D_s^{*+}} > 3.55\,\mathrm{GeV}/c$ are considered relevant. These values, obtained in simulation and data, will be used in later studies of the systematic uncertainty related to the simulated shape of the signal ΔM distribution.

Table 6.9: The ΔM signal mean μ with progressing selection in the $D^0 \to K^-\pi^+$ control sample.

Selection Cut	Fitted Mean μ [MeV/c^2]		
	Monte Carlo	Data	Ratio Data/MC
$E_\gamma < 115.0\,\mathrm{MeV}$	147.9 ± 0.2	149.1 ± 0.2	1.008 ± 0.002
$\cos(\mu, D_s^+) > 0.90$	147.6 ± 0.2	148.9 ± 0.3	1.009 ± 0.002
$E^*_{\mathrm{miss}} > 0.38\,\mathrm{GeV}$	147.5 ± 0.2	148.8 ± 0.3	1.008 ± 0.002
$p_{\mathrm{corr}} > -0.06\,\mathrm{GeV/c}$	147.5 ± 0.3	149.4 ± 0.4	1.013 ± 0.003
$\theta^*_\nu > 0.67$	147.5 ± 0.3	149.5 ± 0.4	1.013 ± 0.003
$p^*_{D_s^{*+}} > 3.55\,\mathrm{GeV/c}$	145.8 ± 0.4	147.0 ± 0.5	1.009 ± 0.004

Table 6.10: The ΔM signal width σ with progressing selection in the $D^0 \to K^-\pi^+$ control sample.

Selection Cut	Fitted Width σ [MeV/c^2]		
	Monte Carlo	Data	Ratio Data/MC
$E_\gamma < 115.0\,\mathrm{MeV}$	20.5 ± 0.2	20.8 ± 0.3	1.015 ± 0.018
$\cos(\mu, D_s^+) > 0.90$	21.0 ± 0.3	21.6 ± 0.3	1.027 ± 0.019
$E^*_{\mathrm{miss}} > 0.38\,\mathrm{GeV}$	21.2 ± 0.3	21.9 ± 0.3	1.033 ± 0.019
$p_{\mathrm{corr}} > -0.06\,\mathrm{GeV/c}$	19.1 ± 0.4	19.5 ± 0.4	1.023 ± 0.028
$\theta^*_\nu > 0.67$	18.7 ± 0.4	19.0 ± 0.4	1.016 ± 0.029
$p^*_{D_s^{*+}} > 3.55\,\mathrm{GeV/c}$	16.8 ± 0.4	18.2 ± 0.5	1.082 ± 0.038

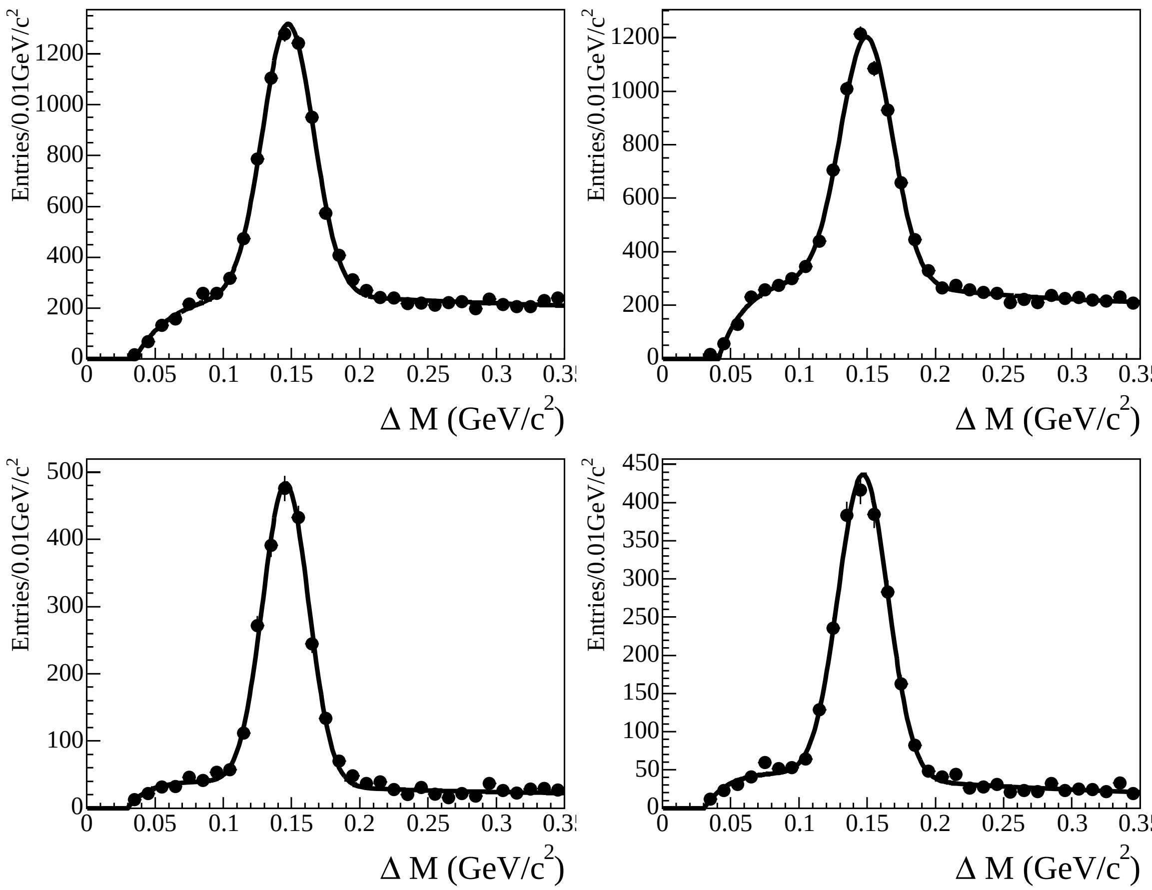

Figure 6.26: χ^2-fit of $\mathcal{PDF}_{\mathrm{CS}\,1}$ to the reconstructed signal ΔM distribution in the control sample $D^{*0} \rightarrow \gamma D^0 \rightarrow \gamma K^- \pi^+$ in simulated generic events (left) and in data (right). In the top plot all selection criteria but the last, ($p^*_{D_s^{*+}} > 3.55\,\mathrm{GeV}/c$), are applied, in the bottom all selection criteria are applied. The mean and width, estimated from the fit, are listed in Table 6.9 and Table 6.10. The sudden change in mean and width from the top to the bottom plot is an artifact of the control sample selection requirements.

The study of this control sample shows that the variables used in the signal selection are well described by the *BABAR* simulation. The Monte Carlo simulation of the signal decays can be trusted to predict the shape of the ΔM distribution correctly. The differences in the estimated mean and width that are found by this study are used to determine the systematic uncertainty arising from a wrongly modeled signal distribution.

6.8.2 Control Sample $D^{*+} \to \pi^+ D^0 \to \pi^+ K^- l^+ \nu_l$ with $l = \mu$, e

This control sample is designed to validate the electron-to-muon detection efficiency correction method on data, and hence to ensure the correctness of the subtraction of the background from semileptonic charm decays and from decays $\tau^+ \to \mu^+ \nu_\mu \bar{\nu}_\tau$.

The selection of the control sample proceeds as follows. In the charm tag sample the decay $D^{*+} \to \pi^+ D^0 \to K^- l^+ \nu$ with $l = \mu, e$ is reconstructed in the recoil of a charm tag. On the signal side, the kaon and the soft pion candidates are selected with the same requirements used for particles in the tag reconstruction, (Section 5.3). The muon candidate has to satisfy the same requirements as for the reconstruction of the signal, (Section 6.1). The electron candidate must fullfill the electron requirements that are mandated for the electron that replaces the muon in the semileptonic-background-subtraction sample, (Section 6.7.2). Bremsstrahlung recovery is applied to the electrons.

Kaon-muon and kaon-electron pairs of zero total charge are formed in the CM frame. The angle between the kaon and the lepton flight direction in the CM frame must be between 0.35 and 1.5 rad. The missing momentum, $\vec{p}_{\text{miss}}$, whose definition is described in Section 6.2, is used to define the missing four-momentum, $\breve{p}^0_{\text{miss}} = (|\vec{p}_{\text{miss}}|, \vec{p}_{\text{miss}})$, assuming zero missing mass. Boosted into the CM frame, the missing momentum has to be above $1\,\text{GeV}/c$. The missing CM four-momentum is added to the kaon-lepton pair to form D^0 candidates. The invariant mass $M(Kl\nu)$ is required to be between $1.8\,\text{GeV}/c^2$ and $2.1\,\text{GeV}/c^2$. The distributions of the reconstructed D^0 mass and of the angle between the kaon and the muon is shown in Figure 6.27.

A slow pion of opposite charge to the kaon and a CM momentum less than 450 MeV/c is added to form a D^{*+}. The reconstructed D^{*+}–D^0 mass difference, $\Delta M_{D^{*+}-D^0}$, is shown in Figure 6.28. Candidates that fullfill the requirement $\Delta M_{D^{*+}-D^0} < 0.155\,\mathrm{GeV}/c^2$ define the control sample.

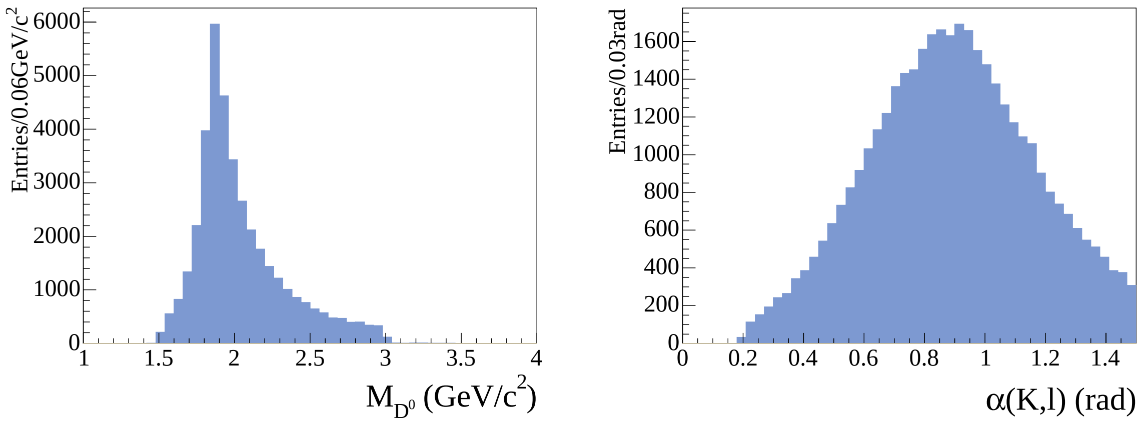

Figure 6.27: Distribution of the reconstructed D^0 mass (left) and the angle between the muon and the kaon (right) for true decays $D^{*+} \to \pi^+ D^0 \to \pi^+ K^- \mu^+ \nu_\mu$.

Simulated events of generic $c\overline{c}$, $B^0\overline{B}^0$, B^+B^-, and uds decays are used to verify the purity of the control sample – the percentage of $D^{*+} \to \pi^+ D^0 \to \pi^+ K^- l^+ \nu_l$ decays among the selected candidates. – The simulation predicts a purity of the control sample of 87.7 % in the muon mode and of 88.2 % in the electron mode, (Table 6.11). Most of remaining candidates in the control sample are other semileptonic charm decays, mostly decays $D^0 \to K^- l^+ \nu_l$ paired with a random slow π^+. However, those decays are equally valid to test the electron-to-muon PID efficiency correction. Therefore, the *semileptonic purity* – the percentage of semileptonic charm decays among the selected candidates – is defined. The semileptonic purity is found to be 96.5 % in the muon mode and of 98.4 % in the electron mode.

The control sample is selected from data. The *data-electron-to-muon PID weights*, as determined from the PID control samples in data, (Section 4.3), are applied to each candidate decay $D^{*+} \to \pi^+ D^0 \to \pi^+ K^- e^+ \nu_e$. The control sample is split into four distinct sets. The *tagged-muon-control* set contains control sample events with the tag being in the tag signal region and the control sample lepton being identified as

Table 6.11: Purity of the control sample $D^{*+} \to \pi^+ D^0 \to \pi^+ K^- l^+ \nu_l$, determined in simulated generic $c\bar{c}$, $B^0\overline{B}^0$, B^+B^-, and uds decays.

Decay	Muon	Electron
$D^{*+} \to \pi^+ D^0 \to \pi^+ K^- l^+ \nu_l$	87.7 %	88.2 %
Other semileptonic charm decays	8.8 %	10.2 %
Other decays	3.5 %	1.6 %

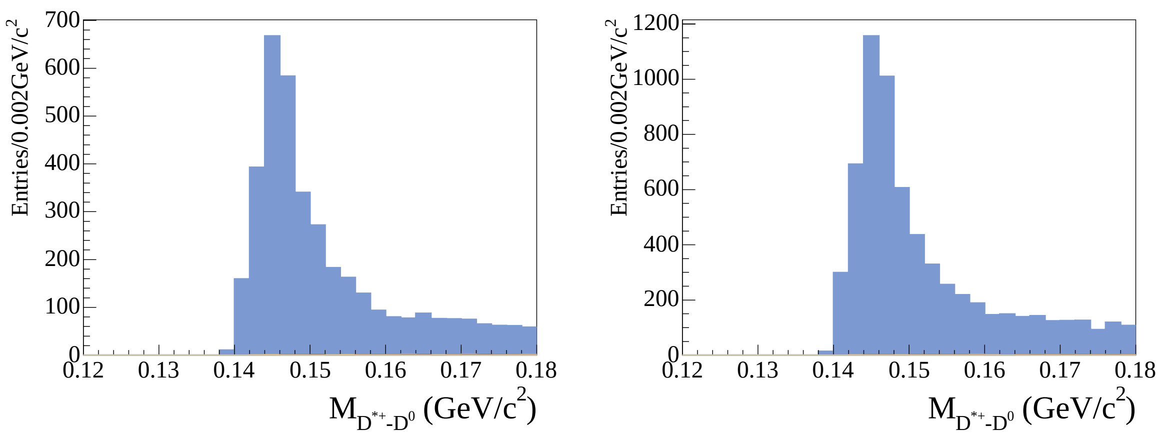

Figure 6.28: Distribution of $\Delta M_{D^{*+}-D^0}$ for $D^{*+} \to \pi^+ D^0 \to \pi^+ K^- \mu^+ \nu_\mu$ (left) and $D^{*+} \to \pi^+ D^0 \to \pi^+ K^- e^+ \nu_e$ (right), found in generic Monte Carlo in the recoil of a real tag.

a muon. In a similar manner the sets *tagged-electron-control*, *tag-sideband-muon-control*, and *tag-sideband-electron-control* are defined, each depending on the tag and the identity of signal lepton. The $\Delta M_{D^{*+}-D^0}$ distribution for all four sets is plotted in Figure 6.29. The *tag-sideband* sets are then subtracted from the *tagged* sets for both, muons and electrons; the resulting $\Delta M_{D^{*+}-D^0}$ distributions are shown in Figure 6.30. A phase space correction factor of 0.971 is applied to the electron distribution. Because of lepton universality the muon and the electron $\Delta M_{D^{*+}-D^0}$ distribution should be equal in shape and size. To compare the two, they are subtracted from each other, (Figure 6.31), and a good agreement between them is found. The difference is $\sum_{0.14<\Delta M<0.152} = 65 \pm 75$, consistent with 0.

The study of this control sample shows that the electron-to-muon PID efficiency correction method that is used in this analysis to subtract the semileptonic and $\tau^+ \to \mu^+\nu_\mu$ background components from the signal, works satisfactorily.

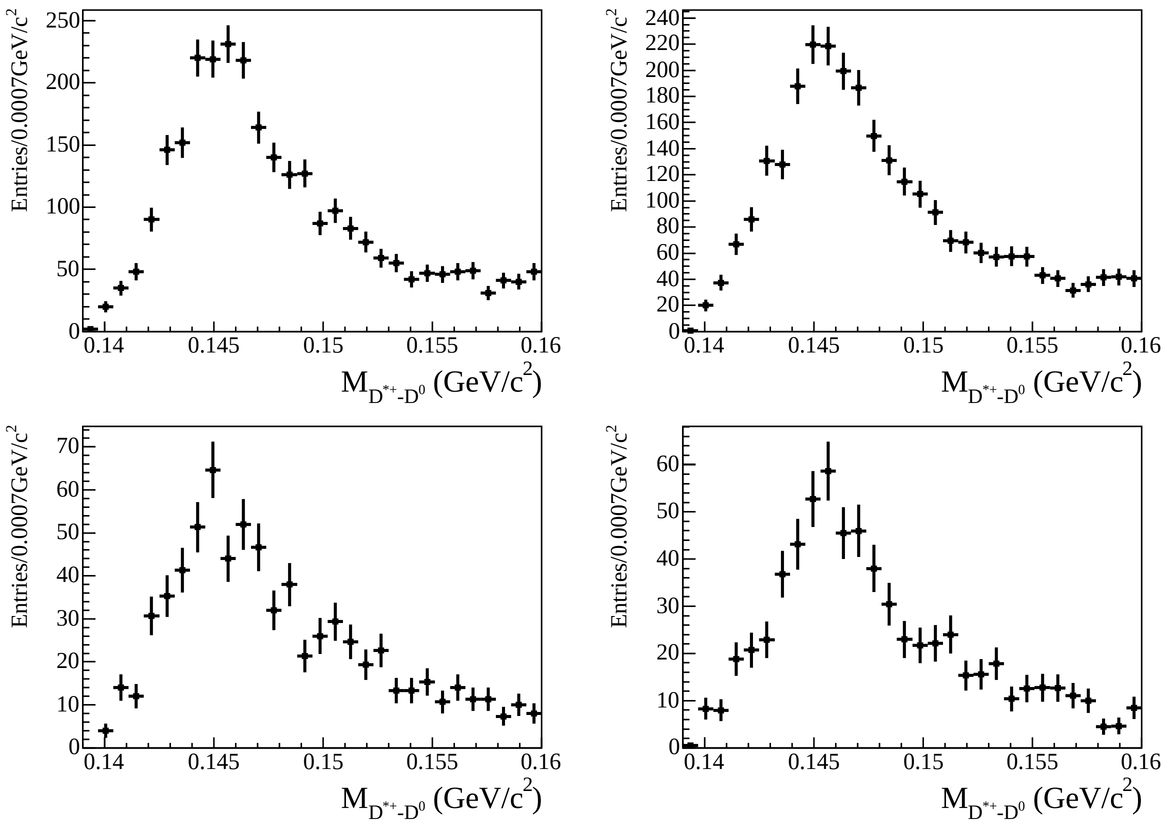

Figure 6.29: Distribution of $\Delta M_{D^{*+}-D^0}$ in the control sample $D^{*+} \to \pi^+ D^0 \to \pi^+ K^- l^+ \nu_l$, with $l = \mu$, e, in data. Shown are the distributions for the four distinct sets *tagged-muon-control* (top left), *tagged-electron-control* (top-right), *tag-sideband-muon-control* (bottom left), and *tag-sideband-electron-control* (bottom right). The sets consist of control sample events, with the tag being either in the signal or the tag sideband region, and the lepton in the $D^0 \to K^- l^+ \nu_l$ being either a muon or a electron. The data-electron-to-muon PID weights are applied to the electrons.

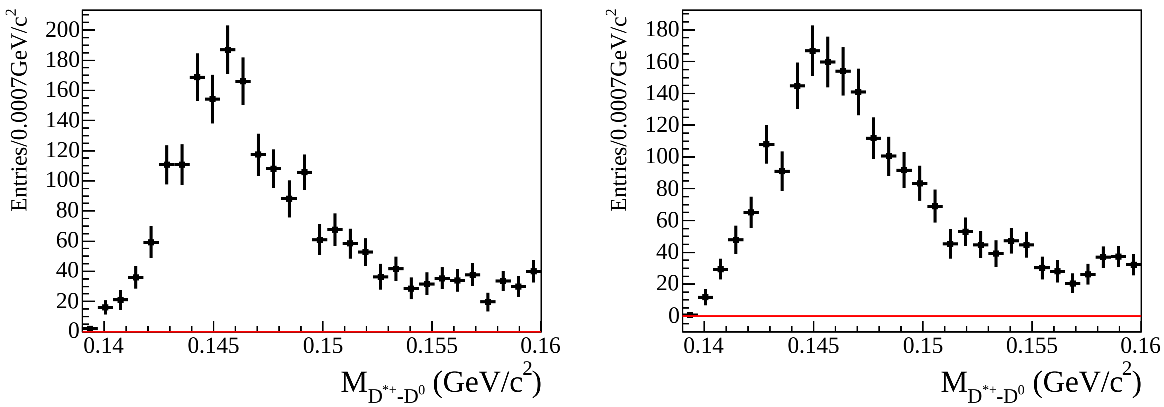

Figure 6.30: Distribution of $\Delta M_{D^{*+}-D^0}$ in the control sample $D^{*+} \to \pi^+ D^0 \to \pi^+ K^- l^+ \nu_l$, with $l = \mu$, e, in data. Shown are the distributions for $l = \mu$ (left) and $l = e$ (right) after the tag sidebands are subtracted. The data-electron-to-muon PID weights are applied to the electrons. The total numbers of events are $\sum_{0.14<\Delta M<0.152} = 1690 \pm 54$ for the muon sample and $\sum_{0.14<\Delta M<0.152} = 1674 \pm 52$ for the electron sample.

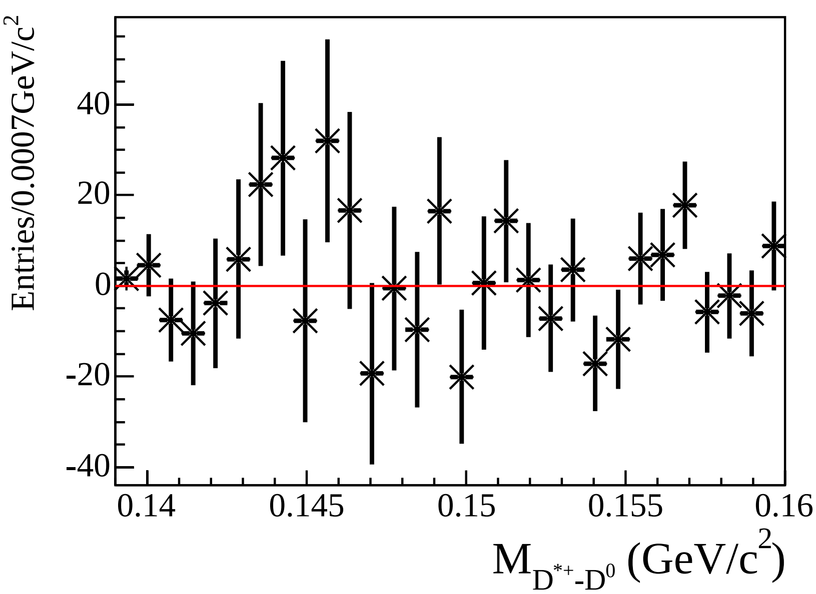

Figure 6.31: Difference in the $\Delta M_{D^{*+}-D^0}$ distribution between the $D^{*+} \to \pi^+ D^0 \to \pi^+ K^- \mu^+ \nu_\mu$ and the $D^{*+} \to \pi^+ D^0 \to \pi^+ K^- e^+ \nu_e$ decay. Before the subtraction the electron sample was scaled by 0.971 to correct for the larger electron phase space. The difference of the number of events is is $\sum_{0.14<\Delta M<0.152} = 65 \pm 75$, consistent with 0.

6.9 $D_s^{*\pm}$ Counting

To calculate the branching ratio $\mathcal{B}(D_s^{*+} \to \gamma D_s^+ \to \gamma\mu^+\nu)$, the total number of D_s^{*+} opposite the tag in the tag sample is needed. Its direct determination by the means of double tagging is not possible, since the *BABAR* experiment operates at an energy above the D_s^+ threshold, and the precise correlation between the particle content on the tag side and the signal side is lost.

The method used in this analysis is to reconstruct another well measured decay of the D_s^{*+} meson in the recoil of the tag. The observed rates of this decay, the *reference decay*, and the signal decay relate to each other like their branching ratios, after the different detection efficiencies in both decays are accounted for.

For this analysis the decay $D_s^{*+} \to \gamma D_s^+ \to \gamma\phi\pi^+$, with the ϕ decaying into a charged kaon pair, is used as the reference decay. The branching ratio, $\mathcal{B}(D_s^+ \to \phi\pi^+) = (4.81 \pm 0.52 \pm 0.38)\,\%$ [16], is large and known with a combined statistical and systematic precision of 13 %. The ϕ is reconstructed in its charged-kaon pair decay mode, for which the branching is $\mathcal{B}(\phi \to K^+K^-) = 0.491 \pm 0.006$.

This method has the advantage that most of the tag-related uncertainties cancel. Well chosen selection criteria for the reference decay potentially help to minimize the uncertainties from the modelling of the D_s^{*+} meson in the charm fragmentation process and the uncertainties related to the photon reconstrcution.

6.9.1 Reconstruction of the Decay $D_s^{*+} \to \gamma D_s^+ \to \gamma\phi\pi^+$

To study the reconstruction and to estimate the selection efficiency of this decay a dedicated Monte Carlo sample, the *$\phi\pi^+$-signal Monte Carlo sample*, is used, (Section 4.5).

ϕ-meson candidates are reconstructed in the decay $\phi \to K^+K^-$. ϕ mesons also decay into $K_L^0 K_S^0$ pairs, but the K_L^0 reconstruction is very imprecise. The requirements on the kaon candidates are identical to those used for the tag reconstruction, (Section 5.3). Pairs of oppositely charged kaons are combined in a vertex-constrained fit, (left plot in Figure 6.32). The fit probability must be above 0.0005. The mass of the fitted kaon pair, $M(K^+K^-)$, must be $|M(K^+K^-) - \mu_\phi| < 2\,\sigma_\phi$, where the mean,

μ_ϕ, and the width, σ_ϕ, are estimated from Gaussian fits to the mass peak of K^+K^- pairs in simulated $D_s^{*+} \to \gamma D_s^+ \to \gamma\phi(K^+K^-)\pi^+$ events and in data, Table 6.12. The fitted kaon pairs that fullfill these two criteria are considered as ϕ-meson candidates.

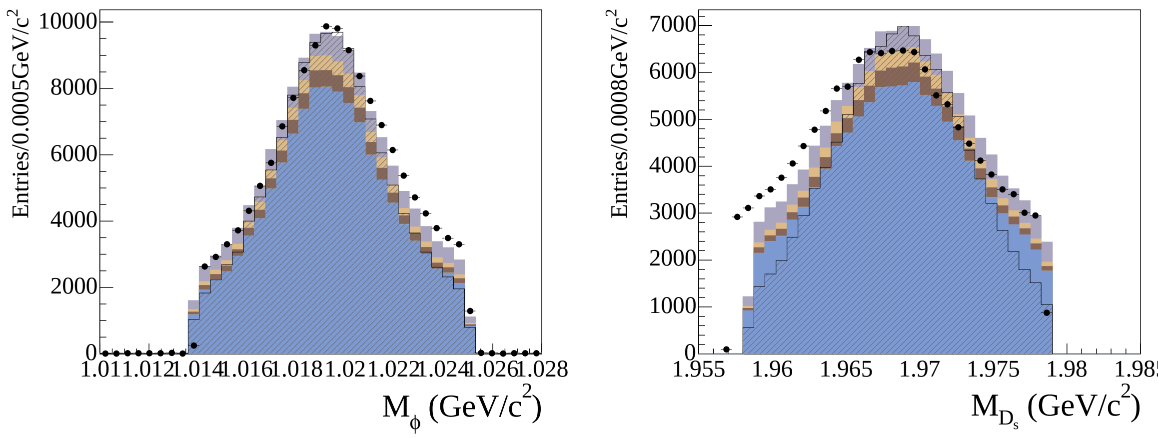

Figure 6.32: Distribution of the mass of ϕ meson candidates constructed from K^+K^- (left) and of the mass of D_s^+ candidates constructed from $\phi\pi^+$, determined in simulated $D_s^{*+} \to \gamma D_s^+ \to \gamma\phi\pi^+$ events and in generic Monte Carlo.

Charged-pion candidates have to fullfill the same charged-pion requirements used for the tag reconstruction. Charged-pion candidates are combined with the ϕ candidates and fit with a vertex constraint to form D_s^+ candidates. A fit probability requirement $P_{D_s^+} > 0.001$ is made, (left plot in Figure 6.33). The mass of fitted ϕ-π^+ pairs, $M(\phi\pi^+)$, is plotted for simulated $D_s^{*+} \to \gamma D_s^+ \to \gamma\phi(K^+K^-)\pi^+$ events and for data, (right plot in Figure 6.32). The estimated mean, $\mu_{D_s^+}$, and width, $\sigma_{D_s^+}$ are determined from a Gaussian fit to the mass peak, (Table 6.12). Pairs with a mass $M(\phi\pi^+)$ within $2\,\sigma_{D_s^+}$ of $\mu_{D_s^+}$ are considered D_s^+ meson candidates. Each D_s^+ meson candidate is weighted by the product of the *MC-to-data PID weights* for the two charged kaons and the charged pion that are used in the reconstruction, (Section 4.3) In addition, each D_s^+ candidate is weighted by the product of the *MC-to-data track weights* of the three D_s^+ daughter particles, to correct for the different track reconstruction efficiencies in simulated events and in data, (Section 4.4).

To form D_s^{*+} meson candidates, the D_s^+ meson candidates are combined with photon candidates that fulfill the same requirements as those used in the reconstruction of

Table 6.12: Mean and width of the mass distributions of the ϕ and the D_s^+ in simulated events and in data. The error of these values is of the order of 10^{-2} MeV/c^2.

	ϕ		D_s^+	
	μ_ϕ [MeV/c^2]	σ_ϕ [MeV/c^2]	$\mu_{D_s^+}$ [MeV/c^2]	$\sigma_{D_s^+}$ [MeV/c^2]
Simulation	1019.39	2.82	1968.65	5.10
Data	1019.53	2.76	1967.72	5.10

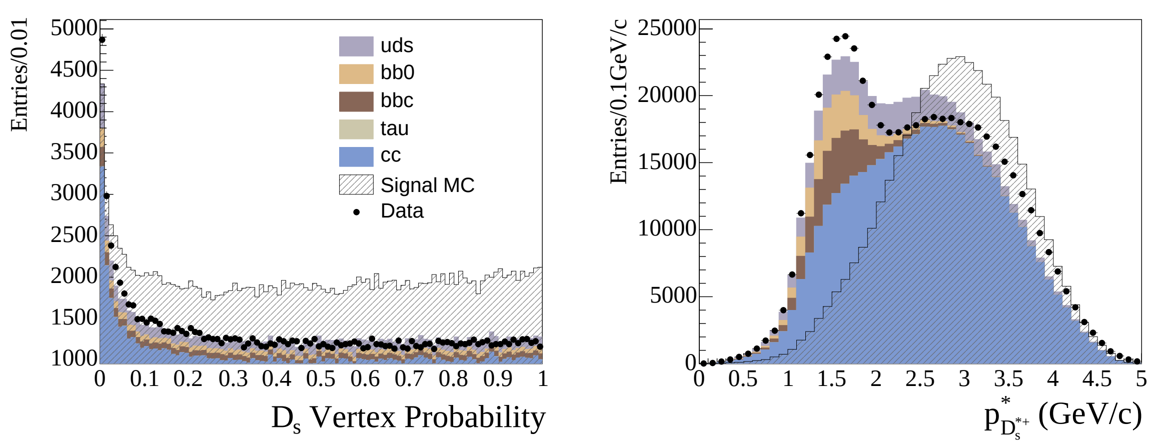

Figure 6.33: Distribution of the fit probability of the vertex constraint for the D_s^+ meson (left) and of the D_s^{*+} CM momentum (right), in simulated $D_s^{*+} \to \gamma D_s^+ \to \gamma\phi\pi^+$ events, in generic Monte Carlo samples, and in data.

Table 6.13: Selection efficiency for $D_s^{*\pm} \to \gamma D_s^{\pm} \to \gamma\phi(K^+K^-)\pi$

Selection Cut	Selection Efficiency		
	By Cut	Cumulative	
	[%]	[%]	[Events]
Tag	-	100.00 ± 0.00	22286
D_s^{*+} reconstructed	37.59 ± 0.18	37.60 ± 0.18	8378
$E_\gamma > 115\,\mathrm{MeV}$	95.76 ± 0.17	36.00 ± 0.17	8022
$p^*_{D_s^{*+}} > 3.55\,\mathrm{GeV/c}$	42.16 ± 0.13	15.18 ± 0.13	3382
True Signal	65.25 ± 0.11	9.90 ± 0.11	2207

the signal decay $D_s^{*+} \to \gamma D_s^+ \to \gamma\mu^+\nu$, (Section 6.1). This includes the requirement on the CM photon energy, $E^*_\gamma > 115\,\mathrm{MeV}$. The D_s^{*+} meson must have a minimum momentum in the CM frame, $p^*_{D_s^{*+}} > 3.55\,\mathrm{GeV/c}$, (right plot in Figure 6.33). Both requirement, on E^*_γ, and on $p^*_{D_s^{*+}}$, are identical to the selection requirement for the signal decay. This is to minimize the influence of the particular fragmentation model used in the simulation of the signal the reference decay on the branching ratio measurement. The selection efficiency in correctly tagged events, $\epsilon_{\phi\pi}$, is

$$\epsilon_{\phi\pi} = (9.90 \pm 0.11)\,\% \,. \tag{6.28}$$

The marginal efficiencies as the selection progresses are listed in Table 6.13.

The signature of the $D_s^{*+} \to \gamma D_s^+ \to \gamma\phi\pi^+$ decay is a peak at 145 MeV in the distribution of the reconstructed D_s^{*+}–D_s^+ mass difference, ΔM. The signal peak is described best by a triple-Gaussian distribution, $\mathcal{PDF}_{\phi\pi\,\mathrm{signal}}$:

$$\begin{aligned}&\mathcal{PDF}_{\phi\pi\,\mathrm{signal}}(\Delta M|\mu,\sigma_1,\Delta\mu_1,\sigma_2,\Delta\mu_2,\sigma_3,f_1,f_2)\\ &= \frac{f_1}{\sqrt{2\pi}\sigma_1}e^{-\frac{(\Delta M-\mu)^2}{2\sigma_1^2}} + \frac{f_2}{\sqrt{2\pi}\sigma_2}e^{-\frac{(\Delta M-\mu-\Delta\mu_1)^2}{2\sigma_2^2}} + + \frac{1-f_1-f_2}{\sqrt{2\pi}\sigma_3}e^{-\frac{(\Delta M-\mu-\Delta\mu_2)^2}{2\sigma_3^2}}\end{aligned} \tag{6.29}$$

The parameters of $\mathcal{PDF}_{\phi\pi\,\mathrm{signal}}$ are estimated from a fit to truth-matched $D_s^{*+} \to \gamma D_s^+ \to \gamma\phi\pi^+$ decays in the recoil of a real tag, using the dedicated Monte Carlo

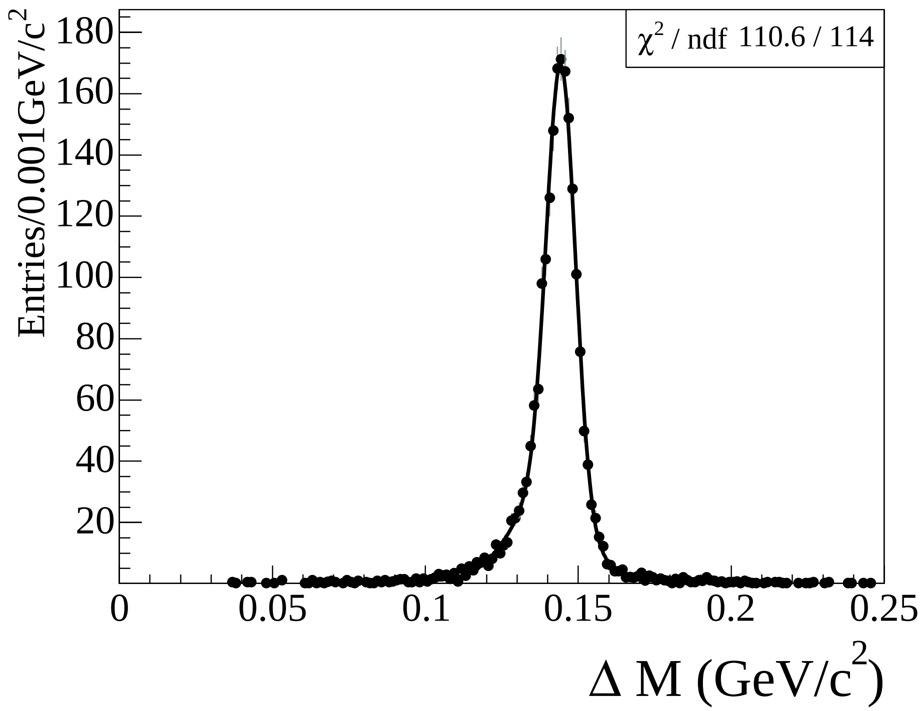

Figure 6.34: Signal ΔM distribution of truth-matched decays $D_s^{*+} \to \gamma D_s^+ \to \gamma\phi\pi^+$ in the recoil of a real tag, found in the $\phi\pi^+$-signal Monte Carlo sample.

sample, shown in Figure 6.34. They are

$$\begin{gathered}
\mu_1 = 144.3\,\mathrm{MeV/c^2}\,,\ \Delta\mu_1 = -4.9\,\mathrm{MeV/c^2}\,,\ \Delta\mu_2 = -6.7\,\mathrm{MeV/c^2} \\
\sigma_1 = 4.7\,\mathrm{MeV/c^2}\,,\ \sigma_2 = 11.2\,\mathrm{MeV/c^2}\,,\ \sigma_3 = 43.1\,\mathrm{MeV/c^2} \\
f_1 = 0.646\,,\ f_2 = 0.293
\end{gathered} \tag{6.30}$$

6.9.2 Background Estimation

The reference decay is analyzed to measure the number of produced D_s^{*+} mesons in the recoil of a true charm tag. Therefore the tag-sideband is subtracted in events with a reconstructed $D_s^{*+} \to \gamma D_s^+ \to \gamma\phi\pi^+$ decay. The sideband subtraction removes all sources of fake-tag backgrounds, but several types of charm decays in the recoil of a true tag remain as background to the $D_s^+ \to \phi\pi^+$ signal. Those are described in

Table 6.14: Decays of the D_s^+ meson into the final state $K^+K^-\pi^+$. The middle column lists the PDG branching ratio. The right column lists the relative size found in generic $c\bar{c}$ Monte Carlo events, scaled to the data luminosity. A total of 48 events of this background are expected.

D_s^+ Decay Mode	Branching Ratio PDG [30]	Relative Background Size
$D_s^+ \to f_0(980)\pi^+$, $f_0(980) \to K^+K^-$	$(4.9 \pm 2.3) \times 10^{-3}$	90 %
$D_s^+ \to K^+K^-\pi^+$	$(9 \pm 4) \times 10^{-3}$	9 %
$D_s^+ \to K^+\bar{K}^*(892)^0$	(3.3 ± 0.9) %	1 %

this section.

Background from $D_s^+ \to f_0(980)\pi^+$ and non-resonant $D_s^+ \to K^+K^-\pi^+$ decays

Besides the decay $D_s^+ \to \phi\pi^+$, the D_s^+ meson can also decay to $K^+K^-\pi^+$ through resonant $f_0(980)\pi^+$ or $K^+\bar{K}^*(892)^0$, or non-resonant decay. These three decays appear as background to the decay $D_s^+ \to \phi\pi^+$. The first column of Table 6.14 lists the branching ratio of each decay, none of which are well measured.

Since the mass of the reconstructed D_s^+ meson does not depend on the particular decay, these backgrounds are indistinguishable from the signal in the ΔM plot, (Figure 6.35). The requirement on the mass of the charged-kaon pair, to be consistent with a ϕ-meson decay, eliminates most of the backgrounds $D_s^+ \to K^+\bar{K}^*(892)^0$ and $D_s^+ \to K^+K^-\pi^+$. The decay $D_s^+ \to f_0(980)\pi^+$ poses a significant source of background, since the $f_0(980)$ meson has a width of 40–100 MeV/c^2 and is only 40 MeV/c^2 lighter than the ϕ-meson. Using generic $c\bar{c}$ Monte Carlo the relative size of the three background decay modes is determined, (last column in Table 6.14), with a total of $48 \pm 7_{\text{stat}} \pm 22_{\text{sys}}$ events to be expected in the data. The systematic uncertainty in this number comes from the poorly known branching ratio.

This background component is described by the distribution $\mathcal{PDF}_{\mathrm{K^+K^-\pi}}$, which is the same distribution that describes the $D_s^+ \to \phi\pi^+$ signal, $\mathcal{PDF}_{\phi\pi\,\mathrm{signal}}$ (6.29). For the extraction of the $D_s^+ \to \phi\pi^+$ yield in data the size of this background component is fixed at 0. For the extraction of the signal branching ratio, this background receives special attention, which is described in Section 7.4.

Other backgrounds

Another source of background with a distinct ΔM distribution is identified as decays $D_s^{*+} \to \pi^0 D_s^+ \to \pi^0 \phi \pi^+$, with the reconstructed signal photon candidate originating in the decay of the π^0 from the D_s^{*+} meson, (Figure 6.36). This background is best described by a single Gaussian:

$$\mathcal{PDF}_{\pi^0}(\Delta M|\mu,\sigma) = \frac{1}{\sqrt{2\pi}\sigma} e^{-\frac{(\Delta M-\mu)^2}{2\sigma^2}} \ . \tag{6.31}$$

The parameters of $\mathcal{PDF}_{\pi^0}$ are estimated from a χ^2 fit of the background, found in generic $c\bar{c}$ Monte-Carlo events in the recoil of a real tag:

$$\mu = 74.4\,\mathrm{MeV}/c^2\,, \text{ and } \sigma = 15.8\,\mathrm{MeV}/c^2\ . \tag{6.32}$$

The remaining background decays do not exhibit any peaking feature in the ΔM distribution. Their ΔM distribution is described by $\mathcal{PDF}_{\mathrm{rndm}}$:

$$\mathcal{PDF}_{\mathrm{rndm}}(\Delta M|\Delta M_0,a,b,c) = \left(1 - e^{-\frac{\Delta M - \Delta M_0}{c}}\right)\left(\frac{\Delta M}{\Delta M_0}\right)^a + b\frac{\Delta M - \Delta M_0}{\Delta M_0}\ . \tag{6.33}$$

However, the function fails to describe the left shoulder of the distribution. Therefore, all three background components are combined and fitted with the combined background PDF, $\mathcal{PDF}_{\phi\pi\,\mathrm{bkgd}}$ (6.31), where the components described by $\mathcal{PDF}_{\pi^0}$ and $\mathcal{PDF}_{\mathrm{rndm}}$ are allowed to vary in size, while the component $\mathcal{PDF}_{\mathrm{K^+K^-\pi}}$ is fixed.

$$\mathcal{PDF}_{\phi\pi\,\mathrm{bkgd}}(\Delta M) = f_{K^+K^-\pi}\mathcal{PDF}_{\mathrm{K^+K^-\pi}} + N_2(f\,\mathcal{PDF}_{\mathrm{rndm}} + (1-f)\mathcal{PDF}_{\pi^0})\ . \tag{6.34}$$

The parameters for $\mathcal{PDF}_{\phi\pi\,\mathrm{bkgd}}$, estimated in the χ^2 fit, are

$$\begin{gathered}\Delta M_0 = 26.8\,\mathrm{MeV/c^2}\,,\ a = -0.952\,,\ b = 0.006\,,\ c = 0.031\,,\\ f_{K^+K^-\pi^+} = 0.239\,,\ N_2 = 22.940\,,\text{ and } f = 0.936\ .\end{gathered} \tag{6.35}$$

in addition to (6.30) and (6.32).

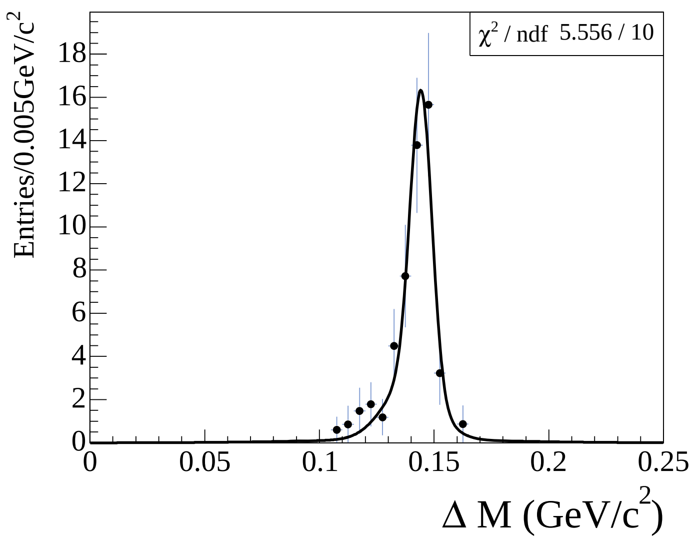

Figure 6.35: Simulated ΔM distribution from background decays $D_s^+ \rightarrow f_0(980)\pi^+$, $D_s^+ \rightarrow K^+K^-\pi^+$, and $D_s^+ \rightarrow K^+\bar{K}^*(892)^0$, where the D_s^+ originates in a decay $D_s^{*+} \rightarrow \gamma D_s^+$. The $c\bar{c}$ Monte Carlo is scaled to the data luminosity.

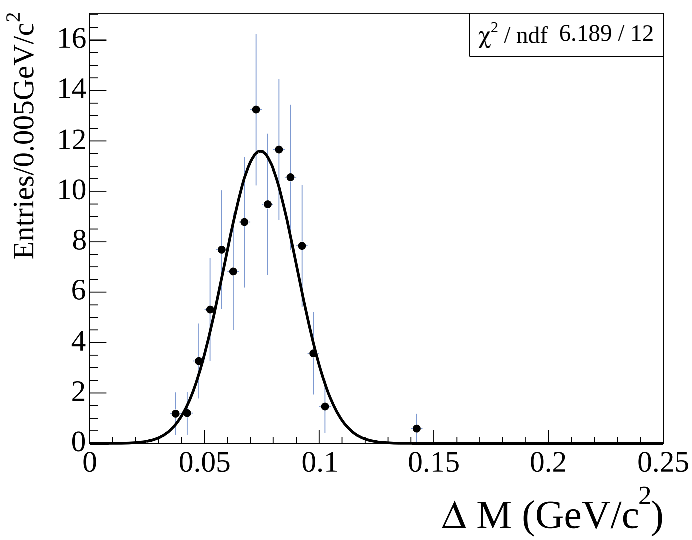

Figure 6.36: Simulated ΔM distribution from background decays $D_s^{*+} \rightarrow \pi^0 D_s^+ \rightarrow \phi\pi^+$, with the reconstructed photon candidate originating in the decay the π^0 from the D_s^{*+} meson. The $c\bar{c}$ Monte Carlo is scaled to the data luminosity.

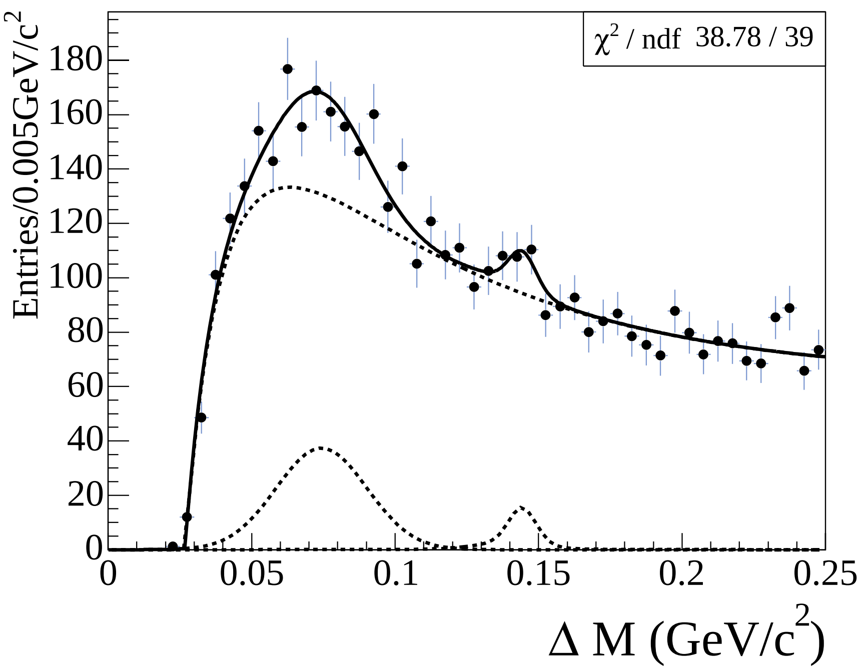

Figure 6.37: Distribution of ΔM for the combined background to the $D_s^{*+} \to \gamma D_s^+ \to \gamma\phi\pi^+$ signal, determined in generic $c\bar{c}$ Monte Carlo events. The function $\mathcal{PDF}_{\phi\pi\,\mathrm{bkgd}}$ is used to parameterize this distribution.

6.10 Tagging Efficiency Correction

The tagging efficiency is defined as the percentage of $e^+e^- \to c\bar{c}$ events that contain a correctly reconstructed tag.

To determine the relative branching fraction for the decays $D_s^+ \to \mu^+\nu_\mu$ and $D_s^+ \to \phi\pi^+$, this analysis measures the ratio of the rates of two decays in the recoil of a tag.

$$\frac{\mathcal{B}(D_s^+ \to \mu^+\nu_\mu)}{\mathcal{B}(D_s^+ \to \phi\pi^+)} = \frac{N_{\mu\nu,\,\mathrm{tag}}/(\epsilon_{\mu\nu} \times \epsilon_{\mathrm{tag}}^{\mu\nu})}{N_{\phi\pi,\,\mathrm{tag}}/(\epsilon_{\phi\pi} \times \epsilon_{\mathrm{tag}}^{\phi\pi})}\,, \tag{6.36}$$

where $N_{\mu\nu,\,\mathrm{tag}}$ and $N_{\phi\pi,\,\mathrm{tag}}$ are the numbers of events with the signal and the reference decay identified in the recoil of a real tag. $\epsilon_{\mu\nu}$ and $\epsilon_{\phi\pi}$ are the reconstruction and selection efficiencies of both decays, $\epsilon_{\mathrm{tag}}^{\mu\nu}$ and $\epsilon_{\mathrm{tag}}^{\phi\pi}$ are the tagging efficiencies the two decays in the recoil. If the tagging efficiency is independent of the decay in the tag recoil, $\epsilon_{\mathrm{tag}}^{\mu\nu}$ and $\epsilon_{\mathrm{tag}}^{\phi\pi}$ cancel.

A priori the tagging efficiency cannot be assumed to be independent of the recoiling decay. For example, the existence of two charged kaons in the reference decay $D_s^{*+} \to \gamma D_s^+ \to \gamma\phi(K^+K^-)\pi^+$, where the signal decay has none, leads to an increase in the tag-candidate multiplicity due to random tag combinations. This in turn lowers the chance of the correctly reconstructed tag candidate being selected as tag, which results in a lower tagging efficiency. Comparing the tagging efficiency in the two simulated event samples $D_s^{*+} \to \gamma D_s^+ \to \gamma\mu^+\nu$ and $D_s^{*+} \to \gamma D_s^+ \to \gamma\phi\pi^+$, the size of this effect is determined. Tables 6.15 and 6.16 show that the tagging efficiency in events containing a signal decay is $(3.54 \pm 0.02)\,\%$, and in events containing the reference decay $(3.49 \pm 0.01)\,\%$. This ratio will be applied as a correction factor, $R_\epsilon^{\mathrm{tag}}$, in the calculation of the branching ratio,

$$R_\epsilon^{\mathrm{tag}} = \frac{\epsilon_{\mathrm{tag}}^{\phi\pi}}{\epsilon_{\mathrm{tag}}^{\mu\nu}} = \frac{(3.49 \pm 0.01)\,\%}{(3.54 \pm 0.02)\,\%} = 0.986 \pm 0.006\,, \tag{6.37}$$

where the error is of purely statistical nature.

Table 6.15: Tagging efficiency in $c\bar{c}$ events containing the decay $D_s^{*+} \to \gamma D_s^+ \to \gamma\mu^+\nu$, determined in the signal Monte Carlo sample.

	Events	Tags	True Tags
MC sample	1284786		290403 (22.6%)
Preliminary Selection	1204005 (93.7%)		281351 (21.9%)
Peak or Sideband	110080 (8.57%)	125490	50472 (3.93%)
Best Tag (Peak or Sb)	110080 (8.57%)	110080	47655 (3.71%)
Tag (Peak)	71810 (5.59%)	71810	45463 (3.54%)

Table 6.16: Tagging efficiency in $c\bar{c}$ events containing the decay $D_s^{*+} \to \gamma D_s^+ \to \gamma\phi\pi^+$, determined in the $\phi\pi$-signal Monte Carlo sample.

	Events	Tags	True Tags
MC sample	2192000		496371 (22.6%)
Preliminary Selection	2160599 (98.6%)		492426 (22.5%)
Peak or Sideband	276796 (12.6%)	325131	86054 (3.93%)
Best Tag (Peak or Sb)	276796 (12.6%)	276796	80162 (3.66%)
Tag (Peak)	156234 (7.13%)	156234	76476 (3.49%)

6.11 Correction for the D_s^{*+} Momentum Spectrum

The fragmentation mechanism of $q\overline{q}$ quark pairs is qualitatively understood but still lacks a good qualitative description, for all energies and quark flavors. The momentum spectrum of D_s^{*+} mesons produced in $c\overline{c}$ events is not well simulated at *BABAR*, (Figure 6.38). The effect of this Monte-Carlo-data discrepancy on the measured branching ratio is studied in this section.

If the selection of signal or the $D_s^+ \to \phi\pi^+$ decay used requirements that are sensitive to the momentum of the D_s^{*+} meson, the simulated selection efficiencies would be very different from reality. Several strategies can be followed to minimize this effect with the premise that only the ratio of the selection efficiencies, $\epsilon_{\mu\nu}/\epsilon_{\phi\pi}$ enters in the result.

- The parameters of the fragmentation model that is implemented in JETSET could be tuned to produce distributions matching the *BABAR* data. The simulation would then correctly describe the data.
- The selection could rely entirely on quantities that do not depend on the D_s^{*+} momentum.
- The selection criteria of $D_s^{*+} \to \gamma D_s^+ \to \gamma\mu^+\nu$ and $D_s^{*+} \to \gamma D_s^+ \to \gamma\phi\pi^+$ decays could be defined in a way that the uncertainty in the true D_s^{*+} momentum distribution does not affect the efficiency ratio $\epsilon_{\mu\nu}/\epsilon_{\phi\pi}$, and hence the calculated branching ratio.

In this analysis the third approach of chosing matching selection criteria for the signal and the reference decay is followed. The signal selection relies on two quantities that are correlated with the momentum of produced D_s^{*+} meson, the reconstructed D_s^{*+} momentum and the photon energy, both in the CM frame:

$$p^*_{D_s^{*+}} > 3.55\,\mathrm{GeV/c}\,,\ \text{and}\ E^*_\gamma > 115\,\mathrm{MeV}\ .$$

Both requirements are applied identically in the selection of the reference decay $D_s^{*+} \to \gamma D_s^+ \to \gamma\phi\pi^+$. However, other signal selection cuts, like on the muon CM momentum and on the missing CM energy, which are correlated with D_s^{*+} momentum, have no equivalent in the $D_s^+ \to \phi\pi^+$ selection. To estimate how sensitive the calculated branching ratio is to the simulated D_s^{*+} meson momentum, the selection efficiencies for both processes are studied as a function of the hardness of the D_s^{*+} momentum spectrum.

First the size of the mismatch between the simulated and the data D_s^{*+} momentum spectra is determined. Data reconstructed decays $D_s^{*+} \to \gamma D_s^+ \to \gamma\phi\pi^+$ in tagged events are used to describe the D_s^{*+} momentum spectrum in data. To retrieve the spectrum below $3.55\,\mathrm{GeV}/c$, the D_s^{*+} momentum requirement is replaced by a cut on the pion CM momentum, $p^*_{\pi^+} > 0.8\,\mathrm{GeV/c}$. The tag sidebands are subtracted and a sample of $D_s^{*+} \to \gamma D_s^+ \to \gamma\phi\pi^+$ decays recoiling against a real charm tag is obtained. To further purify the D_s^{*+} sample, candidates in the sidebands of the $M(\gamma\phi\pi^+) - M(\phi\pi^+)$ distribution are subtracted. The resulting D_s^{*+} meson CM momentum distribution is corrected for the reconstruction efficiency in a momentum dependent manner. Here, the momentum-dependent reconstruction efficiency, $\epsilon(p^*_{D_s^{*+}})$ is determined in simulated $D_s^{*+} \to \gamma D_s^+ \to \gamma\phi\pi^+$ events, $p^*_{D_s^{*+}}$ is the true D_s^{*+} momentum. The resulting D_s^{*+} momentum distribution is compared to the distribution of the true momentum of D_s^{*+} mesons in simulated $D_s^{*+} \to \gamma D_s^+ \to \gamma\phi\pi^+$ decays in the recoil of a real tag, (Figure 6.38).

An empirical description of the data distribution, $\mathcal{PDF}_{\mathrm{Data}}$, is derived from the simulated spectrum, $\mathcal{PDF}_{\mathrm{MC}}$, by shifting the simulated true D_s^{*+} momentum, p, to a higher value, p':

$$p' = (\cos(0.23p) + 0.6) \times p^{0.1p+0.5} \tag{6.38}$$

The ratio of the measured to the simulated spectrum, $r(p)$, is defined:

$$r_p(p) = \frac{\mathcal{PDF}_{\mathrm{Data}}(p)}{\mathcal{PDF}_{\mathrm{MC}}(p)}, \tag{6.39}$$

which is shown in the lower plot of Figure 6.38. The data to Monte Carlo ratio r_p is used to reevaluate the selection efficiencies for the signal and the reference decay in tagged events, $\epsilon'_{\mu\nu}$ and $\epsilon'_{\phi\pi}$, respectively. This is done using the dedicated Monte

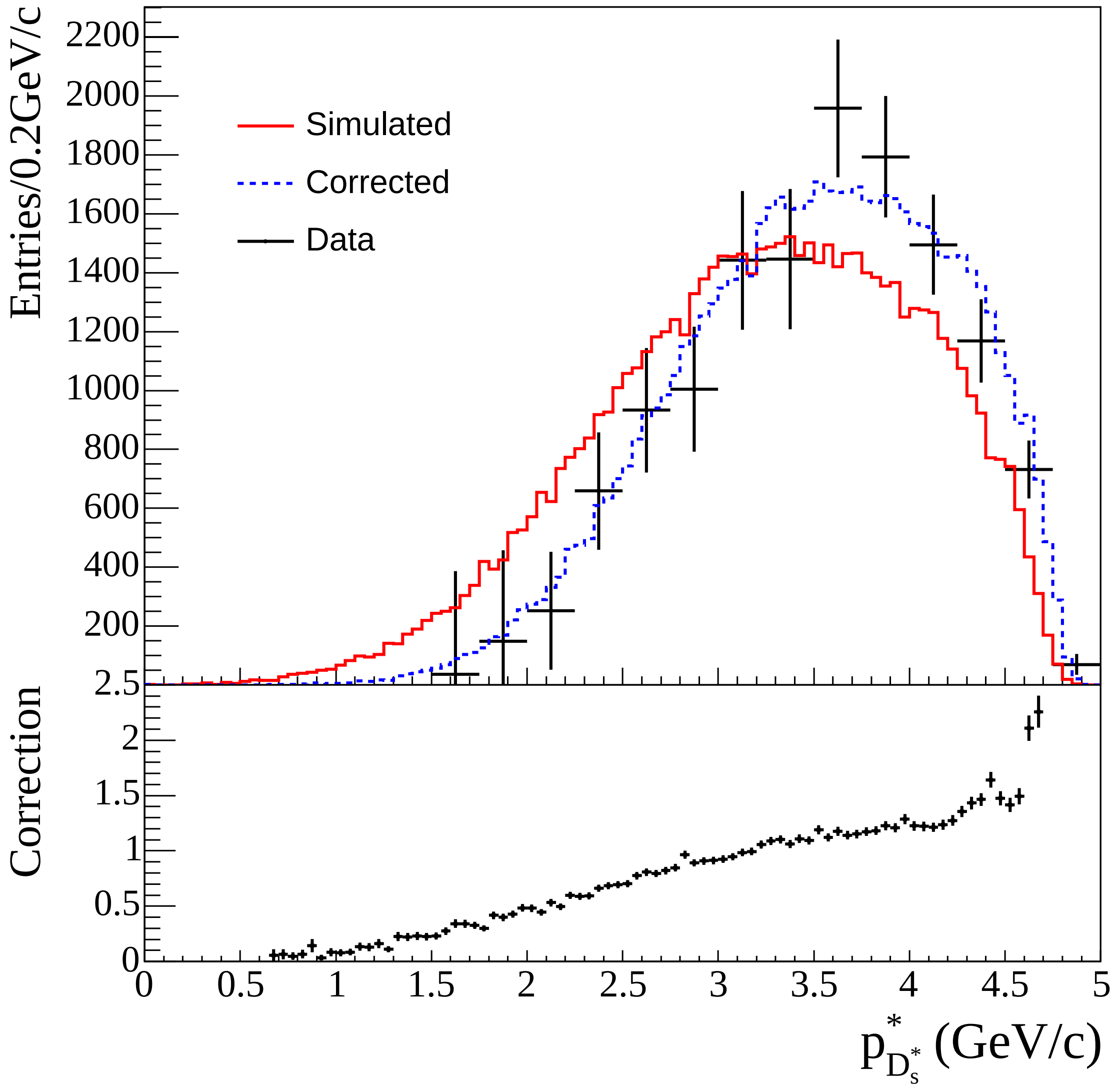

Figure 6.38: True D_s^{*+} CM momentum, $p^*_{D_s^{*+}}$, in simulated $D_s^{*+} \rightarrow \gamma D_s^+ \rightarrow \gamma\phi\pi^+$ events (solid red line), compared to the reconstructed D_s^{*+} CM momentum in data (black marker). An empirical shift is applied to the simulated momentum to obtain a data-matching momentum distribution (blue dashed line). The bottom plot shows the ratio $r(p^*_{D_s^{*+}})$ of the corrected (shifted) spectrum that matches the data, and the simulated spectrum of $p^*_{D_s^{*+}}$.

Table 6.17: Selection efficiency of $D_s^{*+} \to \gamma D_s^+ \to \gamma\mu^+\nu$ and $D_s^{*+} \to \gamma D_s^+ \to \gamma\phi\pi^+$ decays with the simulated and the data-adjusted D_s^{*+} momentum spectrum, measured in Monte Carlo events of both decays. Efficiencies are expected to be about 30 % larger in data. Their ratio, r_ϵ, which enters the calculation of the branching ratio, changes only slightly.

	Uncorrected	Corrected
$D_s^{*+} \to \gamma D_s^+ \to \gamma\phi\pi^+$	$\epsilon = 9.90\,\%$	$\epsilon' = 13.09\,\%$
$D_s^{*+} \to \gamma D_s^+ \to \gamma\mu^+\nu$	$\epsilon = 8.13\,\%$	$\epsilon' = 10.60\,\%$
Efficiency ratio $r_\epsilon = \epsilon_{D_s^+\to\phi\pi^+}/\epsilon_{D_s^+\to\mu^+\nu_\mu}$	$r_\epsilon = 1.22$	$r'_\epsilon = 1.23$

Carlo event samples of the signal and the reference decay. The momentum-spectrum-corrected efficiencies are calculated according to:

$$\epsilon' = \frac{\sum\limits_{\substack{\text{real-tag events}\\ \text{selected signal}}} r_p(p^*_{D_s^{*+}})}{\sum\limits_{\text{real-tag events}} r_p(p^*_{D_s^{*+}})}\,, \tag{6.40}$$

where $p^*_{D_s^{*+}}$ is the true momentum of the D_s^{*+} meson in the simulated $D_s^{*+} \to \gamma D_s^+ \to \gamma\mu^+\nu$ or $D_s^{*+} \to \gamma D_s^+ \to \gamma\phi\pi^+$ decays in the two Monte Carlo samples. The resulting shift in the efficiencies and in their ratio, r_ϵ, is summarized in Table 6.17. It shows that the selection efficiencies of each decay by itself depends strongly on the momentum spectrum, however, the relevant efficiency ratio is almost unaffected. A correction factor $C_{p(D_s^{*+})}$ is defined

$$C_{p(D_s^{*+})} = \frac{r'_\epsilon}{r_\epsilon} = \frac{\epsilon'_{\phi\pi}\epsilon_{\mu\nu}}{\epsilon'_{\mu\nu}\epsilon_{\phi\pi}} = 1.014 \tag{6.41}$$

and applied in the calculation of the $D_s^+ \to \mu^+\nu_\mu$ branching ratio.

Part IV

Results

Chapter 7

Results

In the previous chapter the reconstruction and selection of the signal and the $\phi\pi$-reference decay in tagged events were described, and the efficiency of the selection determined. The backgrounds to both decays were identified, and, if their contribution is not estimated from data, their ΔM distributions were parameterized.

In this chapter these results are combined to determine the branching ratio of the decay $D_s^+ \to \mu^+\nu_\mu$. First, the number of signal and reference decays, $N_{\mu\nu}$ and $N_{\phi\pi}$, in the recoil of a real tag is measured in data. Next, the systematic uncertainties in this ratio are discussed. In the final section, using the efficiencies for the selection of the two decays, the tagging efficiency correction, $R_\epsilon^{\mathrm{tag}}$, and the momentum spectrum correction, $C_{p(D_s^{*+})}$, the ratio of the partial widths,

$$\frac{\Gamma(D_s^+ \to \mu^+\nu_\mu)}{\Gamma(D_s^+ \to \phi\pi^+)} = \frac{N_{\mu\nu}/\epsilon_{\mu\nu}}{N_{\phi\pi}/\epsilon_{\phi\pi}} \times R_\epsilon^{\mathrm{tag}}\, C_{p(D_s^{*+})}\,, \tag{7.1}$$

is determined. The branching ratio $\mathcal{B}(D_s^+ \to \phi\pi^+)$ is used to determine $\mathcal{B}(D_s^+ \to \mu^+\nu_\mu)$ and, given the lifetime of the D_s^+ meson and the CKM-matrix parameter V_{cs}, the decay constant f_{D_s} is calculated. The implications of this measurement are discussed in the next chapter.

7.1 Signal Yield in Data

In data events tag candidates are reconstructed and a tag is identified, either in the tag signal or the tag sidebands region. Tags in the tag sidebands are weighted by $\frac{2}{3}$ to accommodate the larger size of the sidebands. In these tagged events the signal decay $D_s^{*+} \to \gamma D_s^+ \to \gamma\mu^+\nu$ is reconstructed and selected in the recoil of the tag. In addition, the signal reconstruction and selection is performed with the electron requirement substituting the muon requirement. The electron-selected candidates are weighted by a data-derived *data-electron-to-muon PID weights*. Another factor of 0.971 is applied to correct for the differences in the muon and the electron phase-space in charm and τ decays, (Table 6.6). This defines four exclusive sets, the *tagged-muon*, *tagged-electron*, *tag-sideband-muon*, and *tag-sideband-electron* set. The ΔM distributions for all four sets are shown in Figure 7.1. The *tag-sideband* sets are then subtracted from the *tagged* sets for both, muons and electrons; the resulting ΔM distributions are shown in Figure 7.2. The ΔM distribution for the sideband subtracted *electron* set is then subtracted from that of the *muon* set. A χ^2-fit of the function $\mathcal{PDF}_{\mu\nu}$ is performed, (Figure 7.3). The function is

$$\mathcal{PDF}_{\mu\nu}(\Delta M) = N_{\mu\nu} \times \mathcal{PDF}_{\mu\nu\,\mathrm{signal}}(\Delta M) + f_{\mathrm{bkgd}}\mathcal{PDF}_{\mathrm{total\ Bkgd}}(\Delta M)\,, \tag{7.2}$$

with $\mathcal{PDF}_{\mu\nu\,\mathrm{signal}}$ given by (6.10) with the parameters (6.11), and $\mathcal{PDF}_{\mathrm{totalBkgd}}$ given by (6.25) with the parameters (6.20), (6.17), and (6.24). The fit yields

$$N_{\mu\nu} = 489 \pm 55 \tag{7.3}$$

events, where the error is the statistical error, determined in the fit. The fit has a χ^2 per degree of freedom of 31.4/22, which corresponds to a fit probability of 8.9 %.

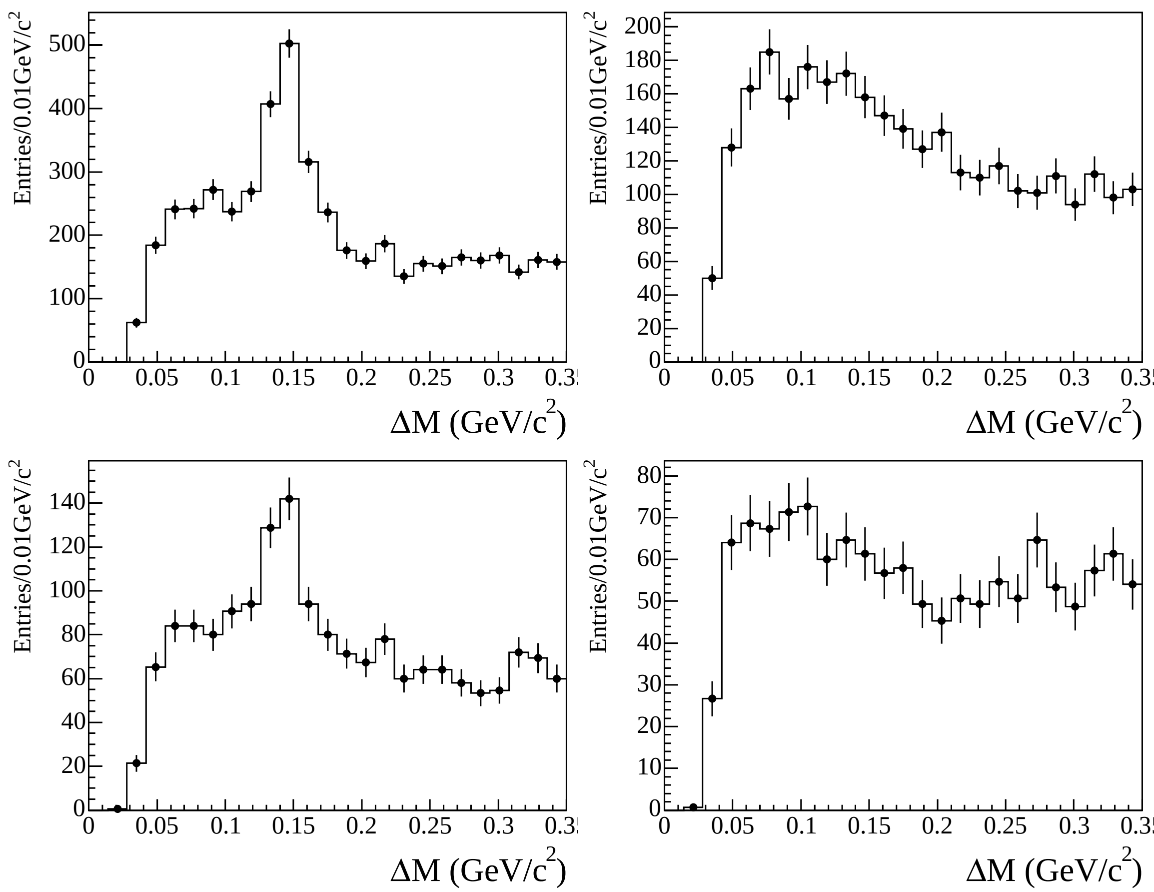

Figure 7.1: Distribution of ΔM in data for the four signal selection sets *tagged-muon* (top left), *tagged-electron* (top right), *tag-sideband-muon* (bottom left), and *tag-sideband-electron* (bottom right). The events in the electron sets are weighted by the *data-electron-to-muon weights*. The *sideband* sets are scaled by a $\frac{2}{3}$ to account for the tag sidebands being 50 % wider than the signal region.

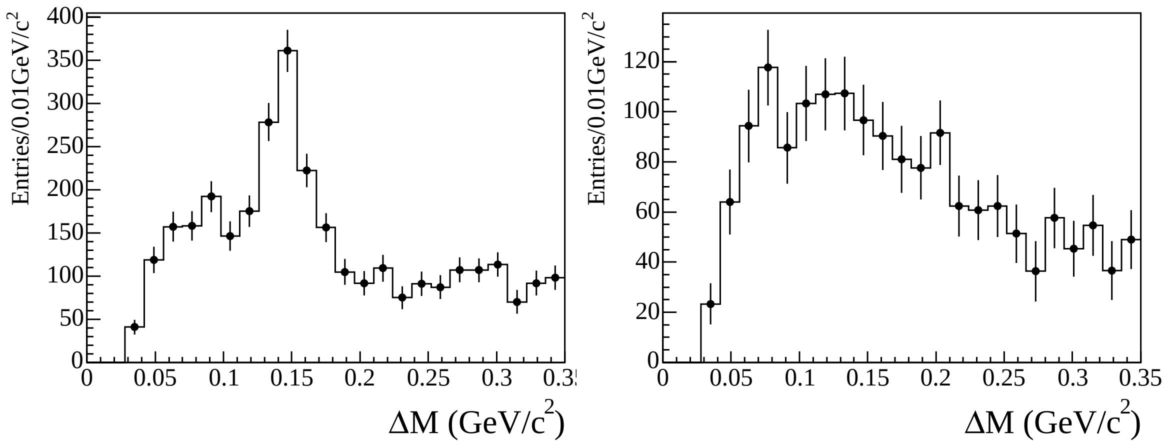

Figure 7.2: Distribution of ΔM in data after the tag-sidebands subtraction for muons (left) and electrons (right).

7.2 Yield of $D_s^{*+} \to \gamma D_s^+ \to \gamma\phi\pi^+$ in Data

In the same data sample of selected tagged events, the decay $D_s^{*+} \to \gamma D_s^+ \to \gamma\phi\pi^+$ in the recoil of the tag is reconstructed and selected. The reconstructed decay candidates are divided into two sets, the *tagged-*$\phi\pi$ and the *tag-sideband-*$\phi\pi$ set, depending on whether the tag lies in the tag signal or sidebands region. The sideband set is scaled by $\frac{2}{3}$ to accommodate for the 50 % wider tag-sidebands compared to the width of the tag signal region. The distributions of ΔM for both sets are shown in Figure 7.4. The *tag-sideband-*$\phi\pi$ subtracted from the *tagged-*$\phi\pi$ set, the resulting distribution of ΔM is shown in Figure 7.5. The following PDF is fitted to the ΔM-distribution:

$$\mathcal{PDF}_{\phi\pi} = N_{\phi\pi} \times \mathcal{PDF}_{\phi\pi\mathrm{signal}}(\Delta M) + f_{\phi\pi\ \mathrm{bkgd}}\mathcal{PDF}_{\phi\pi\mathrm{bkgd}}(\Delta M)\,, \tag{7.4}$$

in which $\mathcal{PDF}_{\phi\pi\mathrm{signal}}$ is given by (6.29) and $\mathcal{PDF}_{\phi\pi\mathrm{bkgd}}$ is given by (6.34). The parameters for the signal PDF are given by (6.30), and for the background by (6.30), (6.32), and (6.35).

The following parameters are allowed to float in the χ^2 fit; from the signal PDF μ (6.30), and from the background PDF, ΔM_0, a, b, and c (6.35). The contribution of the non-resonant and $f_0\pi^+$ background, which peaks under the signal, is fixed at $N_{K^+K^-\pi} = 0$. The χ^2-fit (Figure 7.5) yields

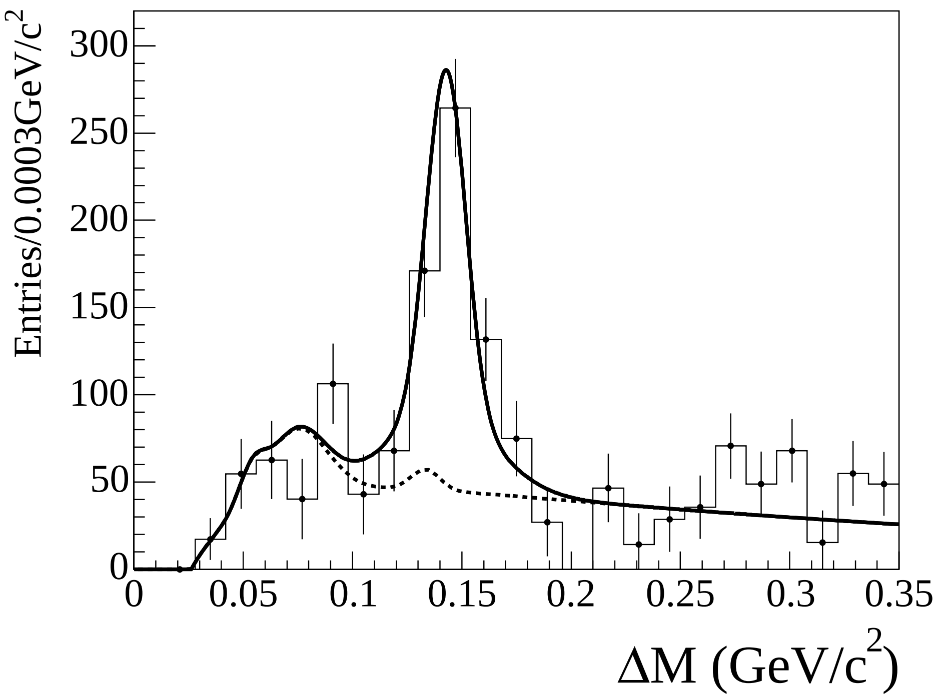

Figure 7.3: Distribution of ΔM after electron subtraction. The χ^2-fit of $\mathcal{PDF}_{\mu\nu}$ yields 489 ± 55 signal $D_s^{*+} \to \gamma D_s^+ \to \gamma\mu^+\nu$ events in the recoil of a real tag.

$$N_{\phi\pi} = 2093 \pm 99 \tag{7.5}$$

events, where the error given is statistical. The χ^2 per degree of freedom is 42.4/37. This corresonds to a fit-probability of 25.0 %.

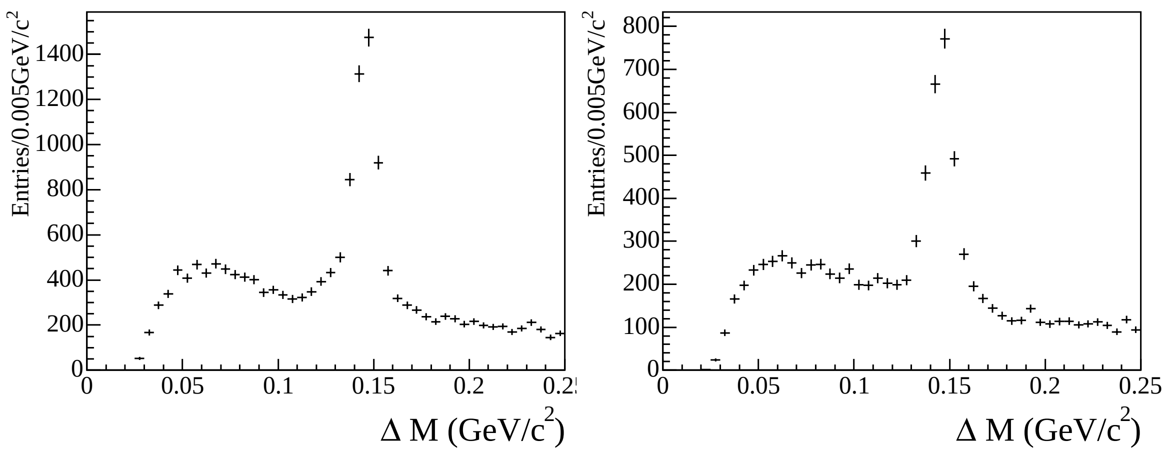

Figure 7.4: Distribution of ΔM for selected $D_s^{*+} \to \gamma D_s^+ \to \gamma\phi\pi^+$ decays in tagged events data, for the two sets, *tagged-*$\phi\pi$(left) and *tag-sideband-*$\phi\pi$ (right). The *side-band* set is scaled by $\frac{2}{3}$ to accomodate for the 50 % wider sidebands region, compared to the tag signal region.

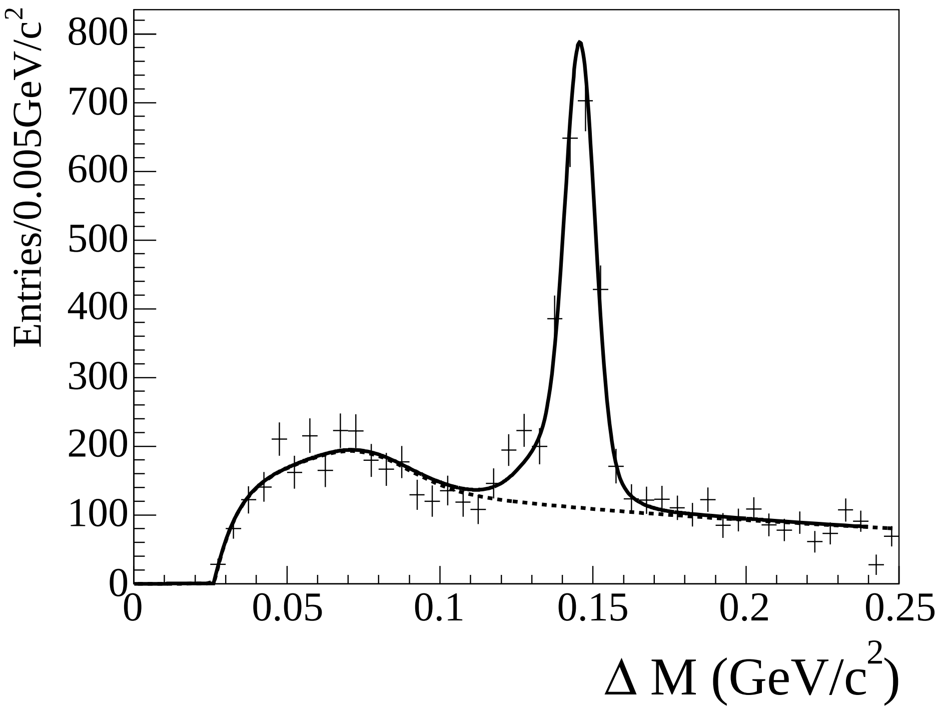

Figure 7.5: Distribution of ΔM for selected $D_s^{*+} \to \gamma D_s^+ \to \gamma\phi\pi^+$ decays with the tag-sidebands subtracted. The χ^2 fit of $\mathcal{PDF}_{\phi\pi\text{signal}}$ yields 2093 ± 99 $D_s^{*+} \to \gamma D_s^+ \to \gamma\phi\pi^+$ events in the recoil of a true tag.

7.3 Systematic Uncertainties

The statistical errors on the $D_s^{*+} \to \gamma D_s^+ \to \gamma\mu^+\nu$ and the $D_s^{*+} \to \gamma D_s^+ \to \gamma\phi\pi^+$ event yields are 11.2 % and 4.7 %; a combined statistical uncertainty of 12.2 %. All remaining sources of uncertainty in the measurement of the branching ratio $\mathcal{B}(D_s^+ \to \mu^+\nu_\mu)$ are systematic uncertainties. Exceptions are the error on the known branching ratios $\mathcal{B}(D_s^+ \to \phi\pi^+)$ and $\mathcal{B}(\phi \to K^+K^-)$, which are errors that are kept separately. Following the course of this analysis, this section describes the systematic uncertainties that are present in this analysis and the evaluation of their sizes.

7.3.1 Tagging

A systematic shift in the tag reconstruction efficiencies between MC and data, which would affect the measurement of a single branching fraction, cancels in the ratio of the event yields of the two decays in the recoil of a real tag. This includes the cancellation of differences in the tracking and PID efficiencies of charged particles, the photon reconstruction efficiency, and cuts on the tag-fit quality, the tag momentum and reconstructed particle masses. Therefore no systematic uncertainty is assigned to that aspect of the tagging procedure.

The tag efficiency correction factor $R_\epsilon^{\mathrm{tag}} = 0.986 \pm 0.006$ is calculated using simulated $D_s^{*+} \to \gamma D_s^+ \to \gamma\mu^+\nu$ and $D_s^{*+} \to \gamma D_s^+ \to \gamma\phi\pi^+$ events. A significant difference in the simulated and measured tag multiplicity would affect $R_\epsilon^{\mathrm{tag}}$. Repeating the study of Section 6.10 with the assumption of a 10 % increase in the number of events with two tag-candidates shows a 0.15 % change of $R_\epsilon^{\mathrm{tag}}$. Since the tag multiplicity shows a perfect agreement between simulated generic decays and data, (Figure 5.11), the uncertainty on the result arising from any tag multiplicity discrepancy is negligible. The 0.6 % statistical error of $R_\epsilon^{\mathrm{tag}}$, arising from the limited size of the Monte Carlo sample, is hence taken as sole contribution to the systematic error, due to the charm tagging.

7.3.2 PID Efficiency MC-to-Data Correction

To ensure the accuracy of the prediction of the data selection efficiency of $D_s^+ \to \mu^+\nu_\mu$ and $D_s^+ \to \phi\pi^+$ decays from Monte-Carlo simulation, the difference of PID efficiencies of muons, kaons, and pions in simulated events and in data must be corrected for. This is done by applying *mc-to-data weights* to the $\mu^\pm$, $K^\pm$, and $\pi^\pm$ in simulated events of the signal and the reference decay.

The weights are derived from PID control samples (Section 4.3), which are selected in simulated events and in data. This principle of using control samples to measure the PID efficiency can introduce uncertainties for different reasons.

- The control sample environment is different from the decay of interest. Because of overlapping signatures from different particles, particle selection efficiencies are generally not the same in low and high-multiplicity events.
- The limited size of the control sample leads to a statistical uncertainty in the measured efficiencies, largest in the phasespace which is less populated by the the control sample. Having a decay process with a momentum and angular distribution that matches the control PID sample keeps this error small.
- The selection efficiencies vary over a range in momentum or angle. This functional dependence is described by a limited number of points in the $p - \theta - \phi$ space. In regions with a rapid change of the efficiency these points must lie resonably dense. The granularity of this binning, which is chosen in the tradeoff between the statistical limitations of the control sample and the rapidness of change of the efficiency, can also influence the correctness of the PID efficiency correction.

Muon Efficiency Correction

The muon control sample consists of well identified $e^+e^- \to \mu^+\mu^-\gamma$ events, (Section 4.3.1). The muon distributions of momentum, θ, and ϕ for the signal decay and the muon control sample are shown in Figure 7.6. The control sample environment is very similar to that of the $D_s^{*+} \to \gamma D_s^+ \to \gamma\mu^+\nu$, a single high-momentum track standing alone in the recoil of a charm tag. In the signal decay additional tracks are present from the fragmentation process, but they are of lower momentum and because of their curvature do not interfere with the muon identification in the IFR. Because of the similarity of the muon environment in the signal decay and in the control sample, no error is assigned to the multiplicity effect.

The statistical errors of the *MC-to-data PID weights* is a source of systematic uncertainty in the muon efficiency correction. The weights are determined from the control sample $e^+e^- \to \mu^+\mu^-\gamma$ in simulation and data, and are given in the form of binned lookup-tables, (Section 4.3). The granularity of the binning is shown in Figure 7.6. The average weight in selected simulated signal events, $\bar{w}$, and its error, $\Delta\bar{w}$, is given by:

$$\bar{w} = \frac{1}{N}\sum_{b=1}^{N_b} n_b w_b, \tag{7.6}$$

$$\Delta\bar{w} = \frac{1}{N}\sqrt{\sum_{b=1}^{N_b} n_b^2 (\Delta w_b)^2}\,, \tag{7.7}$$

where the sums are over all bins in the PID table. N_b is the number of bins in the table, w_b and Δw_b are the weight and the weights' statistical error in a certain bin, n_b is the number of signal muons in each bin, and $N = \sum_{b=1}^{N_b} n_b$ the total number of signal events. The statistical error on $\bar{w}$ is determined to $\Delta\bar{w}/\bar{w} = 0.2\,\%$.

Also tested is the effect of a finer granularity of the binning in p and θ. The effect is studied by introducing a finer momentum binning above $3.5\,\mathrm{GeV}/c$ (left plot of Figure 7.7) and a finer binning in θ between $60°$ and $130°$ (right plot of Figure 7.7). In these regions the momentum and θ distributions of the signal and the control sample are significantly different, which is not reflected in the binning. The weight lookup-tables are reproduced with the finer granularity. A shift in the average weight $\bar{w}$ of $0.4\,\%$ is found, which is taken as the systematic uncertainty due to binning.

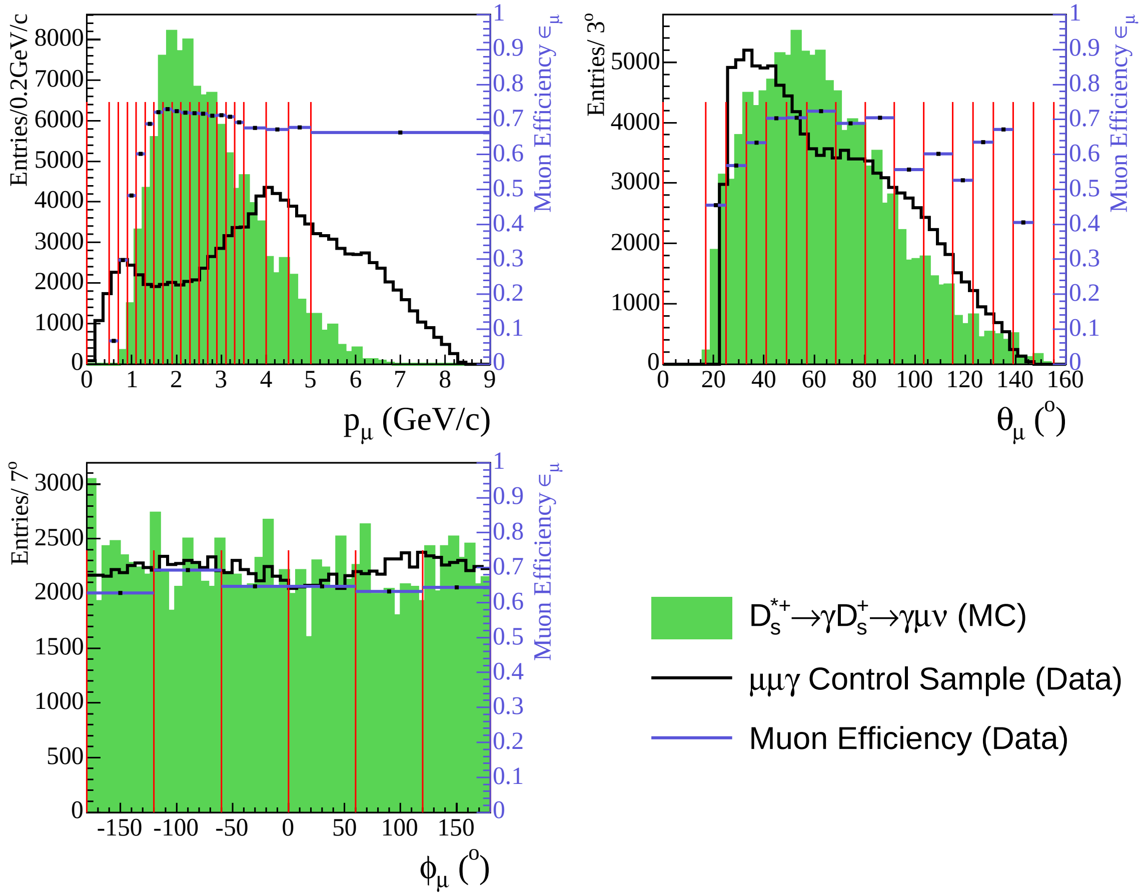

Figure 7.6: Distributions of the momentum, θ, and ϕ of muons identified in signal Monte Carlo (solid green histogram) and in the $e^+e^- \to \mu^+\mu^-\gamma$ control sample in data (black line). Also shown in each plot is the muon efficiency in data averaged over runs 1 through 4. The vertical lines indicate the binning for the look-up table (see text).

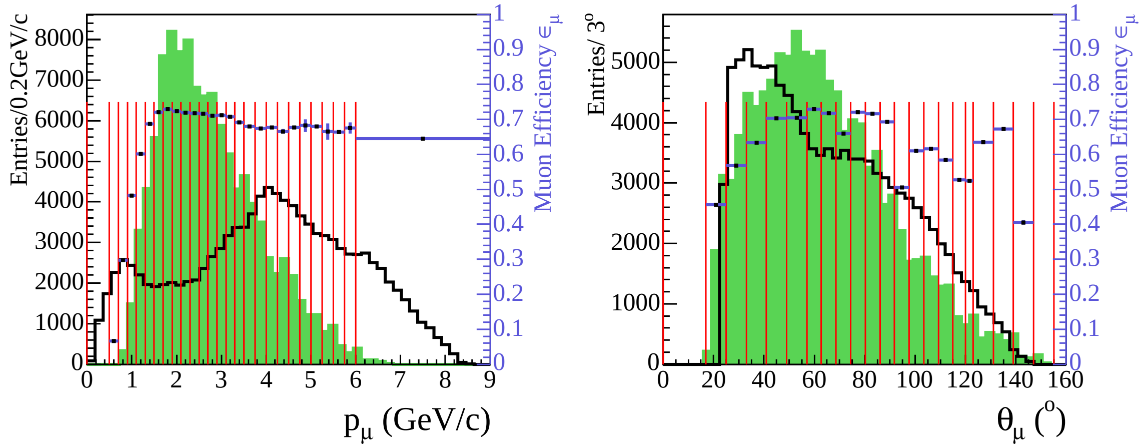

Figure 7.7: The same two plots as in the top row of Figure 7.6, but indicating the finer binning in momentum and θ of the PID tables, used to study the binning effect.

Charged Kaon and Pion Efficiency Correction

To determine the data selection efficiency of the reference decay $D_s^+ \to \phi\pi^+$, $\phi \to K^+K^-$, from simulated events, the PID efficiency MC-to-data correction method is applied on the charged kaons and pion; analogous to that for the muon in the signal decay. The charged-kaon control sample are well identified decays $D^{*+} \to \pi^+ D^0 \to \pi^+ K^- \pi^+$, the charged-pion control sample are τ-3-1 decays, (Section 4.3.1). Both samples have a similar track multiplicity as the reference decay. The *MC-to-data* weights are calculated for $K^\pm$ and $\pi^\pm$ from the control samples. Each candidate decay $D_s^+ \to \phi\pi^+$ is assigned a MC-to-data weight $w_{\phi\pi} = w_{K^+} \times w_{K^-} \times w_\pi$. The average weight, $\bar{w}_{\phi\pi}$, and its error $\Delta\bar{w}_{\phi\pi}$ in simulated truth-matched $D_s^{*+} \to \gamma D_s^+ \to \gamma\phi\pi^+$ decays that fulfill all selection criteria is calculated according to

$$\bar{w} = \frac{1}{N}\sum_{i=1}^{N} w_i, \tag{7.8}$$

$$\Delta\bar{w} = \frac{1}{N}\sqrt{\sum_{i=1}^{N}(\Delta w_i)^2}, \tag{7.9}$$

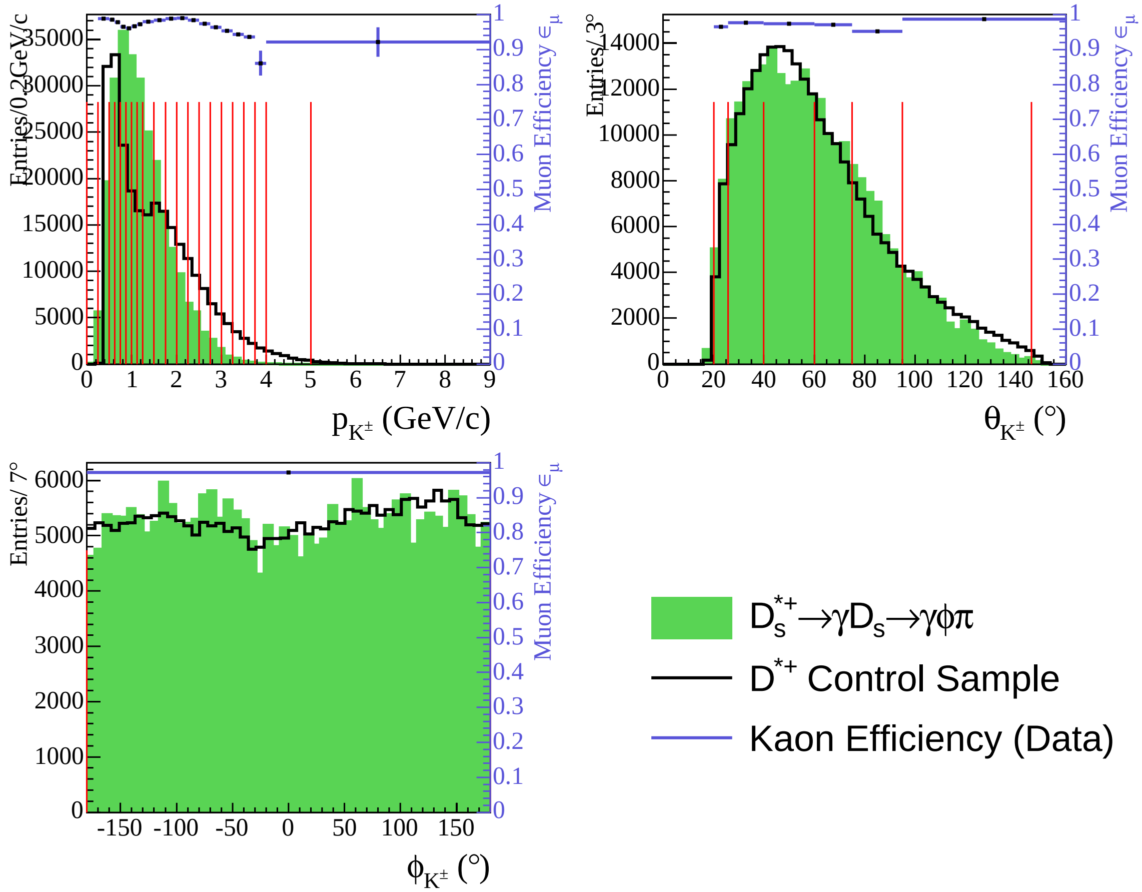

Figure 7.8: Distributions of the momentum, θ, and ϕ of charged kaons identified in $\phi\pi$-signal Monte Carlo (solid green histogram) and in the $D^{*+} \to \pi^+ D^0 \to \pi^+ K^- \pi^+$ control sample in data (black line). Also shown in each plot is the kaon efficiency in data averaged over runs 1 through 4.

where the sums are over all true $D_s^{*+} \to \gamma D_s^+ \to \gamma\phi\pi^+$ events passing the selection. Equation (7.9) is not entirely correct. It neglects the correlation between events with one or more kaons or pions in the same bin of the PID-table. However, the PID-tables are finely binned and the correlation is small. The average weight is $\bar{w}_{\phi\pi} = 1.007 \pm 0.001$, thus the statistical error of $\Delta\bar{w}/\bar{w} = 0.1\,\%$ is the assigned systematic uncertainty from the kaon and pion PID efficiency correction.

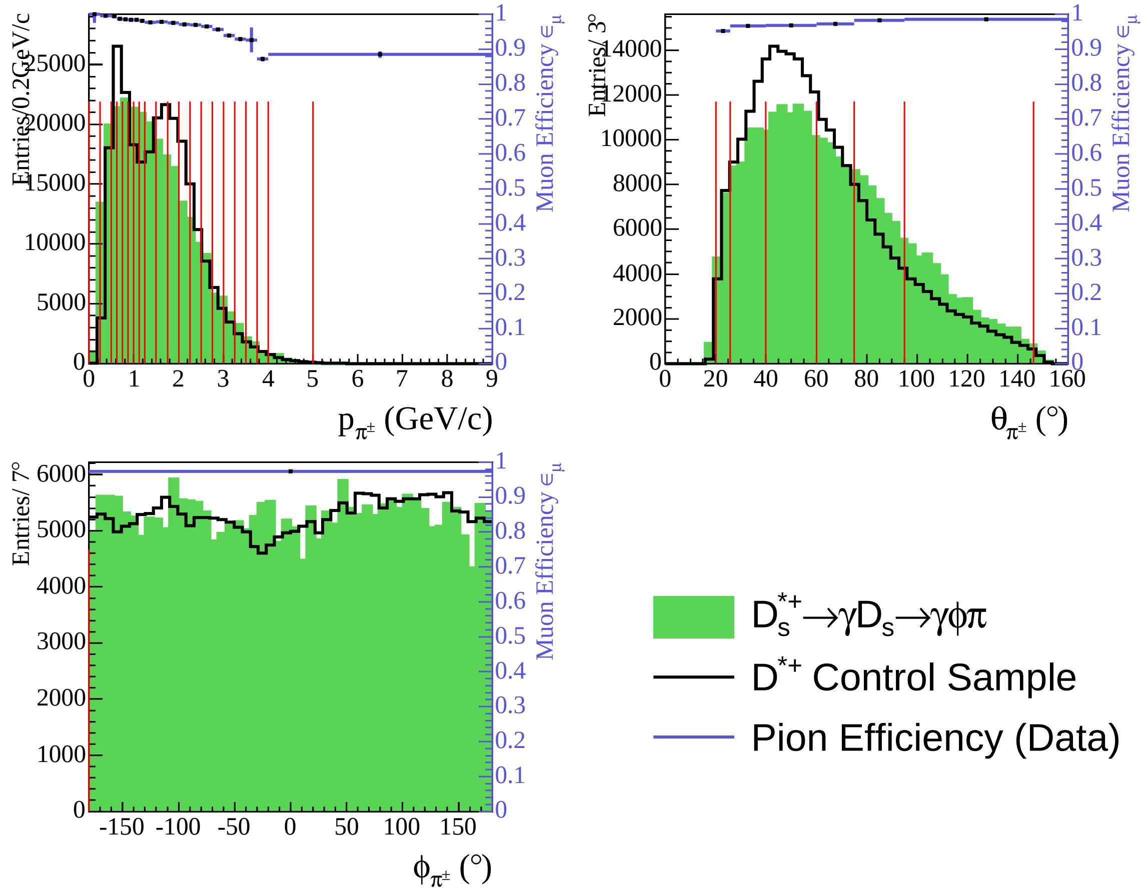

Figure 7.9: Distributions of the momentum, θ, and ϕ of charged pions identified in $\phi\pi$-signal Monte Carlo (solid green histogram) and in the $D^{*+} \to \pi^+ D^0 \to \pi^+ K^- \pi^+$ control sample in data (black line). Also shown in each plot is the pion efficiency in data averaged over runs 1 through 4.

7.3.3 Tracking Efficiency

The simulated efficiency of reconstructing a charged particle track of a certain momentum and angle is corrected using *MC-to-data track weights*, to match the track reconstruction efficiency in data, (Section 4.4). The weights are determined by a deticated tracking working group at *BABAR*. Based on their studies, the group also recommends to assign a systematic error of 0.6 % per reconstructed signal track. The signal decay $D_s^+ \to \mu^+\nu_\mu$ contains one track, the reference decay $D_s^+ \to \phi\pi^+$ contains three. In the calculation of the branching fraction of $D_s^+ \to \mu^+\nu_\mu$ relative to that of $D_s^+ \to \phi\pi^+$, only the ratio of the two simulated efficiencies appears. In this case the systematic error from the muon track from $D_s^+ \to \mu^+\nu_\mu$ cancels with that of one of the three tracks from $D_s^+ \to \phi(K^+K^-)\pi^+$. A systematic error due to the uncertainty of the simulated tracking efficiency of $2 \times 0.6\,\% = 1.2\,\%$ is hence assigned. .

7.3.4 Charm Fragmentation Model

In Section 6.11 the D_s^{*+} momentum distributions in simulated $D_s^{*+} \to \gamma D_s^+ \to \gamma\phi\pi^+$ events and in data are compared. A large discrepancy was found, the D_s^{*+} produced in data are of higher momentum than predicted in the simulation. Despite the large shift in the momentum spectrum the associated correction $C_{p(D_s^{*+})} = r'_\epsilon / r_\epsilon = 1.014$ on the branching ratio is small, due to the choice of identical selection cuts on $p^*_{D_s^{*+}}$ and E^*_γ for the signal and the reference decay. A 0.7 % systematic error is assigned to $C_{p(D_s^{*+})}$, half the size of the correction.

7.3.5 Signal Selection Cuts

The following selection cuts are applied solely in the $D_s^{*+} \to \gamma D_s^+ \to \gamma\mu^+\nu$ and hence discrepancies between the simulation and the data do not cancel with the $D_s^+ \to \phi\pi^+$ selectio:.

- Muon helicity, $\cos\sphericalangle(\mu, D_s^+) < 0.90$
- Missing energy, $E^*_{\text{miss}} > 0.38\,\text{GeV}$

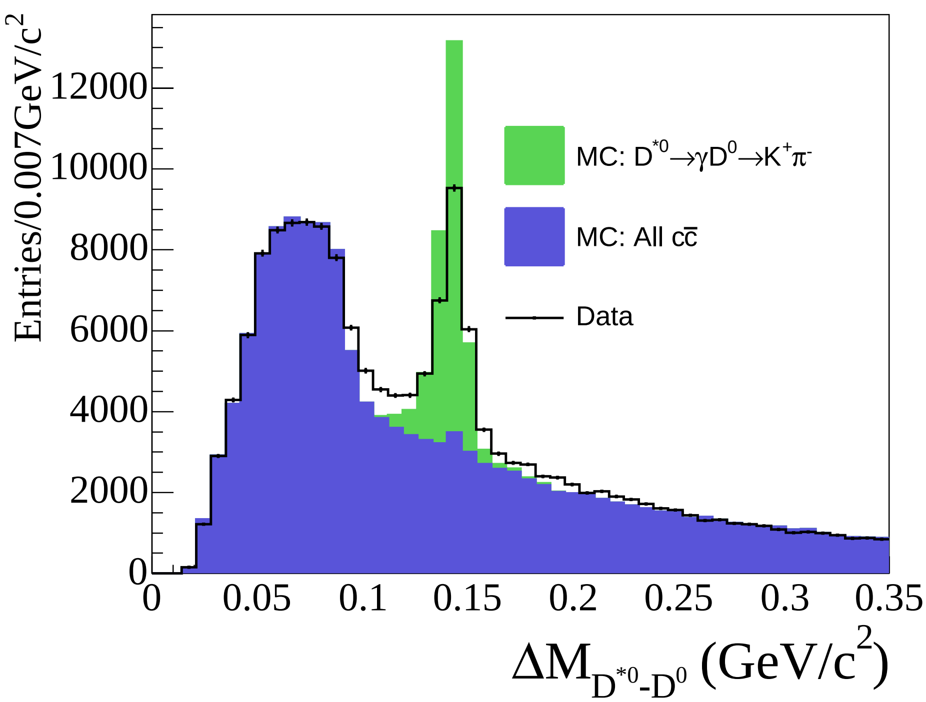

Figure 7.10: $\Delta M = M(\gamma K^-\pi^+) - M(K^-\pi^+)$ distribution in MC and data.

- Neutrino momentum correction, $p_{\rm corr} > -0.06\,\mathrm{GeV/c}$
- Neutrino polar angle, $\theta^*_\nu > 0.67\,\mathrm{rad}$

The control sample $D^{*0} \to \gamma D^0 \to \gamma K^-\pi^+$ is used to study the different efficiencies of these selection requirements in simulated events and in data. The selection of the control sample and the treatment of the $D^0 \to K^-\pi^+$ decay to simulate the signal decay is described in Section 6.8.1.

Simulated generic $c\bar{c}$ events that pass the control sample requirements and where the decay candidate is truth-matched $D^{*0} \to \gamma D^0 \to \gamma K^-\pi^+$ decay, are used to measure the simulated efficiencies of the four selection cuts listed above. In data, candidate decays that pass the control sample selection requirements, including $|\Delta M_{D^{*0}-D^0} - \mu| < 3\,\sigma$, are identified. Candidate decays that pass all control sample selection criteria, but have $4\,\sigma < |\Delta M_{D^{*0}-D^0} - \mu| < 7\,\sigma$ are identified as decays in the $\Delta M_{D^{*0}-D^0}$ sideband. In data, $\Delta M_{D^{*0}-D^0}$-sideband subtracted control sample decays

Table 7.1: Efficiencies of cuts from the signal selection, studied on the control sample $D^{*0} \to \gamma D^0 \to \gamma K^-\pi^+$.

Selection cut	Simulation ϵ_{MC} [%]	Data ϵ_{data} [%]	$\lvert\epsilon_{\text{MC}} - \epsilon_{\text{data}}\rvert/\epsilon_{\text{MC}}$ [%]
$p_{\text{corr}} > -0.23\,\text{GeV/c}$	73.0 ± 0.31	72.1 ± 0.37	1.3
$E^*_{\text{miss}} > 0.38\,\text{GeV}$	82.5 ± 0.27	82.7 ± 0.31	0.2
$\theta^*_\nu > 0.95\,\text{rad}$	96.0 ± 0.14	96.1 ± 0.16	0.1
$\cos\sphericalangle(\mu, D_s^+) < 0.90$	94.7 ± 0.16	95.1 ± 0.18	0.4
$\sum_\oplus$			1.4

$D^{*0} \to \gamma D^0 \to \gamma K^-\pi^+$ are used to measure the cut efficiencies of the four variables.

The distributions of the neutrino polar angle, θ^*_ν, and the neutrino momentum correction, p_{corr} are different in control sample and in signal decays. Since the neutrino is represented by the π^+ in the control sample, the direction of the neutrino candidate is restricted to the fiducial region of the DCH. The difference in the p_{corr} distribution between signal and control sample decays is due to the different masses of the involved decay products. For these two variables the selection cuts are adjusted such that the efficiency of each cut on the control sample matches that on the signal.

The discrepancies between the efficiencies measured in simulated events and in data are taken as the systematic uncertainties for each cut, Table 7.1. A systematic uncertainty of 1.4 % due to the uncertainty in the signal selection efficiency of these cuts is determined. The distributions of these variables in simulated true $D^{*0} \to \gamma D^0 \to \gamma K^-\pi^+$ decays and in data – with and without $\Delta M_{D^{*0}-D^0}$-sideband subtraction - are shown in Figure 7.11.

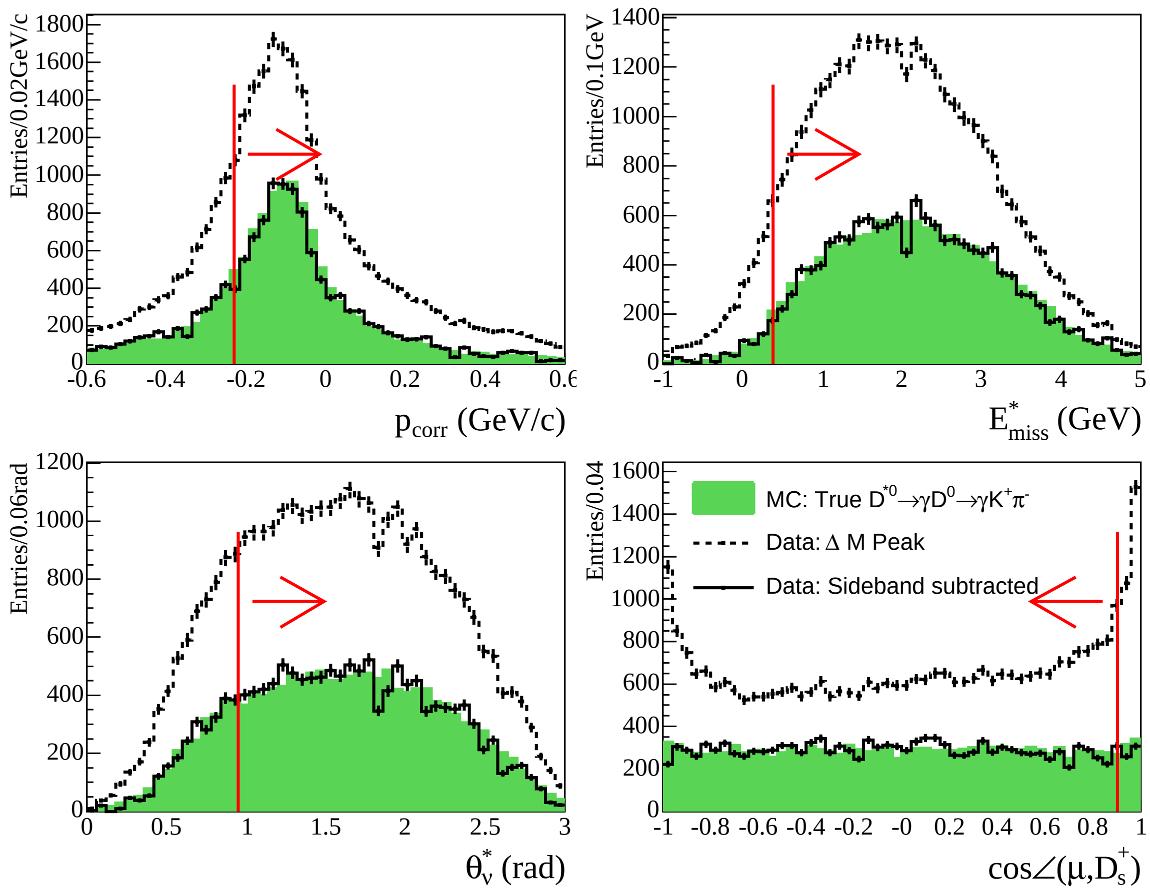

Figure 7.11: Distribution of the quantities used in the signal selection, reconstructed in the control sample $D^{*0} \to \gamma D^0 \to \gamma K^-\pi^+$. From the top left to the bottom right is shown $p_{\rm corr}$, $E_t^* extmiss$, θ_ν^*, and $\cos\sphericalangle(\mu, D_s^+)$.

7.3.6 $D_s^{*+} \to \gamma D_s^+ \to \gamma\phi\pi^+$ Selection Cuts

In the selection of the decay $D_s^{*+} \to \gamma D_s^+ \to \gamma\phi(K^+K^-)\pi^+$ the cuts on the D_s^{*+} momentum and the photon energy are the same as in the selection of the signal decay. The systematic uncertainty arising from these two cuts in both selections cancels in the ratio, $\epsilon_{\mu\nu}/\epsilon_{\phi\pi}$. The only remaining uncertainty lies in the simulation of the D_s^+ reconstruction efficiency.

The mass requirements on the ϕ and D_s^+ candidates are chosen according to the width and mean of the particles, estimated in fits to selected (K^+K^-) and $(\phi\pi^+)$ combinations in simulation of the reference decay and in data, (Table 6.12). Therefore both mass requirements have the same efficiencies in simulation and data. The remaining $D_s^+ \to \phi\pi^+$ selection requirements are on the probability of the vertex-constrained χ^2-fit of the ϕ and D_s^+ meson candidates, $P_\phi > 0.0005$ and $P_{D_s^+} > 0.001$.

To study the uncertainty in the efficiency estimate of these two cuts, $D_s^{*+} \to \gamma D_s^+ \to \gamma\phi\pi^+$ decays in the recoil of a tag are selected in simulated $D_s^{*+} \to \gamma D_s^+ \to \gamma\phi\pi^+$ events and in data. In simulated events the decay candidates are required to be true $D_s^{*+} \to \gamma D_s^+ \to \gamma\phi\pi^+$ decays. In data, the decay candidates must have $\Delta M = M(\gamma D_s^+) - M(D_s^+)$ within 3 standard deviations of the estimated mean. A ΔM sideband between 4 and 7 standard deviations on either side of the estimated mean is defined; decay candidates in the sideband are subtracted from the signal.

In simulated decays the efficiency of both cuts is determined as $\epsilon(P_\phi > 0.0005) = 96.6\,\%$ and $\epsilon(P_{D_s^+} > 0.001) = 93.6\,\%$; the combined efficiency is $\epsilon(P_\phi > 0.0005, P_{D_s^+} > 0.001) = 93.4\,\%$. To estimate the predictive quality of the vertex fit simulation, the agreement of P_ϕ ($P_{D_s^+}$) between simulation and data is measured in the range above 0.0005 (0.001) and extrapolated to values below the cut. In the region above 0.0005 (0.001) the Monte-Carlo-data agreement of P_ϕ ($P_{D_s^+}$) is very good. Both distributions are flat in the region above 0.1, (top plots in Figure 7.12), which is the expected behavior if the errors of the track parameters are treated correctly in the fit.

The agreement between simulation and data is poorer in the very low P_ϕ ($P_{D_s^+}$) region. The first bin in the P_ϕ distribution is about 12.8 % higher in data, and in the $P_{D_s^+}$ distribution about 7.3 %. Zooming into the first bin in each distribution, (bottom plots of Figure 7.12), reveals a data-to-Monte-Carlo ratio that is about constant

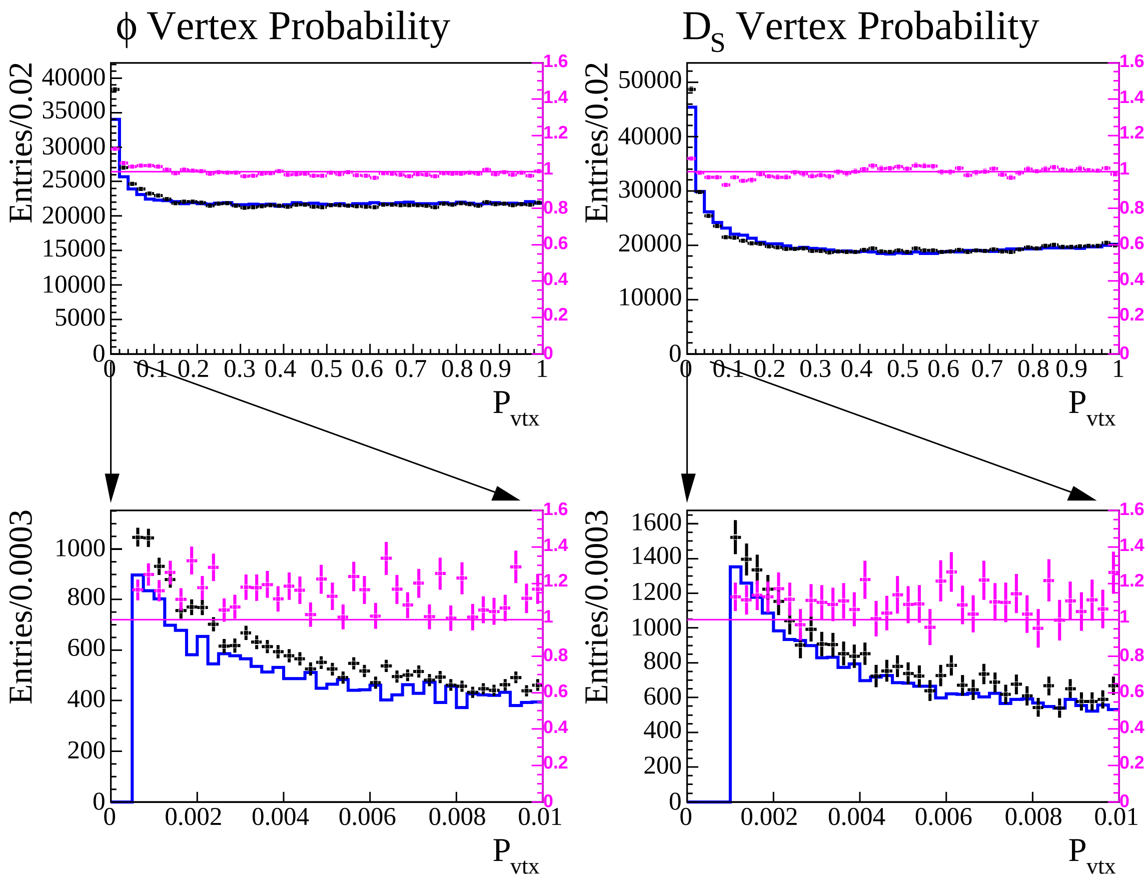

Figure 7.12: Vertex fitting probability for the ϕ (left) and the D_s^+ (right), for simulated events (blue lines) and data (black markers). In purple the data/MC ratio is plotted. The fit probability spectrum for the D_s^+ has been corrected with the data/MC mismatch found in the ϕ fit probability spectrum.

between 0.0005 (0.001) and 0.01. Extrapolating the data-to-Monte-Carlo ratio to probabilities below 0.0005 (0.001), the efficiency of the combined ϕ and D_s^+ vertex-fit probability cuts is estimated. The efficiency is found to be 0.7 % lower in data than in the Monte Carlo simulation. The 0.7 % are taken as the systematic uncertainty associated with the combined cuts $P_\phi > 0.0005$ and $P_{D_s^+} > 0.001$.

7.3.7 $D_s^+ \to \mu^+\nu_\mu$ Signal Shape

The signal yield is obtained from a χ^2 fit of $\mathcal{PDF}_{\mu\nu}$ to the data ΔM distribution, with the parameters fixed to the simulated estimates, (Section 7.1). The study of the control sample $D^{*0} \to \gamma D^0 \to \gamma K^-\pi^+$ showed, that the simulated estimates of the mean and the width of the signal peak do differ from data, $\mu_{\mathrm{Data}}/\mu_{\mathrm{MC}} = 1.013 \pm 0.003$ and $\sigma_{\mathrm{Data}}/\sigma_{\mathrm{MC}} = 1.016 \pm 0.029$, (Section 6.8.1).

In this section the dependence of the fitted signal yield on the estimated mean and width of the signal peak is determined. For that purpose a *toy simulation* study is performed. The inputs of this study are

- The function describing the signal yield $\mathcal{PDF}_{\mu\nu\,\mathrm{signal}}$, and the signal yield $N_{\mu\nu\,\mathrm{signal}} = 489$.
- The function describing the signal background $\mathcal{PDF}_{\mathrm{total\,Bkgd}}$, and the signal yield $N_{\mu\nu\,\mathrm{bkgd}} = 1000$.
- The ΔM distribution for the *tagged-electron*, *tag-sideband-muon*, and *tag-sideband-electron* sample in data, (Figure 7.1). In these three distributions the statistical fluctuations are smoothed out.

The study proceeds by randomly generating a possible ΔM distribution according to $N_{\mu\nu\,\mathrm{signal}} \times \mathcal{PDF}_{\mu\nu\,\mathrm{signal}} + N_{\mu\nu\,\mathrm{bkgd}} \times \mathcal{PDF}_{\mathrm{total\,Bkgd}}$. Since this distribution is to represent the data, the signal mean μ in the generating $\mathcal{PDF}_{\mu\nu\,\mathrm{signal}}$ is shifted from its Monte Carlo estimated value. The statistical uncertainty in each bin of this distribution is enlarged by the contribution from the three data samples *tagged-electron*, *tag-sideband-muon*, and *tag-sideband-electron*. This ensures the proper treatment of the statistical error that arises from the subtraction of the tag-sidebands and the electron sample. The distribution is then χ^2-fitted with the $\mathcal{PDF}_{\mu\nu}$, (7.2), the same that is applied when extracting the signal yield in data.

In repeatedly generated ΔM distributions, 5000 signal yields are obtained. The yields follow a Gaussian distribution, whose mean is estimated in a χ^2-fit. These means as function of the generating signal mean are shown in Figure 7.13. From

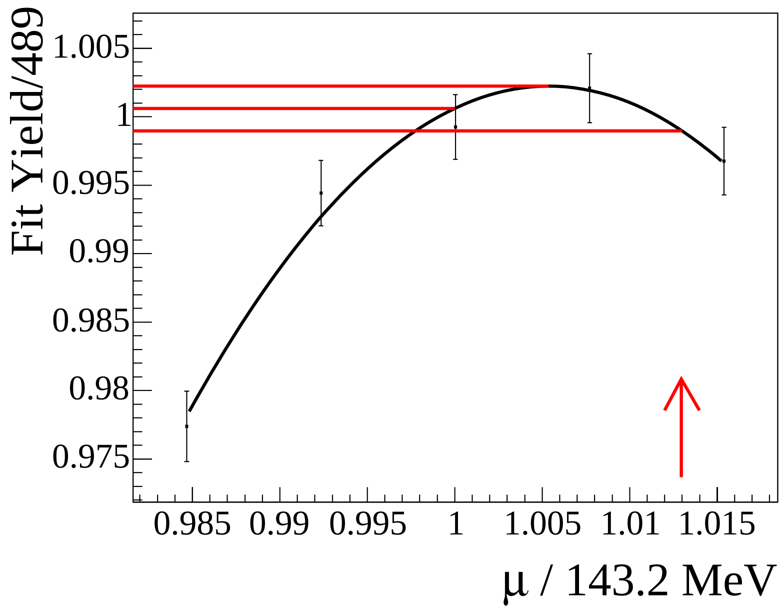

Figure 7.13: Dependence of the fitted signal yield on the true signal peak position parameters. The mean of the simulated signal peak is estimated with 143.2 MeV/c^2. Shown in this plot is the variation of the fitted signal yield if the true mean of the signal peak changes within 1.5 % of the estimated mean. The red arrow at $\mu/143.2\,\mathrm{MeV}/c^2 = 1.013$ indicates the difference in the peak position between Monte Carlo and data, as found in the control sample $D^{*0} \to \gamma D^0 \to \gamma K^-\pi^+$. The largest relative deviation of the fitted yield from 489 in the range between $\mu/143.2\,\mathrm{MeV}/c^2 = 1$ and 1.013 is 0.2 %, taken as the systematic error due to the uncertainty in the true peak position.

the control sample a possible shift in the mean position of the signal peak between simulated events and data of 1.3 % is estimated. Varying the generating mean within 1.3 % of the simulated mean shows a maximum deviation in the signal yield from the generated number of signal events of 0.2 %. This is the assigned systematic error due to the uncertainty in the true peak position.

The same study was done on the width σ_1 of the signal peak. A variation of σ_1 of generating signal distribution within the 1.6 % as predicted from the control sample $D^{*0} \to \gamma D^0 \to \gamma K^-\pi^+$, shows a maximum yield deviation of 0.3 %, (Figure 7.14), taken as the systematic uncertainty.

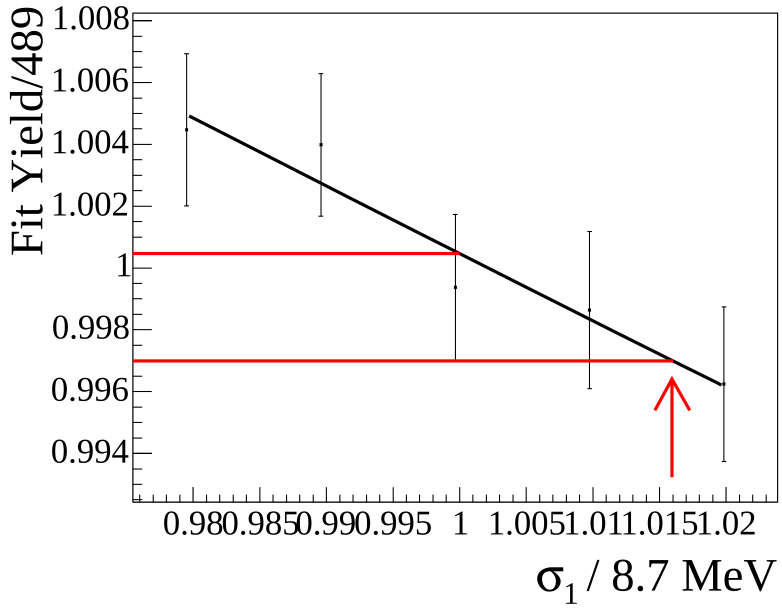

Figure 7.14: Dependence of the fit yield on the signal width. The simulated signal peak has an estimated width of $8.6\,\mathrm{MeV}/c^2$. In the control sample $D^{*0} \to \gamma D^0 \to \gamma K^- \pi^+$ the difference in the peak width between simulation and data is 1.6 %, which, applied here, leads to an estimated systematic uncertainty in the signal yield of 0.3 %.

7.3.8 Normalization of the Electron Sample

The study of the control sample decays $D^{*+} \to \pi^+ D^0 \to \pi^+ K^- l^+ \nu_l$ with $l = \mu, e$, (Section 6.8.2), shows that the electron-to-muon efficiency correction works satisfactorily; the difference between the muon and the electron sample is found to be 64 ± 75, consistent with 0. The study also suggests that a 3.8 % higher average electron-to-muon PID weight would give a muon-electron difference of 0 ± 75.

The effect of a higher electron-to-muon PID weight is studied using the same toy-simulation technique as described in the previous section. Instead of modifying the parameters of the generating function, the size of the *tagged-electron* and *tag-sideband-electron* distribution was varied. A change in the signal yield of 0.4 % is found, taken as the systematic error due to the electron PID efficiency correction, (Figure 7.15).

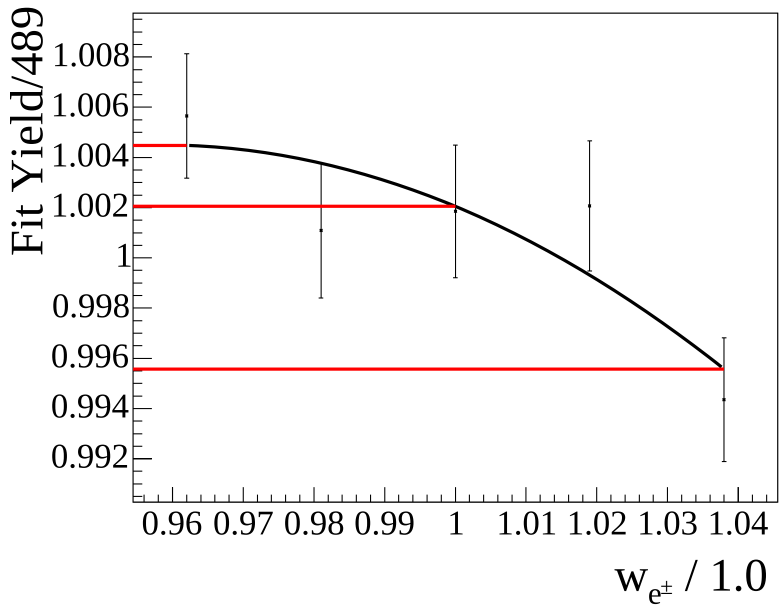

Figure 7.15: Dependence of the fit yield on the electron-to-muon PID efficiency correction. Shown is the effect of an extra overall electron-to-muon correction weight on top of the event by event weight already applied. The study of the control sample $D^{*+} \to \pi^+ D^0 \to \pi^+ K^- l^+ \nu_l$ suggests that a 3.8 % higher overall weight gives perfect agreement between the electron and the muon sample. This plot shows that a 0.4 % shift in the signal yield would be the result, which is taken as the systematic uncertainty due to the electron-to-muon PID efficiency correction.

7.3.9 Shape of Background PDF

The fit result might be quite sensitive to a change of the parameters of the background distribution, $\mathcal{PDF}_{\text{total Bkgd}}$ (6.25). This sensitivity is studied employing the same toy-Monte-Carlo technique as for the study of the signal shape. All parameters of the $\mathcal{PDF}_{\text{total Bkgd}}$ are varied within limits which are three times the uncertainty of each parameter as found in the simulation. The maximum change in the signal yield will be taken as systematic uncertainty due to each parameter.

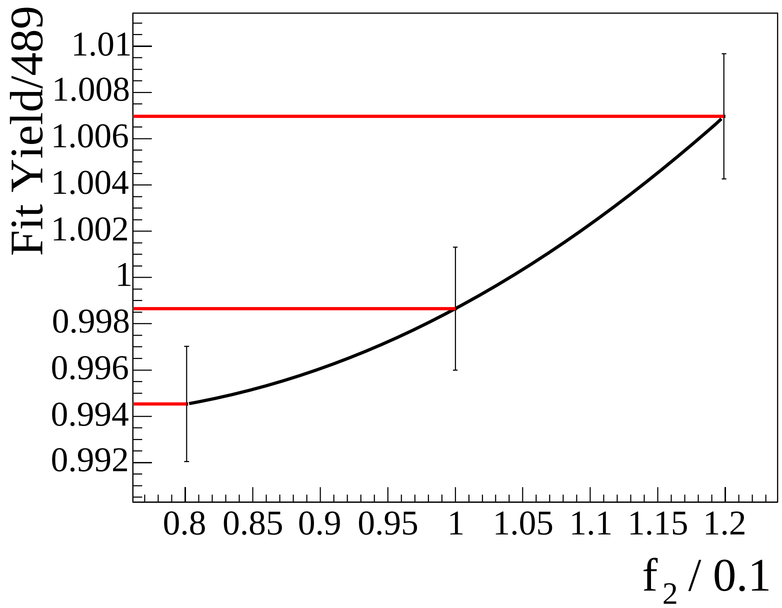

Figure 7.16: Dependence of the fit yield on the size of the background from $D_s^+ \to \tau\nu_\tau \to \pi(\pi^0)$ decays. The size of this background is estimated with 31 ± 6, hence f_2 is varied by 20 %, leading to an uncertainty in the signal yield of 0.8 %.

Size and Shape from Background Decays $D_s^{*+} \to \gamma D_s^+$, $D_s^+ \to \tau\nu_\tau \to \pi(\pi^0)$

This background consists of decays $D_s^{*+} \to \gamma D_s^+$, $D_s^+ \to \tau\nu_\tau \to \pi(\pi^0)$, with the charged pion being misidentified as a muon; it is described in Section 6.7.4. The ΔM distribution of these decays is described by $\mathcal{PDF}_{\mathrm{fake}\,\pi\,\mathrm{from}\,\tau}$, (6.19). Since the background peaks under the signal, (top plot in Figure 6.22), its size cannot be determined by the fit and is therefore fixed; the fraction estimated from the simulation. A variation of its expected size of 20 % (the statistical uncertainty if this background) within the simulated expectation leads to a change in the signal yield of 0.8 % , (Figure 7.16). The mean and the width are also varied within three times their estimated error, shown in Figure 7.17 and summarized in Table 7.2.

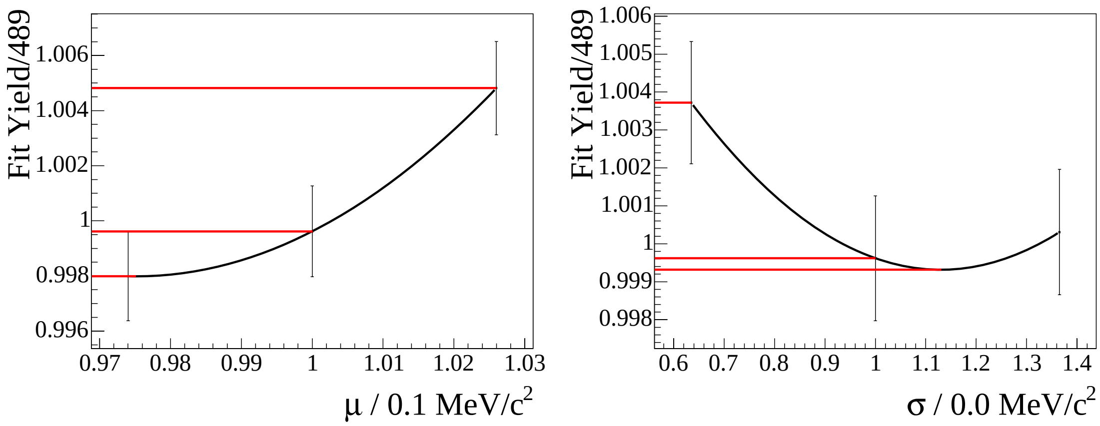

Figure 7.17: Dependence of the fit yield on the parameters μ (left) and σ (right), describing the ΔM distribution of background events from $D_s^+ \to \tau\nu_\tau \to \pi(\pi^0)$ decays.

Size and Shape from Background Decays $D_{(s)}^{*+} \to \pi^0 D_{(s)}^+ \to \mu\nu_\mu$

This background consists of decays $D_{(s)}^{*+} \to \pi^0 D_{(s)}^+ \to \mu\nu_\mu$ with the photon candidate coming from the π^0 of the $D_{(s)}^{*+}$ decay; it is described in Section 6.7.3. The ΔM distribution of this background is limited to the range between $\Delta M = 50$ and $100\,\mathrm{MeV}/c^2$, (top plot in Figure 6.21), and is described by $\mathcal{PDF}_{\gamma\,\mathrm{from}\,\pi^0}$, (6.16). Although it is separated from the signal peak, its size influences the background contribution under the signal peak. Again, the toy-Monte-Carlo study has been performed to determine the effect of this background estimate on the signal yield. Varying the size of this background by 9 % leads to a change in the signal yield of 0.9 %. The parameters describing the shape of $\mathcal{PDF}_{\gamma\,\mathrm{from}\,\pi^0}$ are also studied. Figure 7.18 shows the results of this study.

Combinatoric Background Shape Parameters

The remaining parameters, describing the combinatoric background, are also varied within their estimated errors, (Figure 7.19). The resulting changes in the signal yield for these and all previously mentioned parameters are listed in Table 7.2. The systematic error due to each background parameter is added in quadrature to yield a total systematic error due to the uncertainty in the describtion of the background

Table 7.2: Systematic error due to the uncertainty in the describtion of the background shape for each parameter of $\mathcal{PDF}_{\mathrm{total\,Bkgd}}$ (6.25). All errors are added in quadrature.

Parameter	Change in Signal Yield
N_1	0.9 %
μ_1	0.4 %
σ_1	0.3 %
μ_2	0.4 %
σ_2	0.3 %
N_2	0.8 %
μ	0.5 %
σ	0.4 %
a	0.4 %
b	1.5 %
c	0.4 %
ΔM_0	0.7 %
$\sum_{\oplus}$	2.3 %

shape of 2.3 %.

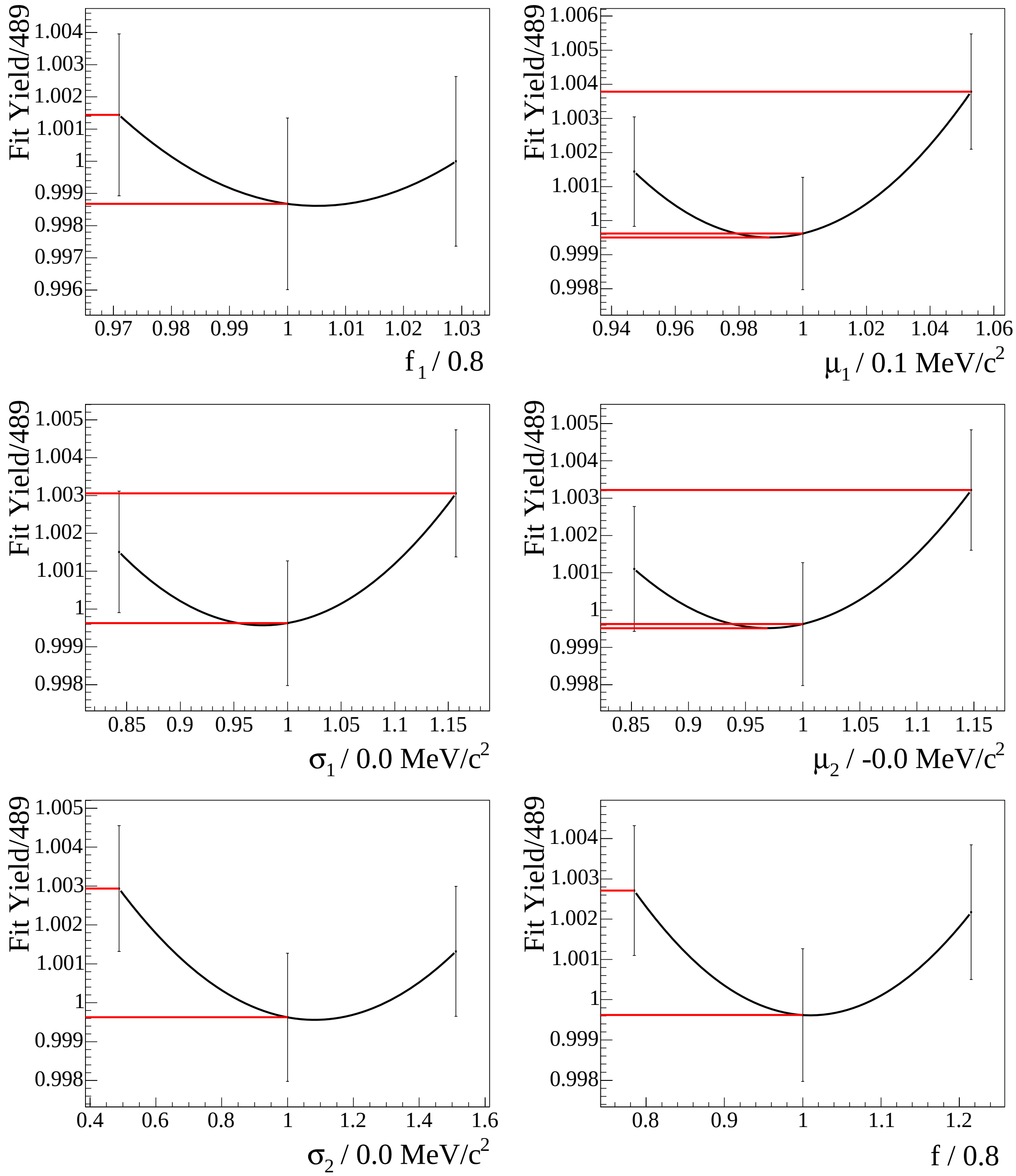

Figure 7.18: Dependence of the fit yield on the size and the shape of the background from $D^{*+}_{(s)} \to \pi^0 D^+_{(s)} \to \mu\nu_\mu$ decays. The size of this background is estimated with 170 ± 13, hence f_1 is varied by 9 %, leading to an uncertainty in the signal yield of 0.9 %. The parameters μ_1, σ_1, $\Delta\mu$, σ_2, and f that describe the ΔM distribution of this background are varied by three times their standard deviation, estimated from simulation.

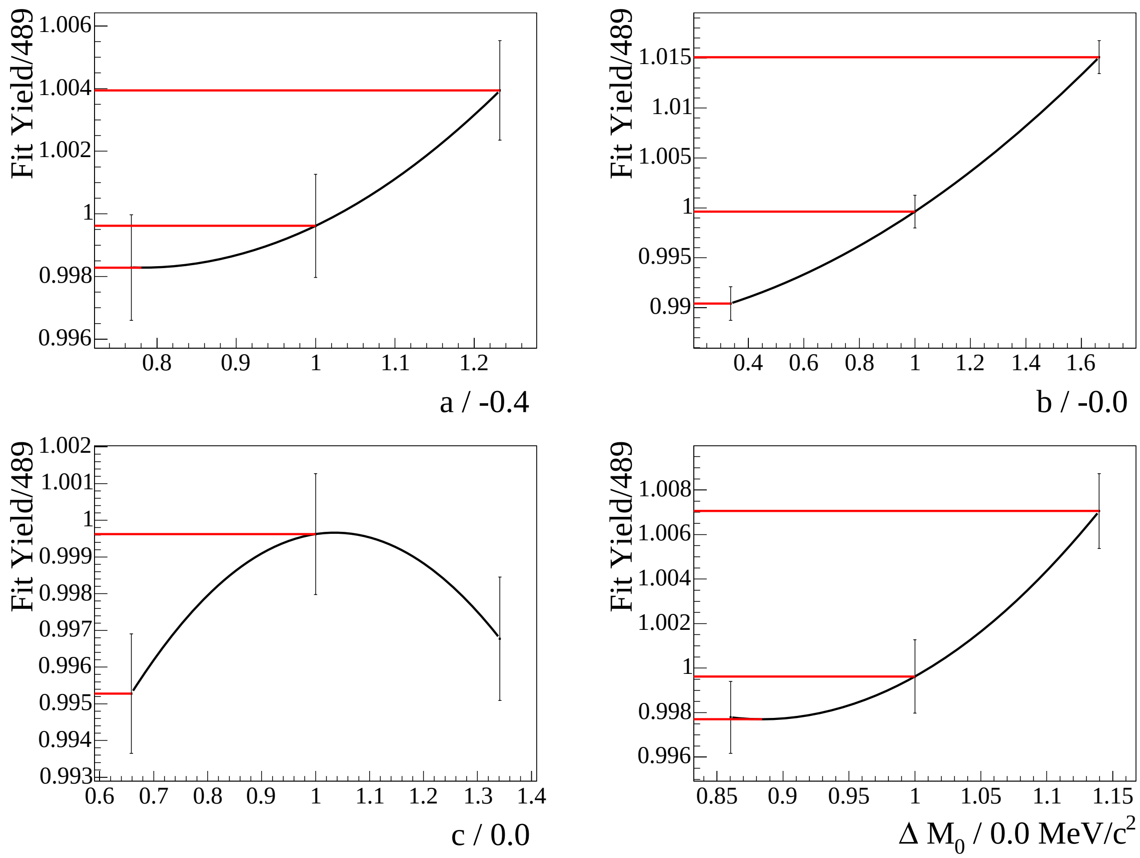

Figure 7.19: Dependence of the fit yield on the background parameters a, b, c, and ΔM_0, as determined in toy-Monte-Carlo studies. The parameters are varied by three times their standard deviation, estimated from simulation.

7.3.10 Summary of Systematic Errors

A summary of all systematic errors on the branching ratio is given in table 7.3. The total systematic error amounts to 3.7 %, approximately one third of the statistical uncertainty.

Table 7.3: Summary of the significant systematic errors.

Source of Systematic Uncertainty	Size in %
Tagging	0.6
Muon PID	$0.2 \oplus 0.4$
Kaon and pion PID	0.1
Tracking	1.2
$p^*_{D_s^{*+}}$ spectrum	0.7
$D_s^+ \to \mu^+\nu_\mu$ selection	1.4
$D_s^+ \to \phi\pi^+$ selection	0.7
Efficiency – MC statistics	1.1
Signal PDF	0.3
Electron Correction	0.4
Background PDF	2.3
$D_s^+ \to \phi\pi^+$ Background PDF	0.3
$\mathcal{B}(\phi \to K^+K^-)$	1.2
$\sum_\oplus$	3.7

7.4 The Treatment of Background from Decays $D_s^+ \to f_0(980)\pi^+$

In Section 6.9.2 it is shown that the decays $D_s^+ \to f_0(980)\pi^+$ and $D_s^+ \to K^+K^-\pi^+$ create a peaking background indistinguishable from the $D_s^+ \to \phi\pi^+$ signal decay. Its size is estimated as $48 \pm 7_{\mathrm{stat}} \pm 22_{\mathrm{sys}}$ events, or $(2.3 \pm 1.2)\,\%$ of the anticipated $D_s^+ \to \phi\pi^+$ yield, using the cuts in the analysis.

For the calculation of the partial width ratio $\Gamma(D_s^+ \to \mu^+\nu_\mu)/\Gamma(D_s^+ \to \phi\pi^+)$ in the next section this background estimate is subtracted from the $D_s^+ \to \phi\pi^+$ signal yield:

$$N'_{\phi\pi} = N_{\phi\pi} - N_{K^+K^-\pi} = (2093 \pm 99) - (48 \pm 23) = 2045 \pm 99_{\mathrm{stat}} \pm 23_{\mathrm{sys}} \tag{7.10}$$

The calculation of the branching ratio $\mathcal{B}(D_s^+ \to \mu^+\nu_\mu)$ depends on the measured branching ratio $\mathcal{B}(D_s^+ \to \phi\pi^+) = (4.81 \pm 0.52 \pm 0.38)\,\%$ [16]. In that analysis the reconstruction of the D_s^+ meson candidates is done in the same manner as it is presented in here. No measures to suppress the background from $D_s^+ \to f_0(980)\pi^+$ and $D_s^+ \to K^+K^-\pi^+$ decays are taken. The only difference, which effects the amount of background from these decays in the $\phi\pi$ signal, is the requirement on the invariant mass $M(K^+K^-)$ of the kaon pair forming the ϕ candidate. In the $D_s^+ \to \phi\pi^+$-analysis of Reference [16], the $M(K^+K^-)$ must lie within $15\,\mathrm{MeV}/c^2$ of the nominal ϕ mass, whereas in the analysis presented here a $2\,\sigma = 10.2\,\mathrm{MeV}/c^2$ requirement is made. That gives an estimated background of

$$(2.3 \pm 1.2)\,\% \times \frac{15\,\mathrm{MeV}/c^2}{10.2\,\mathrm{MeV}/c^2} = (3.4 \pm 1.7)\,\% \tag{7.11}$$

in the measurement of the branching ratio $\mathcal{B}(D_s^+ \to \phi\pi^+)$, that is not accounted for. A background-corrected branching ratio is given by

$$\begin{aligned} \mathcal{B}'(D_s^+ \to \phi\pi^+) &= (1 - (3.4 \pm 1.7)\,\%) \times (4.81 \pm 0.64)\,\% \\ &= (4.65 \pm 0.62 \pm 0.08)\,\%\,, \end{aligned} \tag{7.12}$$

where the first and second error are from the measurement and from the correction uncertainty, respectively.

Rather then using a corrected branching ratio $\mathcal{B}'(D_s^+ \to \phi\pi^+)$ and a corrected $\phi\pi$-signal yield, $N'_{\phi\pi}$, a correction factor $R_{KK\pi}$ is calculated which shows more clearly the effect of the uncertainty introduced by this background.

$$R_{KK\pi} = \left(\frac{\mathcal{B}'(D_s^+ \to \phi\pi^+)}{\mathcal{B}(D_s^+ \to \phi\pi^+)}\right) \Bigg/ \left(\frac{N'_{\phi\pi}}{N_{\phi\pi}}\right) = \frac{1 - (3.4 \pm 1.7)\%}{1 - (2.3 \pm 1.2)\%} = 0.989 \pm 0.005 \tag{7.13}$$

The error on $R_{KK\pi}$ of $0.5\,\%$ is treated as an additional systematic uncertainty in the calculated branching ratio $\mathcal{B}(D_s^+ \to \mu^+\nu_\mu)$.

7.5 Determination of the Branching Ratio $\mathcal{B}(D_s^+ \to \mu^+\nu_\mu)$ and the Decay Constant f_{D_s}

The ratio of the partial widths of the decays $D_s^+ \to \mu^+\nu_\mu$ to $D_s^+ \to \phi\pi^+$ is given by

$$\begin{aligned} \frac{\Gamma(D_s^+ \to \mu^+\nu_\mu)}{\Gamma(D_s^+ \to \phi\pi^+)} &= \frac{N_{\mu\nu}/\epsilon_{\mu\nu}}{N'_{\phi\pi}/\epsilon_{\phi\pi}} \times R_\epsilon^{\mathrm{tag}} \times C_{p(D_s^{*+})} \times \mathcal{B}(\phi \to K^+K^-) \\ &= \frac{(489 \pm 55)/(8.13 \pm 0.13)\,\%}{(2045 \pm 99 \pm 23)/(9.90 \pm 0.11)\,\%} \times 0.986 \times 1.014 \times (49.1 \pm 0.6)\,\% \\ &= 0.143 \pm 0.018_{\mathrm{stat}} \pm 0.006_{\mathrm{sys}}, \end{aligned} \tag{7.14}$$

where the first error is from the statistical uncertainty of the signal yields and the second is systematic.

The branching fraction $\mathcal{B}(D_s^+ \to \mu^+\nu_\mu)$ is given by

$$\begin{aligned}
&\mathcal{B}(D_s^+ \to \mu^+\nu_\mu) \\
&\quad = \frac{N_{\mu\nu}/\epsilon_{\mu\nu}}{N_{\phi\pi}/\epsilon_{\phi\pi}} \times R_\epsilon^{\mathrm{tag}} \times C_{p(D_s^{*+})} \times \mathcal{B}(\phi \to K^+K^-) \times \mathcal{B}(D_s^+ \to \phi\pi^+) \times R_{KK\pi} \\
&\quad = \frac{(489 \pm 55)/(8.13 \pm 0.13)\,\%}{(2093 \pm 99)/(9.90 \pm 0.11)\,\%} \times 0.986 \times 1.014 \\
&\qquad\qquad \times (49.1 \pm 0.6)\,\% \times (4.81 \pm 0.64)\,\% \times (0.989 \pm 0.005) \\
&\quad = (6.65 \pm 0.81_{\mathrm{stat}} \pm 0.25_{\mathrm{sys}} \pm 0.88_{\mathrm{norm}}) \times 10^{-3}
\end{aligned} \tag{7.15}$$

The same result can be obtained using the previously calculated partial width ratio and the background-corrected branching ratio $\mathcal{B}'(D_s^+ \to \phi\pi^+) = (4.65 \pm 0.62)\,\%$

$$\frac{\Gamma_{D_s^+ \to \mu^+\nu_\mu}}{\Gamma_{D_s^+ \to \phi\pi^+}} \times \mathcal{B}'(D_s^+ \to \phi\pi^+) = (6.65 \pm 0.81_{\mathrm{stat}} \pm 0.25_{\mathrm{sys}} \pm 0.88_{\mathrm{norm}}) \times 10^{-3} \tag{7.16}$$

The decay constant of the D_s^+ meson, f_{D_s}, is calculated from the measured branching ratio, $\mathcal{B}(D_s^+ \to \mu^+\nu_\mu)$, the lifetime of the D_s^+-meson, $\tau_{D_s^+} = (146.9 \pm 2.7)\,\mu\mathrm{m}/c$, the CKM-parameter, $V_{cs} = 0.9737 \pm 0.007$, the Fermi coupling constant, $G_F = 1.17 \times 10^{-11}\mathrm{MeV}^{-2}$, and the nominal masses of the D_s^+ meson, $m_{D_s^+} = 1968.3\,\mathrm{MeV}/c^2$, and the muon, $m_\mu = 105.6\,\mathrm{MeV}/c^2$. It is given by

$$\begin{aligned}
f_{D_s} &= \sqrt{\frac{\mathcal{B}(D_s^+ \to \mu^+\nu_\mu)/\tau_{D_s^+}}{\frac{G_F^2}{8\pi} V_{cs}^2 m_{D_s^+} m_\mu^2 \left(1 - \frac{m_\mu^2}{m_{D_s^+}^2}\right)^2}} \\
&= (281 \pm 17_{\mathrm{stat}} \pm 6_{\mathrm{sys}} \pm 19_{\mathrm{norm}})\,\mathrm{MeV}\,,
\end{aligned} \tag{7.17}$$

where the errors are statistical, systematic, and from the uncertainty of the branching ratio $\mathcal{B}(D_s^+ \to \phi\pi^+)$. The error on V_{cs} is part of the systematic uncertainty.

Previous measurements of $\mathcal{B}(D_s^+ \to \mu^+\nu_\mu)$ that are anchored on the decay $D_s^+ \to \phi\pi^+$ use a value $\mathcal{B}(D_s^+ \to \phi\pi^+)_{\mathrm{PDG}} = (3.6 \pm 0.9)\,\%$, which is currently listed in the PDG review [30]. For reasons of easier comparison of the results obtained by this analysis with previous ones, the branching ratio $\mathcal{B}(D_s^+ \to \phi\pi^+)_{\mathrm{PDG}}$ is used to give the following two results:

$$\begin{aligned}
\mathcal{B}(D_s^+ \to \mu^+\nu_\mu)_{\mathrm{PDG}norm} & \\
&= \frac{\Gamma(D_s^+ \to \mu^+\nu_\mu)}{\Gamma(D_s^+ \to \phi\pi^+)} \times \mathcal{B}(D_s^+ \to \phi\pi^+)_{\mathrm{PDG}} \\
&= (0.143 \pm 0.018 \pm 0.006) \times (3.6 \pm 0.9)\,\% \\
&= (5.15 \pm 0.63_{\mathrm{stat}} \pm 0.20_{\mathrm{sys}} \pm 1.29_{\mathrm{norm}}) \times 10^{-3}
\end{aligned} \tag{7.18}$$

and

$$(f_{D_s})_{\mathrm{PDG}norm} = (248 \pm 15_{\mathrm{stat}} \pm 6_{\mathrm{sys}} \pm 31_{\mathrm{norm}})\,\mathrm{MeV} \tag{7.19}$$

The results are summarized in Table 7.4.

Table 7.4: Results for the partial width ratio $\Gamma(D_s^+ \to \mu^+\nu_\mu)/\Gamma(D_s^+ \to \phi\pi^+)$, branching ratio $\mathcal{B}(D_s^+ \to \mu^+\nu_\mu)$, and decay constant f_{D_s}. The branching ratio and the decay constant are given for two different assumptions on $\mathcal{B}(D_s^+ \to \phi\pi^+)$. The errors on the branching ratio and on f_{D_s} are statistical, systematic, and from the error on $\mathcal{B}(D_s^+ \to \phi\pi^+)$.

$\frac{\Gamma(D_s^+ \to \mu^+\nu_\mu)}{\Gamma(D_s^+ \to \phi\pi^+)}$	$0.143 \pm 0.018_{\mathrm{stat}} \pm 0.006_{\mathrm{sys}}$	
	BABAR	PDG
$\mathcal{B}(D_s^+ \to \phi\pi^+)$	$(4.81 \pm 0.64)\,\%$	$(3.6 \pm 0.9)\,\%$
$\mathcal{B}(D_s^+ \to \mu^+\nu_\mu)$	$(6.65 \pm 0.81 \pm 0.25 \pm 0.88) \times 10^{-3}$	$(5.15 \pm 0.63 \pm 0.20 \pm 1.29) \times 10^{-3}$
f_{D_s}	$(281 \pm 17 \pm 6 \pm 19)\,\mathrm{MeV}$	$(248 \pm 15 \pm 6 \pm 31)\,\mathrm{MeV}$

Chapter 8

Conclusions

In this analysis the decay $D_s^+ \to \mu^+\nu_\mu$ has been investigated, and the branching ratio has been measured:

$$\mathcal{B}(D_s^+ \to \mu^+\nu_\mu) = (6.65 \pm 0.81_{\text{stat}} \pm 0.25_{\text{sys}} \pm 0.88_{\text{norm}}) \times 10^{-3} \ . \tag{8.1}$$

The third error is from the uncertainty in the branching ratio $\mathcal{B}(D_s^+ \to \phi\pi^+) = (4.81 \pm 0.64)\,\%$, measured in *BABAR* [16]; it is of similar size (13.3 %) as the statistical and systematic uncertainties combined (12.3 %). The decay constant f_{D_s} is determined, utilizing $\mathcal{B}(D_s^+ \to \mu^+\nu_\mu)$:

$$f_{D_s} = (281 \pm 17_{\text{stat}} \pm 6_{\text{sys}} \pm 19_{\text{norm}})\,\text{MeV} \ . \tag{8.2}$$

Using instead the PDG value for the branching ratio $\mathcal{B}(D_s^+ \to \phi\pi^+) = (3.6 \pm 0.9)\,\%$, the branching ratio and decay constant

$$\begin{aligned} \mathcal{B}(D_s^+ \to \mu^+\nu_\mu)_{\text{PDG}} &= (5.15 \pm 0.63_{\text{stat}} \pm 0.20_{\text{sys}} \pm 1.29_{\text{norm}}) \times 10^{-3} \text{, and} \\ (f_{D_s})_{\text{PDG}} &= (248 \pm 15_{\text{stat}} \pm 6_{\text{sys}} \pm 31_{\text{norm}})\,\text{MeV} \end{aligned} \tag{8.3}$$

are determined. These values may be compared to the current world averages (excluding this measurement), $\mathcal{B}(D_s^+ \to \mu^+\nu_\mu) = (5.96 \pm 1.44) \times 10^{-3}$ and $f_{D_s} = 267 \pm 33$ [30], which (with the exception of the result from BES) are anchored on the same branching ratio for $D_s^+ \to \phi\pi^+$, ((3.6 ± 0.9) %). Figure 8.1 shows the value of the decay constant f_{D_s} determined by this measurement in comparison with previous measurements and with their average.

The current world average of $\mathcal{B}(D_s^+ \to \mu^+\nu_\mu)$ has a combined statistical and systematic uncertainty of 12.1 %; the same precision that is reached by the present measurement. A new world average can be formed, based on this measurement and the PDG value $\mathcal{B}(D_s^+ \to \phi\pi^+)_{\mathrm{PDG}}$:

$$\begin{aligned} \mathcal{B}(D_s^+ \to \mu^+\nu_\mu) &= (5.74 \pm 1.37) \times 10^{-3} \\ f_{D_s} &= (261 \pm 31)\,\mathrm{MeV} \end{aligned} \tag{8.4}$$

The errors on the branching ratio and the decay constant are large, 24 % and 12 %, respectively. Dominating is the 25 % uncertainty of the branching ratio $\mathcal{B}(D_s^+ \to \phi\pi^+)$. However, the statistical uncertainty of f_{D_s} is now at about 4.4 %, in comparison to 6.1 % from the previous average. The is the major contribution of this analysis.

It is most interesting to compare the measured decay constant f_{D_s} with f_D, which was recently measured by the CLEO-c collaboration, $f_D = (223 \pm 17)\,\mathrm{MeV}$ [27]. This measurement uses $e^+e^- \to D^+D^-$ events at the D-pair production threshold. In such events the identification of a D^+ or D^- meson unambiguously asserts the existence of an oppositely charged D meson; a high-purity sample of charged D mesons can be constructed. The measured branching ratio $\mathcal{B}(D^+ \to \mu^+\nu_\mu)$ is hence absolute, independent of any other measurement. The ratio of the measured values f_{D_s} to f_D, from *BABAR* and CLEO-c respectively, is:

$$\frac{f_{D_s}}{f_D} = \frac{(281 \pm 26)\,\mathrm{MeV}}{(223 \pm 17)\,\mathrm{MeV}} = 1.26 \pm 0.12 \tag{8.5}$$

The measured ratio is found to be in good agreement with the prediction from the lattice QCD simulation, $(f_{D_s}/f_D)_{\mathrm{lattice}} = 1.25 \pm 0.07$ [10]:

$$\frac{f_{D_s}}{f_D} \Big/ \left(\frac{f_{D_s}}{f_D}\right)_{\mathrm{lattice}} = 1.01 \pm 0.11\ . \tag{8.6}$$

In summary, the branching ratio $\mathcal{B}(D_s^+ \to \mu^+\nu_\mu)$ and the decay constant of the

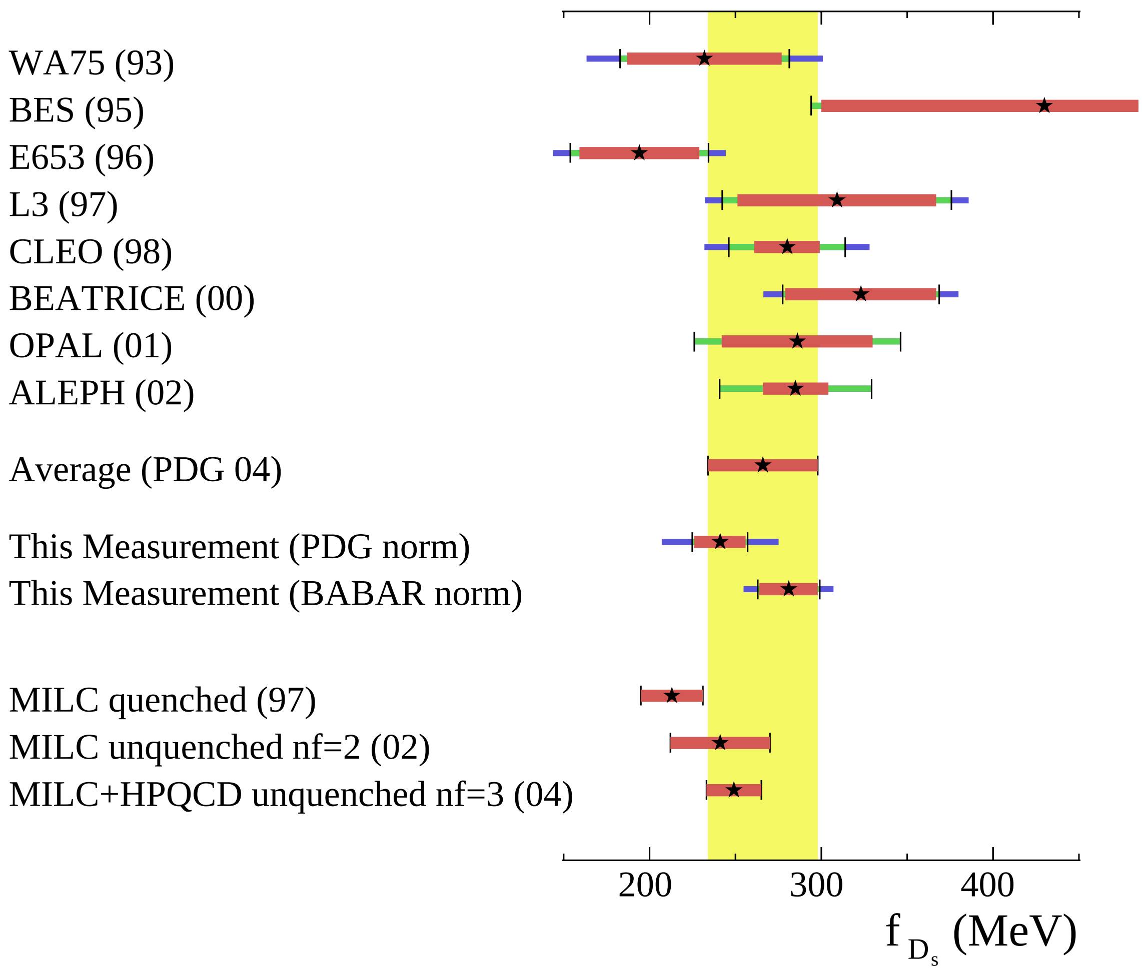

Figure 8.1: Pseudoscalar decay constant f_{D_s} in measurement and theory. Shown are the present result (both, normalized to the *BABAR* and the PDG value of $\mathcal{B}(D_s^+ \to \phi\pi^+)$), all previous measurement and their average, and three lattice QCD results with different degrees of freedom of the dynamic quarks (u, u, d, or u, d, s). The yellow band indicates that previous experimental world average (without this measurement). All previous measurements (except the BES measurement) are normalized to $\mathcal{B}(D_s^+ \to \phi\pi^+)_{\mathrm{PDG}}$ and may be compared to the PDG-normalized *BABAR* measurement. The central values are marked by black stars. For the measurements the statistical error is represented by the thick red line, the additional systematic error is represented by the thinner green line that ends in vertical bars, and the additional normalization error is represented by the blue line. The absolute BES measurement has no normalization error, the OPAL and ALEPH measurement do not quote the exact normalization error.

D_s^+ meson have been measured with a precision that has not yet been achieved by a single experiment. Together with the absolute measurement of f_D by the CLEO-c collaboration, an excellent agreement with the Standard Model predictions from lattice QCD simulations is found. However, the calculation and measurement uncertainties are still large and definite statements about the validity of the lattice calculation would be premature.

Until the end of 2008 the *BABAR* experiment is expected to collect 1 ab^{-1} of data, more than 4 times the data used in this analysis. Repeating the presented analysis on this dataset would result in a measurement of f_{D_s} with less than 4 % combined statistical and systematic uncertainty. Moreover, CLEO-c is anticipated to measure $\mathcal{B}(D_s^+ \to \phi\pi^+)$ and f_D with a precision of about 2 % each. With the combination of these three results the ratio f_{D_s}/f_D can be determined to a precision of less than 5 %, better than the precision of current lattice calculations.

Part V

Appendices

Appendix A

Calculation of $\Gamma(D_s^+ \to \mu^+\nu_\mu)$

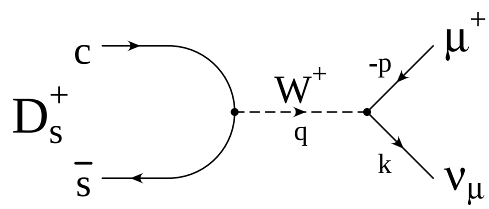

Figure A.1: Feynman diagram for the decay $D_s^+ \to \mu^+\nu_\mu$ with the four momentum $q = p + k$.

In this chapter the partial decay width of the decay $D_s^+(q) \to \mu^+(p)\nu_\mu(k)$, depicted as a Feynman diagram in Figure A.1, is calculated. Here q, p, and k are the momenta of the D_s^+, μ^+, and ν_μ respectively. The decay amplitude is of the form

$$\mathcal{M} = \frac{-ieV_{cs}(\ldots)^\mu}{2\sqrt{2}\sin\theta_W} \times \frac{-ig_{\mu\nu} - \frac{q_\mu q_\nu}{m_W^2}}{q^2 - m_W^2} \times \bar{u}(k)\frac{-ie\gamma_\nu\left(1-\gamma^5\right)}{2\sqrt{2}\sin\theta_W}v(p), \tag{A.1}$$

where $(\ldots)^\mu$ represents the weak quark current. In the decay $D_s^+ \to \mu^+\nu_\mu$ the momentum transfer $q = m_{D_s}$ is much smaller than the mass of the W^+ propagator ($q \ll m_W$). In this limit the propagator term is just $-i\frac{g_{\mu\nu}}{m_W^2}$, and the decay amplitude is

$$\mathcal{M} = i\frac{G_F}{\sqrt{2}}V_{cs}(\ldots)^\mu \bar{u}(k)\gamma_\mu\left(1-\gamma^5\right)v(p), \tag{A.2}$$

where $G_F = \sqrt{2}e^2/(8m_W^2 \sin^2\theta_W)$ is the Fermi constant.

It is tempting to write the quark current as $\bar{u}_c V_{cs}\gamma^\mu(1-\gamma^5)v_{\bar{s}}$. That, though, would be incorrect, since the c and $\bar{s}$ quarks are not free states but bound into a D_s meson. One knows, however, that

- $\mathcal{M}$ is Lorentz-invariant, so $(\ldots)^\mu$ must be a vector or axial-vector, and
- the D_s is spinless, so that q is the only four-vector available to construct $(\ldots)^\mu$.

The only Lorentz invariant scalar that can be formed from q is $q^2 = m_{D_s}^2$, which is constant. One therefore has

$$(\ldots)^\mu = q^\mu f(q^2) \equiv q^\mu f_{D_s}, \tag{A.3}$$

where f_{D_s} is the decay constant of the D_s meson. Inserting equation A.3 into equation A.2 yields

$$\begin{aligned}\mathcal{M} &= i\frac{G_F}{\sqrt{2}}V_{cs}\,(p^\mu + k^\mu)\,f_{D_s}\left[\bar{u}(k)\gamma_\mu(1-\gamma^5)v(p)\right] \\ &= i\frac{G_F}{\sqrt{2}}V_{cs}f_{D_s}m_\mu\bar{u}(k)(1-\gamma^5)v(p).\end{aligned} \tag{A.4}$$

Here the Dirac equation is used for the muon and the neutrino, $(\not{p} - m_\mu)\bar{v}(p) = 0$ and $u(k)\not{k} = 0$, respectively. In the rest frame of the D_s the partial decay rate is

$$d\Gamma = \frac{1}{2m_{D_s}}|\mathcal{M}|^2\frac{d^3\vec{p}}{(2\pi)^3 2E}\frac{d^3\vec{k}}{(2\pi)^3 2\omega}(2\pi)^4\delta(q-p-k), \tag{A.5}$$

where E is the energy of the D_s and ω the energy of the neutrino. Because the *BABAR* detector is blind to the muon polarization, $|\mathcal{M}|^2$ has to be summed over the spin of the muon and the neutrino, using the completeness relations

$$\sum_s u^s(p)\bar{u}^s(p) = \not{p} + m \quad \text{and} \quad \sum_s v^s(p)\bar{v}^s(p) = \not{p} - m. \tag{A.6}$$

It becomes

$$
\begin{aligned}
|\mathcal{M}|^2 &= \frac{G_F^2}{2}|V_{cs}|^2 f_{D_s}^2 m_\mu^2 \mathrm{Tr}\left[\not{k}(1-\gamma^5)(\not{p}-m_\mu)(1+\gamma^5)\right] && \text{(A.7)}\\
&= G_F^2|V_{cs}|^2 f_{D_s}^2 m_\mu^2 \mathrm{Tr}\left[\not{k}(1-\gamma^5)(\not{p}-m_\mu)\right] && \text{(A.8)}\\
&= G_F^2|V_{cs}|^2 f_{D_s}^2 m_\mu^2 \mathrm{Tr}\left[\not{k}\not{p}\right] && \text{(A.9)}\\
&= 4G_F^2|V_{cs}|^2 f_{D_s}^2 m_\mu^2 (k\cdot p) && \text{(A.10)}
\end{aligned}
$$

From (A.7) to (A.8) the relations $\gamma^\mu\gamma^5 = -\gamma^5\gamma^\mu$ and $(1-\gamma^5)^2 = 2(1-\gamma^5)$ were applied. The step from (A.8) to (A.9) uses the fact that the trace over the product of an odd number of γ-matrices is 0. In the D_s rest frame, ($\vec{k} = -\vec{p}$),

$$
k\cdot p = E\omega - \vec{k}\cdot\vec{p} = E\omega + k^2 = \omega(E+\omega). \tag{A.11}
$$

Putting these together results in

$$
\Gamma = \frac{G_F^2|V_{cs}|^2 f_{D_s}^2 m_\mu^2}{(2\pi)^2 2m_{D_s}} \int \frac{d^3\vec{p}\, d^3\vec{k}}{E\omega}\delta(m_{D_s}-E-\omega)\delta^{(3)}(\vec{p}+\vec{k})\omega(E+\omega). \tag{A.12}
$$

The integration of the angular part of $\vec{k}$ simply gives 4π, since there is no angular dependency in $|\mathcal{M}|^2$. Integrating over $d^3\vec{p}$, taken care of by the $\delta^{(3)}$ functional, leads to

$$
\Gamma = \frac{G_F^2|V_{cs}|^2 f_{D_s}^2 m_\mu^2}{(2\pi)^2 2m_{D_s}}\, 4\pi \int_0^\infty d\omega\, \omega^2 \left(1+\frac{\omega}{E(\omega)}\right) \delta(m_{D_s}-E(\omega)-\omega), \tag{A.13}
$$

where $E(\omega) = \sqrt{m_{D_s}^2+\omega^2}$. With $f(\omega) \equiv m_{D_s} - E(\omega) - \omega$ and $|f'(\omega)| = 1+\omega/E(\omega)$ the δ-functional can be written as

$$
\delta(f(\omega)) = \frac{\delta(\omega-\omega_0)}{1+\frac{\omega_0}{E(\omega_0)}}, \tag{A.14}
$$

where

$$
\omega_0 = \frac{m_{D_s}^2 - m_\mu^2}{2m_{D_s}} \tag{A.15}
$$

is the root of $f(\omega)$. This simplification uses the property of the Dirac δ-functional

$$\delta(f(\omega)) = \sum_{\omega_i,\, f(\omega_i)=0} \frac{\delta(\omega - \omega_i)}{\left|\frac{\partial f}{\partial \omega}\right|_{\omega=\omega_i}}, \tag{A.16}$$

The result of the integration in (A.13) is ω_0^2, and the partial decay width is

$$\Gamma = \frac{G_F^2}{8\pi} |V_{cs}|^2 f_{D_s}^2 m_{D_s} m_\mu^2 \left(1 - \frac{m_\mu^2}{m_{D_s}^2}\right)^2. \tag{A.17}$$

Appendix B

IFR Tracking Using a Kalman Filter

B.1 Introduction

In the March 1960 issue of the magazine "Journal of Basic Engineering", published by the American Society of Mechanical Engineering, R.E. Kalman[1] published a paper [48], describing a recursive solution to the so called "Wiener problem", that deals with the prediction of the response of a linear dynamic system in the presence of random Gaussian noise. The simplest solution to this problem is called "Wiener Filter". One of the obstacles found in earlier works was the often enormous amount of computing needed for practical filter application, usually growing exponentially with the measurement complexity. In his now famous paper Kalman describes a new, recursive, approach in which the number of calculation steps grows linearly with the number of measurements, opening an enormous range of applications for the "Kalman Filter".

In experiments in high energy physics Kalman filters are for instance used for fitting the trajectory of a particle to the measurements provided by the tracking system. The dynamic system is the charged particle passing in a magnetic field

[1]Rudolf Emil Kalman, born in Budapest, Hungary, on May 19, 1930, Professor at Stanford 1964-71

through the detector, while losing energy through ionization of the traversed material. The two sources of random noise are the multiple scattering and the fluctuation in the predicted energy loss.

B.2 IFR Tracking and PID

The IFR of the *BABAR* detector is used to separate muons from charged pions. Pions that travel through material undergo a hadronic interaction within a distance L with a probability of $1-e^{-L/\lambda}$, where λ is the hadronic interaction length, the mean free path of a particle between two hadronic interactions. Pions that travel straight outward through the IFR traverse about 5 interaction lengths; the likelihood for a non-elastic interaction – the decay of the particle – is about 99.3 %. Muons on the other hand lose their energy mainly through ionization of the material. Energy loss through photon radiation becomes relevant only at a momentum above 10 GeV/c. Nuclear losses dominate in the momentum region below 100 MeV/c. A muon traversing the whole of the IFR typically loses about 250 MeV in energy.

The IFR is equipped with 19 layers of RPC's, interlaced with the steel plates, which measure the position of the passing particle in two dimensions. The single hit resolution is $\sigma_{\text{hit}} = 1.5$ cm. The trajectory of a charged particle in the IFR is extrapolated from the last known position and direction of the particle in the DCH. The bending of the particle path through the magnetic field and the energy loss in the detector material is taken into account during that extrapolation, for which the forth-order Runge-Kutta approximation is used. Hits, registered in the RPCs, that lie within four σ_{hit} from the extrapolated hit position are associated with the trajectory. From this hit map a number of variables are calculated, which are used for particle identification. Two of these variables have a particularly large discrimination power to separate muons from charged pions. One is the difference $\Delta\lambda$ between the measured number of interaction lengths traversed by the particle and the expected number if the particle were minimum ionizing,

$$\Delta\lambda = \lambda_{\text{meas}} - \lambda_{\text{exp}}. \tag{B.1}$$

The other variable is a χ^2 variable, measuring the agreement of the associated hits with the expected trajectory,

$$\chi^2_{\mathrm{trk}} = \sum_{\mathrm{hits}} \frac{(x_{\mathrm{meas}} - x_{\mathrm{exp}})^2}{\sigma^2_{\mathrm{hit}}}, \tag{B.2}$$

where x_{meas} and x_{exp} are the measured and expected hit positions. For muons $\Delta\lambda$ should be zero, and the distribution of χ^2_{trk}, normalized by the degrees of freedom (d.o.f.), should peak at one. Pions should have a negative $\Delta\lambda$ due to their high likelihood to decay before leaving the detector. Their χ^2_{trk}/d.o.f. should vary over a large range of values, with only a small excess around 1, originating from pions traversing large parts of the IFR without a non-elastic interaction.

The initial approach calculated the expected path as an extrapolation from the DCH; no IFR hit information is used. Multiple scattering, and to a lesser extent the fluctuation in energy loss, change the true path of a particle from its expectation. This broadens the χ^2_{trk} distribution for muons and decreases the muon-pion separation power of this variable.

This can be avoided if the IFR hit information itself, including the effect of multiple scattering and energy-loss fluctuations, is used to determine the most likely particle trajectory. This has been implemented using a Kalman Filter. The implementation however is restricted to multiple scattering, the less significant fluctuations in energy loss are not considered. The errors and correlation of the parameters describing the particle trajectory and the measurement errors are taken into account.

B.3 Multiple Coulomb Scattering through small Angles

The stochastic nature of the Coulomb multiple scattering is that of a Markov process. A particle passing through material is deflected by many small-angle Coulomb scatters on the material nuclei. Hadrons also have a small contribution from strong interaction scatters; in addition a small amount of the scatters have a large deflection angle. Both effects are ignored in the following discussion. The small-angle Coulomb scattering is a three-dimensional process. To treat it mathematically it is sufficient to discuss the planar projection of the scattering process. After the particle travels a distance L through the material with a radiation length X_0, it is displaced from its original path by δx_θ and its direction changed by $\delta\theta$. The variance of this angle is

$$\theta_0 = \frac{13.6\,\mathrm{MeV}}{\beta c p}\sqrt{\frac{L}{X_0}}\left[1 + 0.038\ln\left(\frac{L}{X_0}\right)\right], \tag{B.3}$$

where p and βc are the momentum and velocity of the incident particle, respectively. The constants in (B.3) are determined from fits to the Moliere distribution [49–52]. The angular distribution of $\delta\theta$ is given by

$$\frac{1}{\sqrt{2\pi}\theta_0} e^{-\frac{(\delta\theta)^2}{2\theta_0^2}}. \tag{B.4}$$

B.4 General Kalman Filter Theory

Assume a process is described by an n-dimensional state vector $\boldsymbol{\alpha} \in \mathcal{R}^n$ and a function

$$\boldsymbol{\alpha}_k = \boldsymbol{f}(\boldsymbol{\alpha}_{k-1}, \boldsymbol{\omega}_{k-1}), \tag{B.5}$$

governing its time development in discrete steps, indexed by k. $\boldsymbol{\omega}_k$ represents the process noise present at step k. At each step a measurement of the current state is available,

$$\mathbf{z}_k = \boldsymbol{h}(\boldsymbol{\alpha}_k, \boldsymbol{\nu}_k), \tag{B.6}$$

where the $\boldsymbol{\nu}_k$ represents the measurement error. The covariance matrices of $\boldsymbol{\omega}_k$ and $\boldsymbol{\nu}_k$ are $\boldsymbol{Q}_k$ and $\boldsymbol{R}_k$ respectively. The exact state $\boldsymbol{\alpha}$ of the process is unknown, only an estimate $\hat{\boldsymbol{\alpha}}$ can be made. Also unknown are the size of the process noise $\boldsymbol{\omega}_k$ and the measurement error $\boldsymbol{\nu}_k$ at each step k. From the previous estimate $\hat{\boldsymbol{\alpha}}_{k-1}$, under a no-process-noise assumption ($\boldsymbol{\omega}_k = \mathbf{0}$), the current state $\bar{\boldsymbol{\alpha}}_k$ can be extrapolated.

Assuming no measurement error ($\boldsymbol{\nu}_k = \mathbf{0}$), the measurement $\bar{\mathbf{z}}_k$ can be predicted:

$$\bar{\boldsymbol{\alpha}}_k = \boldsymbol{f}(\hat{\boldsymbol{\alpha}}_{k-1}, \mathbf{0}), \tag{B.7}$$

$$\bar{\mathbf{z}}_k = \boldsymbol{h}(\bar{\boldsymbol{\alpha}}_k, \mathbf{0}), \tag{B.8}$$

The extrapolation $\bar{\boldsymbol{\alpha}}_k$ is not yet the estimate $\hat{\boldsymbol{\alpha}}_k$ for step k, which is calculated from the $\bar{\boldsymbol{\alpha}}_k$ and the measurement $\mathbf{z}_k$. Let $\boldsymbol{\Delta}\mathbf{z}$ denote the difference between the measurement and its prediction,

$$\boldsymbol{\Delta}\mathbf{z}_k = \mathbf{z}_k - \bar{\mathbf{z}}_k. \tag{B.9}$$

The Kalman Filter in its simplest form applies only to linear functions $\boldsymbol{f}$ and $\boldsymbol{h}$. If the process or the relationship between the process state and the measurement is non-linear, the *extended Kalman filter* must be used. This requires a linearization of $\boldsymbol{f}$ and $\boldsymbol{h}$ through a first order Taylor expansion. For this the Jacobian matrices of $\boldsymbol{f}$ and $\boldsymbol{h}$ with respect to $\boldsymbol{\alpha}$, $\boldsymbol{\omega}$, and $\boldsymbol{\nu}$ are calculated. The process Jacobians are

$$\boldsymbol{A}_{k\,[ij]} = \frac{\partial f_i}{\partial \alpha_j}(\hat{\boldsymbol{\alpha}}_{k-1}, \mathbf{0}) \quad \text{and} \tag{B.10}$$

$$\boldsymbol{W}_{k\,[ij]} = \frac{\partial f_i}{\partial \omega_j}(\hat{\boldsymbol{\alpha}}_{k-1}, \mathbf{0}), \tag{B.11}$$

and the measurement Jacobians are

$$\boldsymbol{H}_{k\,[ij]} = \frac{\partial h_i}{\partial \alpha_j}(\bar{\boldsymbol{\alpha}}_k, \mathbf{0}) \quad \text{and} \tag{B.12}$$

$$\boldsymbol{V}_{k\,[ij]} = \frac{\partial h_i}{\partial \nu_j}(\bar{\boldsymbol{\alpha}}_k, \mathbf{0}), \tag{B.13}$$

all evaluated with the estimate $\hat{\boldsymbol{\alpha}}_{k-1}$. The process Jacobians are used to calculate the stepwise development of the $n \times n$ error covariance matrix of the state parameters, $\boldsymbol{P}_k$, which is defined as

$$\boldsymbol{P}_k = \langle \Delta\boldsymbol{\alpha}_k \Delta\boldsymbol{\alpha}_k^T \rangle, \tag{B.14}$$

with $\Delta\boldsymbol{\alpha}_k = \boldsymbol{\alpha}_k - \hat{\boldsymbol{\alpha}}_k$. The two equations that describe the extrapolation of the process state and its error covariance matrix from the previous step $k-1$ to the current step k are summarized in the *time update equations*

$$\bar{\boldsymbol{\alpha}}_k = \boldsymbol{f}(\hat{\boldsymbol{\alpha}}_{k-1}, \mathbf{0}) \quad \text{and} \tag{B.15}$$

$$\bar{\boldsymbol{P}}_k = \boldsymbol{A}_k \boldsymbol{P}_{k-1} \boldsymbol{A}_k^T + \boldsymbol{W}_k \boldsymbol{Q}_k \boldsymbol{W}_k^T. \tag{B.16}$$

In (B.16) the correlated process noise errors add to the state error covariance matrix. To weight the importance of the measurement of step k, whose error is given by $\boldsymbol{R}_k$, relative to all previous measurements, whose errors are accumulated in $\boldsymbol{P}_k$, the *Kalman gain*, $\boldsymbol{K}_k$, is defined,

$$\boldsymbol{K}_k = \bar{\boldsymbol{P}}_k \boldsymbol{H}_k^T \left(\boldsymbol{H}_k \bar{\boldsymbol{P}}_k \boldsymbol{H}_k^T + \boldsymbol{V}_k \boldsymbol{R}_k \boldsymbol{V}_k^T \right)^{-1}. \tag{B.17}$$

Using the gain $\boldsymbol{K}_k$ and the measurement $\mathbf{z}_k$, the process state and its error covariance matrix are updated according to the *measurement update equations*

$$\hat{\boldsymbol{\alpha}}_k = \bar{\boldsymbol{\alpha}}_k + \boldsymbol{K}_k \boldsymbol{\Delta} \mathbf{z}_k \quad \text{and} \tag{B.18}$$

$$\boldsymbol{P}_k = (\boldsymbol{I} - \boldsymbol{K}_k \boldsymbol{H}_k) \bar{\boldsymbol{P}}_k. \tag{B.19}$$

This iterative process repeats until the last measurement is reached, resulting in a set of state vectors $\hat{\boldsymbol{\alpha}}_k$ describing the process in its time development.

B.5 Implementation for the IFR

B.5.1 Definition of the Track and Measurement Representations

What has been generally described as process in the previous section is, in the concrete implementation of particle tracking in the IFR, the passing of a charged track through the layers of the IFR. The 6-dimensional state vector $(n = 6)$ is composed of the position and the momentum of the particle,

$$\boldsymbol{\alpha} = \begin{pmatrix} x \\ y \\ z \\ p_x \\ p_y \\ p_z \end{pmatrix}. \tag{B.20}$$

Each RPC layer measures the track position in two dimensions, whose orientations are, with the exception of the innermost RPC, orthogonal to each other. The 2-dimensional measurement vector ($m = 2$) depends on the orientation of the RPC plane within the IFR,

$$\mathbf{z} = \begin{pmatrix} z_u \\ z_v \end{pmatrix} = z_u \, \hat{u} + z_v \, \hat{v}, \tag{B.21}$$

where $\hat{u} = (u_x, u_y, u_z)$ and $\hat{v} = (v_x, v_y, v_z)$ are unit vectors that span the RPC plane, and that point along the two directions of the RPC strips in each layer. The measurements of the position in the two dimensions are independent of each other. The measurement error covariance matrix is

$$\boldsymbol{R}_k = \begin{pmatrix} \sigma_m^2 & 0 \\ 0 & \sigma_m^2 \end{pmatrix}, \tag{B.22}$$

with $\sigma_m = 1.5$ cm.

The process noise $\boldsymbol{\omega}$ is the multiple Coulomb scattering. It is described by two variables, the previously introduced scatter angle $\delta\theta$ and the spatial offset δx_θ, now normalized to the thickness of the traversed material,

$$\boldsymbol{\omega}_k = \begin{pmatrix} \delta x_\theta / L \\ \delta\theta \end{pmatrix}. \tag{B.23}$$

B.5.2 The Process Covariance Matrix

From (B.4) follows immediately

$$\left\langle (\delta\theta)^2 \right\rangle = \left\langle \left(\delta\theta - \langle\delta\theta\rangle\right)^2 \right\rangle = \theta_0^2. \tag{B.24}$$

The scatter angle $\delta\theta$ is the sum of a number of independent small angle single scatters, $\delta\theta = \sum_i \theta_i$. Each of those single scatters contributes to the final displacement $\delta x_\theta = \sum l_i \theta_i$, where l_i is the distance of the i-th single scatter point from the point where the displacement is measured. For the remainder of the covariance matrix $\boldsymbol{Q}_k$ two terms are calculated,

$$\begin{aligned} \langle \delta x_\theta \delta\theta \rangle &= \left\langle \sum l_i\theta_i \sum \theta_i \right\rangle = \left\langle \bar{l} \left(\sum \theta_i\right)^2 \right\rangle \\ &= \left\langle \bar{l} \right\rangle \left\langle (\delta\theta)^2 \right\rangle = \frac{L}{2}\,\theta_0^2 \end{aligned} \tag{B.25}$$

and

$$\begin{aligned} \left\langle (\delta x_\theta)^2 \right\rangle &= \left\langle \left(\sum l_i\theta_i\right)^2 \right\rangle = \left\langle \left(\sum l_i\right)^2 \left(\sum \theta_i\right)^2 \right\rangle = \left\langle \sum l_i^2 \left(\sum \theta_i\right)^2 \right\rangle \\ &= \left\langle\, \overline{l^2}\, \right\rangle \left\langle (\delta\theta)^2 \right\rangle = \frac{L^2}{3}\,\theta_0^2, \end{aligned} \tag{B.26}$$

where the independence of the scatter angles θ_i and the scatter locations l_i has been used. The process covariance matrix is

$$\boldsymbol{Q}_k = \left\langle \left(\frac{\delta x_\theta}{L}, \delta\theta\right)^T \left(\frac{\delta x_\theta}{L}, \delta\theta\right) \right\rangle = \theta_0^2 \begin{pmatrix} \frac{1}{3} & \frac{1}{2} \\ \frac{1}{2} & 1 \end{pmatrix}. \tag{B.27}$$

B.5.3 The Process Jacobians

The process Jacobians $\boldsymbol{A}_k$ and $\boldsymbol{W}_k$ are difficult to calculate, since the process of a particle traversing the IFR has no closed analytic expression. Rather the particle trajectory is extrapolated from the previous estimate $\boldsymbol{\alpha}_{k-1}$ to $\bar{\boldsymbol{\alpha}}_k$ using the detector model and the magnetic field information, a method dubbed *swimming of the particle*.

$\boldsymbol{A}_k$	6×6	$\boldsymbol{H}_k$	2×6
$\boldsymbol{W}_k$	6×4	$\boldsymbol{V}_k$	2×2

Table B.1: Dimensions of Jacobians

The Jacobian $\boldsymbol{A}_k$

The 6×6 matrix $\boldsymbol{A}_k$ relates the previous estimate $\boldsymbol{\alpha}_{k-1}$ with the current extrapolation $\bar{\boldsymbol{\alpha}}_k$.

$$\begin{aligned}\bar{\boldsymbol{\alpha}}_k &= \boldsymbol{f}(\hat{\boldsymbol{\alpha}}_{k-1}) = \hat{\boldsymbol{\alpha}}_{k-1} + \Delta\boldsymbol{\alpha} \\ &= (\boldsymbol{I}_6 + \boldsymbol{A}_k(p_x, p_y, p_z))\,\hat{\boldsymbol{\alpha}}_{k-1}\end{aligned} \tag{B.28}$$

where $\boldsymbol{I}_6$ is the six-dimensional identity matrix. The matrix $\boldsymbol{A}_k$ depends only on the particle momentum but not on the particle position. The increment $\boldsymbol{A}_k\hat{\boldsymbol{\alpha}}_{k-1}$ is the output of the steps algorithm, the *swimmer*. The swimmer is stepping through the IFR from layer $k-1$ to layer k using Runge-Kutta approximation of the equations describing the motion of a charge particle in a magnetic field. The precision of this method is of the order 10^{-10}. For each of these steps the average momentum $\bar{p}$ and the distance L between the start and end point of the step are calculated. The matrix $\widetilde{\boldsymbol{A}}$, relating the states before and after a single step, is

$$\widetilde{\boldsymbol{A}} = \begin{pmatrix} \boldsymbol{I}_3 & \dfrac{L}{p}\boldsymbol{I}_3 \\ \boldsymbol{0}_3 & \boldsymbol{M} \end{pmatrix}, \tag{B.29}$$

with the 3×3 matrix $\boldsymbol{M}$ describing the rotation the track direction undergoes during this step. The matrix $\boldsymbol{M}$ is given by

$$
\begin{aligned}
\boldsymbol{M} &= \cos\phi\,\boldsymbol{I}_3 + (1-\cos\phi)\begin{pmatrix} a_1^2 & a_1a_2 & a_1a_3 \\ a_1a_2 & a_2^2 & a_2a_3 \\ a_1a_3 & a_2a_3 & a_3^2 \end{pmatrix} + \sin\phi \begin{pmatrix} 0 & -a_3 & a_2 \\ a_3 & 0 & -a_1 \\ -a_2 & a_1 & 0 \end{pmatrix} \\
&= \cos\phi\,\boldsymbol{I}_3 + (1-\cos\phi)\,\hat{\boldsymbol{a}}^T\hat{\boldsymbol{a}} + \sin\phi\,\hat{\boldsymbol{a}} \times \begin{pmatrix} \hat{\boldsymbol{e}}_x & \hat{\boldsymbol{e}}_y & \hat{\boldsymbol{e}}_z \end{pmatrix},
\end{aligned} \tag{B.30}
$$

where $\hat{\boldsymbol{a}}$ is the axis of the track rotation and ϕ is the rotation angle. Assuming N is the number of steps involved to *swim* a particle trajectory from region $k-1$ to region k the matrix $\boldsymbol{A}_k$ can be written as

$$
\boldsymbol{A}_k = \widetilde{\boldsymbol{A}}_N\,\widetilde{\boldsymbol{A}}_{N-1}\cdots\widetilde{\boldsymbol{A}}_2\cdots\widetilde{\boldsymbol{A}}_1 \tag{B.31}
$$

$$
= \begin{pmatrix} \boldsymbol{I}_3 & \dfrac{L_1}{p_1} + \left(\cdots\left(\dfrac{L_{N-1}}{p_{N-1}} + \dfrac{L_N}{p_N}\boldsymbol{M}_{N-1}\right)\cdots\right)\boldsymbol{M}_1 \\ \boldsymbol{0}_3 & \boldsymbol{M}_N\boldsymbol{M}_{N-1}\cdots\boldsymbol{M}_2\boldsymbol{M}_1 \end{pmatrix}. \tag{B.32}
$$

The calculation of $\boldsymbol{A}_k$ is the task of the swimmer.

The Jacobian $\boldsymbol{W}_k$

The Jacobian $\boldsymbol{W}_k$, the derivative of the process dynamics $\boldsymbol{f}(\boldsymbol{\alpha}, \boldsymbol{\omega})$ with respect to the process noise $\boldsymbol{\omega}$ can be written as the product of $\boldsymbol{A}_k$ and a matrix $\boldsymbol{T}_k$ that transforms $\boldsymbol{\omega}_k$ into the state coordinate system,

$$
\begin{aligned}
\boldsymbol{W}_{k\,[ij]} &= \frac{\partial f_i}{\partial \omega_j}(\hat{\boldsymbol{\alpha}}_{k-1}, 0) \\
&= \left(\frac{\partial f_i}{\partial \alpha_l}\frac{\partial \alpha_l}{\partial \omega_j}\right)(\hat{\boldsymbol{\alpha}}_{k-1}, 0) \\
&= \boldsymbol{A}_{k\,[il]}\frac{\partial \alpha_l}{\partial \omega_j}(\hat{\boldsymbol{\alpha}}_{k-1}, 0) \\
&= \boldsymbol{A}_{k\,[il]}\boldsymbol{T}_{k\,[lj]} = (\boldsymbol{A}_k\boldsymbol{T}_k)_{[ij]}.
\end{aligned} \tag{B.33}
$$

Thus (B.16) can be written as

$$\bar{\boldsymbol{P}}_k = \boldsymbol{A}_k \left(\boldsymbol{P}_{k-1} + \boldsymbol{T}_k \boldsymbol{Q}_k \boldsymbol{T}_k^T \right) \boldsymbol{A}_k^T. \tag{B.16'}$$

In order to calculate the 6×4 matrix $\boldsymbol{T}_k$, the process noise $\boldsymbol{\omega}_k$ is extented to four dimensions,

$$\boldsymbol{\omega}_k = \begin{pmatrix} \delta x_{\theta_t}/L \\ \delta x_{\phi_t}/L \\ \delta\theta_t \\ \delta\phi_t \end{pmatrix}, \tag{B.34}$$

describing the multiple scattering in the two perpenticular planes $\hat{n}_t \times \hat{\theta}_t$ and $\hat{n}_t \times \hat{\phi}_t$. In (B.34) $\delta x_{\theta_t}, \delta x_{\phi_t}, \delta\theta_t$, and $\delta\phi_t$ are the displacements and the deflection angles in the two planes. The orthogonal unit vectors

$$\hat{n}_t = \begin{pmatrix} p_x \\ p_y \\ p_z \end{pmatrix} / \sqrt{p_x^2 + p_y^2 + p_z^2} = \begin{pmatrix} \sin\theta_t \cos\phi_t \\ \sin\theta_t \sin\phi_t \\ \cos\theta_t \end{pmatrix}, \tag{B.35}$$

$$\hat{\theta}_t = \begin{pmatrix} \cos\theta_t \cos\phi_t \\ \cos\theta_t \sin\phi_t \\ -\sin\theta_t \end{pmatrix}, \quad \text{and} \tag{B.36}$$

$$\hat{\phi}_t = \begin{pmatrix} -\sin\phi_t \\ \cos\phi_t \\ 0 \end{pmatrix} \tag{B.37}$$

form a right handed system. Writing $\Delta\boldsymbol{\alpha}_k = \boldsymbol{T}_k\,\boldsymbol{\omega}_k$ down explicitly,

$$\Delta\begin{pmatrix} x \\ y \\ z \\ p_x \\ p_y \\ p_z \end{pmatrix} = \begin{pmatrix} L\cos\theta_t\cos\phi_t & -L\sin\phi_t & 0 & 0 \\ L\cos\theta_t\sin\phi_t & L\cos\phi_t & 0 & 0 \\ -L\sin\theta_t & 0 & 0 & 0 \\ 0 & 0 & p\cos\theta_t\cos\phi_t & -p\sin\phi_t \\ 0 & 0 & p\cos\theta_t\sin\phi_t & p\cos\phi_t \\ 0 & 0 & -p\sin\theta_t & 0 \end{pmatrix} \begin{pmatrix} \delta x_{\theta_t}/L \\ \delta x_{\phi_t}/L \\ \delta\theta_t \\ \delta\phi_t \end{pmatrix} \tag{B.38}$$

leads to

$$\boldsymbol{T}_k = \begin{pmatrix} L\,\boldsymbol{C}_1 & \boldsymbol{0} \\ \boldsymbol{0} & p\,\boldsymbol{C}_1 \end{pmatrix}, \quad \text{where} \quad \boldsymbol{C}_1 = \begin{pmatrix} \cos\theta_t\cos\phi_t & -\sin\phi_t \\ \cos\theta_t\sin\phi_t & \cos\phi_t \\ -\sin\theta_t & 0 \end{pmatrix} \tag{B.39}$$

The noise covariance matrix $\boldsymbol{Q}_k$, extended to a 4×4 matrix, transforms into the state coordinate system according to

$$\boldsymbol{T}_k\boldsymbol{Q}_k\boldsymbol{T}_k^T = \theta_0^2\,\boldsymbol{T}\begin{pmatrix} \frac{1}{3} & 0 & \frac{1}{2} & 0 \\ 0 & \frac{1}{3} & 0 & \frac{1}{2} \\ \frac{1}{2} & 0 & 1 & 0 \\ 0 & \frac{1}{2} & 0 & 1 \end{pmatrix}\boldsymbol{T}^T = \theta_0^2\begin{pmatrix} \dfrac{1}{3}L^2\,\boldsymbol{C}_2 & \dfrac{1}{2}Lp\,\boldsymbol{C}_2 \\ \dfrac{1}{2}Lp\,\boldsymbol{C}_2^T & p^2\,\boldsymbol{C}_2 \end{pmatrix}, \tag{B.40}$$

where

$$\boldsymbol{C}_2 = \begin{pmatrix} 1-\sin^2\theta_t\cos^2\phi_t & -\sin^2\theta_t\sin\phi_t\cos\phi_t & -\sin\theta_t\cos\theta_t\cos\phi_t \\ -\sin^2\theta_t\sin\phi_t\cos\phi_t & 1-\sin^2\theta_t\sin^2\phi_t & -\sin\theta_t\cos\theta_t\sin\phi_t \\ -\sin\theta_t\cos\theta_t\cos\phi_t & -\sin\theta_t\cos\theta_t\sin\phi_t & \sin^2\theta_t \end{pmatrix}$$
$$= \begin{pmatrix} 1-d_x^2 & -d_xd_y & -d_xd_z \\ -d_xd_y & 1-d_y^2 & -d_yd_z \\ -d_xd_z & -d_yd_z & 1-d_z^2 \end{pmatrix}, \quad \text{with } \vec{d} = \vec{p}/p \tag{B.41}$$

B.5.4 The Measurement Jacobians

The measurement Jacobians $\boldsymbol{H}_k$ and $\boldsymbol{V}_k$ are easier to calculate then the process Jacobians, since $\boldsymbol{h}$ has a simple analytic expression. The function $\boldsymbol{h}$ relates the coordinate system of the RPCs $(\hat{u}, \hat{v}, \hat{u} \times \hat{v})$, in which the measurements $\mathbf{z}$ are taken, with the global *BABAR* coordinate system $(\hat{x}, \hat{y}, \hat{z})$ in which the state vector $\boldsymbol{\alpha}$ is described.

The Jacobian $\boldsymbol{H}_k$

The 2×6 matrix $\boldsymbol{H}_k$ transforms the error of the state vector $\Delta\boldsymbol{\alpha}_k$ into the local two-dimensional coordinate system of the current RPC plane, which is defined by two orthogonal unit vectors $\hat{u}$ and $\hat{v}$. The RPC plane has an offset vector $\vec{r}_p$, which points from the origin of the global coordinate system into the plane, so that the points in the plane can be described by

$$\vec{r}_p + \beta\vec{u} + \gamma\vec{v}, \tag{B.42}$$

where β and γ are the local coordinates of the point. The state vector can be written as

$$\boldsymbol{\alpha} = (x, y, z, p_x, p_y, p_z) = (\vec{r}_t, p\hat{n}_t)\,. \tag{B.43}$$

The intersection between a line, the approximation of the trajectory in the vicinity of the RPC, and a plane is given by

$$\vec{r}_t + \alpha\hat{n}_t = \vec{r}_p + \beta\vec{u} + \gamma\vec{v} \tag{B.44}$$

which gives the relation between the local coordinates β and γ and x, y, and z. Equation (B.44) can be rewritten as

$$\begin{pmatrix} a_x & u_x & v_x \\ a_y & u_y & v_y \\ a_z & u_z & v_z \end{pmatrix} \begin{pmatrix} \alpha \\ \beta \\ \gamma \end{pmatrix} = \begin{pmatrix} x - r_{p\,x} \\ y - r_{p\,y} \\ z - r_{p\,z} \end{pmatrix}, \tag{B.45}$$

or

$$\begin{pmatrix} \alpha \\ \beta \\ \gamma \end{pmatrix} = \boldsymbol{B}(\vec{r}_t - \vec{r}_p) \tag{B.46}$$

The partial derivatives of $\boldsymbol{h}$ with respect to x, y, and z can now be calculated as

$$\frac{\partial h_1}{\partial x_i} = \frac{\partial \beta}{\partial x_i} = \boldsymbol{B}_{2i} \tag{B.47}$$

$$\frac{\partial h_2}{\partial x_i} = \frac{\partial \gamma}{\partial x_i} = \boldsymbol{B}_{3i} \tag{B.48}$$

The matrix $\boldsymbol{H}_k$ is

$$\boldsymbol{H}_k = \begin{pmatrix} \frac{\partial h_1}{\partial x} & \frac{\partial h_1}{\partial y} & \frac{\partial h_1}{\partial z} & 0 & 0 & 0 \\ \frac{\partial h_2}{\partial x} & \frac{\partial h_2}{\partial y} & \frac{\partial h_2}{\partial z} & 0 & 0 & 0 \end{pmatrix} = \begin{pmatrix} \boldsymbol{B}_{21} & \boldsymbol{B}_{22} & \boldsymbol{B}_{23} & 0 & 0 & 0 \\ \boldsymbol{B}_{31} & \boldsymbol{B}_{32} & \boldsymbol{B}_{33} & 0 & 0 & 0 \end{pmatrix} \tag{B.49}$$

More elegantly the elements of $\boldsymbol{B}$ can be written as

$$\boldsymbol{B}_{2i} = \frac{(\hat{v} \times \hat{n}_t)_i}{(\hat{v} \times \hat{n}_t) \cdot \hat{u}} \tag{B.50}$$

$$\boldsymbol{B}_{3i} = \frac{(\hat{u} \times \hat{n}_t)_i}{(\hat{u} \times \hat{n}_t) \cdot \hat{v}}, \tag{B.51}$$

simplifying

$$\boldsymbol{H}_k = \frac{1}{(\hat{u} \times \hat{v}) \cdot \hat{n}_t} \begin{pmatrix} (\hat{v} \times \hat{n}_t)^T & \vec{0} \\ (\hat{n}_t \times \hat{u})^T & \vec{0} \end{pmatrix} \tag{B.52}$$

The Jacobian $\boldsymbol{V}_k$

The 2×2 matrix $\boldsymbol{V}_k$ is just the identity matrix $\boldsymbol{I}_2$, since the measurement errors are already in the RPC local coordinate system,

$$\boldsymbol{V}_k = \begin{pmatrix} 1 & 0 \\ 0 & 1 \end{pmatrix}. \tag{B.53}$$

B.5.5 Calculation of χ^2

As previously mentioned, a variable χ^2_{trk} is used to quantify the agreement of the measured hits with the predicted trajectory. Each RPC layer contributes toward the χ^2 with its measurement $\mathbf{z}_k$ according to

$$\chi^2_{\text{trk}} = \sum_k \chi^2_k = \sum_k (\boldsymbol{\Delta}\mathbf{z}_k)^T \boldsymbol{R}_k^{-1} \left(\boldsymbol{I} - \boldsymbol{H}_k \boldsymbol{P}_k \boldsymbol{H}_k^T \boldsymbol{R}_k^{-1} \right) (\boldsymbol{\Delta}\mathbf{z}_k), \tag{B.54}$$

where the first term comes from the measurement uncertainty and the second term from the error in the track parameters.

B.6 Results

The most important aspect of an improved tracking algorithm is the effect it has on the muon identification. The identification of muons in the *BABAR* detector is performed by neural net based muon selectors with different efficiencies. It is desired that the pion rejection power of the selectors goes up, while the muon selection efficiency stays constant. The selector performance is evaluated using a muon and a charged pion control sample, (Section 4.3.1).

Distribution of $\sqrt{\chi^2_{\mathbf{trk}}/\mathbf{d.o.f.}}$ and Muon Selector Performance

The variable that changes with the employment of the Kalman filter, and that underlies the muon selection, is $\chi^2_{\rm trk}$, Figure B.1 compares the distribution of $\sqrt{\chi^2_{\rm trk}/{\rm d.o.f.}}$ for muons from before and after the Kalman filter algorithm was implemented. The Kalman filter improves $\sqrt{\chi^2_{\rm trk}/{\rm d.o.f.}}$, resulting in a narrower distribution for muons, with a peak centering at one. The $\sqrt{\chi^2_{\rm trk}/{\rm d.o.f.}}$ distribution of pions looks distinctly

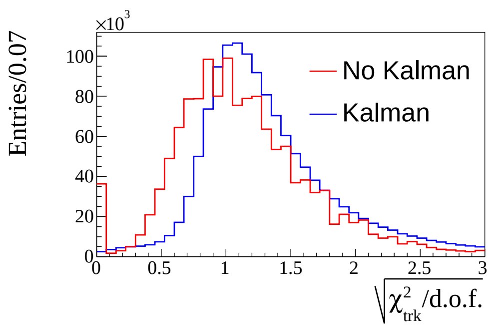

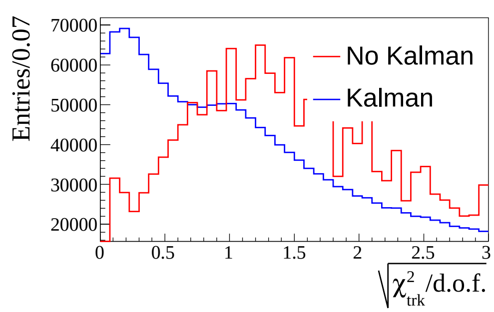

Figure B.1: The distribution of $\sqrt{\chi^2_{\rm trk}/{\rm d.o.f.}}$ for muons (left) and pions (right) before (red) and after (blue) the Kalman filter was implemented. The data are taken from Run 1 through Run 3.

different from that of muons with the Kalman filter employed. The small excess around 1 includes pions that traverse the IFR for some distance before they decay.

After the Kalman filter algorithm had been implemented, the neural nets of the muon selectors were retrained. The muon and pion selection efficiencies of the tight neural net based muon selector, which is used in this analysis to select the signal muons, are shown in Figure B.2 as a function of the particle momentum. With an only slightly lower muon efficiency the pion selection rate has decreased by at least 30 % over the entire momentum range.

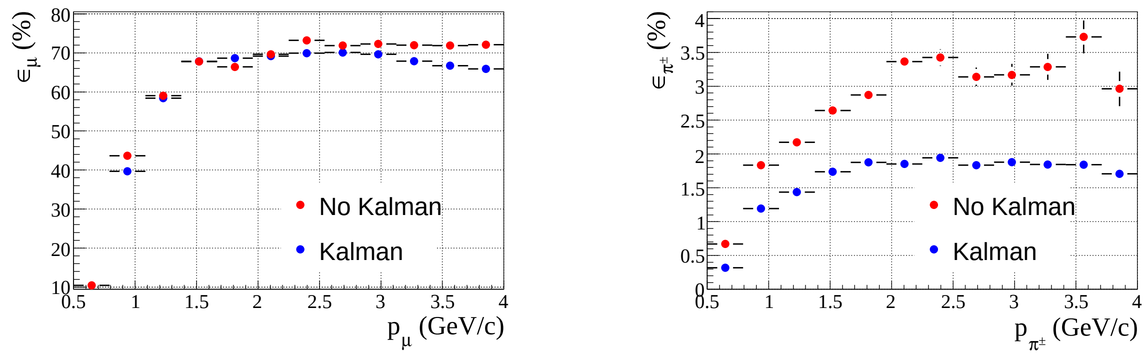

Figure B.2: Selection efficiency of the tight neural net based muon selector as a function of the particle momentum for muons (left) and pions (right). The red histograms show the performance before the Kalman filter implementation, the blue histograms thereafter. The data are taken from Run 2.

In order to fulfill the demands that the broad spectrum of *BABAR* physics analysis has on the efficiency and purity of the muon selection, four different neural net based muon selectors were defined. Figure B.3 shows the performance of each selector in the forward and the central region of the detector, for low and high momentum muons and pions. Plotted is the pion rejection rate versus the muon efficiency. The closer that a selector approaches the upper right corner, the better is its performance. With the Kalman filter implemented the selectors perform consistently better.

Conclusion and Remarks

The employment of the Kalman filter technique within the IFR tracking algorithm has been a great success. Especially in the high-momentum region, which is most important for this analysis, the pion rejection rate increased, in absolute terms, by 0.5 % to 2 %, while keeping the muon efficiency constant. This translates to a drop in the pion misidentification rate of 15 % to 30 % for the tight selectors, which are characterized by a lower muon efficiency and a higher pion rejection rate.

There will always be a small amount of charged pions that traverse the IFR without any inelastic interaction. Exactly like muons they only lose their energy through minimum ionization. Due to the similar masses of charged pions (140 MeV) and muons (106 MeV) the difference in energy loss has negligible effect on the particle

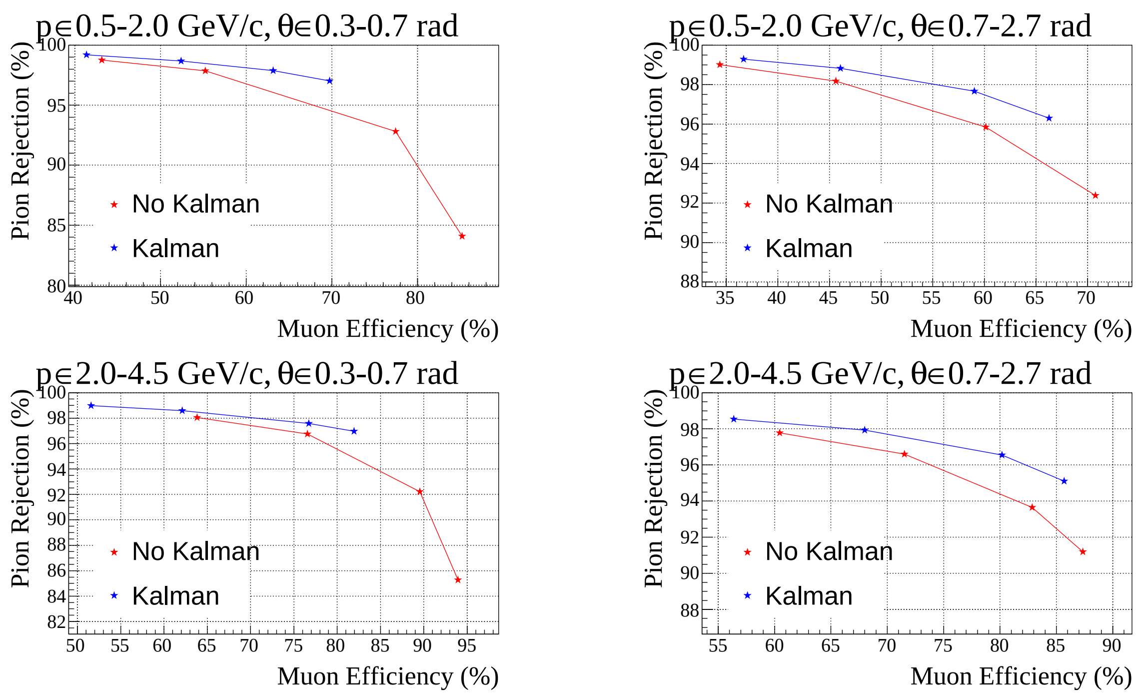

Figure B.3: Performance curves – pion rejection versus muon efficiency – for different momentum and theta ranges. The red curves show the performance before the Kalman filter implementation, the blue curves thereafter. The data are taken from Run 2.

trajectory within the position resolution of the IFR. For that reason it is not possible to determine the true nature of these pions and a small rate of pions faking muons will remain.

Multiple scattering has a non-Gaussian contribution at large scattering angles. This part of the scatter spectrum can not be handled by the Kalman filter, resulting in a large tail to the right side of the χ^2_{trk}/d.o.f. spectrum, or even the loss of the particle trajectory. This was already the case in the IFR tracking algorithm before the Kalman filter was implemented, hence there is no loss in performance after the Kalman filter was employed.

Bibliography

[1] K. G. Wilson, Phys. Rev. D **10**, 2445 (1974).

[2] C. T. H. Davies *et al.* [HPQCD collaboration], Phys. Rev. Lett. **92**, 022001 (2004).

[3] V. A. Novikov *et al.*, Phys. Rept. **41**, 1 (1978).

[4] D. J. Broadhurst, Phys. Lett. B **101**, 423 (1981).

[5] T. M. Aliev and V. L. Eletsky, Sov. J. Nucl. Phys. **38**, 936 (1983).

[6] L. J. Reinders, H. Rubinstein and S. Yazaki, Phys. Rept. **127**, 1 (1985).

[7] M. A. Shifman, A. I. Vainshtein and V. I. Zakharov, Nucl. Phys. B **147**, 385 (1979).

[8] S. Narison, Phys. Lett. B **520**, 115 (2001).

[9] A. G. Grozin, *Heavy Quark Effective Theory* (Springer, 2004).

[10] C. Aubin *et al.*, Phys. Rev. Lett. **95**, 122002 (2005).

[11] A. X. El-Khadra, A. S. Kronfeld, P. B. Mackenzie, S. M. Ryan and J. N. Simone, Phys. Rev. D **58**, 014506 (1998).

[12] K. C. Bowler *et al.* [UKQCD collaboration], Nucl. Phys. B **619**, 507 (2001).

[13] C. Bernard *et al.* [MILC collaboration], Phys. Rev. D **66**, 094501 (2002).

[14] J. L. Rosner, Phys. Rev. D **42**, 3732 (1990).

[15] D. S. Hwang and Y.-Y. Keum, Phys. Rev. D **61**, 073003 (2000).

[16] B. Aubert *et al.* [*BABAR* collaboration], Phys. Rev. D **71**, 091104 (2005).

[17] Stockdale, I. E. [MARK-III collaboration], Presented at the Int. Sympos. on the Production and Decay of Heavy Flavors, Stanford, CA, Sep 1-5, 1987.

[18] S. Aoki *et al.* [WA75 collaboration], Prog. Theor. Phys. **89**, 131 (1993).

[19] K. Kodama *et al.* [Fermilab E653 collaboration], Phys. Lett. B **382**, 299 (1996).

[20] J. Z. Bai *et al.* [BES collaboration], (1996), SLAC-PUB-7147.

[21] J. D. Standifird, (1997), UMI-97-34359.

[22] M. Acciarri *et al.* [L3 collaboration], Phys. Lett. B **396**, 327 (1997).

[23] M. Chadha *et al.* [CLEO collaboration], Phys. Rev. D **58**, 032002 (1998).

[24] Y. Alexandrov *et al.* [BEATRICE collaboration], Phys. Lett. B 478 , 31 (2000).

[25] G. Abbiendi *et al.* [OPAL collaboration], Phys. Lett. B **516**, 236 (2001).

[26] A. Heister *et al.* [ALEPH collaboration], Phys. Lett. B **528**, 1 (2002).

[27] M. Artuso *et al.* [CLEO collaboration], hep-ex/0508057.

[28] M. Ablikim *et al.* [BES collaboration], Phys. Lett. B **610**, 183 (2005).

[29] B. Aubert *et al.* [*BABAR* collaboration], hep-ex/0408091.

[30] S. Eidelman *et al.* [Particle Data Group collaboration], Phys. Lett. B **592**, 1 (2004).

[31] W.-S. Hou, Phys. Rev. D **48**, 2342 (1993).

[32] P. Bock *et al.* [ALEPH, DELPHI, L3 and OPAL collaboration], CERN-EP-2000-055.

[33] K. Abe *et al.* [Belle collaboration], hep-ex/0507034.

[34] J. Charles *et al.* [CKMfitter Group collaboration], Eur. Phys. J. C **41**, 1 (2005).

[35] e. Harrison, P. F. and e. Quinn, Helen R. [BABAR collaboration], (1998), The BaBar physics book: Physics at an asymmetric B factory.

[36] K. Anikeev *et al.* [HFAG collaboration], hep-ex/0505100.

[37] S. Aoki *et al.* [JLQCD collaboration], Phys. Rev. Lett. **91**, 212001 (2003).

[38] D. Becirevic, ECONF C **0304052**, WG202 (2003).

[39] R. H. Siemann, Lect. Notes Phys. **425**, 327 (1992).

[40] T. Sjostrand *et al.*, Comput. Phys. Commun. **135**, 238 (2001).

[41] D. J. Lange, Nucl. Instrum. Meth. A **462**, 152 (2001).

[42] S. Agostinelli *et al.* [GEANT4 collaboration], Nucl. Instrum. Meth. A **506**, 250 (2003).

[43] S. Jadach, B. F. L. Ward and Z. Was, Comput. Phys. Commun. **130**, 260 (2000).

[44] S. Jadach, Z. Was, R. Decker and J. H. Kuhn, Comput. Phys. Commun. **76**, 361 (1993).

[45] G. C. Fox and S. Wolfram, Phys. Rev. Lett. **41**, 1581 (1978).

[46] N. Berger, Package for the simultaneous optimization of selection cuts based on MINUIT.

[47] A. Anastassov *et al.* [CLEO collaboration], Phys. Rev. D **55**, 2559 (1997).

[48] R. E. Kalman, Transactions of the ASME, Journal of Basic Engineering, Series D **82**, 35 (1960).

[49] H. A. Bethe, Phys.R̃ev. **89**, 1256 (1953).

[50] W. T. Scott, Rev. Mod. Phys. **35**, 231 (1963).

[51] V. L. Highland, Nucl. Instr. Meth. **129**, 497 (1975).

[52] G. R. Lynch and O. I. Dahl, Nucl. Instrum. Meth. B **58**, 6 (1991).